12-18-2014

Development of Novel Protein-Based MRI Contrast Agents for the Molecular Imaging of Cancer Biomarkers

Fan Pu

DEVELOPMENT OF NOVEL PROTEIN-BASED MRI CONTRAST AGETNS FOR THE MOLECULAR IMAGING OF CANCER BIOMARKERS

by

Fan Pu

Under the Direction of Jenny J. Yang, PhD

ABSTRACT

Temporal and spatial molecular imaging of disease biomarkers using non-invasive MRI with high resolution is largely limited by lack of MRI contrast agents with high sensitivity, high specificity, optimized biodistribution and pharmacokinetics. In this dissertation, I report my Ph. D. work on the development of protein-based MRI contrast agents (ProCAs) specifically targeting different cancer biomarkers, such as grastrin-releasing peptide receptor (GRPR), prostate specific membrane antigen (PSMA), and vascular endothelial growth factor receptor-2 (VEGFR-2). Similar to non-targeted ProCAs, these biomarker-targeted ProCAs exhibit 5 - 10 times higher r_1 and r_2 relaxivites than that of clinical MRI contrast agents. In addition, these biomarker-

targeted ProCAs have high Gd^{3+} binding affinities and metal selectivities. The highest binding affinity of the three GRPR-targeted contrast reagents obtained by grafting a GRPR ligand binding moiety into ProCA32 for GRPR is 2.7×10^{-9} M. We further demonstrate that GRPR-targeted ProCAs were able to semi-quantitatively evaluate GRPR expression levels in xenograft mice model by MRI. In addition, we have also created a PSMA-targeted ProCA which has a binding affinity to PSMA biomarker of 5.2×10^{-7} M. Further, we developed VEGFR-targeted contrast agent which is able to image VEGFR2 in mice models using T1-weighted and T2-weighted sequences. Moreover, the relaxivities and coordination water numbers of ProCAs can be tuned by protein design of ProCA4. Since disease biomarkers are expressed in various tumors and diseases, our results may have strong preclinical and clinical implications for the diagnosis and therapeutics of cancer and other type of diseases.

INDEX WORDS: MRI contrast agent, GRPR, prostate cancer, PSMA, VEGFR-2.

DEVELOPMENT OF NOVEL PROTEIN-BASED MRI CONTRAST AGETNTS FOR THE MOLECULAR IMAGING OF CANCER BIOMARKERS

by

FAN PU

A Dissertation Submitted in Partial Fulfillment of the Requirements for the Degree of

Doctor of Philosophy

in the College of Arts and Sciences

Georgia State University

2014

DEVELOPMENT OF NOVEL PROTEIN-BASED MRI CONTRAST AGETNS FOR THE MOLECULAR IMAGING OF CANCER BIOMARKERS

by

FAN PU

Committee Chair: Jenny J. Yang

Committee: Zhi-ren Liu

Daqing Wu

Donald Hamelberg

Hao Xu

Electronic Version Approved:

Office of Graduate Studies

College of Arts and Sciences

Georgia State University

December 2014

ACKNOWLEDGEMENTS

All the work in this dissertation is under the guidance of my advisor, Dr. Jenny J. Yang. In the past five-year Ph.D. studies, she has helped me to understand the fundamental basics of research and shaped me from various aspects including my experimental skills and critical thinking. I learned from her the valuable capabilities to communicate with others, collaboration, and teamwork. She continuously encourages and supports me to achieve my goals even we met some really tough problems and challenges. I think she works as the aphorism in her office, "Winner never set limits, and they set goals." This kind of attitude inspires me to battle life challenges. Besides academic research, she also takes care of my personal issues and life. When I met some healthy problems, she and Dr. Liu come to my home to see me and cook for me even she is very busy. I really appreciate her warm care.

I would like to express my deeply gratitude to Dr. Hua Yang, Dr. Hans GrossniKlaus and Dr. Lily Yang for the great help in animal model set-up and preparation, IHC and IF training. I would like to sincerely thank Dr. Zhi-Ren Liu, Dr. Hans Grossnikclaus, Dr. Lily Yang, Dr. Daqing Wu, Dr. Hui Mao, Dr. Xiao-Ping Hu, Dr. Ritu Aneja and Dr. Qun Zhao for their important and unique perspectives in my experiment preparation and data analysis. My sincere thanks to Dr. Robert Long and Dr. Khan Heckmatayar for MRI scanning, Dr. George Pierce for large-scale protein expression and purification, and Dr. Chalet Tan for the great suggestions on the pharmacokinetics. Many thanks to my committee members, Dr. Donald Hamelberg, Dr. Daqing Wu and Dr. Hao Xu for their kind attention and helpful advice.

I would like to sincerely thank Dr. Jingjuan Qiao, Dr. Liangwei Li, Dr. Lixia Wei, Dr. Jie Jiang, Dr. Yusheng Jiang, Dr. Sheng Tang, Dr. Yanyi Chen, Dr. Xue Wang, Dr. Chen Zhang, Dr. Michael Kirberger, Ling Wei, Andriana, Kendra Hubbard, Matthew Cameron, Jie Feng, Anvi Patel, Bing Xu, Ying-Wei Zhang, Shanshan Tan, Li Zhang, Corrie Purser and other group members of Dr. Yang and Dr. Liu for the great help in the lab. This work is supported by the grants from the National Institutes of Health.

I can never forget the precious friendship of my close friends Jingjuan Qiao, Liangwei Li, Shuo Wang, Bin Zhou, Lei Zhong, and Xiaojun Xu for their warm care during my Ph.D. study. Finally and most importantly, I want to thank my parents, grandparents and my husband, Sheng-Hui Xue, give me their patient love and help to support me finish my research work.

TABLE OF CONTENTS

LIST OF TABLES

LIST OF FIGURES

LIST OF ABBREVIATIONS

ADC: apparent diffusion coefficient

Akt: protein kinase B

Alphascreen : Amplified Luminescent Proximity Homogenous Assay

BN: bombesin

BPH: benign prostatic hyperplasia

cAMP: 3’-5’-cyclic adenosine monophosphate

CT: Computed Tomography

DCE-MRI: dynamic contrast-enhanced MRI

DRE: Digital Rectal Examination

DTPA: diethylene triamine pentaacetic acid

DW-MRI: diffusion-weighted MRI

ECE: extracapsular extension

EPCA: early prostate cancer antigens

EPR: The enhanced permeability and retention

ERK: extracellular signal-regulated kinases

FACS: fluorescence-activated cell sorting

FITC: fluorescein isothiocyanate

FPLC: Fast protein liquid chromatography

GPCR: G protein coupled receptor

GRP: gastrin-releasing peptide

GRPR: gastrin-releasing peptide receptor

GST: Glutathione S-transferase

HER2: human epidermal growth factor receptor 2

ICP-OES: inductively coupled plasma optical emission spectrometry

IF: immunofluorescence

IPTG: Isopropyl β-D-1-thiogalactopyranoside

LB: Lysogeny broth

MAPK: mitogen-activated protein kinase

MP-MRI: multi-parametric magnetic resonance imaging

MRI: Magnetic Resonance Imaging

MRSI: proton magnetic resonance spectroscopic imaging

NAALADase I: N-acetyl-α-linked acidic dipeptidase I

NIR: Near Infrared

NSF: Nephrogenic Systemic Fibrosis

PEG: polyethylene glycol

PET: Positron Emission Tomography

PCa: prostate cancer

PCA3: prostate cancer antigen 3

PlGF: Placenta growth factor

PIPES: piperazine-N,N'-bis(2-ethanesulfonic acid)

PI3K: phosphatidylinositol 3-kinase

PKA: protein kinase A

PKC: protein kinase C

PMSF: phenylmethanesulfonylfluoride

PSA: Prostate-Specific Antigen

PSMA: Prostate-Specific Membrane Antigen

QDs: Quantum dots

SCLC: small cell lung cancer

SNR: signal to noise ratio

SPECT: single-photon emission computerized tomography

SPR: Surface Plasmon Resonance

US: ultrasound

VEGF: Vascular endothelial growth factor

TRUS: transrectal ultrasound

1 INTRODUCTION

1.1 Importance of early detection of cancer and its stage

Cancer is used to describe a series of fatal diseases in which abnormal cells grow without any control and then invade into nearby organs and metastasize to other tissues by blood and lymph systems (Fig.1.1) . It is usually named as the organ or cell which it originally generated from. For example, prostate cancer generates from prostate tissues.

Prostate cancer is the most common cause of tumor-related death in men in the western world. According to National Cancer Institute's estimation, about 240,890 new cases were reported and 33,720 people were killed by this disease in 2011. The most prevalent pattern of prostate cancer is the typical adenocarcinoma which occupies more than 95% of all prostate neoplasms. Additionally, other malignancies include tumors of neuroendocrine differentiation, atypical variants of adenocarcinomas, squamous or transitional cell carcinomas, carcinosarcomas, pure sarcomas and hematopoietic malignancies [1].

Tumor stage and grading is important for clinicians to predict the extent of malignancies spread and make a precise decision about surgery and medical care. To evaluate the stage of cancer, both clinical stage and pathologic stage are monitored. Clinical stage includes physical examination, laboratory findings and imaging studies. Pathologic stage includes following surgical detection of disease invasion and histological examination of tissue. Accurate identification and classification of neoplasm requests clinicians, pathologist and radiologists to work closely together [2]. The tumor-node-metastases (TNM) system is currently used criteria for cancer staging which includes tumor size and local growth (T), extent of lymph node metastases (N)

and occurrence of distant metastases (M) [2]. In general, if the malignancy is restricted in prostate gland, it is curable, otherwise it is incurable [1]. The detailed TNM staging criteria for prostate cancer is listed in Table 1.1.

Table 1.1 TNM classification and stage grouping for prostate adenocarcinoma, modified after [1].

Stage	Grouping	Descriptions
I	T1a, N0, M0, G1	T1a: Tumor clinically inapparent. Tumor incidental histological finding in 5% or less of prostate tissue resected N0: No regional lymph node metastasis M0: No distant metastasis G1: Gleason grade 1
II	T1a, N0, M0, G2-4 T1b, N0, M0, Any G T1c, N0, M0, Any G T2, N0, M0, Any G	T1b: Tumor clinically inapparent. Tumor incidental histological finding in more than 5% of tissue resected T1c: Tumor clinically inapparent. Tumor identified by needle biopsy T2: Tumor confined within prostate G2-4: Gleason grades 2, 3, and 4
III	T3, N0, M0, Any G	T3: Tumor extends through the prostate capsule
IV	T4, N0, M0, Any G Any T, N1, M0, Any G Any T, Any N, M1, Any G	T4: Tumor is fixed or invades adjacent structures other than seminal vesicles: bladder neck, external sphincter, rectum, levator muscles, and/or pelvic wall N1: Metastasis in regional lymph node(s) M1: Distant metastasis

The Gleason grading system is first described by Gleason in 1966 [3]. After annual modifications, it becomes the most frequently accepted method to qualitatively evaluate the degree of loss of the normal glandular tissue architecture from tissue section samples. The Gleason score is utilized to grade extent of gland malignancy of 2-10 and high scores represent the worst invasion and prognosis [2]. The overall Gleason score is constituted with primary score and secondary score. The primary score describes the condition of the majority component in tumor tissues and the secondary score refers the condition of the minority component in tumor tissues [2].

The Gleason grading system depends on the experience of the medical expert which is subjective and even difficult to reproduce. Most of patients today have a Gleason score be-

tween 6 and 8 [4-9]. Gleason scores 2 - 4 [10] are hard to detect while Gleason scores 9 - 10 are rare. Tissue samples are obtained by biopsies with large sampling errors and are very invasive (Fig.1.2). To improve the accuracy of diagnosis of prostate patients at different stages, the Gleason score of biopsy of surgical specimen in pathologic stage should be correlated with imaging techniques such as MRI.

Right now, although a lot of anti-cancer drugs have been developed, most of them cannot cure cancer in the ate stage. As the opinions from National Cancer Institute, the sooner a cancer is found and treated, the better the chances are that the treatment will be successful. One of the major way to reduce the mortality rate of cancer by scientists and physicians is to improve early diagnose and detection of cancer.

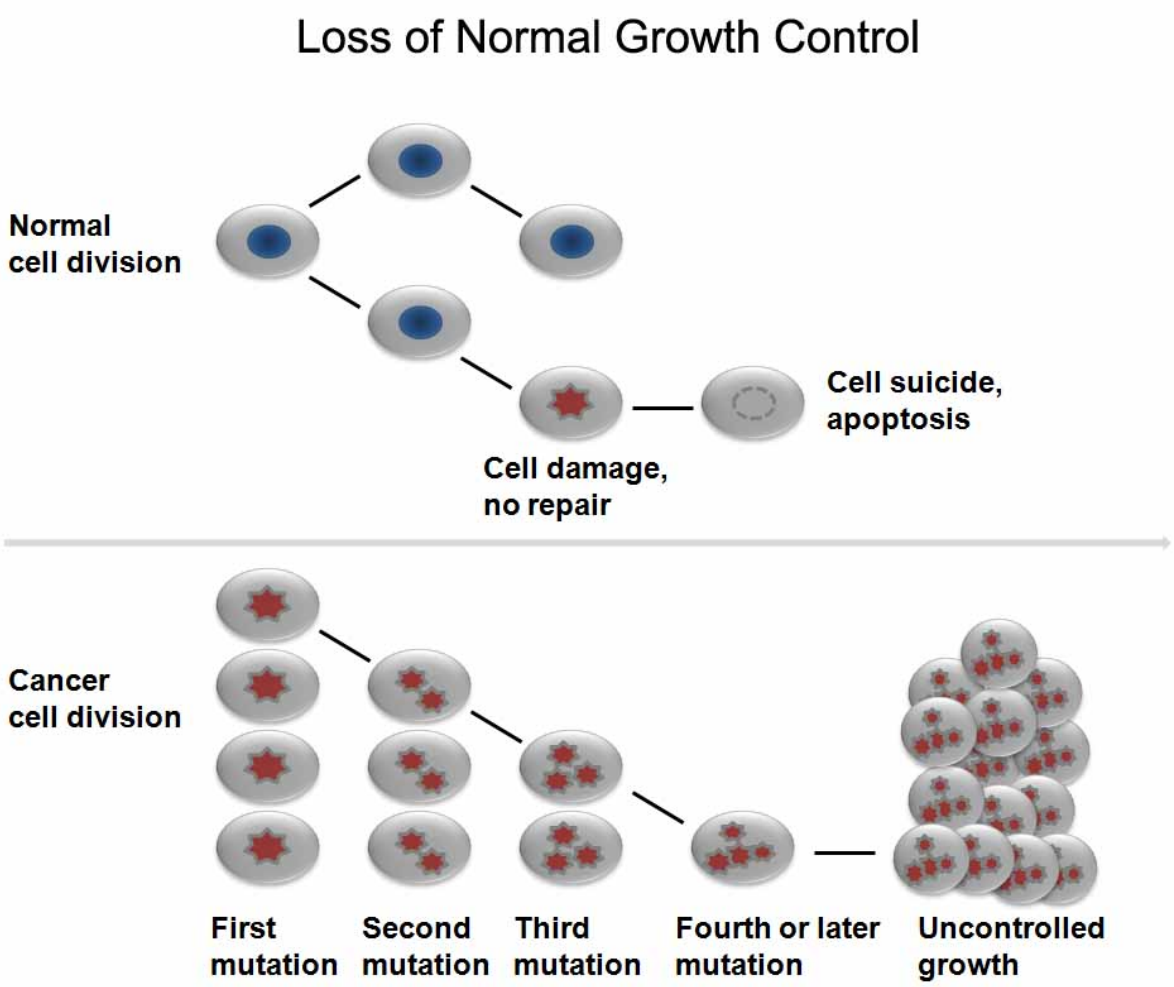

Figure 1.1 Comparison of normal cell and cancer cell division.

Cancer originated from the normal growth is out of control. In normal tissues, cells go to death following a programmed procedure called "apoptosis". While, in tumors, such a balance was broken and the growth of mutated cells is out of control.

1.2 Prostate cancer diagnosis

The main prostate cancer clinical diagnosis methods include PSA test, biopsy, digital rectal examination, and imaging methods such PET and SPECT summarized in Fig.1.2. Here we provide some description of their capability and limitations.

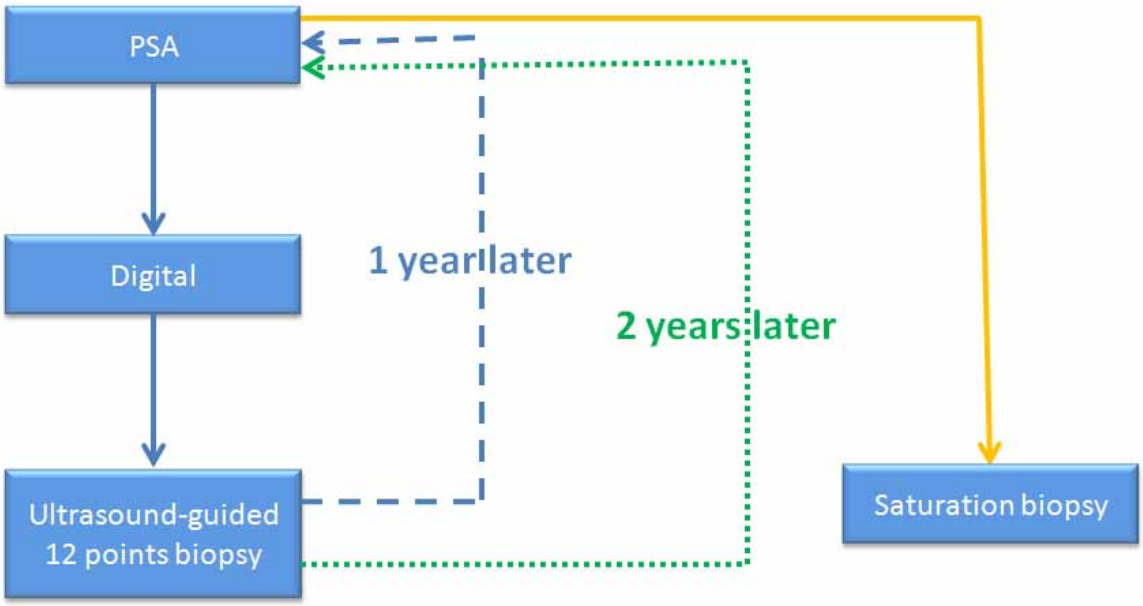

Figure 1.2 Current strategies for prostate cancer diagnosis.

The confirmation of prostate cancer may take more than two years. In order to diagnose prostate cancer, patient needs to have PSA test, digital rectal examination (DRE) and unltrasound-guided biopsy. If these examinations cannot confirm prostate cancer, the patient will wait for one year to follow the same procedure for prostate cancer diagnosis. If prostate cancer still cannot be confirmed, the patient will wait for another year before repeating the same diagnostic procedure one more time. If prostate cancer still cannot be confirmed by PSA, DRE and 12-point biopsy after two years, saturation biopsy will be applied to comprehensively exam whether the patient has prostate cancer or not.

1.2.1 Prostate specific antigen (PSA) test

Prostate specific antigen (PSA) is a glycoprotein mainly produced by the epithelial cells of the prostate gland and is involved in seminal coagulation [11]. In spite of this, minute amounts of PSA are detected in women by a recent report [12-14]. PSA is also named as kallikrein-3 (KLK3) which belongs to the kallikrein-related peptidase family and is recognized as a prostate cancer biomarker [15, 16]. PSA is secreted into the blood with an increased level from prostate cancer cells through the basement membrane of the tumor-invasive gland [11]. In the early 1990s, the PSA test was introduced for prostate cancer diagnosis and its occurrence significantly increased the incidence of prostate cancer as well as decreased the incidence of death [11].

PSA test as a screening test has its limitations despite the fact that high level of PSA in blood is reported to be mainly related with the occurrence of prostate cancer. First, the normal range for PSA levels is between 0 to 4 ng/ml while the abnormal cut-off value for prostate cancer usually from 2.5 to 4 ng/ml is still in debate [11, 17]. Second, high level of PSA is not precisely related to prostate cancer and vice versa. Several factors are reported to affect the PSA level such as volume of prostate, age, BPH [18, 19], diagnostic examinations, physical exercise [20], ejaculation acute and chronic prostatitis, and ductal obstruction [21-23]. Third, the sensitivity (possibility of identifying true positives of the disease), specificity(possibility of identifying true negatives of the disease), positive and negative predictive values (possibility that a proposed positive/negative person actually has/does not have this disease) of the PSA test is not sufficient[17]. A series of PSA assays are developed such as monoclonal Hybritech Tandem-R, Tandem-E, IRMA-Count, Abbott Imx PSA assays and the polyclonal Yang Pros-Check. The difference

of these assays is insignificant [17]. To improve the accuracy of the PSA test, various PSA indices have been employed such as the PSA density (the PSA level divided by the suspected prostate volume), the PSA velocity (the proliferation rate of PSA during a period of time), and the PSA doubling time. Among them, the lower percentage of free PSA level in total PSA incline to represent prostate cancer rather than benign prostatic hypertrophy [11, 24].

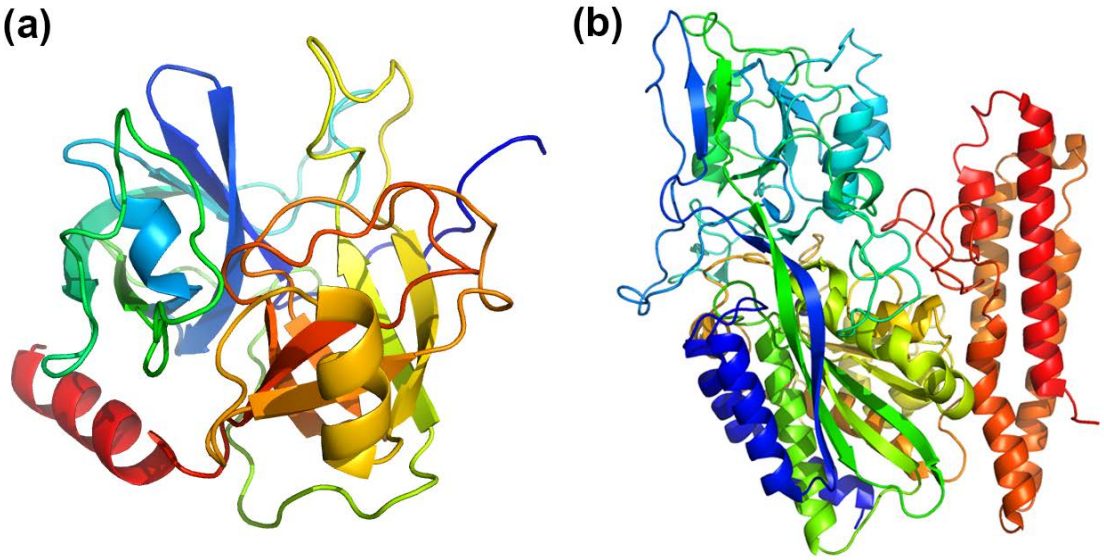

Figure 1.3 Crystal structures of PSA (a) (pdb: 3QUM) and PSMA (b) (pdb: 1Z8L). [25, 26]

1.2.2 TRUS-guided biopsy

Trans-rectal ultrasonography (TRUS), which could characterize the shape and volume of prostate, is used to direct needle biopsy to suspected regions of prostate cancer [27]. TRUS-guided biopsy could identify and evaluate tumor grade, clinical stage, disease extent and prognosis [28-32]. The standard process is extracting 2 - 3 tissue samples by 18 - gauge needle from 6 regions per prostate such as the right and left bases, the mid-gland, and the apex in the outer peripheral zone [11]. To successfully interpret the results of biopsy, we need to pay attention to the adequacy of the obtained specimen and the accuracy of the interpretation of the specimen [17]. This approach may increase the detection rate as well as the grading [33].

Several problems related with biopsy also exist such as the low specificity and sensitivity [27, 34, 35]. Considering the complication of prostate biopsy such as a urinary tract infection, septicaemia(< 1%), bleeding, hemospermia for about 6 weeks, and the objective conditions of patients with coagulopathy or on warfarin [27], not all of patients with suspected prostate cancer could take this test.

1.2.3 Digital rectal examination

Digital rectal examination (DRE) is a “first line” diagnostic test in urological practice, prior to the introduction of the PSA test in 1980s. Digital rectal examination is designed to detect whether the prostate tumor is palpable. During the process, a finger is inserted into the rectum to detect the existence of abnormal mass [17]. About 50 - 95% of localized prostatic tumors could be distinguished by DRE [36-40]. However, it also has high false positive rates (40 - 50%) [37, 40-42] with respect to other conditions such as benign prostate hyperplasia (BPH), retention cysts, prostatic calculi, prostatic atrophy and even non-malignant mass increases with age

[43]. The sensitivity and specificity of localized prostate cancer detected by DRE are 44% - 97% and 22% - 96%, respectively [43-45]. The detection of localized prostate cancer by DRE alone is between 0.2% and 1.7%, lower than that of PSA [39, 46-50]. Recently, DRE is combined with other techniques such as PSA test to increase the diagnosis rate of prostate cancer.

1.2.4 Imaging methods

1.2.4.1 Ultrasound imaging for prostate cancer

TRUS-guided systematic biopsy currently is the golden standard for detecting prostate cancer [51].Transrectal ultrasound (TRUS) was first developed in the 1960s and 1970s [52, 53]. The basic mechanism of TRUS-based cancer detection is relying on the hypoechoic appearance which may be due to the solid tumor mass replacing the normal loose glandular tissues. Ultrasound has its own advantages over other medical imaging techniques such as no radiation and low cost. TRUS benefits from the location of the probe head close to the rectal wall which makes higher resolution and higher quality scans possible. TRUS can be used to identify the classic examples as cancers happened in hypoechoic nodule in the peripheral zone which cannot be attributed to benign tissues. Generally speaking, TRUS is relatively accurate for local staging such as evaluating the extra-capsular extension and participation in seminal vesicle. TRUS plays important roles in guiding biopsy, therapy, and measuring the volume of the prostate.

About 40% to 60% of prostate cancers cannot be detected by TRUS, especially the low-grade cancers. This is due to the existence of the more infiltrative tumors, tumors with glandular structure are not sensitive in TRUS and only 50% hypoechoic nodules are cancers. Some le-

sions such as hyperplasia, prostatitis and cysts can be detected by their hypoechoic appearance [51]. Besides, tumors generated in the very heterogeneous transition zone and the far anterior are difficult to detect on TRUS since they are far away from the probe placed in the rectum.

Recently, contrast-enhanced ultrasound is emerging. Compared with the conventional color/power Doppler US imaging, the microbubble contrast agent can enhance the US signal of the angiogenesis in neoplasm in some cases. Some investigators claimed the sensitivity of the contrast-enhanced US is higher than the unenhanced US, but the specificity of the contrast-enhanced ultrasound is not more significant than that of the conventional ultrasound [51, 54-56].

1.2.4.2 MRI imaging for prostate cancer

Multi-parametric magnetic resonance imaging (MP-MRI) including T2-weighted, diffusion weighted MRI (DW-MRI), proton magnetic resonance spectroscopic imaging (MRSI) and dynamic contrast-enhanced MRI (DCE-MRI) as components have been used clinically to identify and stage the localized prostate cancer [57]. T2-weighted MRI is most commonly used to provide soft tissues contrast and delineation of the zonal anatomy (Fig.1.4). The basic mechanism for the T2-weighted imaging of prostate cancer is based on the normal glandular loss-caused low intensity. The extracapsular extension (ECE) indicates the phenomenon in which the prostate cancer invades into the nearby tissues. The detection of extracapsular extension (ECE) plays an important role in staging a patient. If a patient has extracapsular extension (ECE), the staging of his disease will be upgraded to T3a stage. A recent report shows T2-weighted MRI can detect tumors larger than 1 cm in parameter with 80-90% accuracy but not sensitive for the smaller tumors [58, 59]. and also provide additional information about lesion size [60]. Low T2

intensity is not limited to prostate cancer; other diseases such as benign prostate hypertrophy (BPH) and prostatitis also have similar signal responses. However, the false positive extracapsular extension often shows on T2-weighted MRI because of the interruption from the peri-prostate fat. Based on the above reasons, T2-weighted MRI mainly depends on its operator [61].

Diffusion weighted MRI (DW-MRI) is a kind of magnetic resonance imaging test which measures the water proton movement within the tissues. The most important value measured in DW-MRI is called the apparent diffusion coefficient (ADC) which is used to describe the water proton diffusion. [62-64] The tumor has lower ADC values than that of normal tissues which enables DW-MRI to detect prostate cancer. DW-MRI has been used to quantitatively evaluate the prostate cancer treatment effects and monitor the post-therapeutic recurrence. DW-MRI used with the standard MRI, often improves the diagnosis efficiency [65, 66].

Proton magnetic resonance spectroscopic imaging (MRSI) is another imaging technique which evaluates the metabolism conditions in the prostate cancer. The chemical resonances of the metabolites as citrate, creatine and choline monitored by three-dimensional MRSI are different from that of normal prostate tissues. The ratios of choline to citrate or choline plus creatine to citrate are used to characterize prostate cancers. MRSI coupled with T2-weighted MRI can help the determination of tumor localization as well as tumor volume estimation [67]. However, MRSI-MP-MRSI is still limited to its specificity; it is usually used to confirm the aggressiveness of lesions instead of staging the local tumor [57].

Dynamic contrast-enhanced MRI (DCE-MRI) is a functional MRI imaging technique which focuses on the dynamic change before and after injection of MRI contrast agent by T1-weighted

fast spin echo sequence. The basic mechanism of DCE-MRI, based on the wash-in and wash-out rate of angiogenesis in the tumor is much faster than that of normal tissues. DCE-MRI monitors and assesses the potential tumor region, lesions and cancer aggressiveness, and therapeutic effects then provides an assessment of the permeability and perfusion in the prostate [68, 69]. However, with current available contrast agents, DCE-MRI cannot differentiate the benign prostate hyperplasia (BPH) and inflammation in the central gland [70]. Considering angiogenesis always happens in the late stage, the smaller tumors also couldn't be detected by DCE-MRI [71]. Like MRSI, DCE-MRI with current contrast agents has low spatial resolution and does not have capability to stage local prostate cancer [72, 73].

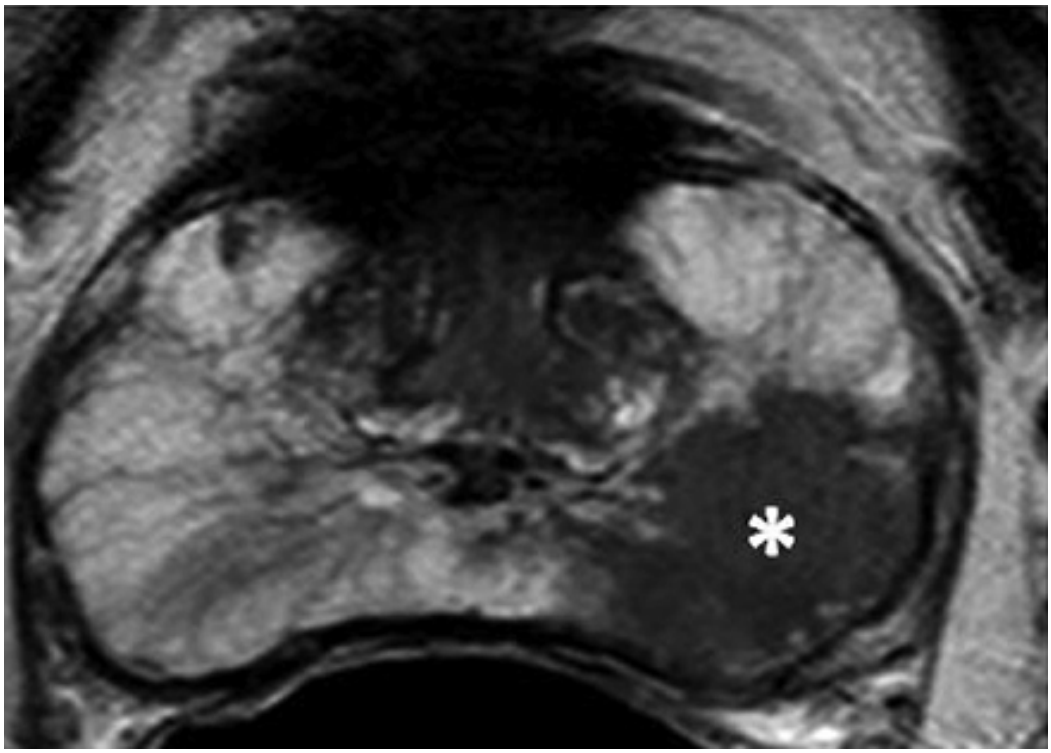

Figure 1.4 Axial T2-weighted magnetic resonance imaging (MRI) (Asterisk)of a 63-year-old man with a serum prostate-specific antigen (PSA) of 14 ng/dl [56].

*** indicate the position of prostate cancer.**

1.2.4.3 PET/CT imaging for prostate cancer

Positron emission tomography (PET) is a radiological imaging technique which was designed to identify various types of tissues in human body and reveal the conditions of certain diseases. Several radioactive tracers are already involved in the PET imaging of clinical prostate cancer, such as ^{18}F-FDG, ^{11}C- and ^{18}F-choline, ^{11}C- and ^{18}F-acetate.

Warburg effect is an evident hallmark of cancer which differentiates malignancy from normal tissues with abnormal elevated glucose metabolism. ^{18}F-FDG can accumulate in those tumors so as to indicating the disease location. However, the uptake of ^{18}F-FDG is not specific for cancer; in fact the benign prostate tissues and normal tissues also uptake ^{18}F-FDG for their metabolism. Only the poor-differentiated tumors and prostatitis show higher uptake of ^{18}F-FDG. The tumors in its early stage with well-defined structure and slow growth rate exhibits moderate uptake of ^{18}F-FDG, which limit the application of ^{18}F-FDG dependent PET imaging for initial detection of prostate cancer [74].

^{11}C-choline PET was introduced for prostate cancer detection in 1998 [75]. In 2002, ^{11}C-acetate was invented for measuring the oxidative metabolism in prostate cancer [76]. Acetate and choline are accumulated through different carrier systems during the tumor growth phase for involvement in the increased lipid synthesis by fatty acid synthase and choline kinase, respectively. In addition, they have same problem as FDG which means the uptake is not unique to the cancer cells. They all show intestinal uptake and non-specific accumulation in the lymph node [77]. ^{11}C was used to label choline and acetate but its application was limited to a hospital with a cyclotron due to its half-time being is only 20 minutes. ^{18}F labeled tracers have longer half-life (110 min) which allow it has longer retention time, but it is limited by its clinically rele-

vant urinary excretion (7.5%) which made it difficult to detect the prostate bed [78]. For ^{11}C labeled radiotracers, ^{11}C-acetate has lower retention in liver than that of ^{11}C-choline which is supposed to improve the detection of liver metastases, but still can detect disease in the very late stage, which significantly lowers the clinical value. In general, both choline and acetate don't have sufficient diagnostic accuracy to stage the primary tumor and differentiate prostate cancer from other diseases, such as benign prostate hyperplasia. To our knowledge, the minimal tumor size which can be detected by PET is 5 mm [79]. Watanabe et al. [80] found that MRI was superior to ^{11}C-choline PET/CT with higher sensitivity and accuracy for the primary tumor detection.

1.2.4.4 SPECT/CT imaging for prostate cancer

As positron emission tomography (PET), Single-photon emission computed tomography (SPECT) is another conventional radioactive tracer-based imaging technique. Right now, the hybrid modality imaging technique (SPECT/CT) increased the availability such as shorten acquisition time, improving the attenuation correction, enhancing specificity and determining the exact disease location so as to broaden its diagnostic applications in many aspects [81]. SPECT/CT has its own advantage on visualizing bone structure than MRI. Compared with bone scintigraphy, SPECT/CT could precisely locate the anatomical abnormalities in bone [82].

1.2.4.5 Fluorescence imaging for prostate cancer

Fluorescence imaging has been applied preclinically to detect cancer due to rapid development of optimal probes such as QDs with high sensitivity and stability. Quantum dots (QDs) are fluorescent semiconductor nanometer-sized crystals with unique optical and electronic

properties which can emit light and thus emerge as a new generation of fluorescence imaging probes for cancer [83-86]. QDs are constituted of an inorganic elemental core and surrounding metal shell with diameters of 2-10 nm. Compared to the traditional organic dyes, QDs show 10 - 20 times brighter than that of organic dyes. In addition to this, QDs exhibit 100 - 1000 times stability against photobleaching than traditional fluorophores because of its high resistance to metabolic degradation which made it possible to tracking and imaging in long-term [87, 88]. Moreover, QDs generate less autofluorescence than organic dyes when they were used to image biological specimen. QDs can image multicolor samples which can't be achieved by organic dyes. Those above advantages made QDs able to image small living subjects for real-time detection. The emission wavelength of QDs can be tuned from visible light to NIR spectrum (650-950 nm), thus the different targets within the same sample can be gained with different sensitivity. In addition, NIR imaging provides deeper tissue penetration so as to avoiding the autofluorescence interference from specimen [89, 90]. However, some of the QDs still have toxic problems in certain conditions such as Cd-containing QDs, which urge the development of less toxic QDs [91-93]. Overall, fluorescence imaging is largely limited to preclinical application to tumors located at the surface of small animal due to limitation of penetration depth and toxicity.

1.2.5 Limitations of current detection methods and major need in cancer diagnosis

Current methods of diagnosis, including biopsy, digital rectal examination (DRE), PSA test, suffer from a wide range of drawbacks. Biopsy of prostate cancer is an invasive technique and this method is not accurate because it is restricted to a small region of patient's prostate. To confirm the diagnosis, a biopsy usually needs to be repeated several times [17]. Digital rectal

examination (DRE) is dependent on a doctor's experience which couldn't meet the requirement of quantification [17]. PSA test suffers from accuracies according to recent reports. High levels of prostate specific antigen in serum is more related with benign prostate hyperplasia (BPH) rather than prostate carcinoma [17]. Limited by their intrinsic properties, current imaging techniques cannot clinically be used for imaging the progression of prostate cancer. Although PET and single-photon emission computed tomography (SPECT) is sensitive, they have limited application due to non-specific update of FDG in prostate and other related organs in addition to its limited spatial resolution and requirement of radioactive isotopes. Due to the low penetration properties, fluorescence imaging has only been used preclinically and only used for imaging the biomarker on the animal surface, without capability to image the tumors inside the animals and human. Although CT is low costing and has good spatial resolution, the CT contrast agents are insensitive and have strong toxicity to the kidney. Current verification of prostate cancer types by invasive clinical diagnostic procedures based on biopsy could easily take three years since the initial finding of elevated levels of PSA. Clearly, there is an urgent need to develop sensitive and accurate non-invasive imaging method to determine the nature of cancer based on the biomarkers, and subsequently monitor tumor progression, metastasis, and the effectiveness of the various treatments with high specificity.

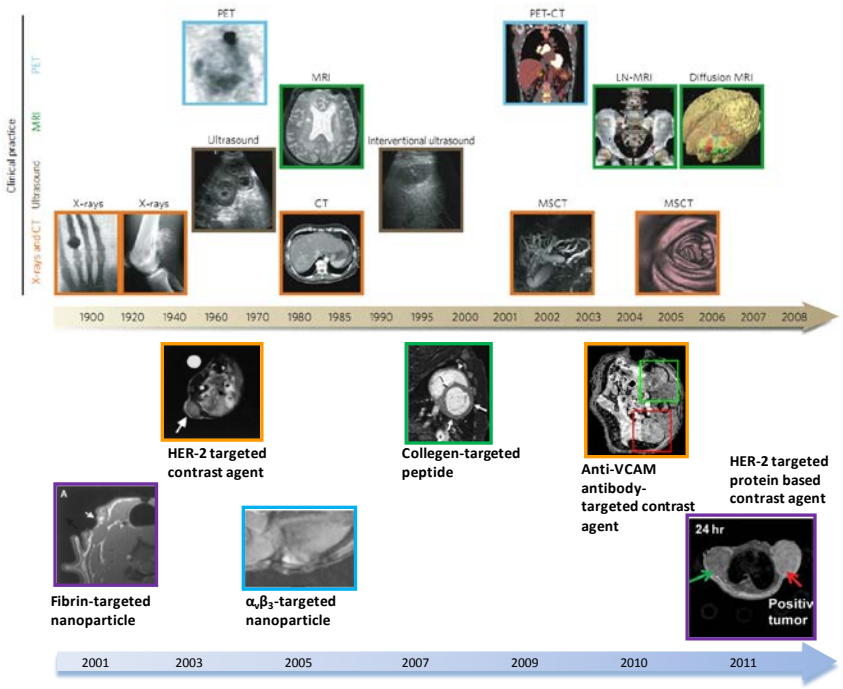

der et al., *Magnetic Resonance in Medicine*, 2005, 621-627; Spuentrup et al., *Circulation*, 2009, 1768-1775; Flacke et al., *Circulation*, 2001-1280-1085
v et al., *Cancer Research*, 2003, 2723-2727; Weissleder et al., *Nature*, 2008, 580-590; Qiao, *PLoSone*, 2010, e18103 ; Akhtar et al., *PloSone*, 2011, e 12800

Figure 1.5 The development of molecular imaging.

X-ray has been applied for human imaging since early 19th century. PET and ultrasound were invented in 1960's. MRI and CT were invented in 1980's. PET/CT and diffusion MRI were invented in the recent twenty years. Molecular imaging of disease biomarkers using MRI contrast agents were reported since 2001. However, largely due to the lack of sensitive MRI contrast agents, reported literature on molecular imaging using MRI is very limited compared with other imaging techniques.

1.3 Biomarkers for prostate cancer

One of the emerging trends to improve detection sensitivity and specificity is to trace biomarkers whose expression specifically correlated with the extent of prostate cancer. Table 1.2 summarizes recent biomarkers identified for diagnosis and prognosis including prostate

cancer antigen 3 (PCA3), early prostate cancer antigens (EPCA), gastrin-releasing peptide receptor (GRPR), and prostate specific membrane antigen (PSMA) [94].

To identify the golden standard biomarker for prostate cancer diagnosis and treatment, several criteria need to be met. Fig 1.6 shows that primary restriction to prostate, abundant expression at all stages of disease, presence on the cell surface, and enzymatic activity or signal pathway are often considered.

Table 1.2 List of candidate biomarkers for prostate cancer and their possible clinical utility [94].

Candidate CaP biomarker	Assessed clinical utility	References
KLK2	Diagnostic and prognostic predictor of extracapsular extension, tumor volume, and biochemical recurrence	*(11–14)*
PSMA	Imaging marker and target for therapy	*(15, 16)*
KLK11	Early predictor of CaP in serum	*(17, 18)*
PCA3	Urinary biomarker for detecting CaP	*(19–23)*
EPCA/EPCA-2	Immunohistochemical detection of CaP; serum marker to differentiate local from metastatic CaP	*(24–27)*
AMACR	Increased detection of autoantibodies in CaP; immunohistochemical detection as a prognostic factor for biochemical recurrence and death	*(28–33)*
uPA/uPAR	Increased tissue and serum concentrations predict biochemical recurrence and metastasis	*(34–37)*
IGF/IGFBP	IGF-1 slightly increased in CaP serum; IGFBP concentration inversely correlated to CaP progression	*(38–40)*
TMPRSS2:ERG/ETV1	Increased detection in urine of CaP and PIN patients vs BPH patients; gene fusion present in CaP tissue by FISH[a]	*(41–44)*
TGF-β_1	Increased immunohistochemical and serum concentrations with CaP progression and biochemical recurrence	*(45–47)*
EZH2	Gene expression in CaP tissue predicts progression	*(48, 49)*
GSTP1	Detection of gene promoter hypermethylation in urine to assess for biopsy	*(50, 51)*
PSP94	Predictor of Gleason sum, surgical margin status, and biochemical recurrence after local surgery	*(52)*
CRISP-3	Increased immunohistochemical staining in prostate tissues of men with high-grade PIN; independent predictor of CaP recurrence	*(53, 54)*
Chromogranin A	Monitoring of patients with androgen-independent late-stage CaP with neuroendocrine differentiation	*(55, 56)*
Progastrin-releasing peptide	Monitoring of patients with metastatic CaP with neuroendocrine and androgen-independent phenotype	*(57, 58)*
E-cadherin	Reduced immunohistochemical expression in CaP correlated with stage and reduced survival	*(59, 60)*
Annexin A3	Decreased production in CaP tissues by immunohistochemistry; prognostic risk marker	*(61)*
PSCA	Immunohistochemical marker associated with Gleason sum and stage; target for therapy	*(62, 63)*
Hepsin	Immunohistochemical detection in PIN and CaP compared with BPH	*(64, 65)*
IL-6	Elevated serum concentrations in late-stage CaP	*(66–68)*

[a] FISH, fluorescence in situ hybridization.

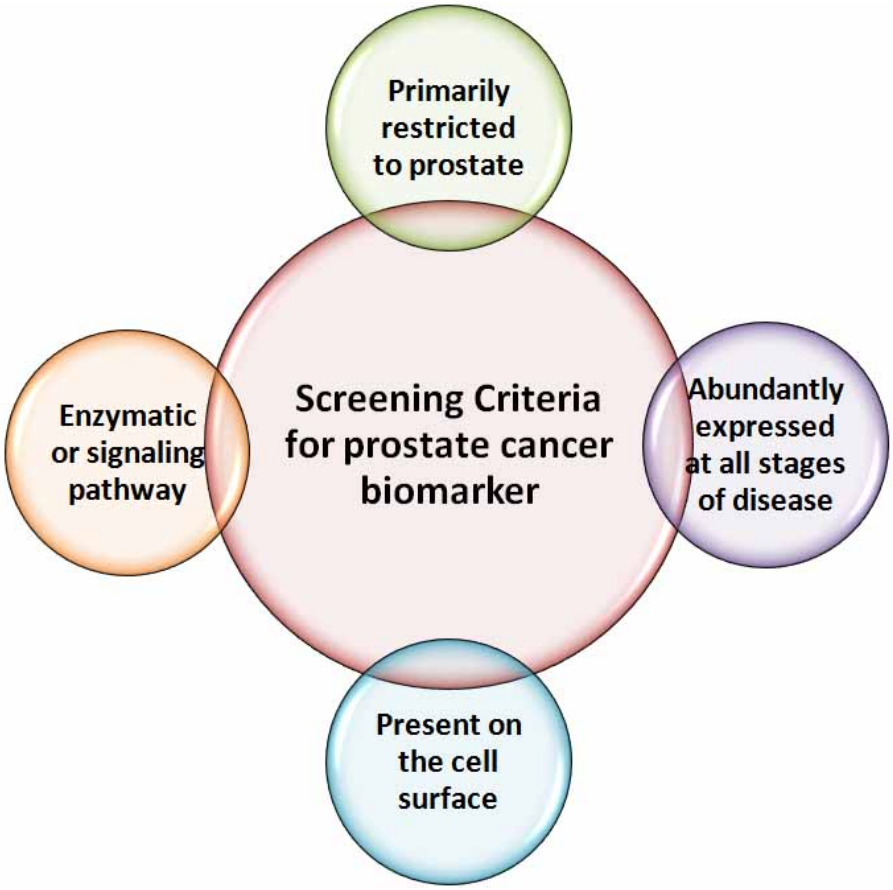

Figure 1.6 Screening criteria for prostate cancer biomarker.

1.3.1 Prostate specific membrane antigen (PSMA)

Prostate specific membrane antigen (PSMA) is a type II transmembrane glycoprotein which belongs to G protein coupled receptor (GPCR) family. It is a glutamate carboxypeptidase II (EC 3.4.17.21) and acts as folate hydrolase and N-acetyl-α-linked acidic dipeptidase I (NAALADase I). [25] PSMA plays important roles in some physiological processes such as signal transduction, receptor function, nutrient uptake and cell migration. Further studies of the role which PSMA plays in prostate cancer remains an active research field.

Overexpression of PSMA is already validated to be related with prostate cancer [95, 96]. PSMA is expressed in the tumor metastasis from prostate to spleen and bone. The expression

of PSMA is androgen-dependent, and the expression levels of PSMA increase when androgen receptor is down regulated. This unique mechanism makes PSMA one of the favorable biomarkers for the imaging and treatment of prostate cancer.

Several antibodies against PSMA have been applied for the diagnosis of prostate cancer (as shown in Table 1.3). Some of these antibodies, such as 7E11 [97], target the intracellular region of PSMA. The monoclonal antibody such as J591 was designed to target the extracellular domain of PSMA. Currently, PSMA antibodies have been linked to radioactive isotopes and quantum dots to image prostate cancer in preclinical and clinical studies. ^{111}In-capromab was the first SPECT agent to target PSMA in prostate cancer. A murine antibody mAb7E11 labeled with ^{111}In formed this agent ProstaScint which is approved by FDA. This mAb has been identified to bind to the intracellular epitope of PSMA so its binding usually indicates necrosis or apoptosis with some limitations in diagnosis [98-103]. Targeting to the extracellular domain of PSMA, J591 is the newer generation of SPECT agent with capability to detect the viable tumor. While there are several other new characterized mAbs with different binding epitopes and pharmacokinetics are under development [96], antibody targeting exhibits several limitations for tumor penetration and undesired PK and PDs, due to its large size (150 kDa) [104]. PSMA-specific targeting peptide is an alternative way of the molecular imaging of PSMA; however, the binding affinity of the reported peptide is very weak [105]. There is a strong need to develop a new targeting method for quantitatively imaging of biomarker PSMA expression level. This need will be addressed in Chapter 4.

Table 1.3 Reported antibodies against PSMA applied for the diagnosis of prostate cancer.

Name	Recognition domains in PSMA	Application for imaging or therapy	References
7E11*	First six amino acids of the N-terminal PSMA (intracellular domain)	^{111}In (ProstaScint)	[106, 107]
J591	Extracellular domain	^{111}In, ^{177}lu, ^{89}Zr, QDs	[108-112]
3/A12	Extracellular domain	^{34}Cu	[113]
3/F11	Extracellular domain	^{34}Cu	[113]
3/A12	Extracellular domain	^{34}Cu	[113]
J533	Extracellular domain	N/A	[108]
J415	Extracellular domain	N/A	[108]
E99	Extracellular domain	N/A	[108]
PEQ226.5	Extracellular domain (173-437)	N/A	[114]
3C2	Extracellular domain	N/A	[115]
3E11	Extracellular domain	N/A	[115]
4E10-1.14	Extracellular domain	N/A	[115]
3C9	Extracellular domain	N/A	[115]
1G3	Extracellular domain	N/A	[115]
3/E7	Extracellular domain	$^{34}Cu^{2+}$	[113]

Table 1.4 Examples of developed imaging and therapeutic agents against PSMA.

Imaging/Therapy	Name/description	Targeting moiety	Imaging/Therapy moiety	References
Fluorescence imaging	QD-PSMA Ab bioconjugate	Antibody: JM591	QDs	[112]
NIR imaging	800CW 2 and others	PSMA inhibitor	IRDye800CW, Cy7, et al.	[116]
CT/Therapy	PSMA Aptamer-Conjugated GNPs	Aptamer	nanoparticle	[117]
MRI	J591-MNP	Antibody: JM591	nanoparticle	[118]
MRI	J591–SPIO	Antibody: JM591	nanoparticle	[119]
PET	89Zr-7E11	Antibody: 7E11	^{89}Zr	[120]
PET	[^{11}C]DCMC	PSMA inhibitor	^{11}C	[121]
PET/CT	(124)I-MIP-1095	PSMA inhibitor	^{124}I	[122]
PET/CT	(64)Cu-labeled inhibitors of PSMA	PSMA inhibitor	^{64}Cu	[123]
PET/CT	BAY 1075553	PSMA inhibitor	^{18}F	[124]
PET/CT; PET/MRI	68Ga-labelled HBED-CC-PSMA	PSMA inhibitor	^{68}Ga	[125]
SPECT	ProstaScint	Antibody: 7E11	^{111} In	[106, 107]
SPECT	J591C diabody	Antibody fragment of JM591	^{99m}Tc	[126]
SPECT	(99m)Tc-MIP-1404	PSMA inhibitor	^{99m}Tc	[127]
Ultrasound	Targeted nanoscale microbubbles	PSMA monoclonal antibody	Microbubbles	[128]
Therapy	PSMA ADC	PSMA monoclonal antibody	monomethyl auristatin E	[129]
Therapy	Pt-NP-Apt	Aptamer	nanoparticle	[130]

1.3.2 GRPR

Gastrin releasing peptide receptor (GRPR), belongs to G-protein coupled receptor family, is an important biomarker for many types of diseases, such as prostate cancer, cervical cancer, uveal melanoma and pruritus. Like other G-protein coupled receptors, GRPR has 7 transmembrane domains, an intracellular region and an extracellular region. Human prostate cancer has shown high gastrin-releasing peptide receptor (GRPR) expression, while normal prostate tissue reveals to be predominantly GRPR-negative. GRPR appears up to almost 100 percent on the prostate tumors that is significantly higher than that of other tissues [131]. In addition, 33 - 72% of breast cancer, 40 - 50% of grastric cancer, 85% of carcinoids cancer, 29 - 85% of small cell lung cancer also has high GRPR expression.

The natural ligand for GRPR is grastrin-releasing peptide (GRP). GRP is the first peptide isolated from porcine gastric and intestinal tissues. GRP is a 27-residue peptide that belongs to the family of bombesin (Bn)-like peptides. GRP acts by binding to a specific member of the 7-transmembrane spanning, G protein-coupled receptor super family [132]. Bombesin (BBS) is a 14 amino acid peptide which was separated from the skin of a frog *Bombina bombina* [133], which also has nM level binding affinity to GRPR. Table 1.6 shows that different GRPR-binding ligands have different GRPR-binding affinity. For example, full-length GRP and C-terminus GRP (18-27) has GRPR-binding affinity of 15 nM and 20 nM, respectively. Among these natural peptide ligands, full-length bombesin has the strongest GRPR binding affinity of 4 nM.

The ligand binding to GRPR trigers Gq signaling pathway, which further induces intracellular Ca^{2+} concentration increase, PKC activation and ERK/MAPK phosphorylation. The ligand binding to GRPR also triggers Gs pathway, which induces cAMP activation by activating

adenylate cyclase. cAMP further activates PKA. In addition, GRPR also activate PI3K/AKT pathway. Finally, these signal cascades induce a series of physiological responses, such as the release of gastrointestinal hormones, smooth muscle cell contraction, and epithelial cell proliferation and is a potent mitogen for neoplastic tissues. GRP, bombesin and their analogues have been often used to link to radioactive reagents such as ^{68}Ga, ^{111}In, ^{18}F, ^{177}Lu, ^{99}mTc and ^{86}Y to label target of prostate cancer and potentially treat prostate cancer (Table 1.7) [134]. In addition, GRP, bombesin and their analogs were also conjugated to QDs and fluorophore for near infrared (NIR) imaging. However, the molecular imaging of GRPR using MRI is limited largely due to the lack of sensitive MRI contrast agents. The molecular imaging of GRPR using protein MRI contrast agents will be described in details in section 6.

Releasing Peptide (GRP) or bombesin (BN) analogues have been used to link to radioactive reagents such as ^{68}Ga and ^{86}Y to label target of prostate cancer and potentially treat prostate cancer (as shown in Table 1.7) [134]. In chapter 3, we will report our effort in developing a grafting approach to create a molecular imaging contrast agent for MRI against GRPR.

Table 1.5 Expression of GRP and its receptors in tumors [110].

Tumor	GRP				GRP-R			
	No. positive/ Total no.	%	Method	Ref.	No. positive/ Total no.	%	Method	Ref.
Lung	23/31	74	RIA	[98]	17/20	85	PCR	[115]
(SCLC)	NS	71	RIA	[249]	11/38	29	PCR	[53]
	9/20	45	RIA	[250]	3/9	33	Binding	[116]
	16/32	50	PCR	[97]				
Prostate	18/30	60	IH	[102]	30/30	100	Binding	[119]
	27/41	64	IH	[251]	50/80	63	Binding	[120]
					20/22	91	PCR	[120]
					12/12	100	Binding	[116]
Breast	16/41	39	RIA	[104]	33/100	33	Binding	[124]
	5/28	18	NB	[105]	29/46	63	Binding	[59]
					41/57	72	Binding	[116]
Gastric					13/23	50	Binding	[125]
					8/20	40	PCR	[126]
Pancreatic	52/88	59	RIA	[106]	2/26	8	PCR	[132]
					2/12	17	Binding	[133]
Colorectal	42/50	84	IH	[109]	6/15	40	Binding	[144]
	23/23	100	PCR	[63]	5/21	24	Binding	[147]
					27/29	93	PCR	[148]
					38/50	76	IH	[109]
					23/23	100	PCR	[63]
Carcinoids	12/20	60	IH	[113]	22/26	85	IH	[114]
	9/19	47	IH	[114]				

Table 1.6 Affinity of bombesin receptor subtypes for various natural ligands. [135]

Peptide	Affinity, nM		
	Neuromedin B receptor	Gastrin-releasing peptide receptor	Bombesin-like receptor 3
GRP	440	18	>10,000
NMB	4	248	>10,000
Bombesin	34	4	>10,000
Litorin	7	6	>10,000
Ranatensin	13	2	>10,000
Alytesin	460	62	>10,000
Phyllolitorin	47	240	>10,000
Neuromedin C (GRP_{18-27})	140	20	>10,000

Table 1.7 Examples of developed imaging and therapeutic agents against GRPR.

Imaging/Therapy	Name/description	Targeting moiety	Imaging/Therapy moiety	References
Fluorescence imaging	Qdot-bombesin	Bombesin	QDs	[136]
NIR imaging	BBN[7–14]–SA–PEG–MPA	Bombesin	MPA	[137]
NIR imaging	AF680-BBN	Bombesin	Alexa Fluor 680	[138]
MRI	ProCA1.GRP(52)	GRP	ProCA1	[139]
PET	(18) F-Al-NOTA-MATBBN	MATBBN	^{18}F	[140]
PET	NOTA-P2-RM26	RM26	^{18}F	[141]
PET	NODAGA-RM1 and NODAGA-AMBA	RM1 and AMBA	^{64}Cu and ^{18}F	[142]
PET	^{68}Ga-AMBA-chelators	AMBA	^{68}Ga	[143]
PET/CT	^{68}Ga-NOTA-PEG$_n$-RM26	Bombesin analog	^{68}Ga	[144]
PET/CT	BAY86-7548	Bombesin analog	^{68}Ga	[145]
SPECT & Therapy	^{99m}Tc/^{177}Lu-AuNP-Tat-BN	Bombesin	^{99m}Tc, ^{177}Lu, and nanoparticle	[146]
SPECT/CT	[(99m)Tc]DB4	Bombesin	^{99m}Tc	[147]
SPECT/CT	^{111}In-Bombesin Conjugates	Bombesin	^{111}In	[148]
SPECT/CT& Therapy	^{188}Re-liposome-BBN	Bombesin	^{188}Re and liposome	[149]
Therapy	^{177}Lu-DOTA-PEG5k-lys-BN	Bombesin	^{177}Lu	[150]
Therapy	EHCO	Bombesin	siRNA	[151]
Therapy	GRP1-siRNA	GRP	siRNA	[152]

1.4 Methods to characterize the binding between imaging probes to cancer biomarkers

One of the key determinants to achieve quantitative molecular imaging is the strong binding affinity reflected by disassociation constant K_d. To characterize the binding capability between imaging probes to cancer biomarkers, several common strategies have been applied such as immunofluorescence imaging, flow cytometry (FACS), surface plasmon resonance (SPR), Alphascreen assay, anisotropy and radioactive assay. In addition, some other assays based on the unique properties of the specific targeting proteins have also been utilized. For example, NAALADase assay has been developed to measure PSMA inhibition. I will describe each of these methods applied to determine prostate cancer biomarkers below.

1.4.1 Immunofluorescence imaging and Flow cytometry to detect cell targetingPSMA

Immuno reactions of protein biomarker such as PSMA and its antibody have been applied widely to determine cellular binding capabilities via immuofluorescence, absorbance (HRP) and flow cytometry (FACS) [128]. Schol et al. [153]developed anti-PSMA antibody-coupled gold nanorods which can bind to PSMA on LnCaP cells. The secondary antibody conjugated with a fluorochrome (QDs, Q11001MP) was added to recognize the probe and the fluorescence generated from fluorochrome was recorded by fluorescent microscope (Axiovert 40) [153]. Secondary antibody conjugated HRP via absorbance also provides quantitative determination of binding affinity. In another study, Wang et al. [128]constructed a kind of PSMA-targeted nanoscale microbubbles which can be used in the ultrasound for prostate cancer imaging. The nanoscale MBs were prepared with PSMA monoclonal antibody by using biotin-avidin technology. The secondary antibody labeled with a fluorescence dye DyLight488 was used to capture the targeted nanoscale MBs.

Flow cytometry is a technique which can monitor the emission light at different wavelengths and analyze the physical and chemical properties of fluorescence-labeled cells or other components in a fluid as they pass through and are excited by lasers. This technology can be used to perform several procedures such as cell sorting, cell counting, protein engineering and biomarker detection based on the antigen-antibody interactions. Kim et al. [154]designed a CMP-based self-assembly of tribodies with PSMA-targeting capability. LnCaP cells or PC3 cells (2 x 10^4) were incubated with their FITC-labeled monomeric or trimeric ligands at room temperature for 30 min and washed twice with 1 x PBS buffer. The samples were analyzed by flow cytometry (BD FACS Canto flow cytometer). FITC-labeled anti-PSMA antibody was used as a positive control [154]. The results proved the binding existence. In recent years, high-throughput flow cytometry has emerged as a new trend to perform multiplexed cell-based and bead-based screens. It overcomes the limitation of traditional flowcytometry in handling tremendous samples [155].

1.4.2 Surface Plasmon Resonance to detect EGFR targeting

Surface plasmon Resonance (SPR) is a label-free kinetic analysis of protein-protein interactions which arose in the late 90's [156]. When the polarized light strikes an electrically conducting gold layers at the interface between the glass of a sensor surface with high refractive index and a buffer with low refractive index, the signal generating under conditions of total internal reflection is called surface Plasmon resonance (SPR). The reflected light is affected by a slight change which happens at the interface, such as film thickness and the signal is recorded by Biacore system. Barclay et al. [157-159]first presented that SPR was suitable for determining the low-affinity interactions between the immunoglobulin superfamily and its receptors. Kim et

al. [154] used SPR to measure the binding affinity of their CMP-based self-assembly of tribodies to recombinant human EGFR. Based on their study, tribody with multiple binding sites significantly increased the local concentration of the affinity unit as well as provided a decreased overall off-rate [154]. Surface plasmon resonance (SPR) has been widely used for monitoring the protein-protein interaction, DNA-small molecule interaction and vice versa. Although the dissociation constant can normally be calculated by k_{on} and k_{off} rate provided by SPR, we still need to notice that some protein samples will irreversibly bind to the sensor chip which leads to the failure of chip regeneration [156]. SPR was applied to characterize the interaction between PMSA and antibodies. Norbert Schülke et al., [160] used SPR to characterize the interaction between antibodies and PSMA. Monoclonal antibody mAb 4.40 bound both monomeric and dimeric PSMA, while mAb 026 only bound to the dimeric PSMA. Sugimoto et al.,[161] developed recombinant PSMA antibodies with therapeutic potential by fusing C-terminus interleukin-2 (IL-2) to PSMA antibodies. The binding of PSMA to these antibodies was characterized by SPR. These antibodies bound to human PSMA immobilized sensor chip with K_d of 9.3 – 11.2 nM. In addition, these antibodies exhibit anti-tumor activities in xenografted tumor model generated from PSMA-overexpressed prostate cancer cells.

1.4.3 Alphascreen assay to measure PSMA binding

Amplified Luminescent Proximity Homogenous Assay (Alphascreen) assay is a beads-based proximity assay which is ideal for measuring molecular interactions such as receptor-ligand interactions (Fig. 1.7). The large proteins and complexes with size up to 200 nm can be measured by this assay. In Dr. Shen and his colleagues' work, peptides and prostate-specific membrane antigen (PSMA) interaction was tested and determined by Alphascreen assay [162].

In this study, the PSMA-binding peptide 563 was biotinylated and incubated with His-tagged PSMA (PSMA-His_6) at room temperature for 1 h and then added with nickel chelator acceptor beads for the second incubation at room temperature for 1 h in dark. Finally, streptavidin donor beads were added to incubate at room temperature for 30 min in dark. Once the donor beads were excited and the peptide-protein complex had formed, the emission light can be monitored by a synery H4 hybrid multi-mode microplate reader (Biotek).

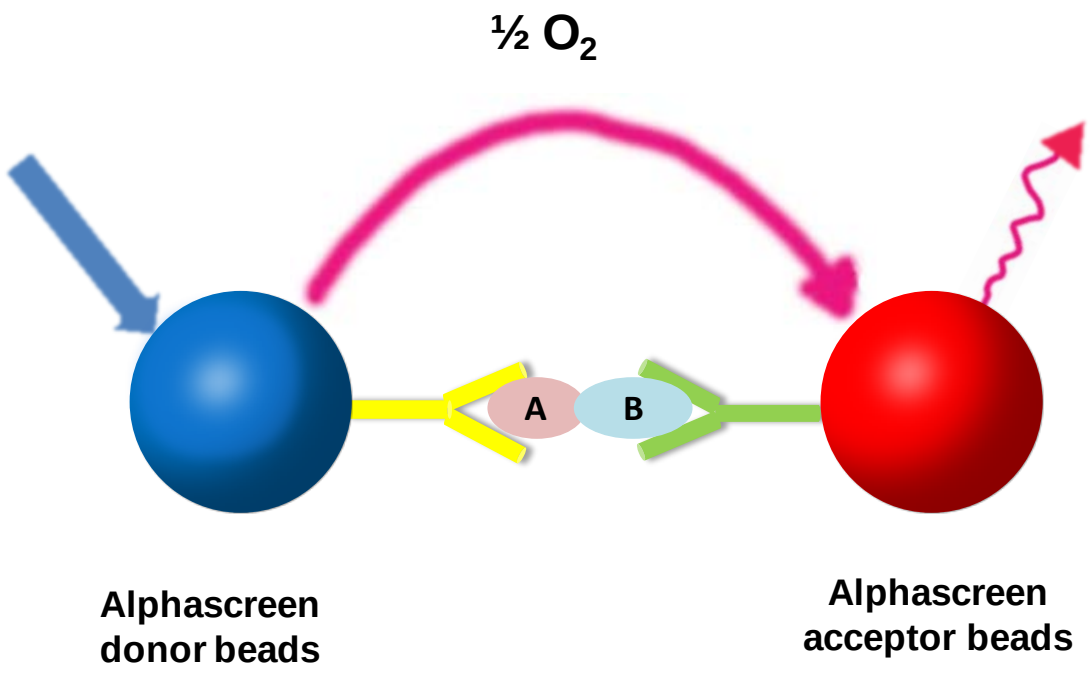

Figure 1.7 Basic mechanism of Alphascreen assay.

In the figure, the blue ball indicates the donor bead and the red ball represents the acceptor bead. The donor bead is typically constructed with streptavidin conjugates, while acceptor bead is primarily conjugated with types of antibodies. The substrate A and B which interaction need to be detected are designed to bind to donor bead and acceptor bead, respectively. The donor bead contains a photosensitizer which can generate singlet oxygen with a single excited electron from environmental oxygen when it was excited at 680 nm. The energy transfer happened between donor bead and acceptor bead only when the distance between substrate A and B interact with each other (< 200 nm). The fluorophore emission light can be detected at 520 - 620 nm.

1.4.4 Radioactive assay to measure PSMA and GRPR binding

Radioactive assay is a traditional method which can directly monitor the binding process. Hiller et al. [163] used a series of binding assay, such as direct binding, saturation binding and internalization, to detect the inhibitor-based PSMA targeting. Synthesized inhibitors MIP-1072 and MIP-1095 were first conjugated to ^{123}I, respectively. Then, these ^{123}I-labeled MIP-1072 and MIP-1095 were incubated with LnCaP and PC3 cells separately and unlabeled MIP-1072 or MIP-1095 and natural substrate PMPA were used as competitors. The signal coming from the radioactive rays confirmed the binding only occurs between the inhibitors and PSMA in LnCaP cells since PC3 has no PSMA expression. The binding can be inhibited when the unlabeled MIP-1072 or MIP-1095 and natural substrate PMPA were added to compete with these ^{123}I labeled inhibitors. Furthermore, saturation assay was done to calculate the affinity of the inhibitors to PSMA in LnCaP cells and receptor numbers per cell. Different concentrations of LnCaP cell lysate (0.001-1000 nM) were incubated with the ^{123}I labeled inhibitors for 1 h at 4°C. By obtaining the signal from the specific binding without the effects generated from nonspecific binding, the kd and Bmax can be calculated. In addition, the internalization of the ^{123}I labeled MIP-1072 and MIP-1095 in LnCaP cells was measured as well. The ^{123}I labeled MIP-1072 and MIP-1095 were incubated with LnCaP cells at 4°C and 37°C for 2 h, respectively. And then a mild acidic buffer was used to wash those nonspecific binding. Finally, by counting the radioactive signals, the amount of ^{123}I labeled inhibitors internalized in cells was determined. This result also confirmed the binding occurred between the inhibitors and PSMA [163].

Varasteh et al. [164] also used radioactive assays to determine the affinity of a NOTA-conjugated bombesin antagonist for GRPR in PC3 cells. Rradiolabeled ^{111}In- and ^{68}Ga NOTA-P2-

RM26 were firstly used to incubate with cultured PC3 cells at a concentration of 1 nM. At the same time, the PC3 cells were also pretreated with a 100 - fold molar excess of non-labeled NOTA-P2-RM26 before incubating the radiolabeled conjugate. This result proved that the conjugate binds to the GRPR in PC3 cells. Moreover, the cell internalization study was also performed. The radiolabeled conjugate was incubated with PC3 cells for 30 min at 37 °C and those non-binding conjugates were washed away. The signals from the total radiolabeled conjugate and internalized conjugate were measured by counting the radioactive signal. The conclusion of the real binding can be drawn. To further determine the binding affinity of the conjugate to GRPR, he did saturation binding and calculated the k_d and B_{max} [164].

1.4.5 NAALADase assay to measure PSMA inhibition

Besides the general methods mentioned above, some other methods based on the unique property of the specific protein were also used to determine the affinity. NAALADase assay is one of them and designed based on the enzymatic activity of PSMA. PMSA has N-Acetylated alpha-linked acidic dipeptidase (NAALADase) activity which can catalyze the hydrolysis of N-acetylaspartylglutamate (NAAG) to glutamate and N-acetylaspartate (NAA). Dr. Banerjee and his colleagues incubated their synthesized inhibitors with LnCaP cell lysate in the presence of NAAG and monitored the amount of released glutamate by incubating with a working solution of the Amplex Red Glutamic Acid Kit (Life Technologies, Grand Island, NY) for 60 min. The fluorescence signal was read by VICTOR3V multilabel plate reader. By using this method, the inhibitory curve can be plotted and IC_{50} can be determined. Enzyme inhibitory constant (k_i) was used to describe the binding affinity of the inhibitors to PSMA in LnCaP cell lysate [165].

1.5 Approaches of biomarker targeting for molecular imaging

Molecular imaging has been used to trace and image the dynamic changes of biomarkers which are over-expressed on disease-related organ surface, for example, cancer [131, 166]. Molecular imaging extends the observation depth from organ to cellular or sub-cellular levels including a series of imaging techniques such as positron emission tomography (PET) [167], X-ray computed tomography (CT) [168], Fluorescence and MRI [139, 169]. Preclinically, QDs have already been conjugated to a variety of molecules and ligands such as peptides, nucleotides, inhibitors, antibodies with various methods to achieve the goal of biomedical imaging [170-172].

Compared to the traditional imaging techniques, the most important advance of molecular imaging is it can trace the biomarkers on the cell surface so as to monitor the whole dynamic process of the biomarker changes in a specific region which is likely related to the disease development and stage. To achieve this goal, quantitatively analysis of the biomarkers is preferred. We can utilize those above techniques to detect whether the imaging probes bind to the cancer biomarkers *in vitro* and further quantitatively calculate the binding constant (K_d) which will help us to select the one with highest binding affinity among all the candidates.

1.6 MRI and MRI contrast agents

1.6.1 The principle for relaxivity

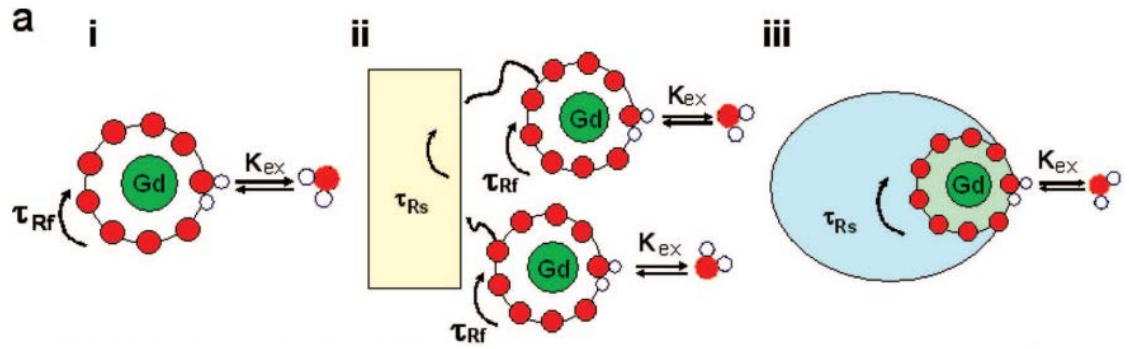

Figure 1.8 Schematic descriptions of different classes of MRI contrast agents [137].

Fig i. represents the early contrast agent. It is formed by an organic molecule chelates a Gd^{3+} ion. Its taoR is too low due to taoR is related to the small molecular weight and the slow mobility of the contrast agent. Fig ii. shows the second generation of contrast agent. Scientists linked small molecule-Gd^{3+} compound to a bigger compound to increase its molecular weight. However, the internal mobility may be fast, the taoR of the small molecule and Gd^{3+} compound is still low. Fig iii. introduces our design, which is a protein-based contrast agent with a designed metal binding site embedded in the protein frame that reduces the internal mobility.

1.6.2 MRI contrast agents

Magnetic Resonance Imaging (MRI) is capable of detecting abnormalities in deep tissues and allows for whole body imaging. MRI remains a powerful and promising imaging technique in cancer diagnosis and treatment, as it enables high resolution, non-invasive, 3-dimensional imaging of organs and tissues without the depth limitation. Because of the high resolution, no

depth limitation, no radiation and three dimensional capabilities compared with other imaging techniques, MRI became one of the most useful and reliable imaging techniques. The sensitivity of MRI may be enhanced by contrast agents designed to enhance the signal for certain types of tissues, organs or molecules. Signals detected by MRI come from hydrogen atoms from water which are present in tissues. MRI contrast agents enhance the MRI signal by altering the longitudinal and transverse relaxation time (T_1 and T_2) of water protons [173].

The ability of a contrast agent to change a relaxation rate is represented quantitatively as relaxivity, r_1 or r_2, where the subscript refers to either the longitudinal ($1/T_1$) or the transverse rate ($1/T_2$). Relaxivity is dependent on external field, the electronic properties of the gadolinium, water exchange, rotational diffusion, first and second coordination sphere hydration, and the ion to water proton distance. Especially, relaxivity is dependent on molecular motion which is based on molecular size, rigidity, and potential protein binding [173].

1.7 Criteria as contrast agents for the molecular imaging

In order to achieve molecular imaging of cancer biomarker by MRI using MRI contrast agents, people have to develop MRI contrast agents based on several criteria.

First, MRI contrast agent must have high relaxivity. In most cases, the expression of the biomarker is limited in the nanomolar or picomolar level. In order to detect these biomarkers, the MRI contrast agents must be extremely sensitive. The current clinically approved MRI contrast agents, however, only have an r1 relaxivity about 3-5 mM^{-1} s^{-1}. Due to such low relaxivity, the local concentration of these MRI contrast agents have to achieve more than 10 μM to show significant difference between background water and tissue. The detection limit of contrast agent concentration will be improved to 0.69 μM if a contrast agent has a r1 of approximately

100 $mM^{-1}s^{-1}$. As the local concentration of cancer biomarkers are limited, high relaxivity is one of the key factors for the development of MRI contrast agents for molecular imaging of biomarkers.

Second, MRI contrast agents should have high stability. Free Gd^{3+} is toxic with LD_{50} of 0.2 mmol/kg in mice. Releasing of MRI contrast agents *in vivo* is believed to be the major cause of Nephrogenic Systemic Fibrosis (NSF), a serious and rare syndrome found in patient with impaired end stage rental function. The physiological metal ions, such as Zn^{2+}, Cu^{2+} and Ca^{2+}, are the potential competitors for Gd^{3+} to interact with chelators. Thus, high stability and metal selectivity are extremely important for the safety administration of MRI contrast agents *in vivo*.

Third, optimized tumor penetration must be considered for the development of MRI contrast agents. Most cancer biomarkers, such as HER2 and GRPR, are deeply buried in cancer tissues outside of the blood vessel. In order to image these biomarkers, MRI contrast agents must have high penetration capability to the tissue and interact with cancer biomarkers. The unbounded MRI contrast agents must be easily washed out to avoid false positive results. De Jong et al. report particles with a size larger than 40 kDa have low efficiency to penetrate to cancer tissue, while particle with a size 4.7-10 kDa can penetrate more than 35 µm within 30 minutes. [174] Although large particles (40-778 kDa) are reported to accumulate in tumor tissue due to enhanced permeability and retention effect (EPR) effects [175], these particles stay in the tumor for long time and are hard to wash out. Thus, an ideal MRI contrast agents must have a good tumor penetration for the molecular imaging of cancer biomarkers with expressed in the cancer tissue outside the blood vessel [176].

Forth, MRI contrast agents must have good pharmacokinetics and desired tissue distribution. Receptor-ligand interaction is a kinetic process. An ideal MRI contrast agent should have a good blood half-life and desired tissue distribution, which allow contrast agents to have sufficient time to interact with cancer biomarker. After imaging, the contrast agents must robustly excreted out to avoid potential toxicity and side effects.

Fifth, contrast agents must incorporate with targeting moieties to interact with the biomarker to achieve molecular imaging. The targeting moiety must have high specificity and selectivity to biomarkers. In addition, the targeting moieties incorporated in the contrast agents must have high stability *in vivo*.

In the past three decades, clinical contrast agents have been successfully applied to the diagnosis of diseases such as cancer, inflammation, neuronal disease. However, the molecular imaging of cancer biomarkers by MRI cannot be achieved by these clinical MRI contrast agents because of unsatisfaction with above criteria. The contrasts which meet above criteria for molecular imaging are highly desired for the molecular imaging of MRI contrast agents.

1.8 Challenges in developing MRI contrast agents for molecular imaging

To date, the molecular imaging of biomarkers by MRI has not been developed due to the lack of the MRI contrast agents with high sensitivity and high binding specificity to the biomarkers. Disease biomarkers usually have limited expression level, and the sensitivity of the clinical MRI contrast agents, around 0.05 mM, make it extremely hard to generate significant MRI signal change. In addition, clinical MRI contrast agents do not incorporate with targeting moiety, which make them impossible for the molecular imaging by MRI [176].

Another challenge for molecular imaging is the non-optimized pharmacokinetics, low disease tissue penetration and low stability. The pharmacokinetics is one of the key factors for the molecular imaging. If the contrast agents have a short half-life, they couldn't have sufficient time to interact with biomarkers. On the other hand, if the half-life is too long, it could cause potential toxicity due to the Gd^{3+} release.

Current targeting strategies, including antibody-based targeting, peptide-based targeting, inhibitor-based targeting and aptamer-based targeting, which have limitations for quantitative targeting and determination of biomarker expression *in vivo*. Antibodies have low tissue penetration with limited capability to reach deep tumor tissue far away from the tumor blood vessels [104]. While having high tumor penetration, their low stability and binding affinity of natural secreted peptides or peptide fragments restrict their applications for the molecular imaging of disease biomarkers *in vivo* by MRI [176].

1.9 Previously achievement in our lab for the development of MRI contrast agents

To over the challenges for molecular imaging by MRI, the Yang lab at GSU has devoted tremendous efforts to develop a series of novel protein-based MRI contrast agents (ProCA) and therapeutic agents for several years [177-182]. We designed Gd^{3+} binding site(s) into a stable protein which shows significantly enhanced relaxivity and decreased the detection limits [183]. Our ProCA is a protein-based contrast agent. We chose domain 1 of rat CD2, a cell adhesion protein with a common immunoglobin fold, as a scaffold protein. We muted five amino acids on the CD2 to form a metal binding site with desired dynamic properties and optimized relaxivity [183].

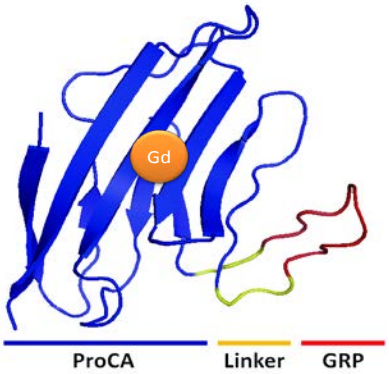

Figure 1.9 Design of GRPR targeted ProCA1 by grafting approach.

The blue color indicates the original ProCA, the yellow color suggests the linker sequence (GGSGG) connecting ProCA and the targeting sequence, and the red color indicates the GRPR targeted peptide sequence.

We have further PEGlyated protein contrast agents to improve *in vivo* imaging capability. The major function of PEGylation is reducing immunogenicity, increasing solubility and corresponding optimal blood rentention time and tissue penetration property. In addition, PEGylation of protein-based contrast agents markedly increase relaxivity as well as decrease the corresponding *in vivo* dose efficiency [184]. To further develop novel contrast agents with molecular imaging capability of breast cancer and prostate cancer, we linked a targeting sequence (HER2-affibody and gastrin-releasing peptide (GRP) into different regions of ProCA1 [139, 169]. The results show us the targeting peptide grafted into the loop region of ProCA1 has much better targeting capability in imaging nude mouse with xenografted tumor models [139].

1.9.1 Introduction of grafting approach for targeting biomarkers

Understanding the structure and function of peptide fractions in certain proteins is restricted by lack of defined structure of the peptide itself. The low stability of the peptide also restricts the peptide research. In addition, the synthesis of peptide is time consuming. Thus, alternative approaches are strongly needed to understand the structure, function and molecular interaction of the peptide.

To overcome the limitations of the peptide research, our lab developed a grafting approach by inserting the peptide into the stable host protein, such as CD2. The flexible linkers, such as GGSGG, were used to link the peptide and the scaffold protein to improve the flexibility of the peptide. To test the grafting approach, we inserted the four different calcium binding peptides from calmodulin, we demonstrated that these calcium binding peptides maintain the calcium binding after inserting into CD2. Since EF-hand has two Ca^{2+} binding sites with high coopertivity, grafting approach enables the evaluation of site-specific calcium binding affinity.

Thus, the grafting approach is a useful tool to evaluate peptide binding properties with well defined structure and improved stability [185, 186].

Our previous lab members further applied the grafting approach to identify novel calcium binding sites in viral protein and receptors, such as Calcium sensing receptor and mGluR [187-195]. They demonstrated that the grafting approach is extremely helpful to identify the unknown calcium binding site in various proteins.

Since grafting approach can maintain the binding properties of the peptides to calcium, we hypothesize that grafting approach can also maintain the binding properties of the peptides to other large molecules, such as proteins. Gastrin releasing peptide (GRP) is a mammalian peptide with high affinity to gastrin-releasing peptide receptor, an important biomarker for many types of cancers. However, GRP has low stability, which restricts its successful applications in molecular imaging. proGRP has a serum stability less than 4 hours [196], 6-28% of which is degraded in serum within 2 h [176, 197].

To overcome this limitation, we applied the grafting approach to insert the C-terminal GRP into the 52 position of ProCA1. [139] (Fig.1.5). This new protein is stable in serum for at least 24 hours [176]. The interaction between this new protein to GRPR was successfully detected by various binding methods. These results demonstrate that the grafting approach is not only good for the study of the calcium peptide interaction, but also good for the study of the protein-peptide interaction. Thus, the grafting approach can be applied to the protein MRI contrast agents to target cancer biomarkers with high affinity and specificity. In addition, the improvement of the peptide stability is very helpful for the *in vivo* application of the targeted MRI contrast agents for the molecular imaging of cancer biomarker. However, previous lab member

didn't achieve the *in vivo* molecular imaging of GRPR through tail vein injection. In this dissertation, I will show my results on the molecular imaging of GRPR by optimizing the GRPR-targeting peptide inserted in ProCA1 by the grafting approach.

1.10 Research questions

To overcome these challenges and explore the potential application of molecular imaging, we developed protein-based MRI contrast agents with high relaxivity and high sensitivity. We also generated different kinds of cancer biomarker-targeted protein MRI contrast agents for the cancer diagnosis. In my dissertation, we ask the following research questions for the prostate cancer diagnosis, since prostate cancer is the leading cause of the cancer-related death in men in the western world. Can we optimize biomarker-targeting capability of the ProCAs by optimizing the targeting peptide using grafting approach?

Do these modifications of the ProCAs influence their *in vitro* properties, such as metal binding affinity, relaxivity, stability, and biomarker targeting properties?

Can we achieve molecular imaging of cancer biomarkers *in vivo* in the mice models? Can we target different types of cancer biomarkers for different types of tumors, by inserting different targeting peptides?

First, can we detect GRPR expression in prostate cancer?

Second, can we semi-quantitatively evaluate GRPR expression levels in different tumors? Third, since PSMA is a golden standard for the prostate cancer diagnosis, can we design a PSMA-targeted MRI contrast agent?

In my dissertation, we ask whether we can design a protein-based MRI contrast agents for the molecular imaging of angiogenesis. In addition to prostate cancer, I have also extended

my studies on the imaging of tumor biomarkers in different types of cancers including angiogenesis such as VEGFR-2.

Since ProCAs have both high r1 and r2, does this mean ProCAs can be functioned as both T1-weighted MRI contrast agents and T2-weighted MRI contrast agents?

In addition, can we tune the metal binding affinity, oxygen coordination, and relaxivity of ProCAs? As the current application of ProCAs is largely limited by the small scale expression and purification, can we achieve large scale expression and purification of ProCAs? These research questions will be answered in my dissertation.

1.11 Overview of the dissertation

1.12 Objectives and questions to be addressed in this dissertation and overview of this dissertation

The goal of this dissertation study is to further develop protein-based MRI contrast agents with high relaxivity and high sensitivity by generating several cancer biomarker-targeted protein MRI contrast agents for the cancer diagnosis. To achieve quantitatively determination and monitor temporal and spatial expression of biomarkers, we aim to develop biomarker-targeted MRI contrast agents by utilizing a targeting sequence to lead a contrast agent to specifically target overexpressed biomarkers on cancer cell surface.

In Chapter 2, **we provide descriptions of all the methods used in the dissertation.**

In Chapter 3, we design experiments to ask the following research questions.

Can we optimize biomarker-targeting capability of the ProCAs by optimizing the targeting peptide using grafting approach? Do these modifications of the ProCAs influence their *in*

vitro properties, such as metal binding affinity, relaxivity, stability, and biomarker-targeting properties? Can we achieve molecular imaging of cancer biomarkers *in vivo* in the mice models? Can we detect GRPR expression in prostate cancer? Second, can we semi-quantitatively evaluate GRPR expression levels in different tumors?

We will report our achievement in designing a new generation of ProCAs with GRPR-targeting capability. The binding affinity of ProCA variants to GRPR were determined by indirect ELISA. We next confirmed the GRPR-targeting by immunofluorescence, IHC and ICP-OES. The Gd^{3+} binding affinity of ProCAs was determined by dye competition methods. We further determined the binding affinity of ProCAs to other physiological metal ions, such as Zn^{2+}. To further explore the imaging capability of ProCAs at high magnetic field, we measured the relaxivity of the ProCAs under 7T Varian MRI scanner. We implanted PC3 and H441 cells in the xenograft mice model. We compared the tumor imaging capability of ProCA1B14 and ProCA1G10. We injected ProCA1 without targeting capability as our negative control. After MR imaging, we further studied the distribution of ProCA1s by IHC, ICP-OES and ELISA.

In Chapter 4, we design experiments to answer these questions

Can we develop grafting approach for targeting different types of prostate cancer biomarkers for different types of tumors by inserting different targeting peptides? As discussed in Section 4.2.3, PSMA has differential expression pattern in different types of prostate cancer cells and have been validated to be an important clinical biomarker for diagnosis and treatment of prostate cancer. However, currently no PSMA-targeted MRI contrast agents were reported due to the lack of a sensitive MRI contrast agent and penetration problem of antibody. Here we

aim to develop a PSMA-targeted contrast agent to monitor prostate cancer type such as PSMA are largely expressed on the LnCaP cells instead of PC3.

We hypothesize that inserting PSMA-targeting peptide to ProCA1 by grafting approach will maintain the native structure of the peptide, which will improve its binding affinity to PSMA. We also hypothesize that by our rational design, our protein-based MRI contrast agents are able to quantitatively evaluate the PSMA expression in prostate tumor.

We report the design of PSMA targeted contrast agent by computation and grafting the prostate-specific membrane antigen (PSMA) targeting peptide [105, 198] into ProCA1. The targeting property of those two agents was monitored by ELISA, cell imaging AND immunofluorescence.

In Chapter 5, we design experiments to address the question whether we design Protein-based MRI contrast agents for the molecular imaging of angiogenesis. VEGFR-2 is an important biomarker for the angiogenesis, which is a key feature for the tumor with a diameter larger than a few millimeters. We report our design the VEGFR-2 targeted MRI contrast agents by genetically linking the VEGFR-2 targeting peptide in the C-terminal of ProCA32. We demonstrated that this VEGFR-2 targeted MRI contrast agents has high Gd^{3+} binding affinity, high relaxivity and is able to target VEGFR-2 *in vitro*. In addition, the molecular imaging of VEGFR-2 was achieved in two different mice models *in vivo*. Interestingly, since this contrast agent has both high r1 and r2 relaxivities, VERGR-2 targeted ProCA can be applied for both T1-weighted sequence and T2-weighed MRI sequence.

In chapter 6, we ask several questions about tuning metal binding affinity and relaxivity of a protein-based blood-pool contrast agent.

Can ProCAs be functioned as both T1-weighted MRI contrast agents and T2-weighted MRI contrast agents?

Can we tune the metal binding affinity, oxygen coordination, and relaxivity of ProCAs?

In this chapter, the relaxivity and water coordination numbers of the ProCAs were tuned by protein design. By mutation S66 to E at 9 position of EF-hand ProCA4, the water number of ProCA4 decrease from 2.71 to 1.59. Consequently, the relaxivity of the ProCA4 decrease from 24.9 to 12.7. Since ProCA4 is the smallest ProCA, ProCA4 can accumulated in the tumor due to EPR effects without involve in any tumor targeting sequence. Such tumor imaging property was further confirmed by ICP-OES.

In chapter 7 we report our achievement on the large scale expression and purification of ProCAs.

Can we achieve large scale expression and purification of ProCAs since the current application of ProCAs is largely limited by the small scale expression and purification?

Current application of ProCAs was limited by their relatively low yield and high cost compared with clinical MRI contrast agents. Here we reported that 217.88 g of bacteria cell pellets were harvested after one month culturing in 60 liters of LB medium using traditional shaking methods. These cells pellets were then purified by the heating-streptomysin-FPLC methods established in our lab. We obtained 800 mg of proteins from cell pellets of 30 L LB medium within one month, which can be used for the injection of one dog. This is the pioneering work for the large scale expression, purification and commercialization of protein-based MRI contrast agents.

In Chapter 8, the major funding of this dissertation and significance will be described.

Table 1.8 Summary of the protein-based MRI contrast agents used in this dissertation.

Name of ProCA	Description	Biomarker Targeting
ProCA1	The first generation of ProCAs with one Gd^{3+} binding site in a scaffold protein.	No targeting
ProCA1B10	ProCA1 inserted with 10 amino acid peptide from bombesin using grafting approach.	GRPR
ProCA1B14	ProCA1 inserted with full length peptide from bombesin using grafting approach.	GRPR
ProCA1G10	ProCA1 inserted with 10 amino acid peptide from GRP using grafting approach.	GRPR
ProCA1.sau	ProCA1 inserted with PSMA-targeting peptide, sau, using grafting approach.	PSMA
ProCA1.wp	ProCA1 inserted with PSMA-targeting peptide, wp, using grafting approach.	PSMA
ProCA32	The third generation of ProCAs with two Gd^{3+} binding sites in a scaffold protein.	No targeting
ProCA32.562	PSMA-targeted peptide (562) was fused at C-terminal of ProCA32 via GGSGG linker.	PSMA
ProCA32.563	PSMA-targeted peptide (563) was fused at C-terminal of ProCA32 via GGSGG linker.	PSMA
ProCA32.564	PSMA-targeted peptide (564) was fused at C-terminal of ProCA32 via GGSGG linker.	PSMA
ProCA32.VEGF	VEGFR2-targeted peptide was fused at C-terminal of ProCA32 via GGSGG linker.	VEGFR2
ProCA4	The fourth generation of ProCA with two Gd^{3+} binding sites in a scaffold protein.	No targeting
ProCA4S66E	ProCA4 with additional S66E mutation to modulate water coordination number, relaxivity and metal binding affinity of ProCA4.	No targeting
ProCA4S28E	ProCA4 with additional S28E mutation to modulate water coordination number, relaxivity and metal binding affinity of ProCA4.	No targeting

2 METHODS

2.1 Molecular Cloning

Domain 1 of rat CD2 was selected as a scaffold and several amino acids were muted to form a Gadolinium binding site on its surface, which is called 7E15 or ProCA1. Our previous lab member Dr. Lixia Wei cloned the ten amino acids from the C-terminal of GRP into ProCA1 to form a new contrast agent with GRPR-targeting capability, which is called 7E15G10 or ProCA1G10. All of these plasmids were cloned into pET-20b vector. The plasmid of ProCA1G10 was used as a template and the new sequences coming from bombesin were inserted to replace G10 to form some new ProCA1 variants. The constructed plasmids of ProCA1 variants were confirmed by DNA sequencing at GSU core facility.

The general procedure for the molecular cloning is shown in Fig. 2.1 and Fig. 2.2. The primers were designed based on the sequences of plasmid and targeting peptide, which is listed in Table 2.1. Polymerase chain reaction is described as the following: denature at 95 °C for 10 min, anneal at 58 °C for 45 seconds and then elongate at 72 °C for 10 minutes within 30 cycles. The PCR products were identified by agarose gel and the corresponding DNA band were cut and extracted by kit QIAquick Gel Extraction Kit (250). The amplified linear DNA sequences were phosphorylated by PNK (New England Biolabs), ligated by T4-ligase (New England Biolabs) and then were used to transfect *E.Coli* competent cells DH5α. The transfected competent cells were scratched on LB plate with 0.1% ampicillin. The single colony grown up on the plate was collected and amplified in LB medium with 0.1% ampicillin. The plasmid extracted from the culture was sent to GSU core facility or GENEWIZ for DNA sequencing.

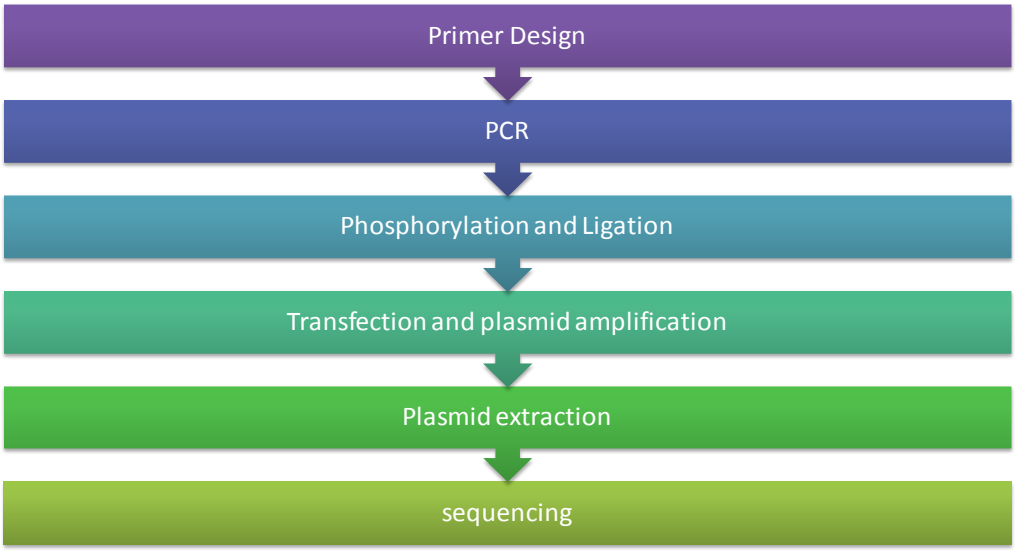

Figure 2.1 General procedure for molecular cloning.

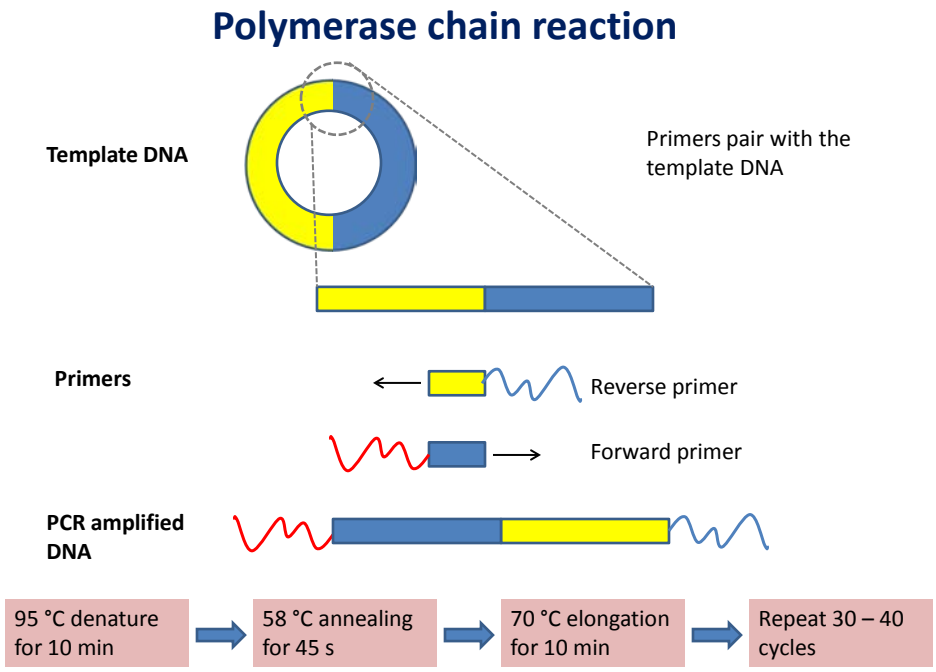

Figure 2.2 Polymerase chain reaction (PCR) for plasmids of ProCAs.

Table 2.1 The primer design of ProCA1B14 and ProCA1G10.

Primer	sequence	Tm	Template
B14for	aatgggcagtaggccatctaatgggcggatcaggtggagcatttgagatcgacgcaaa	68	pET20b-7E15, pGEX2T-7E15
B14brev	ggtttcccagtctttgttcgccacctgatccgcccgatttcaaaaaaggcttcatcttc	68	Same
G10for	agtaggccatctaatgggcggatcaggtggagcatttgagatcgacgcaaat	68	Same
G10rev	gcccagtggtttccgccacctgatccgcccgatttcaaaaaaggcttcatcttc	68	Same

2.2 Protein expression, purification and PEGylation

2.2.1 Protein expression

ProCA1 variants were expressed by *E.Coli* Tuner, BL21DE3, BL31PlysS and BL21DE3plysS competent cell strains. At initial, competent cells were transfected with the plasmids of ProCA1 variants and scratched on LB plate with 0.1% ampicillin. The plate was cultured at 37°C over-night. In the next day, a single colony was selected from the plate and inoculated into LB medi-um with 0.1% ampicillin and cultured in a shaker (220 rpm, 37 °C) overnight. In the third day, 500 µl of the inoculated culture was added to 10 ml LB medium with 0.1% ampicillin and the OD value was monitored at 600 nm every 30 min by a UV spectrophotometer (Shimadzu Scientific Instruments, Norcross, GA) until it was located between 0.6 and 0.8. Once the growth of the

bacteria was up to the exponential phase, 0.1, 0.5 or 1.0 mM Isopropyl β-D-1-thiogalactopyranoside (IPTG) was added to each flask to induce protein expression at 37 °C. After 3 hours protein expression, the temperature of the shaker was decreased to 30 °C or kept at 37 °C and the protein expression was continued overnight. After overnight expression, the cell pellets were collected by centrifuge (Sorvall RC SB Plus Centrifuge, Thermo Scientific, Bruswick, NJ) at 7000 rpm in 4 °C for 30 min and stored at -20 °C until purification. The SDS-PAGE was used to quantify the protein expression level. The whole procedure of protein expression is described in Fig. 2.3 in Chapter 2.

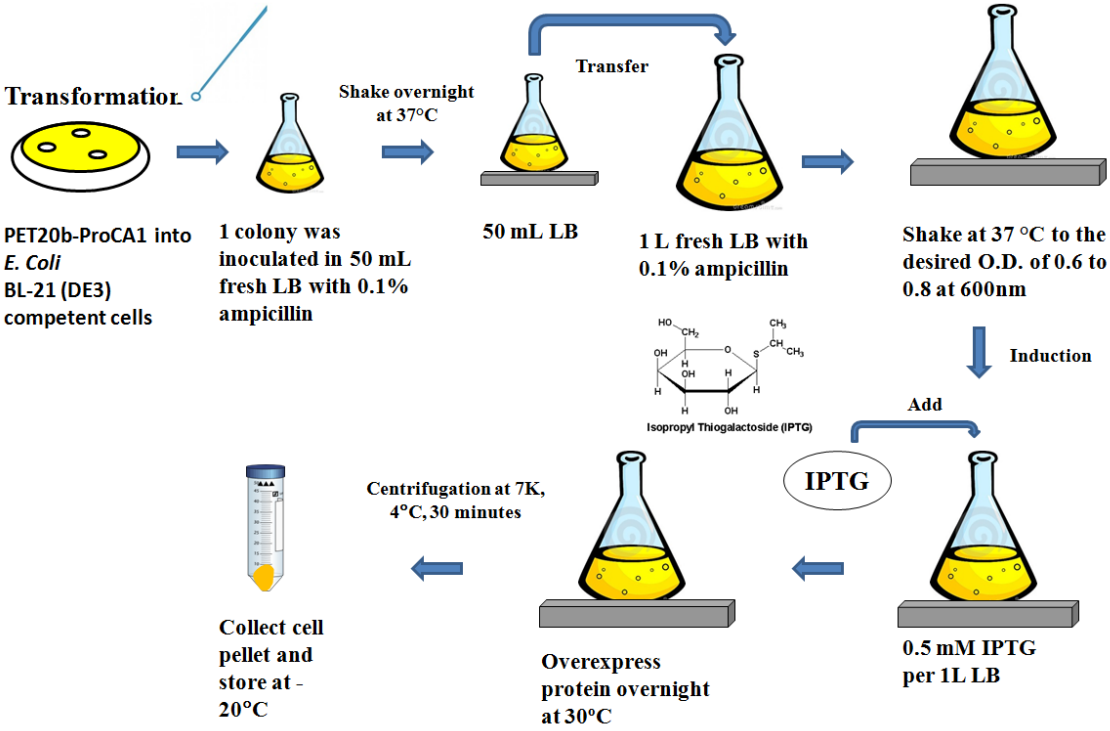

Figure 2.3 General procedure of ProCA1 variants expression.

2.2.2 Protein purification

Cell pellets from 2 L LB culture were resuspended in 40 ml PBS buffer (pH 7.4). 1 µl benzonase nuclease (Novagen) was added to degrade all forms of DNA or RNA. 100 µl PMSF (phenylmethanesulfonylfluoride) was added to inhibit serine protease in the cell lysates. The re-suspended mixture was sonicated five times at intervals of 30 sec each and further broken by French Press or Cell Disruptor. Then, the mixture was centrifuged at 17000 rpm for 20 min and the cell pellets were collected and washed by 1% Triton X-100 for 3-4 times until the color turned white. Then it was dissolved in 8 M urea at 4 °C overnight and centrifuge at 17000 rpm for 20 min to remove those insoluble impurities. The supernatant was placed in the dialysis bag and dialyzed in 4 M urea at 4 °C overnight and then in 2 M urea and finally in 10 mM HEPES buffer (pH 8.0). The refolded protein solution was filtered using 0.45 µM pore size syringe filters (25 mm GD/X disposable filter service, PVDF filter media, Whatman^{TM}, GE Healthcare Life Science) and further purified by FPLC-Q column or SP column. The whole procedure for protein purification is shown in Fig 2.4.

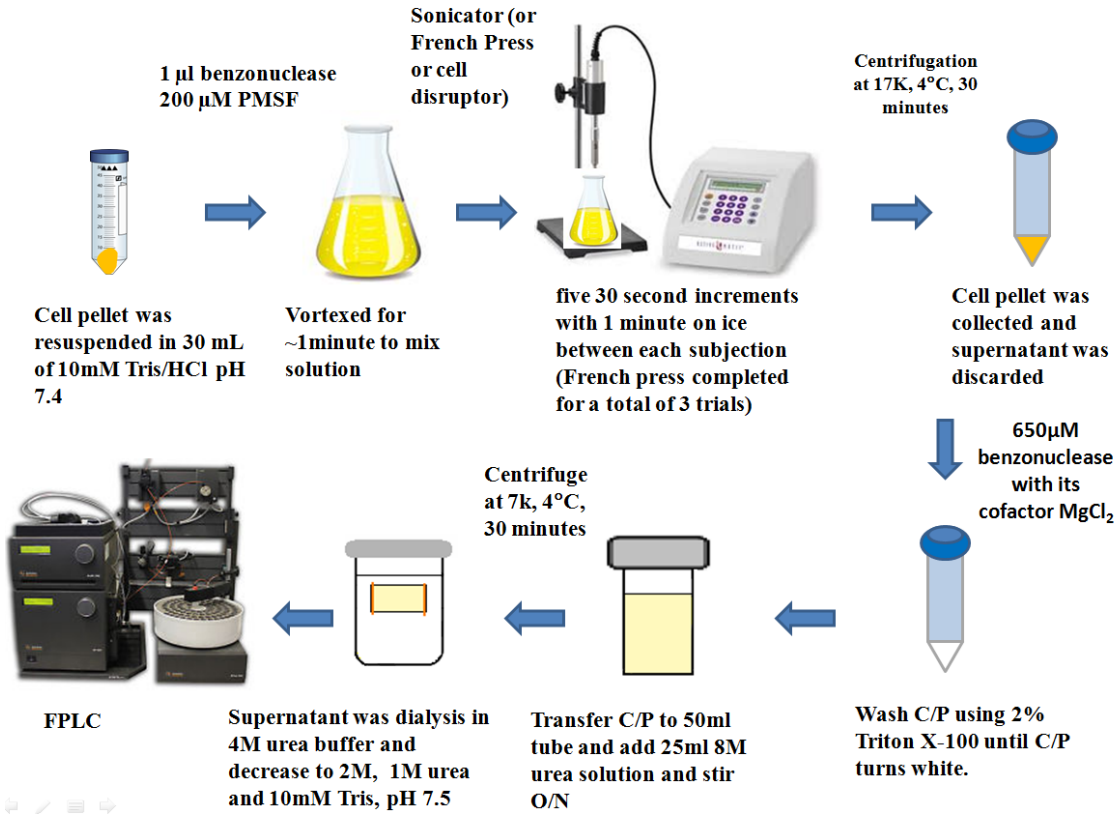

Figure 2.4 General procedure of PET20b-ProCA1 variants purification.

2.2.3 Protein PEGylation

Polyethylene glycol (PEG) is a polyether compound which can covalently interact with another molecule such as protein. PEGylation is one powerful strategy to improve the drug delivery, pharmacokinetics and pharmacodynamics by increasing water solubility, protecting enzymatic degradation, decreasing renal clearance and immunogenecity. [199] The detailed procedure is as follows.

At first, ProCA1 variants were dissolved in 10 mM HEPES buffer (pH 7.0) to make sure there is no any existing Tris, which can react with PEG-NHS ester. Second, ProCA1 variants were mixed with PEG-40 at 1:5 ratios at room temperature for 4 hours or at 4 °C overnight. Third,

100 mM Tris/HCL was added to the reaction system to stop the reaction by quenching unreacted free PEG-NHS ester. Fourth, the mixture was purified by FPLC-Q column to get the pure PEGylated ProCA1 variants. SDS-PAGE can identify the PEGylation procedure. Coomassie brilliant blue can stain the proteins while iodine staining shows the PEGylated one.

2.3 Secondary and Tertiary Structure Study

2.3.1 Tryptophan Fluorescence

Tryptophan fluorescence was monitored by a QM1 fluorescence spectrophotometer (PTI) with a xenon short arc lamp at ambient temperature. The excitation wavelength is at 280 nm while the emission wavelength is between 300 and 400 nm with 2 - 4 nm slit width. The protein samples were prepared in 20 mM PIPES, 10 mM KCl (pH 6.8) and respectively placed in a 1-cm path length cell for spectral measurements. Tryptophan is used as a control.

2.3.2 Circular Dichroism Spectroscopy

The Circular Dichroism (CD) spectrum was obtained by a Jasco-810 spectropolarimeter at ambient temperature. The protein samples were prepared at 25 μM in 10 mM Tris-HCl (pH 7.4), 10 mM KCl with 1 mM EGTA or 1 mM $CaCl_2$ in a 1 mm quartz cell. The CD signals were monitored by the wavelength from 190 nm to 260 nm. 25 μM or 1 mM $GdCl_2$ was loaded in the quartz cell to combine with ProCA1 variants, which was used to detect the binding effects on the protein structure.

2.4 The Determination of Metal Binding Affinity

2.4.1 The Determination of Gd^{3+}-binding affinity by dye competition method

The Ca^{2+} dye Fluo-5N binds Gd^{3+} and produce a fluorescence signal. The binding affinity of ProCA1 variants to Gd^{3+} was determined by a competition method in Fluo5N-Gd^{3+} buffer system. Gd^{3+}-binding affinity of ProCA1 variants were determined by a competition method with Fluo-5N which is a Ca^{2+} dye. Fluo-5N emission spectrum was monitored from 500 nm to 650 nm when it was excited at 488 nm. The binding affinity of Fluo-5N to Gd^{3+}, K_{d1}, was determined by a Gd^{3+} titration in Gd^{3+} buffer system where 1 mM NTA was used to control the concentration of free Gd^{3+}. As the binding affinity of NTA to Gd^{3+} was known, the concentration of free Gd^{3+} could be calculated. Fluo-5N was mixed with Gd^{3+} at 1:1 ratio. Then ProCA1 variants were gradually added into the buffer system to compete Fluo-5N with Gd^{3+}. An apparent dissociation constant, K_{app}, was estimated by fitting the fluorescence emission intensity of Fluo-5N at 520 nm with different concentrations of ProCA1 variants as a 1:1 binding model. Gd^{3+}-binding affinities of ProCA1 variants, K_{d2}, were calculated with the following equation (2.1):

$$k_{d2} = k_{app} \times \frac{k_{d1}}{k_{d1} + [Fluo-5N]_T} \qquad (2.1)$$

2.4.2 The Determination of Zn^{2+}-binding affinity by dye competition method

The Zn^{2+} dye Fluozin-1 binds Zn^{2+} and produce a fluorescence signal. The binding affinity of ProCA1 variants to Zn^{2+} was determined by competition method in Fluozin-1-Zn^{2+} buffer system. Zn^{2+}-binding affinity of ProCA1 variants were determined by a competition method with Fluozin-1 which is a Zn^{2+} dye. Fluozin-1 emission spectrum was monitored from 500 nm to 600

nm when it was excited at 495 nm. The binding affinity of Fluozin-1 to Zn^{2+}, K_{d1}, was reported as 8 µM. Fluozin-1 was mixed with Zn^{2+} at 1:1 ratio. Then ProCA1 variants were gradually added into the buffer system to compete Fluozin-1 with Zn^{2+}. An apparent dissociation constant, K_{app}, was estimated by fitting the fluorescence emission intensity of Fluozin-1 at 515 nm with different concentrations of ProCA1 variants as a 1:1 binding model. Zn^{2+}-binding affinities of ProCA1 variants, K_{d2}, were calculated with the following equation (2.2):

$$k_{d2} = k_{app} \times \frac{k_{d1}}{k_{d1} + [Fluozin-1]_T} \qquad (2.2)$$

2.4.3 The Determination of Tb^{3+}-binding affinity by Tb^{3+}-DTPA or EGTA buffer system

Determining Tb^{3+} binding affinity of ProCA was based on Tb^{3+} luminescence resonance energy transfer (LRET) experiment. When Tb^{3+} binds to ProCA, the emission spectrum of the internal phenylalanine and tryptophan in ProCA was changed. 30 µM ProCA was prepared in 5 mM DTPA (or EGTA), 50 mM HEPES, 150 mM NaCl at pH 7.2. DTPA (Kd is 10^{-22} M, NIST) and EGTA (Kd is 10^{-18} M, NIST) were used to control the free Tb^{3+} concentration in the system, separately. Then, $TbCl_3$ was titrated in the system to interact with ProCA. The excitation wavelength was at 280 nm for ProCA while the emission wavelength was monitored from 500 to 650 nm. The free Tb^{3+} concentrations in the solution were calculated by using the equation (2.3) and the $Kd_{Tb,\ ProCA}$ is calculated by Hill Equation (2.4)

$$[Tb^{3+}]_{free} = kd_{Tb,DTPA} \times \frac{[Tb - DTPA]}{[DTPA]_{free}} \qquad (2.3)$$

$$f = \frac{[Tb^{3+}]_{free}{}^{n}}{kd_{Tb,\mathrm{Pr}oCA}{}^{n} + [Tb^{3+}]_{free}{}^{n}} \qquad (2.4)$$

2.5 Relaxivity measurement

The T1 and T2 relaxation time of ProCA1 variants were measured by 1.4 T bruker minispec. T1 (the spin-lattice relaxation time) is the time to recover from the longitudinal magnetization to its equilibrium value. T2 (the spin-spin relaxation time) is the time to recover from the transverse magnetization to its equilibrium value. Different concentrations of ProCA1 variants were mixed with fixed concentration of Gd^{3+}. Those tubes were incubated in the relaxometer to an equilibrium state and then measured to get the T1 and T2 values. r1 and r2 were calculated by the same equation ri=(1/Ts-1/Tc)/C, i= 1, 2, where Ts is the relaxation time of contrast agent, Tc is the relaxation time of buffer and C is the concentration of Gd^{3+}.

2.6 Water number measurement by Tb^{3+} lifetime luminescence

Tb^{3+} luminescence decay in H_2O and D_2O are different which is used to determine the number of water ligands coordinated to ProCA -Gd^{3+} complex. Protein samples and $TbCl_3$ are mixed with 1:1 ratio in H_2O and D_2O respectively and measured in a 10 mm path length quartz cuvette at room temperature by using a fluorescence spectrophotometer (Photon Technology International, Inc.) . Tb^{3+} was excited at 265 nm with a XenoFlash lamp (Photon Technology International, Inc.) and emitted at 545 nm in both H_2O and D_2O solutions. Tb^{3+} luminescence decay lifetime in H_2O and D_2O were obtained by fitting the data with a mono exponential decay function. To correlate the water number (q) with ΔK_{obs} (the difference of the decay constant between H_2O and D_2O), a standard curve was established. The water number of Gd aquo (9),

Gd-DTPA (1), Gd-EDTA (2.8), Gd-NTA (5) has been reported in the literature. [183] The Tb^{3+} luminescence decay of Gd-chelators is different. The standard curve of water number can be plotted by using water number as the X-axis while ΔK_{obs} as the Y-axis. The water number of ProCA variants was calculated comparing the standard curve.

2.7 Cell Culture

PC3, a prostate cancer cell line, has a high expression level of gastrin-releasing peptide receptor (GRPR) on cell surface. H441, a lung cancer cell line, has a relatively low expression level of GRPR on cell surface. Both of the cells were cultured in RMPI1640 medium supplemented with 1% Penicillin-Streptomycin (P/S) and 10% fetal bovine serum (FBS) at 37°C and 5% CO_2 / 95% air incubator. 1 ml Trypsin was added to the dish to digest the cell. All the cells were thawed immediately at 37 °C water bath and refreshed with 8 ml medium when they were taken from the liquid nitrogen. In the next day, the cells needed to be transferred to new medium to prevent the toxic effects coming from the cell freezer. When the cells' density in the original dish is too high to limit their growth, the cells will be treated with 2% Trypsin and washed with HBSS buffer by centrifuge. After washing, the cells are transferred to more dishes.

2.8 Cell lysate Preparation

Cells (PC3, H441 and LnCaP) were cultured in 75 cm^2 flasks of RMPI 1640 medium supplemented with 10% fetal bovine serum (FBS) and 1% penicillin- streptomycin (P/S) in 5% CO_2 / 95% air at 37 °C. After washing with HBSS buffer, the cells were scratched by cell scraper and suspended by 800 µl HBSS buffer and transferred to 1.5 ml tube. The suspended cells were centrifuged at 1000 rpm for 5 min to discard the supernatant. After that, 500 µl lysate buffers (50

mM tris, 150 mM NaCl, 1% triton, pH 7.4) or RAPI buffer plus 0.1 % PMSF were added to re-suspend the cells again. Then, the mixture was left shaking at 4 °C for 4 h. After centrifuging the lysate at 12000 rpm for 30 min, the supernatant was collected and stocked at -80 °C for use.

2.9 Cryostorage of Cancer Cells

Cells (PC3, H441 and LnCaP) were cultured in 75 cm^2 flasks of RMPI 1640 medium supplemented with 10% fetal bovine serum (FBS) and 1% penicillin and streptomycin (P/S) in 6% CO_2/ 95% air at 37 °C. The cells were collected from 10 cm petri dish by Trpsin and washed with 5-6 ml HBSS by centrifuge at 1000 rpm for 5 min. Then, the cells from one of 10 cm petri dish were re-suspended by 1 ml cyro medium. The cells were frozen at - 20 °C for several hours and transferred to - 80 °C to freeze overnight. Finally, the cells were stored in liquid nitrogen for use.

2.10 Western blot

The cell lysate of (PC3, H441 or LnCaP) were mixed with 2X SDS sample buffer at 1:1 ratio and boiled at 90-95°C for 3-5 min. The samples were loaded to the SDS-PAGE to differentiate various proteins existing in the cell lysate based on the molecular weight (KD) difference. GAPDH existing in the lysate was used as a loading control. After running protein electrophoresis, the gel was transferred to the nitrocellulose or PVDF membrane at 22v in 4 °C cold box overnight. After electronic transfer, the gel was blocked with 5% non-fat milk in TBST for 1h. Then, the primary antibody (mouse anti-GAPDH and rabbit anti-GAPDH) was added with different dilution ratios (0.33:1 and 1:1000) to incubate at 4°C overnight, respectively. In the next day, the membranes were washed with TBST for 3 - 4 times to remove non-specific binding of the primary antibody. Then, ALP-conjugated goat anti-mouse secondary antibody diluted with a

ratio of 1:10000 in 5% blocking milk was added to incubate the membranes at room temperature for 1 h. After washing the non-specific secondary antibody, 1 ml substrate plus 25 µL enhancer (Immun-Star^{TM} AP Substrate Pack #170-5012) were added to exposure the film.

2.11 Cell imaging

The fluorescence of the cells or tissue after immunostaining were observed using Zeiss or Leica fluorescence microscope with selected filters to specifically show the fluorescence staining from DAPI, fluorecein, FITC, alexa fluor 488 and alexa fluor 568. The cell structures images were taken at the same field of view using bright field image. The fluorescence intensities were quantified using ImageJ.

2.12 Determination of the binding affinity of ProCA variants to biomarkers and biomarker numbers on cell surface by ELISA and Scatchard Plot

The GRPR expression levels of two different cell lines (PC3 and H441) were first measured by western blot and chosen as two different representatives of GRPR-expression cell lines. Indirect ELISA and Scatchard plot were used to further identify the GRPR numbers on these cell lines and the dissociation constants of ProCA1 variants to them. Cell lysate of PC3 (from 5 x 10^4 cells) and H441 (from 5 x 10^4 cells) were separately precultured in 96-well plate at 4 °C over night. Then, the medium were exchanged with 5% BSA to block the non-specific binding. ProCA1 variants were added to interact with GRPR in cell lysates. Rabbit anti ProCA1 antibody was used as the primary antibody. A stabilized goat anti rabbit HRP-conjugated antibody (Pierce) was used as the secondary antibody. The absorbance intensity was detected by a FLUOstar OPTIMA plate reader at a fix absorbance wavelength of 450 nm.

2.13 MR imaging of mice model

$5x10^6$ PC3 and H441 cells were injected into both flanks of the athymic mice to generate xenografted model. Around 8 weeks, tumors grew up to 1 cm. The contrast agent, Gd-ProCA1B14 (5 mM, 100 µl) was injected into the mouse with xenografted tumors by tail vein injection. Mice were scanned under a 7 T MRI scanner (Varian) using a dedicated rodent coil. The mouse was anesthesized with isoflurane during the MR scan process. MR images were acquired by spin echo sequences (TR = 400 ms, TE = 14.52 ms) with field of view of 4 × 4 cm, matrix of 128 × 128, and slice thickness of 1mm.

2.14 NIR labeling and NIR imaging

ProCA1 variants were conjugated with NIR dye Cy5.5 with the ratio 5:1. Before adding NIR dye, ProCA1 variants reacted with reduced agent TCEP with the ratio 1:5. The reaction happened in nitrogen saturated solution, and the aluminum was used to protect NIR dye away from light because the NIR dye is light sensitive.

After MRI contrast agent ProCA1B14 was injected into the mice, the NIR images of mice were taken after 4, 24, and 48 h. ProCA1B14 with conjugated NIR dye exhibited fluorescence excitation and emission maxima at 640 and 695 nm, respectively.

2.15 Gd^{3+} distribution by ICP-OES

After MR and NIR imaging, the mice were sacrificed and various tissues were extracted. One part was encapsulated by O.C.T and conserved at -80 °C for IHC analysis, while the other part was digested by 70% HNO_3 (Optima) at 110 °C over night. The digested solution was evaporated to 1 ml and 2% HNO_3 (Optima) was added to make the sample volume up to 5ml. Gd^{3+}

concentrations in samples were calculated based on the standard curve (0 ppb, 5 ppb, 50 ppb, 100 ppb and 500 ppb).

2.16 Clinical chemistry study of ProCA1 variants

Basically, clinical chemistry makes use of a series of simple chemical tests to investigate the components of bodily fluids such as blood and urine. In our case, normal mice of 25 - 30 g were selected to do the I.V. injection with 0.03 mmol/kg of ProCA1 variants. After two days, the the mice blood was collected using heparin-coated capillary. Then, the blood was centrifuged at 3000 rpm at 4 °C for 10 min to separate the serum. The serum was sent to IDEXX Laboratories for clinical study which evaluates renal, liver functions, blood disorders, electrolytes and minerals.

2.17 ProCA1B14 target GRPR on PC3 and H441 xenograft tumors by immunofluorescence staining (IF)

After MRI and NIR imaging, the mice were sacrificed and various tissues were extracted. The PC3 and H441 tumors were encapsulated by O.C.T and frozen in liquid nitrogen. The frozen specimens were cut as 5 µm thick in the cryostat at -20°C. The air dried samples were fixed with methanol at -20°C for 10 min and then blocked with horse serum. After the blocking solution was removed, the diluted primary antibody (OX-34) was added to each section and incubated overnight at 4 °C. In the next day, the primary antibody was washed away with 1 x PBST buffer, and the secondary antibody was added to the sections to incubate for 30 min at room temperature. After the secondary antibody was washed away, the slides were mounted with DAB mounting solutions and sealed in the following day.

2.18 ProCA1B14 distribution in different tissues by immunohistochemistry staining

After MRI and NIR imaging finished, the mice were sacrificed and various tissues were extracted. The PC3 and H441 tumors were encapsulated by O.C.T and frozen in liquid nitrogen. The frozen specimens were cut as 5 µm thick in the cryostat at -20 °C. At initial, the frozen slides were placed in room temperature for 5 min to warm up and were immersed in 1 x PBS buffer for 5 min to be permeable. Horse serum as blocking buffer was added onto each section to incubate at room temperature for 30 min. After draining of blocking buffer, donkey anti-mouse IgG was added to the slides to block the immunogenecity coming from the mice tissues. Then, diluted primary antibodies (OX-34) were added on the slides and incubated in the humidified chamber overnight at 4 °C. In the next day, the slides were rinsed with 1 x PBS buffer and incubated with HRP-conjugated secondary antibodies at room temperature for 1 h. After rinsing the slides, DAB substrate solution was added on the slides to reveal the color of the antibody staining. Then, the slides were washed with dH_2O, counterstained the slides with hematoxylin and dehydrated by passing through different concentrations of alcohol (30%, 50%, 70% 90%, 100%, and 100%). Finally, the tissue slides were cleaned by xylene and covered with mounting solution.

2.19 Pharmacokinetic studies by ICP-OES

To further study the pharmacokinetics of ProCA1 variants, plasma of mice were collected at different time points after injection. After serum was digested by 70% nitric acid, each sample was diluted by 3% nitric acid to 4 ml and ready to run by ICP-OES. Pharmacokinetic models are hypothetical structures that are used to describe the fate of a drug in a biological system following its administration. In the two-compartment model, the tissues were proposed

to central compartment and peripheral compartment. This model is based on the hypothesis that when a drug is administered into body, it cannot achieve instantaneous distribution and equilibrium between two kinds of compartments. In fact, volume of distribution (V_d) is apparent volume of distribution, which means the volume of plasma in which the total amount of drug in the body would be required to be dissolved in order to reflect the drug concentration in the plasma. The time required to reduce the plasma concentration to one half its initial value is defined as the half-life ($t_{1/2}$). Drug clearance (CL) is defined as the volume of plasma in the vascular compartment cleared of drug per unit time by the processes of metabolism and excretion.

3 GRPR-TARGETED PROTEIN CONTRAST AGENT EABLES MOLECULAR IMAGING OF RECEPTOR EXPRESSION IN PROSTATE CANCERS BY MRI

3.1 Introduction

As discussed in Chapter 1, prostate cancer is the most common cause of tumor-related death in men in the western world. According to National Cancer Institute's estimation, about 240,890 new cases occur in 2011 while 33,720 people are dead. One of the major causes for such high death rate is due to our limitations of current methods such as PSA coupled with digital rectal examination (DRE) and biopsy coupled with immunohistochemistry (IHC) for the earlier detection, accurate diagnosis, and capability in monitor treatment of this disease[200]. Current verification of prostate cancer types by invasive clinical diagnostic procedures based on biopsy could easily take three years since initial finding of elevated level of PSA. Clearly there is an urgent need to develop a sensitive and accurate non-invasive imaging method to determine the nature of cancer based on the biomarkers, and subsequently monitor tumor progression, metastasis, and the effectiveness of the various treatments with high specificity.

In addition to PSMA, biomarkers such as gastrin-releasing peptide (GRP) receptor (GRPRs) was reported to be over-expressed in prostate carcinoma and androgen-independent human cancer cells such as PC3 and DU-145 (Section 1.3.2) [201, 202]. GRPR is a member of the mammalian bombesin receptor and highly expressed in well-differentiated prostate cancer, while has relatively low expression at poorly differentiated and metastatic prostate cancers [203](Table 1.5). A massive GRP receptor overexpression was observed in prostate and breast tissues [203, 204] during malignant transformation. Both GRPR and PSMA were reported recently to express in the primary prostate tumor and metastasis tumor in bone and lymph nodes

with strong correlation, although expression pattern seems different [205]. It has reported that GRPR is a GPCR with a capability to bind to short peptides of GRP or Bombesin (Table 1.6)[206]. While 7-14 residues from the C-terminal of GRP and Bombesin were commonly used to develop imaging reagents such as PET, SPET and florescence with capabilities to target to biomarker GRPR, it is not clear that how these peptides are recognized by the receptor due to lack of 3-D structures (Table 1.7). Although using a short ligand peptide as a targeting moiety has the advantages for tumor penetration compared to large size of antibody, there are several limitations and concerns such as having less desired specificity/affinity as well as *in vivo* biostability due to lack of defined structures of short peptides [139]. Therefore, it is important to develop a new targeting approach for molecular imaging.

As one of the leading diagnostic techniques in clinical and preclinical settings[207], MRI has the unique advantage of capturing the 3-dimensional anatomical images with increased body depth and without ionized radiation. In addition, it enables the non-invasive and repetitive assessment of biological processes of the same living subject at different time points which significantly reduces the number of animals required, and cost associated with preclinical studies[207]. Clinical TNM (Tumor, Node, and Metastasis) staging is commonly used in the USA. MRI is more accurate (range from 50% to 2%) than CT, ultrasound and DRE in the assessment of unilateral or bilateral disease (stage T2), extracapsular extension and seminal vesicle invasion (stage T3), and the invasion of adjacent structures (stage T4) [208]. Molecular imaging of cancer biomarkers using MRI potentially improves our understanding of the disease and drug activity during preclinical and clinical drug treatment [209, 210]. However, one of the major barriers for the application of MRI, to assess specific disease markers for diagnosis and monitoring drug ef-

fect is the lack of desired contrast agents capable of enhancing the contrast between normal tissues and tumors with high relaxivity, targeting capability, tumor permeability and reduced toxicity. Clinical MRI contrast agents, such as Gd-DTPA, have relaxivity less than 5 mM^{-1} s^{-1} which require high injection doses (0.3 - 0.5 mM) with a risk of NSF due to metal toxicity. This is a major limitation for the molecular imaging of biomarkers by MRI. Recently approved MRI contrast agents using iron oxide nanoparticles, such as Feridex, also exhibit limited tumor penetration and tend to accumulate in liver and intestines[211]. In addition, it has a T2 dark effect which is less desired by imaging analysis. This class of contrast agent is non-targeted and cannot provide information about changes in biomarkers. Taken together, there is an urgent need in developing MRI contrast agent with strong capability in relaxivity and target capability to monitor the changes of the disease biomarkers with temporal and spatial information.

We have developed a novel class of protein-based MRI contrast agents (ProCAs) by creating a Gd binding site into a scaffold protein CD2 (ProCA1) with high relaxivities compared with clinical MRI contrast agents both *in vitro* and *in vivo* [212]. In our effort to develop a molecular imaging MRI reagent, we have developed GRPR targeted reagent (ProCA1.GRP) that enable us to enhance the tumor region after intratumoral injection [139]. In this chapter, we report our development of GRPR–targeted reagent with improved targeting capability using a grafting approach and computational modeling of the molecular recognition between GRPR and its designed protein ligand. The designed GRPR-targeting reagent (B14) has the unique capability to selectively enhance the xenografted prostate tumor with MRI signal depending on the expression levels of the biomarker GRPR *in vivo* of mice due to its improved relaxivity, targeting capa-

bility and specificity. We finally show that the designed GRPR-targeting reagent (B14) has no detectable acute toxicity and tissue toxicity.

3.2 Results

3.2.1 Design of ProCA1 variants with high receptor binding affinities, high metal binding affinities and relaxivities

ProCA1 is the first generation of protein-based MRI contrast agent developed in our lab. At initial phase of the contrast agent design, domain 1 of rat CD2 was selected as a scaffold in consideration of the structural stability and several mutations (D56, D58, D60 and D62 and E15) were made on its surface to create a Gd^{3+} binding site. The re-constructed ProCA1 maintained its secondary structure with additional strong Gd^{3+} binding affinity, optimal metal selectivity and high relaxivity [212]. However, to specifically target the disease biomarker such as GRPR on cellular or sub-cellular level, ProCA1 need to be further modified with targeting moiety.

Gastrin-releasing peptide (GRP) is the natural ligand for GRPR. GRP is a peptide with 27 amino acids derived from pre-GRP (Table 1.6). The pre-GRP were then cleaved by signal peptide to form proGRP and modified by a series of enzymes to form the mature GRP (GRP_{1-27}) [131]. Bombesin is a 14 amino acid peptide which was first isolated from the skin of the European fire-bellied toad *Bombina bombina* [133] [213, 214]. Gastrin-releasing peptide is bombesin's counterpart in mammalian family, which is the natural ligand to GRPR. According to Jensen's report, the ten amino acids in the C-terminal of bombesin/GRP are critical for its binding affinity to GRPR [135].

Lixia Wei, a previous member from Drs. Jenny Yang and Zhiren Liu's research groups at GSU created GRPR-targeted MRI contrast agents using two different strategies [139], the C-terminal peptide from GRP (G10) was designed to infuse into ProCA1. The C-terminal peptide from GRP (G10) infused at the C-terminal of ProCA1 is called ProCA1.GRPC, while the peptide G10 grafted between the Gly52 and Gly53 of ProCA1 is called ProCA1.GRP (52).

Qualitative assays such as cell imaging, western blot and Biacore assay suggest that the ProCA1.GRP (52) exhibits stronger binding capability than ProCA1.GRPC to GRPR expressed in cancer cells. While ProCA1.GRP (52) is able to result in MRI enhancement of the PC3 xenografted tumor in mice with high GRPR expression by intra-tumor injection, it failed to result in any tumor enhancement via tail vein injection. These previous results suggest that the targeting capability of ProCA1.GRP (52) is likely too weak to achieve GRPR molecular imaging *in vivo.* Thus, there is an urgent need to develop a GRPR-targeted MRI contrast agent with improved biomarker binding properties.

Table 1.6 summarizes the sequences of GRP and bombesin peptides. Although ten amino acids in the C-terminal of the bombesin are essential for the binding to GRPR, Wang et al., [215] report that full length bombesin peptide has a strong GRPR binding affinity than that of 10 amino acids from C-terminal bombesin/GRP. Full length bombesin has affinity of 4 nM to GRPR, which is about 4 times and 10 times higher affinity than 10 amino acids from C-terminal bombesin and GRP have affinity, respectively. Thus, we hypothesize that grafting full length sequence of bombesin (named ProCA1B14) rather than 10 amino acids from C-terminal of GRP or Bombesin (named ProCA1G10 or ProCA1B10, respectively) in ProCA1 will generate a GRPR-targeted MRI contrast agents with improved GRPR binding affinity.

To further understand the key molecular mechanism between GRPR and its peptide ligands, we generated a series of model structure of GRPR based on the existing GPCR structures in the protein data bank. We first applied BLAST search to identify the proteins which have the highest similarities in the protein data bank. Neurokinin 1 receptor (NK1R), a protein in the family B of GPCR, has the highest homogeneity with identity of 26% and coverage of 85% to GRPR in the primary sequence (Table 3.1). In addition, opioid receptor also has high homogeneity to GRPR with identity (28%) and coverage (79%). Thus, NK1R and opioid receptor are the most reliable templates to build model structure of GRPR.

Different from BLAST search based on homogenous alignment, 3D models built by I-TASSER are based on multiple-threading alignments. Interestingly, multiple-threading alignments by I-TASSER also indicate that NK1R is the most reliable template to build a model structure of GRPR. Finally, we used NK1R as a template to build the model structure of GRPR (Figure 3.1).

Next, we have performed *in silicon* study of the interaction between GRPR and GRPR-targeted ProCA1 (ProCA1B14, ProCA1G10 and ProCA1B10) using HADDOCK. As reported by Gayen et al. [216], residues Asn3, Val4, Leu5, Asp10, Ile15, Thr17, Thr19, Ser20, and Glu21 play essential roles on the interaction between NK1R and its peptide ligand. Since GRPR shows high homology to NK1R, GRPR is assumed to have a similar ligand binding pocket compared with the Substance P binding pocket in NK1R. Thus, we define these amino acids as the key residues in the interaction interface between GRPR and GRPR-targeted ProCAs. As shown in the HADDOCK results (Figure 3.2), ProCA1B14 has the lowest binding energy (HADDOCK SCORE -131.8), compared with B10 (HADDOCK SCORE -127.3) and G10 (HADDOCK SCORE -122.2), indicating the

ProCAB14 potentially binds much stronger than that of B10 and G10. Thus, we hypothesize that the longer peptide sequence of bombesin14 with well-maintained structure has stronger binding affinity.

Fig. 3.3 shows the modeled structure of ProCA1 variants with grafting peptides binding to GPPR. This contrast agent was designed based on the following considerations. First, ProCA1 is a protein-based MRI contrast agent with a designing a gadolinium binding site into scaffold protein, domain 1 of rat CD2. The relaxivity of ProCA1 is much higher than that of clinically approved Gd-DTPA [176, 184]. Second, a GRPR targeting moiety of B14 encompasses Bombesin 14-amino acid that has a K_d of about 2.1 nM. This B14 peptide is reported to have a stronger affinity than that of GRP about 6.6 nM [131]. Three targeting moieties B10, G10 and B14 are used to test the contribution of ligand length and the residue H in bombesin in ligand binding. Ten residues of C-terminal of GRP (G10) and bombesin (B10) and fourteen residues of Bombesin with mutation H to Q from GRP (B14) are designed. Third, based on the well-defined conformation of ligand moiety required for molecular recognition from modeling studies and reported NMR studies [216], we hypothesize that peptide ligand grafted into a scaffold protein retaining native conformation will have a better capability for molecular recognition to the receptor thus facilitate molecular imaging. We have shown previously that a grafting EF-hand calcium binding site with a flexible linker into a scaffold protein is able to maintain its native conformation and metal binding capability [185]. As shown in the HADDOCK results, ProCA1B14 has the lowest binding energy (HADDOCK SCORE -131.8), compared with B10 (HADDOCK SCORE -127.3) and G10 (HADDOCK SCORE -122.2), suggesting that ProCA1B14 is likely to have the strongest binding affinity to GRPR. Fourth, we further modify the protein surface by PEGylation

P-40 to increase protein solubility, stability and *in vivo* retention time. Fifth, a NIR dye was conjugated to the ProCA1 to provide NIR fluorescence modality to verify molecular imaging by MRI.

Table 3.1 Blast analysis of GRPR sequence in the pdb data bank.

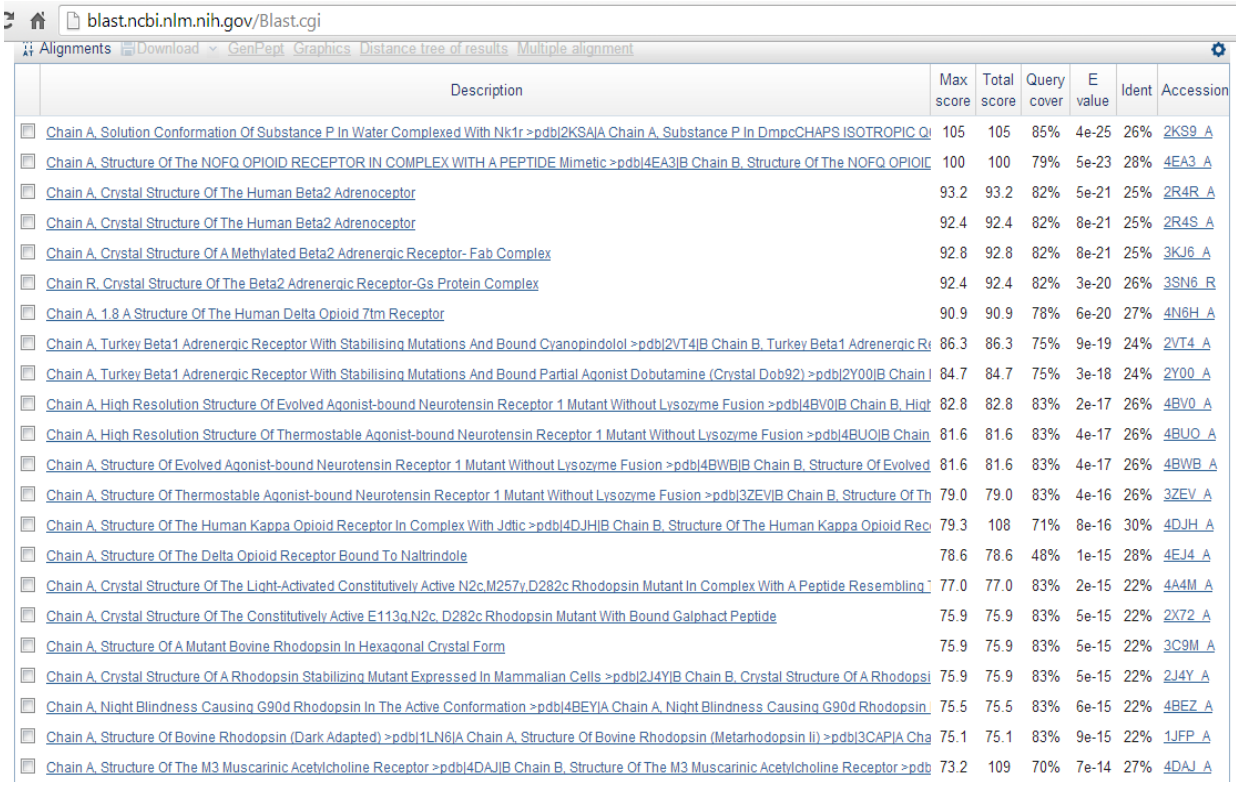

blast.ncbi.nlm.nih.gov/Blast.cgi

Alignments | Download | GenPept | Graphics | Distance tree of results | Multiple alignment

Description	Max score	Total score	Query cover	E value	Ident	Accession
Chain A, Solution Conformation Of Substance P In Water Complexed With Nk1r >pdb|2KSA|A Chain A, Substance P In DmpcCHAPS ISOTROPIC Q	105	105	85%	4e-25	26%	2KS9_A
Chain A, Structure Of The NOFQ OPIOID RECEPTOR IN COMPLEX WITH A PEPTIDE Mimetic >pdb|4EA3|B Chain B, Structure Of The NOFQ OPIOID	100	100	79%	5e-23	28%	4EA3_A
Chain A, Crystal Structure Of The Human Beta2 Adrenoceptor	93.2	93.2	82%	5e-21	25%	2R4R_A
Chain A, Crystal Structure Of The Human Beta2 Adrenoceptor	92.4	92.4	82%	8e-21	25%	2R4S_A
Chain A, Crystal Structure Of A Methylated Beta2 Adrenergic Receptor- Fab Complex	92.8	92.8	82%	8e-21	25%	3KJ6_A
Chain R, Crystal Structure Of The Beta2 Adrenergic Receptor-Gs Protein Complex	92.4	92.4	82%	3e-20	26%	3SN6_R
Chain A, 1.8 A Structure Of The Human Delta Opioid 7tm Receptor	90.9	90.9	78%	6e-20	27%	4N6H_A
Chain A, Turkey Beta1 Adrenergic Receptor With Stabilising Mutations And Bound Cyanopindolol >pdb|2VT4|B Chain B, Turkey Beta1 Adrenergic R	86.3	86.3	75%	9e-19	24%	2VT4_A
Chain A, Turkey Beta1 Adrenergic Receptor With Stabilising Mutations And Bound Partial Agonist Dobutamine (Crystal Dob92) >pdb|2Y00|B Chain	84.7	84.7	75%	3e-18	24%	2Y00_A
Chain A, High Resolution Structure Of Evolved Agonist-bound Neurotensin Receptor 1 Mutant Without Lysozyme Fusion >pdb|4BV0|B Chain B, High	82.8	82.8	83%	2e-17	26%	4BV0_A
Chain A, High Resolution Structure Of Thermostable Agonist-bound Neurotensin Receptor 1 Mutant Without Lysozyme Fusion >pdb|4BUO|B Chain	81.6	81.6	83%	4e-17	26%	4BUO_A
Chain A, Structure Of Evolved Agonist-bound Neurotensin Receptor 1 Mutant Without Lysozyme Fusion >pdb|4BWB|B Chain B, Structure Of Evolved	81.6	81.6	83%	4e-17	26%	4BWB_A
Chain A, Structure Of Thermostable Agonist-bound Neurotensin Receptor 1 Mutant Without Lysozyme Fusion >pdb|3ZEV|B Chain B, Structure Of Th	79.0	79.0	83%	4e-16	26%	3ZEV_A
Chain A, Structure Of The Human Kappa Opioid Receptor In Complex With Jdtic >pdb|4DJH|B Chain B, Structure Of The Human Kappa Opioid Rec	79.3	108	71%	8e-16	30%	4DJH_A
Chain A, Structure Of The Delta Opioid Receptor Bound To Naltrindole	78.6	78.6	48%	1e-15	28%	4EJ4_A
Chain A, Crystal Structure Of The Light-Activated Constitutively Active N2c,M257y,D282c Rhodopsin Mutant In Complex With A Peptide Resembling	77.0	77.0	83%	2e-15	22%	4A4M_A
Chain A, Crystal Structure Of The Constitutively Active E113q,N2c, D282c Rhodopsin Mutant With Bound Galphact Peptide	75.9	75.9	83%	5e-15	22%	2X72_A
Chain A, Structure Of A Mutant Bovine Rhodopsin In Hexagonal Crystal Form	75.9	75.9	83%	5e-15	22%	3C9M_A
Chain A, Crystal Structure Of A Rhodopsin Stabilizing Mutant Expressed In Mammalian Cells >pdb|2J4Y|B Chain B, Crystal Structure Of A Rhodopsi	75.9	75.9	83%	5e-15	22%	2J4Y_A
Chain A, Night Blindness Causing G90d Rhodopsin In The Active Conformation >pdb|4BEY|A Chain A, Night Blindness Causing G90d Rhodopsin	75.5	75.5	83%	6e-15	22%	4BEZ_A
Chain A, Structure Of Bovine Rhodopsin (Dark Adapted) >pdb|1LN6|A Chain A, Structure Of Bovine Rhodopsin (Metarhodopsin Ii) >pdb|3CAP|A Cha	75.1	75.1	83%	9e-15	22%	1JFP_A
Chain A, Structure Of The M3 Muscarinic Acetylcholine Receptor >pdb|4DAJ|B Chain B, Structure Of The M3 Muscarinic Acetylcholine Receptor >pdb	73.2	109	70%	7e-14	27%	4DAJ_A

Neurokinin 1 receptor (NK1R), a protein in the family B of GPCR, has the highest homogeneity with identity of 26% and coverage of 85% to GRPR in the primary sequence. In addition, opioid receptor also has high homogeneity to GRPR with identity (28%) and coverage (79%).

Figure 3.1 Model structure of GRPR.

The modeled structure of GRPR (blue) were generated by I-TASSER based on x-ray structure of neurokinin 1 receptor (purple) (pdb: 2KS9), a G-protein coupled receptor in tachykinin receptor sub-family. The natural ligand for neurokinin 1 receptor is substance-P, which is labeled in red color. The residues influencing the affinity of GRPR binding (Ala2, Leu3, Asn4, Leu9, Asp14, Phe16, His18, Cys19, and Asn20) were highlighted in yellow.

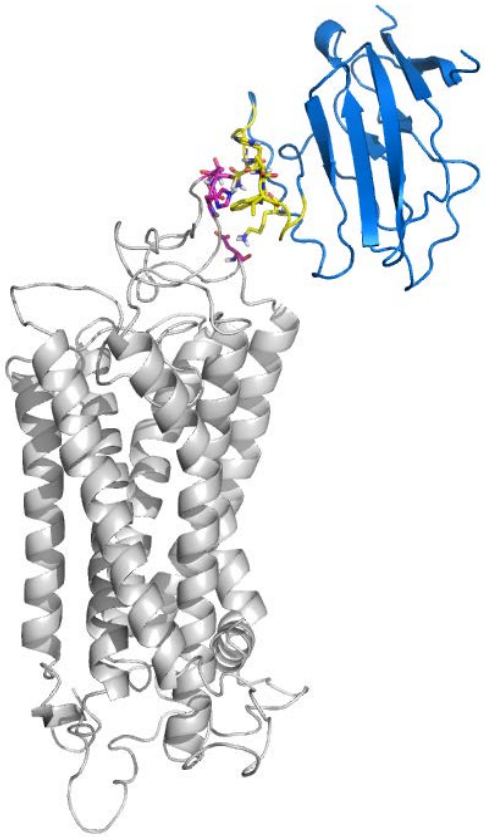

Figure 3.2 Model structure of ProCA1B14 binding to GRPR.

The docking structure of ProCA1B14 binding to GRPR is generated by HADDOCK. Gray indicates the modeled structure of GRPR and blue indicates the modeled structure of ProCA1B14. All the modeled structures were created by I-TASSER. Yellow indicates the bombesin14 peptide and purple indicates the active binding residue on GRPR.

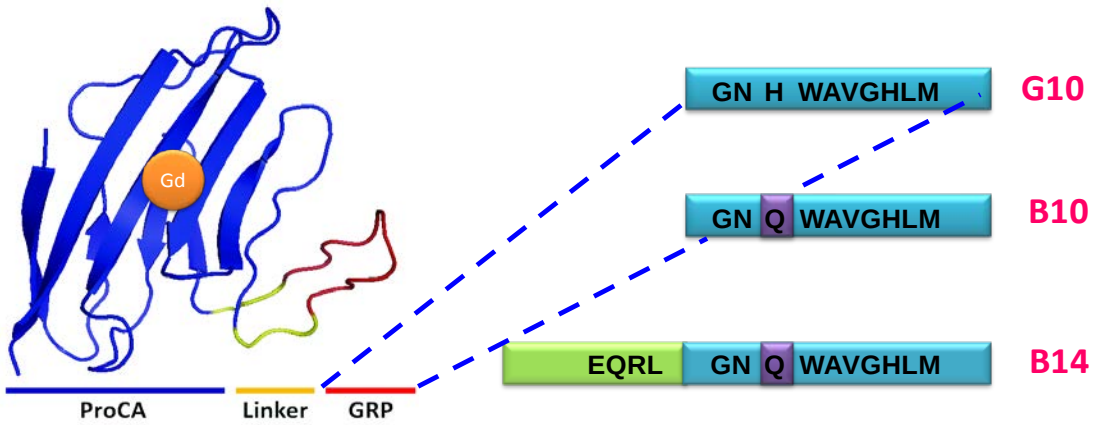

Figure 3.3 Model structure of GRPR-targeted protein contrast agents ProCA1 variants by I-TASSER.

G10 and B10 represent the 10 amino acids from the C-terminal of GRP and bombesin peptides, respectively. G10 and B10 share the similar sequences except only one amino acid residue difference. B14 represents the whole sequence of bombesin.

3.2.2 Molecular cloning of ProCA1 variants

The general process of molecular cloning of ProCA1 variants is shown in Fig. 2.2 in Chapter 2. The plasmid ProCA1B10 in PET20b vector was provided by our previous lab member Dr. Lixia Wei in Dr. Liu's lab. [139] In order to construct the new variant ProCA1B14 and ProCA1G10, the primers were designed to pair with the template (ProCA1) and PCR reactions were done by following the method described in Tables 2.1, 3.2 and Figs 2.1-2.2. After PCR reactions, the products were identified by agarose gel and the linear DNA sequences were extracted by a gel extraction kit (QIAquick Gel Extraction Kit (250)). The linear DNA sequences were phosphorylated by T4 polynucleotide kinase (Biolabs) and linked as a cycle plasmid by T4 ligase (Biolabs). The product after ligation was used to transform *E.Coli* competent cell strains DH5α which is

specifically used to amplify plasmid. The transformed cells were scratched on the LB plate complimented with 100 µg/ml ampicillin and cultured at 37°C overnight. In the next day, single colony was selected and inoculated in 25ml LB medium at 37°C overnight to amplify the plasmid. Then, the cell pellets were harvested and plasmid was extracted by mini kit (QIAprep Spin Miniprep Kit (250)). The plasmid was sequenced by GENEWIZ to verify the DNA sequences. Fig. 3.4 shows that the targeting sequences of B14 and G10 were successfully inserted into the ProCA1 plasmid.

Table 3.2 Primer design of ProCA1B14 and ProCA1G10.

primer	sequence	Tm	Template
bombfor	aatgggcagtaggccatctaatgggcggatcaggtggagcatttgagatcgacgcaaa	68	pET20b-7E15, pET20b-7E15bombcys
bombrev	ggtttcccagtctttgttcgccacctgatccgcccgatttcaaaaaaggcttcatcttc	68	same
grpfor	agtaggccatctaatgggcggatcaggtggagcatttgagatcgacgcaaat	68	same
grprev	gcccagtggtttccgccacctgatccgcccgatttcaaaaaaggcttcatcttc	68	same

A

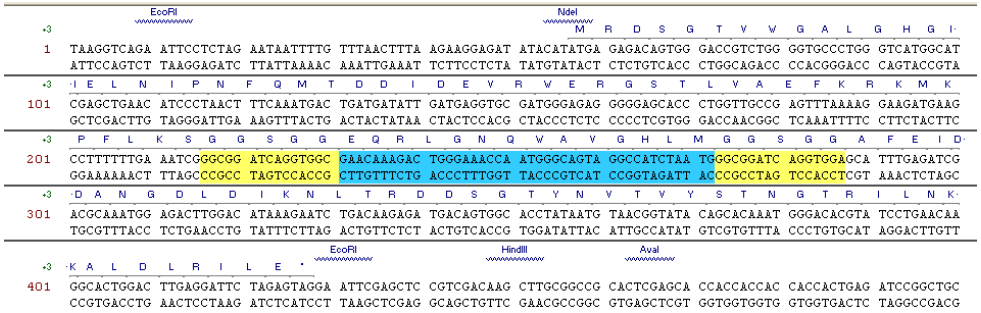

B

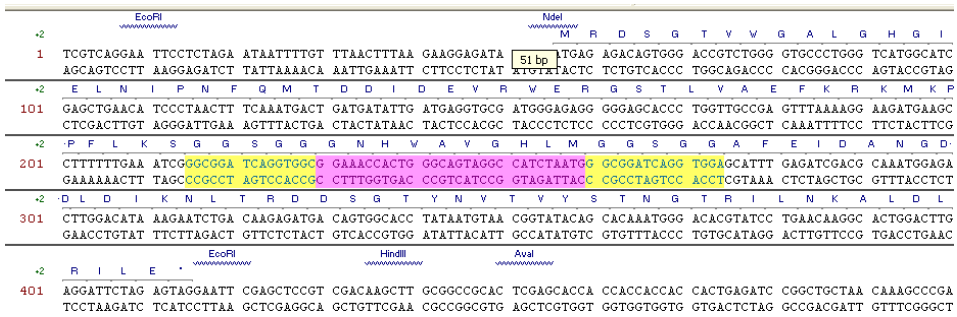

C

```
7E15_GRP10        MRDSGTVWGALGHGIELNIPNFQMTDDIDEVRWERGSTLVAEFKRKMKPFLKSGGSGG-- 58
7E15_Bomb14       MRDSGTVWGALGHGIELNIPNFQMTDDIDEVRWERGSTLVAEFKRKMKPFLKSGGSGGEQ 60
CD2_Rat           -RDSGTVWGALGHGINLNIPNFQMTDDIDEVRWERGSTLVAEFKRKMKPFLKSG------ 53
                   **************:************************************

7E15_GRP10        --GNHWAVGHLMGGSGGAFEIDANGDLDIKNLTRDDSGTYNVTVYSTNGTRILNKALDLR 116
7E15_Bomb14       RLGNQWAVGHLMGGSGGAFEIDANGDLDIKNLTRDDSGTYNVTVYSTNGTRILNKALDLR 120
CD2_Rat           -----------------AFEILANGDLKIKNLTRDDSGTYNVTVYSTNGTRILNKALDLR 96
                                  **** ***** .*********************************

7E15_GRP10        ILE 119
7E15_Bomb14       ILE 123
CD2_Rat           ILE 99
                  ***
```

Figure 3.4 DNA sequences alignment of ProCA1B14 (A) and ProCA1G10 (B) with rat CD2.

The DNA sequences of ProCA1 variants in pET20b vector were analyzed by vector NTI (A and B). The DNA sequences of the new constructed plasmids were sequenced by GSU core facility and were translated to peptide sequence by ExPASy and aligned with original rat CD2 protein sequence by ClustalW (C). The results showed the targeting sequences of B14 and G10 were successfully inserted into the ProCA1 plasmid.

3.2.3 Protein expression and purification

3.2.3.1 Protein expression

ProCA1 variants were cloned into PET20b vectors and expressed by *E.Coli* competent cell strains (Tuner, BL21DE3, BL21plysS and BL21DE3plysS). The typical growth of *E.Coli* includes several phases: cells initially adjust to the new environment and the growth is slow (lag phase), cells start dividing exponentially and doubling in number every few minutes (log phase), the exponential growth of cells are limited and the cells stop dividing (stationary phase), and eventually the cells lose viability (death phase). The OD values between 0.6 and 0.8 indicate the cells grow exponentially. At this OD value, different concentrations of IPTG (0.1, 0.5 and 1.0 mM) were added to the bacteria culture (1L) to induce protein expression. In the same conditions (temperature, IPTG concentration, induction time), Tuner, BL21DE3 and BL21plysS show good expression, while BL21DE3plysS shows none expression of ProCA1B10. In Figure 3.5, the SDS-gel results indicate that there is no significant increase of the protein expression when the concentration of IPTG increased from 0.1 mM to 1.0 mM. As shown in Fig. 3.5 and Fig. 3.6, Tuner cells can express ProCA1B10 at 37°C for 3 h, overnight or at 30°C overnight. Among these three conditions, Tuner cells have the highest expression yield of ProCA1B10 at 37°C overnight. BL21DE3 can express ProCA1B10 at 37°C for 3 h or at 30°C overnight. They didn't show significant difference from each other, but it can't express at 37°C overnight. BL21plysS cell can express ProCA1B10 at 37°C for 3 h, overnight or at 30°C overnight. Among these three conditions, BL21plysS cells have the highest expression yield of ProCA1B10 at 30°C overnight. Based on these results, we conclude that Tuner, BL21plysS, and BL21DE3 cells have the highest expression yield of ProCA1B10 with 0.1-1.0 mM IPTG induction at 37°C for 3 h or at 30°C overnight in a

small volume condition (10 ml LB medium). The results coming from 50 ml LB culture as shown in Fig. 3.7 also confirm this conclusion.

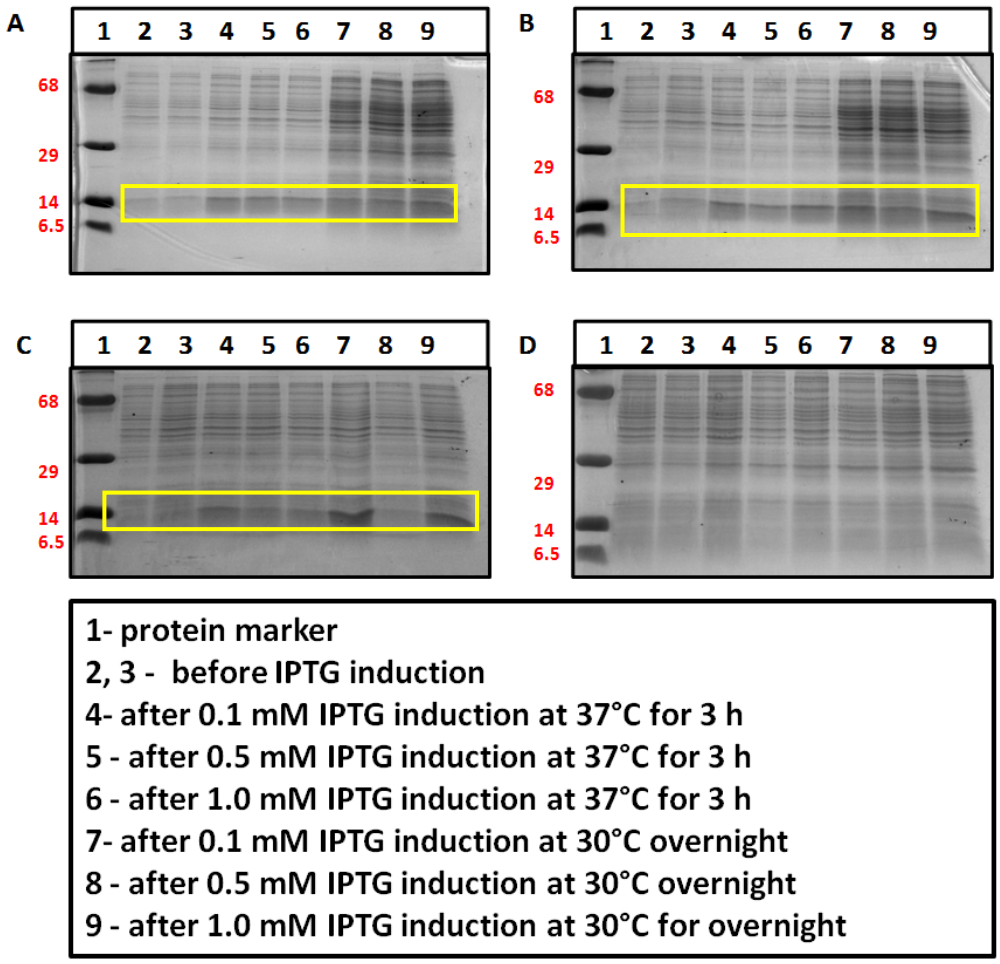

Figure 3.5 Small volume expression of ProCA1B10.

The expression of ProCA1B10 were optimized using small volume (10 ml LB medium) expression under different temperature/induction time (at 37°C for 3h and 30°C overnight) , different *E.Coli* competent cell strains [Tuner (A), BL21DE3 (B), BL21plysS (C) and BL21DE3PlysS (D)] and different IPTG concentrations (0.1, 0.5 and 1.0 mM) .

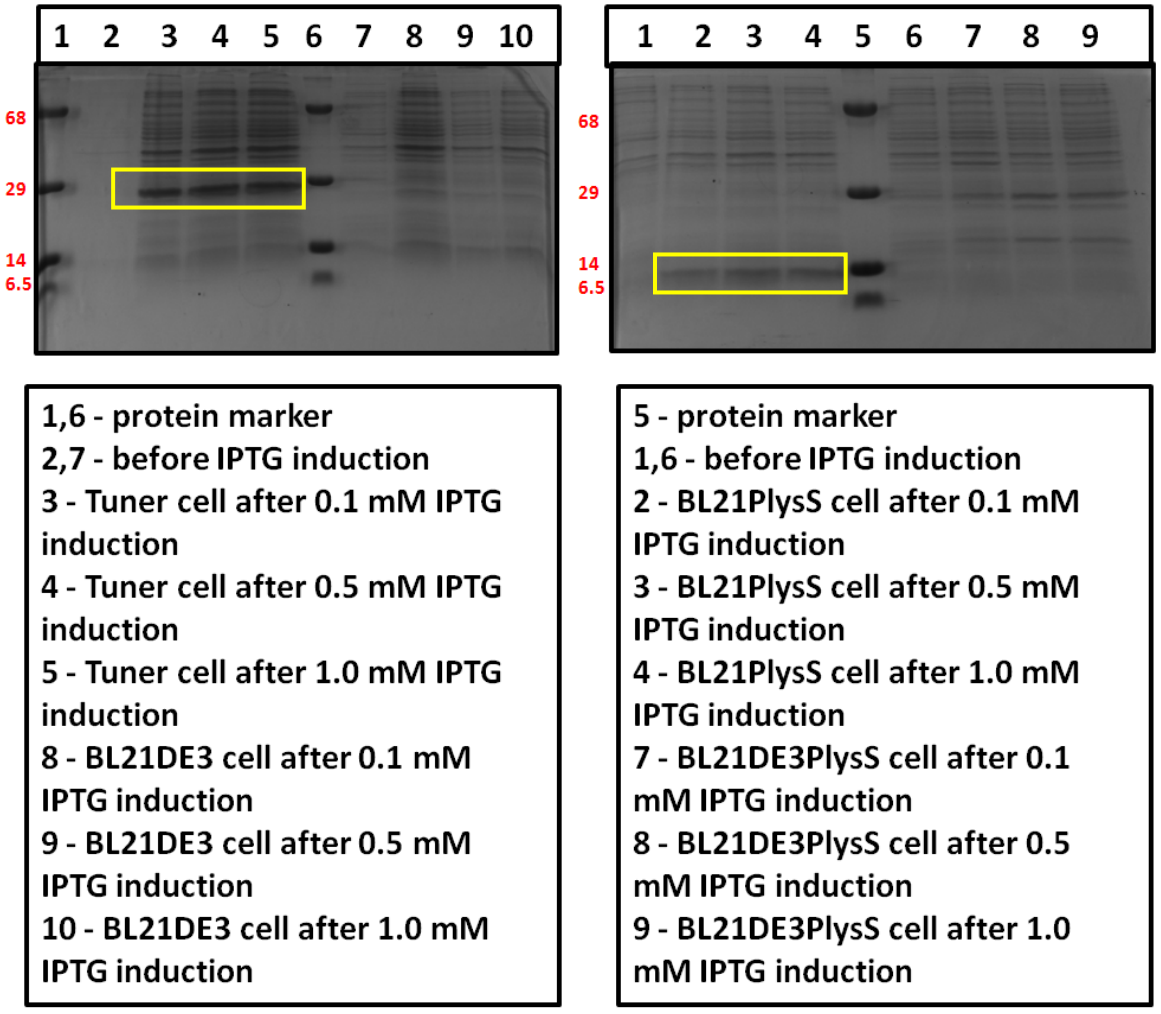

Figure 3.6 SDS-gels of ProCA1B10 expressed in a small volume (10 ml LB medium) under conditions of at 37°C overnight by using different *E. Coli* competent cell strains (Tuner, BL21DE3, BL21PlysS, BL21DE3PlysS) and IPTG concentrations (0.1, 0.5 and 1.0 mM) .

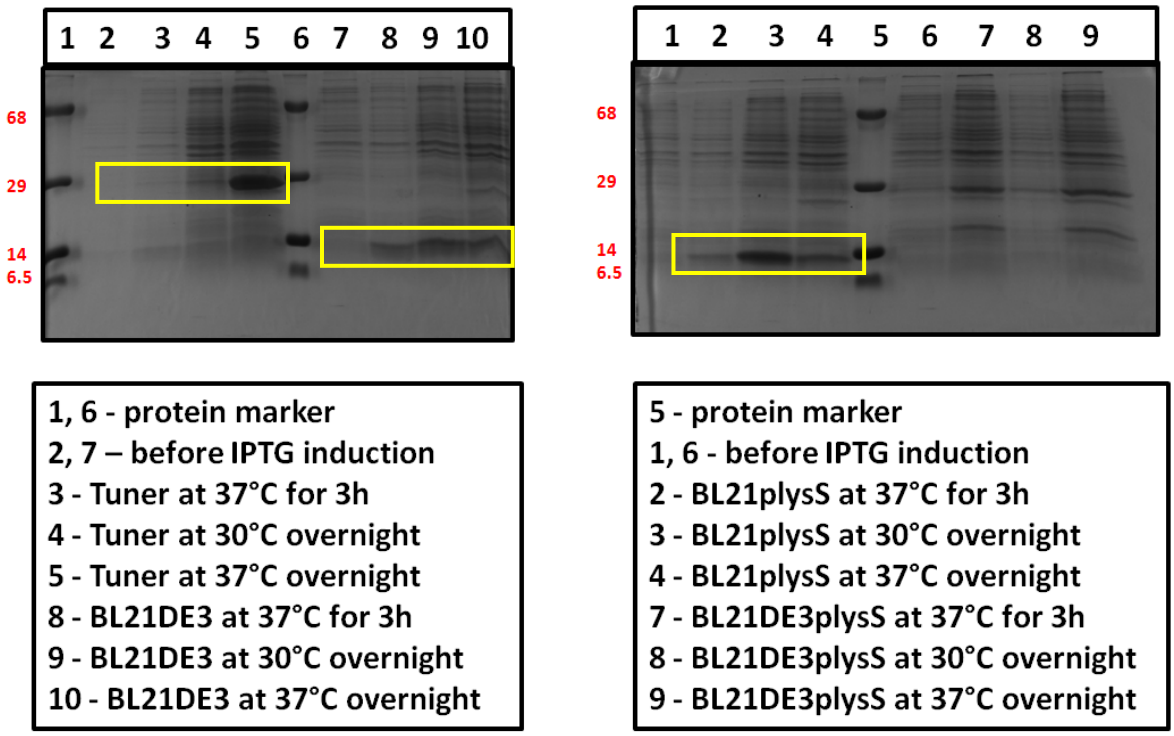

Figure 3.7 SDS-gels of ProCA1B10 expressed at small volume (50 ml LB medium) under expression conditions at 37°C for 3h, overnight or at 30°C overnight using different *E. Coli* competent cell strains (Tuner, BL21DE3, BL21PlysS, BL21DE3PlysS) and IPTG concentrations (0.1, 0.5 and 1.0 mM).

3.2.3.2 Tagless Protein purification

To avoid the interference of affinity tag for *in vivo* application and reduce the cost, protein without affinity tag was expressed as inclusion body and purified without using affinity columns. Figure 2.4 in Chapter 2 shows the purification procedure for tagless ProCA1 variants. Inclusion bodies are usually misfolded protein aggregates in the cells after rapid production and they are usually less subjected to protein cleavage and degradation by endogenous proteases. The tagless protein purification method involves rapid separation of inclusion body protein, protein unfolding and refolding . After the cell pellets of 2 liter LB medium are harvested, they are re-suspended in 30 ml PBS buffer with 1 µl benzonase nuclease and 100 µl of 100 mM PMSF protease inhibitor. The re-suspended cell pellets are fully lysated by sonication or cell disruptor. After centrifuge, the soluble mixtures of proteins and nucleotides in supernatant were discarded while the precipitate containing misfolded ProCA1s were saved for further purification. The precipitate was dissolved with 8M urea to unfold ProCA1s and the unsoluble impurities were removed by centrifuge. Then, the protein solution in 8M urea was dialyzed gradually in 4M urea, 2M urea, 1M urea and 10 mM HEPES buffer (pH 8.0) to help ProCA1s refold well. After refolding, ProCA1s solution was filtered with 0.45 µM pore size syringe filters (25 mm GD/X disposable filter service, PVDF filter media, Whatman^{TM}, GE Healthcare Life Science) and purified by a FPLC system with a Q column.

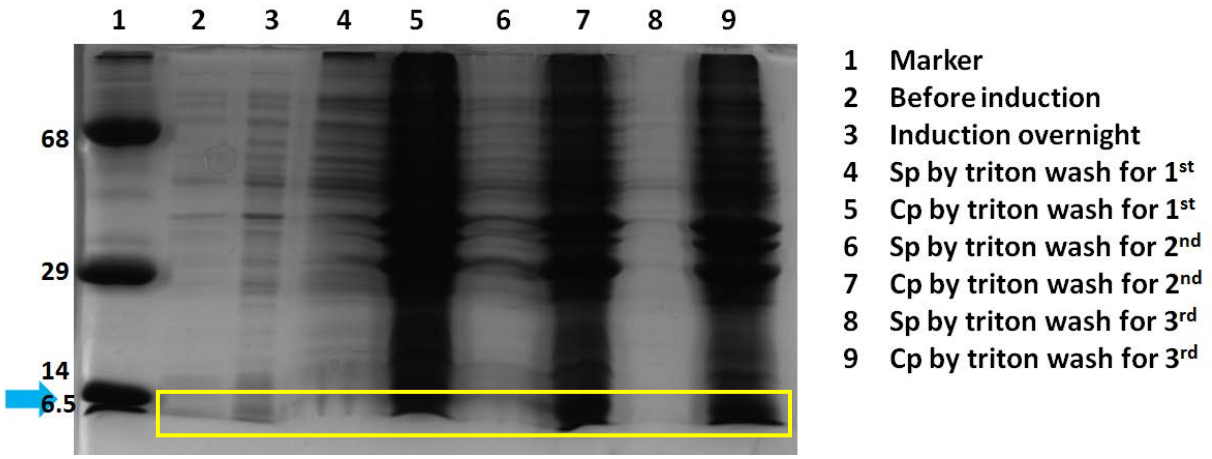

Figure 3.8 SDS-PAGE gel of tagless ProCA1B10 purification.

Cell pellets are washed by 1% Triton for 3 times to remove some soluble impurities.

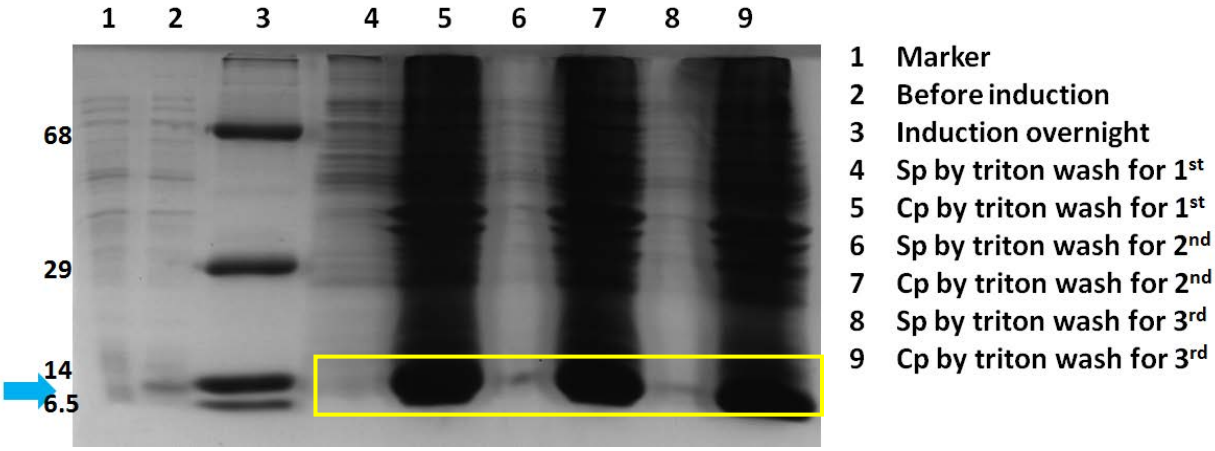

Figure 3.9 SDS-PAGE gel of tagless ProCA1B14 purification.

Cell pellets are washed by 1% Triton for 3 times to remove some soluble impurities.

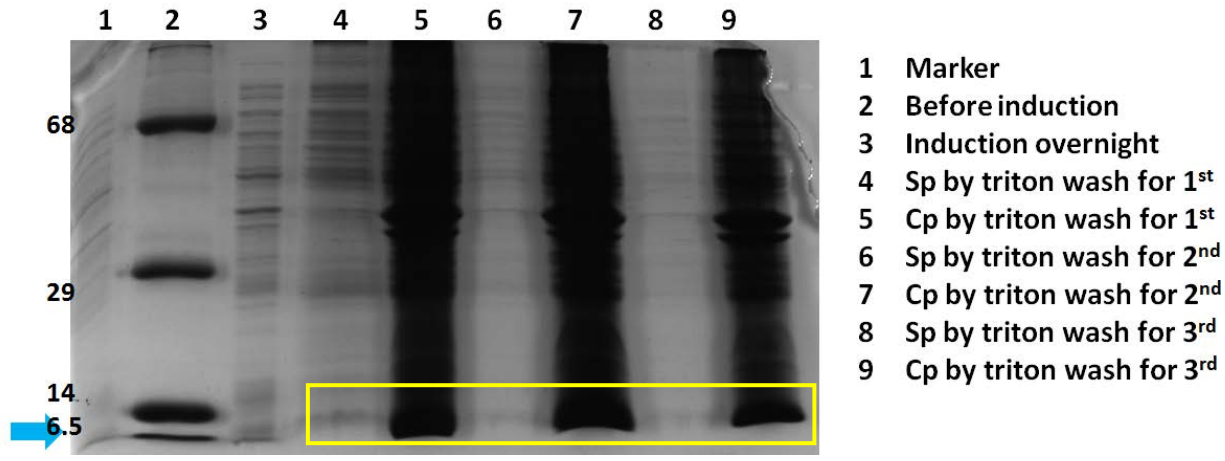

Figure 3.10 Tagless ProCA1G10 purification.

Cell pellets are washed by 1% Triton for 3 times to remove some soluble impurities.

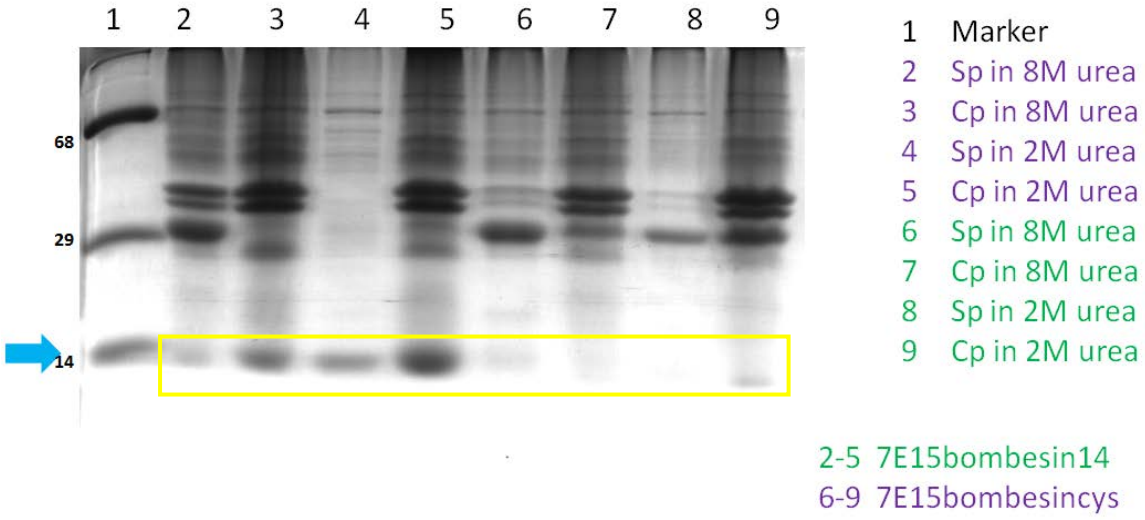

Figure 3.11 Tagless ProCA1B14 and ProCA1B10 refolding process.

Lane 1 indicates the protein marker. Lane 2 and 3 represents supernatant and cell pellets of the protein ProCA1B14 unfolded in 8M urea, respectively. Lane 4 and 5 represents supernatant and cell pellets of the protein ProCA1B14 refolded in 2M urea, respectively. Lane 6 and 7 represents supernatant and cell pellets of the protein ProCA1B10 unfolded in 8M urea, re-

spectively. Lane 8 and 9 represents supernatant and cell pellets of the protein ProCA1B10 re-folded in 2M urea, respectively.

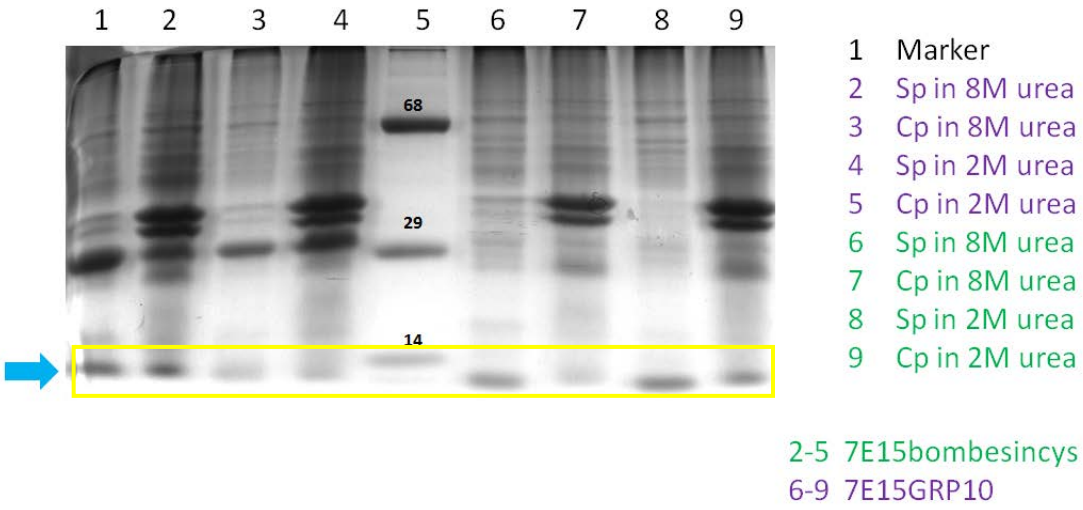

Figure 3.12 Tagless ProCA1B10 and ProCA1G10 refolding process.

Lane 1 indicates the protein marker. Lane 2 and 3 represents supernatant and cell pellets of the protein ProCA1B10 unfolded in 8M urea, respectively. Lane 4 and 5 represents supernatant and cell pellets of the protein ProCA1B10 refolded in 2M urea, respectively. Lane 6 and 7 represents supernatant and cell pellets of the protein ProCA1G10 unfolded in 8M urea, respectively. Lane 8 and 9 represents supernatant and cell pellets of the protein ProCA1G10 re-folded in 2M urea, respectively.

The basic mechanism for ProCA1s purification is ion exchange chromatography (SP column or Q column) which can separate proteins with differences in charge. ProCA1s and DNA bind to a column when they were loaded. Once conditions (pH or salt concentration) were altered gradually, the bound substances were eluted separately. The simple procedure is shown in Fig. 3.13.

Figure 3.13 Basic procedure of FPLC purification.

After install/connect the Q column on FPLC, the column were first equilibrated with loading buffer A (10 mM HEPES buffer, pH 8.0). Then, protein samples (10 ml) were injected into the FPLC and load into the column. After washing out unbounded proteins and other biomolecules by buffer A, the bounded proteins were further eluted out by gradually increase of elution buffer B (1 M NaCl, 10 mM HEPES buffer, pH 8.0). After proteins were eluted out from the column, the remaining biomolecules such as DNA which bound to the column will be further washed with high salt. The column will be re-equilibrated before the next around of protein purification.

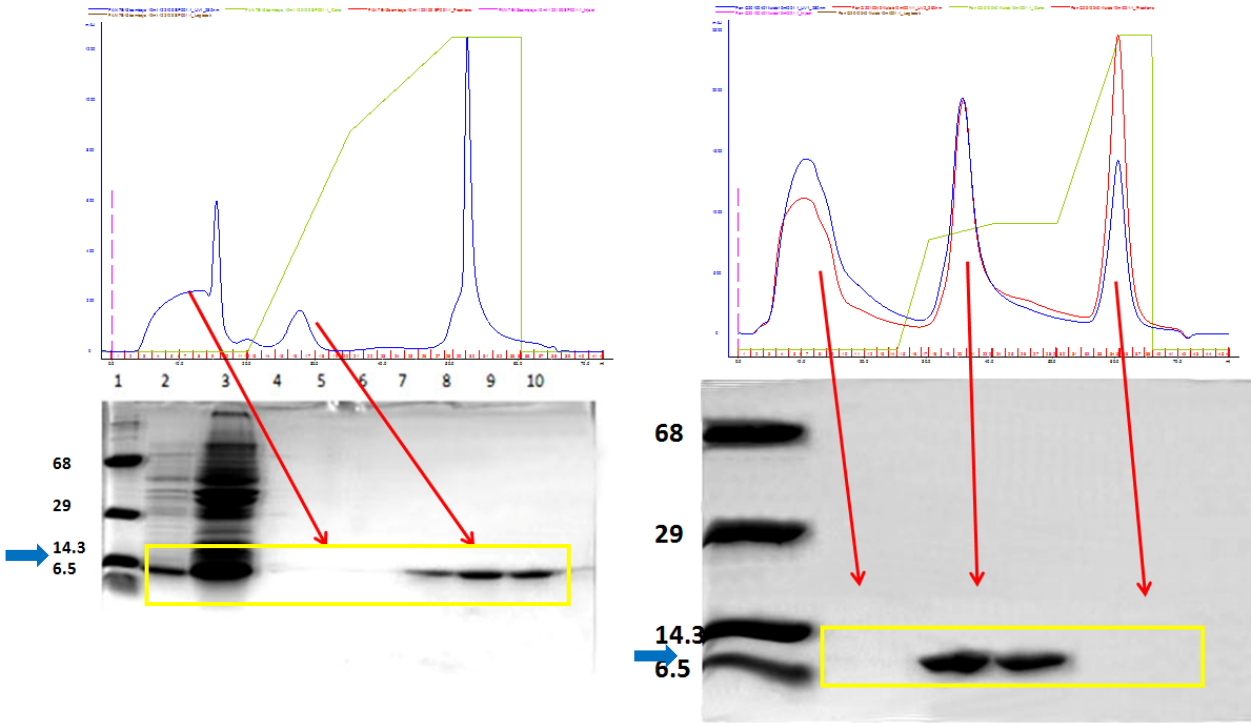

Figure 3.14 ProCA1 (left) and ProCA1B10 (right) purified by FPLC. ProCA1 and ProCA1B10 were purified using urea refolding methods before loaded into FPLC equipped with HP Q column. The proteins and other biomolecules will be eluted out using salt gradient. Three major peaks were shown in FPLC. Peak 1 stand for the unbounded biomolecules, peak 2 is PrpCA1/ProCA1B10, and peak 3 contains DNA/RNA.

Based on the specific characteristics of each protein, different columns can be selected. Q column and SP column are two strong ion exchangers, which are fully charged over a broad pH range (pH 2 -12). Q column is an anion exchange column while SP column is a cation exchange column. ProCA1s can be separated by SP column based on pH difference. For SP column purification, the buffer A is 50 mM NaAC at pH 4.0 and the buffer B is 50 mM Tris-HAC at pH 8.0.

ProCA1s can also be separated by Q column based on the salt concentration difference. For Q column purification, the buffer A is 10 mM HEPES buffer at pH 8.0 and the buffer B is 10 mM HEPES buffer at pH 8.0 plus 1 M NaCl. However, when the pH value is lower than 7, ProCA1s are not stable and inclined to precipitate. In considering of this, Q column is preferred.

3.2.3.3 GST-fusion protein purification

ProCA1 was fused into pGEX-2T vector and expressed as a GST-fusion protein with MW of 38 kDa using a GST affinity column method described in Chapter 2. The cell pellets from 2 L LB culture were re-suspended by 40 ml lysis buffer (1% N-lauroylsarcosine sodium Tris-HCl, pH 7.0, 5 mM DTT, 10 µl benzonase nuclease (Novagen)) and broken completely by Sonicator and French Press, separately. The mixture was centrifuged at 17000 rpm for 30 min to separate the supernatant. The supernatant (S/N) contained the soluble proteins such as well-folded GST fusion ProCA1, while the cell pellet (C/P) was comprised of insoluble membrane, proteins and unbroken cells. At the same time, Glutathione-S-Sepharose 4B affinity columns (GE healthcare) was cleaned by 9 M glutathione (GSH) and balanced with PBS buffer. Then, the supernatant filtered by 0.45 µM pore size syringe filters (25 mm GD/X disposable filter service, PVDF filter media, Whatman™, GE Healthcare Life Science) was applied to the balacnced Glutathione-S-Sepharose 4B affinity columns (GE healthcare) 3-4 times to let the GST fusion ProCA1 bind to the beads. After binding process, PBS buffer was applied to rinse the beads to remove those nonspecific binding proteins. Then, 20 µl of thrombin was added to the column to cleave the GST tag from the ProCA1. The column was capped and sealed with parafilm which was placed on an agitator at 4°C overnight. In the next day, ProCA1 was eluted by PBS buffer and Glutathione-S-Sepharose 4B affinity column (GE healthcare) was regenerated by 9 M glutathione (GSH).

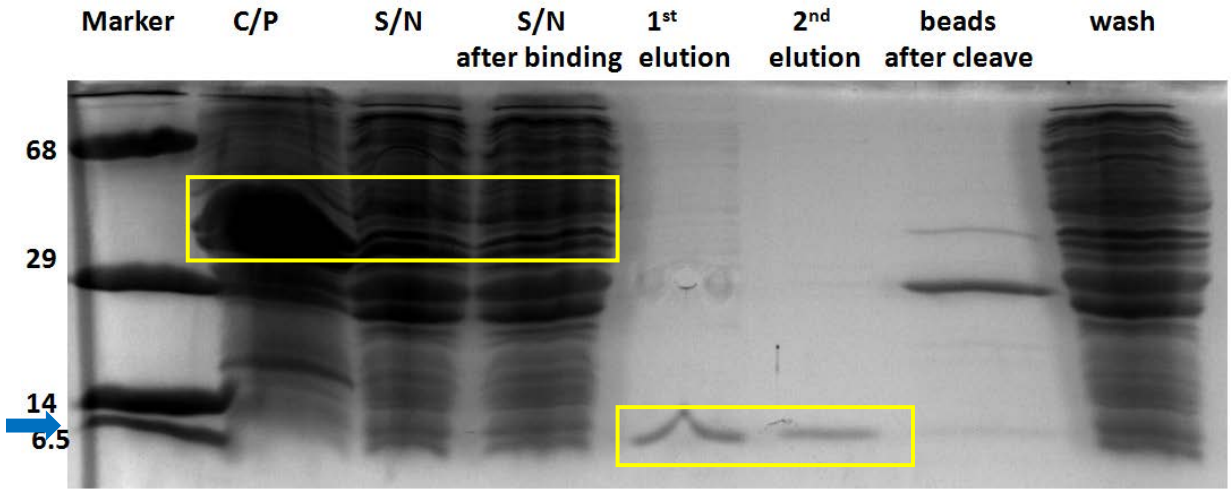

Figure 3.15 ProCA1-GST purification.

Lane "Marker" indicates protein marker. Lane "C/P" and "S/N" represents the cell lysis pellet and supernatant of ProCA1-GST with MW of 38 kDa from *E.Coli* bacteria culture harvest, respectively. Lane "S/N after binding" indicates the supernatant after binding to the Glutathione-S-Sepharose 4B affinity columns. Lane "1st elution" and "2nd elution" represents the protein samples after first and second elution with PBS buffer. Lane "beads after cleave" indicates the ProCA1 under conditions of the beads after thrombin cleavage. Lane "wash" represents the waste that didn't bind to the column and washed away by PBS buffer.

3.2.3.4 Protein structure characterization

Since ProCA1 variants were purified, the UV absorbance spectra were monitored. ProCA1s have UV absorbance peak at 280 nm as shown in Fig.3.16 which is consistent with literature report [212]. UV absorbance indicates that purified ProCA1s don't contain DNA or RNA.

We also run agarose gel to check the existence of DNA/RNA and the gel didn't show any bands which support this conclusion.

The Trp fluorescence emission maxima of ProCA1 variants with addition of the targeting sequences are also located around 330 nm similar to ProCA1, but largely blue shifted compared with free Trp amino acid excited at 280 nm. This result suggests that the aromatic Trp residues remain well packed as in the native scaffold protein [185, 217].

The secondary structures of ProCA1 variants were investigated by CD spectrum. As shown in Fig. 3.17, the secondary structures of our proteins were maintained. When concentration of Gd^{3+} to our protein was 1:1 (25 μM Gd^{3+}), the secondary structures of ProCA1 variants are similar to that of ProCA1 and are not altered in the presence of 1:1 Protein: Gd ratio.

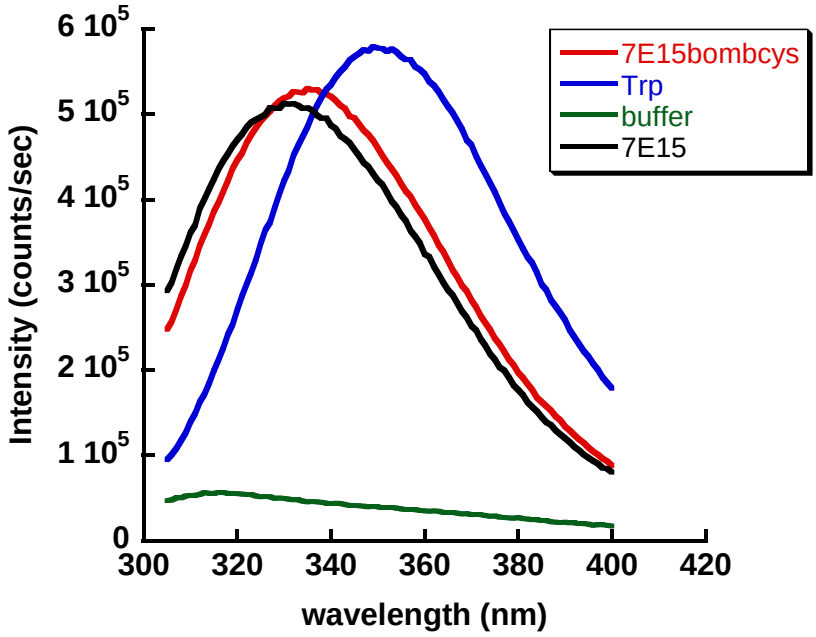

Figure 3.16 Trp fluorescence spectra of 5 µM ProCA1 variants excited at 282 nm in20 mM PIPES, 10 mM KCl (pH 6.8) buffer.

The excitation wavelength is at 282 nm while the emission wavelength is between 300 and 400 nm with 2 - 4 nm slit width. The protein samples were prepared in 20 mM PIPES, 10 mM KCl (pH 6.8) and respectively placed in a 1-cm path length cell for spectral measurements. Tryptophan is used as a control. The red and black curve indicate the Trp fluorescence emission maxima of ProCA1B10 and ProCA1 are located at 330 nm, respectively. The blue curve indicates the free Trp fluorescence emission maxima is located at 350 nm. The green curve represents the fluorescence emission of buffer only.

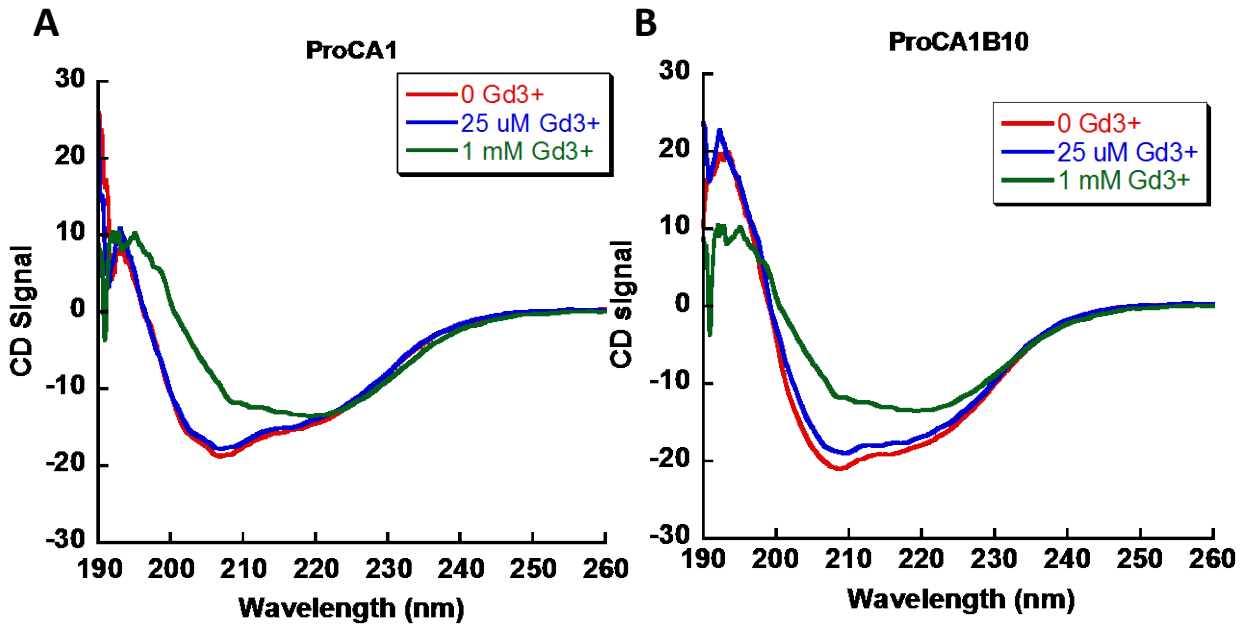

Figure 3.17 Circular Dichroism (CD) spectra of ProCA1 variants in the absence and presence of Gd^{3+} in 10 mM Tris buffer at pH 7.4.

The protein samples were prepared at 25 µM in 10 mM Tris-HCl (pH 7.4), 10 mM KCl with 1 mM EGTA or 1 mM $CaCl_2$ in a 1 mm quartz cell. The CD signals were monitored by the wavelength from 190 nm to 260 nm. 25 µM or 1 mM $GdCl_2$ was loaded in the quartz cell to combine with ProCA1 variants, which was used to detect the binding effects on the protein structure.

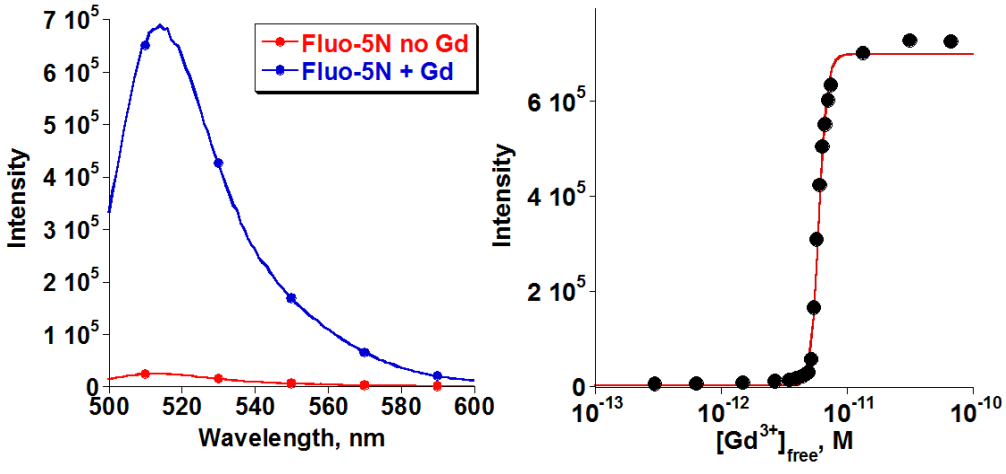

Figure 3.18 The K_d determination of 1 µM Fluo-5N to Gd^{3+} using fluorescence emission from 500 nm to 650 nm excited at 488 nm with a Gd-NTA buffer system (50 mM HEPES, 100 mM NaCl and 5 mM NTA at pH 7.0). 0 - 5 mM $GdCl_3$ were titrated into the system to generate a free Gd^{3+} concentration range from 10^{-13} to 10^{-10} M. K_d of Fluo-5N to Gd^{3+} is determined by Hill equation.

3.2.4 Metal selectivity of ProCA1 variants

3.2.4.1 Determine Gd^{3+} binding affinity of Fluo-5N using Gd-NTA buffer system

Before we determine the affinity between Gd^{3+} and ProCAs, we need to calculate the affinity of Gd^{3+} to a fluorescence indicator Fluo-5N using Gd^{3+}-NTA buffer system. Fluo-5N shows enhanced fluorescence signal when it binds with Gd^{3+}. In order to determine the K_d of FLUO-5N to Gd^{3+}, the concentration of FLUO-5N was fixed at 1 µM and titrated with standard Gd^{3+} solution in NTA buffer system. The buffer system contained 5 mM NTA. The fluorescence signal of FLUO-5N from 500 nm to 650 nm(excited at 488 nm) increased till it was saturated (Fig. 3.18).

The fluorescence signal intensity plots were fitted by HILL equation. The calculated K_d value (5.2 x 10^{-12} M) was consistent with the result (K_d = 3.8 x 10^{-12} M) previously published in our lab [212].

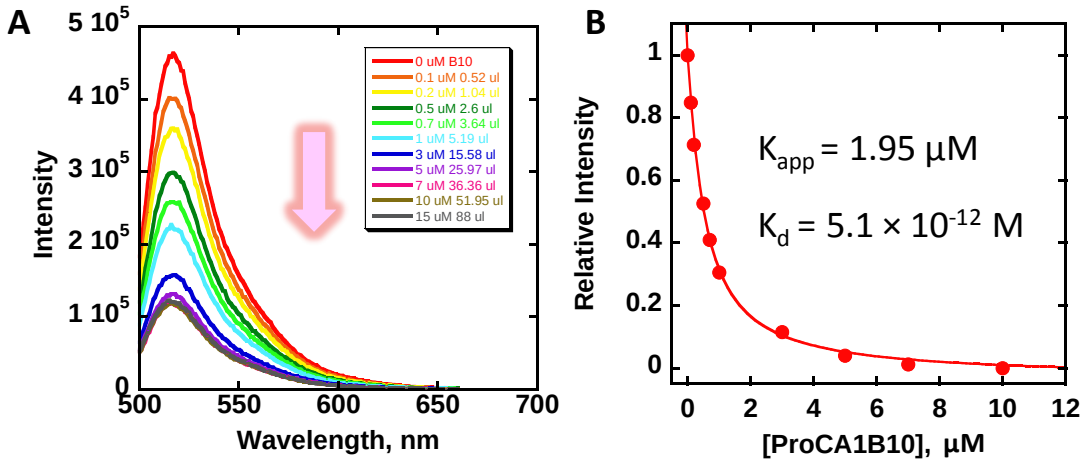

	ProCA1	ProCA1B14	ProCA1B10	ProCA1G10
K_{app}, µM		0.80 ± 0.21	1.95 ± 0.17	0.48 ± 0.02
K_d, M	8.7×10^{-13}	$2.1 \pm 0.6 \times 10^{-12}$	$5.1 \pm 0.1 \times 10^{-12}$	$1.3 \pm 0.1 \times 10^{-12}$

Figure 3.19 Determine the binding affinity of ProCA1 variants to Gd^{3+} by competition methods. This experiment was performed by titrating different concentrations of ProCA1 variants in 50 mM HEPES, 100 mM NaCl, 1 µM Fluo-5N at pH 7.0 and room temperature. The decrease of Fluo-5N emission signal from 500 nm to 650 nm (excited at 488 nm) up addition of ProCA1 variants is originated from the removal of Gd^{3+} by protein contrast agents.

Fluo-5N emission spectrum was monitored from 500 nm to 650 nm when it was excited at 488 nm. Because ProCA1 variants can compete Gd^{3+} out of the Fluo-5N, Fluor-5N shows decreased fluorescence signal.

3.2.4.2 Determine Gd^{3+} binding affinity of ProCA1 variants by using Fluo-5N competition assay

Next, we determined the Kd of ProCA1 variants to Gd^{3+} by the competition between ProCA1 variants and FLUO-5N. When the concentrations of FLUO-5N and Gd^{3+} were fixed, ProCA1 variants were gradually titrated to the sample solution to compete Gd^{3+} with FLUO-5N. After normalizing the fluorescence intensity, K_d (4.6 x 10^{-13} M) was calculated by the equation (3-1).

$$Kd2 = Kapp\frac{Kd1}{Kd1+[FLUO-5N]T} \quad (3\text{-}1)$$

Where K_{d1} is the dissociation constant for FLUO-5N, $[FLUO\text{-}5N]_T$ is the total concentration of FLUO-5N, K_{app} is the apparent dissociation constant for protein and K_{d2} is the dissociation constant for protein.

As shown in Fig.3.19, addition of GRPR-targeted ProCA1variants result in the decrease of florescence signal of Fluo5N due to competition. All of three GRPR targeting contrast agent exhibit Gd binding affinity around 2×10^{-12} M.

3.2.4.3 Determine Zn^{2+} binding affinity of ProCA1 variants by using Fluozin-1 competition assay

Metal selectivity reflects kinetic stability of contrast agents over physiological metal ions. It is defined by the log value of Gd association constant (pKa Gd) over the log value of association constants of physiological metal ions. Zn^{2+} is one of the major physiological metal ions which involve in the de-chelation of Gd^{3+} from clinical MRI contrast agents. Clinical MRI contrast agents have high Zn^{2+} affinity that is close to their Gd^{3+} affinity. For example, DTPA has a Zn^{2+} affinity of 6.3×10^{-19} M, while DTPA has Gd^{3+} affinity of 1.9×10^{-21} M (NIST). There is an extremely low metal selectivity (logKaGd/LogKaZn = 2.5) between Zn^{2+} and Gd^{3+} for clinical MRI contrast agents, such as Gd-DPTA. Because of such low metal selectivity, Gd^{3+} could be released

from clinical MRI contrast agents *in vivo* due to Zn^{2+} competition. Thus, there is an urgent need to improve the metal selectivity for the MRI contrast agents.

The Zn^{2+} affinities to ProCA1 variants were determined by the competition between ProCA1 variants and dye Fluozin-1. When the concentrations of Fluozin-1 and Zn^{2+} were fixed, ProCA1 variants were gradually added to the sample solution to compete Zn^{2+} with Fluozin-1. After normalizing the fluorescence intensity, K_d (4.6×10^{-13} M) was calculated by the equation (3-2).

$$Kd2 = Kapp \times \frac{Kd1}{Kd1+[Fluozin-1]T} \quad (3\text{-}2)$$

Where K_{d1} is the dissociation constant for Fluozin-1, $[\text{Fluozin-1}]_T$ is the total concentration of Fluozin-1, K_{app} is the apparent dissociation constant for protein and K_{d2} is the dissociation constant for protein. As shown in Fig. 3.20 and table 3.2, the K_d of ProCA1 variants are all at 10^{-8} M level which indicates they have much weaker Zn^{2+} stability compared with Zn-DTPA and other clinical MRI contrast agents. The Gd^{3+} selectivities (the log value of Gd^{3+} association constant (pKa Gd) over the log value of association constants of physiological metal ions) over Zn^{2+} are 5.4, 4.1,3.7 and 4.6 for ProCA1, ProCA1B14, ProCA1B10 and ProCA1G10, respectively, which is much better than that of DTPA (2.5). Because of the improved metal selectivity, ProCAs could have reduced Gd^{3+} release *in vivo*, compared with that of clinical MRI contrast agents. Such improvement facilitates the *in vivo* application of ProCA1 variants.

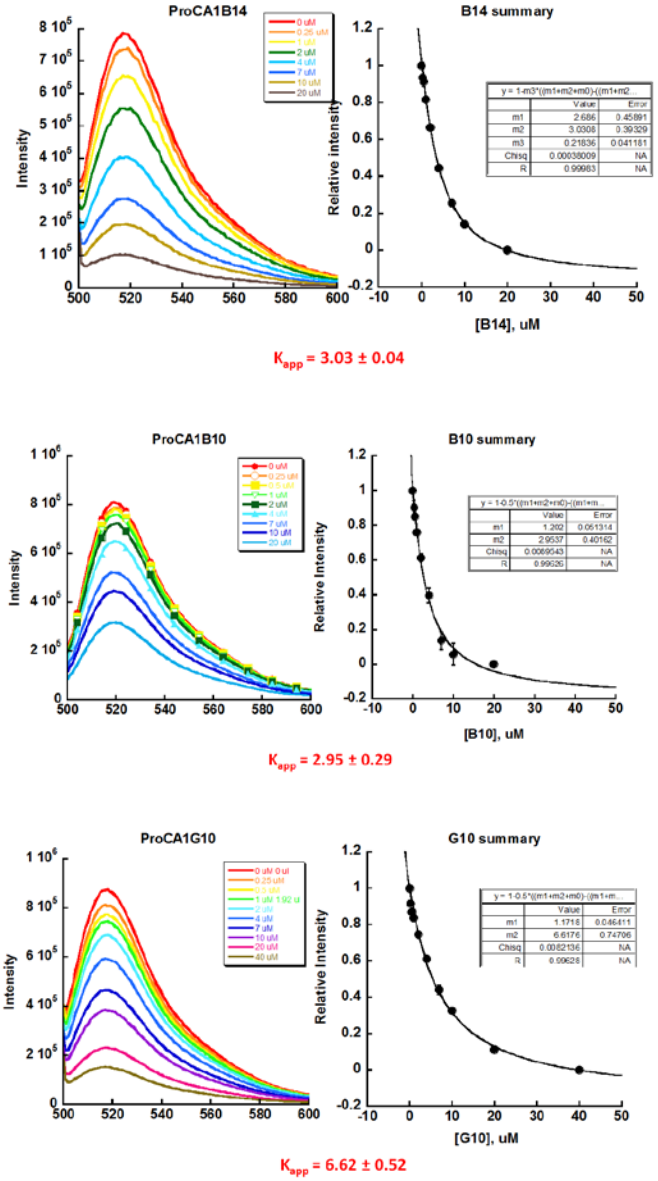

Figure 3.20 Fluorescence emission spectra (left) and intensity at 520 nm (right) excited at 495 nm of 1 µM of Fluozin-1 upon addition of different concentrations of ProCA1 variants to determine Zn^{2+} binding affinity (K_d) by a competition assay.

This experiment was performed by titrating different concentrations of ProCA1 variants in 50 mM HEPES, 100 mM NaCl, 1 µM Fluozin-1 at pH 7.0. Fluozin-1 emission spectrum was moni-

tored from 500 nm to 600 nm when it was excited at 495 nm. Because ProCA1 variants can compete Zn^{2+} out of the Fluozin-1, Fluorzin-1 shows decreased emission fluorescence signal.

Table 3.3 The Zn^{2+} binding affinity and selectivity to ProCA1 variants determined by Fluozin-1 competition assay.

	ProCA1	ProCA1B14	ProCA1B10	ProCA1G10
k_{app}, μM		3.03 ± 0.04	2.95 ± 0.29	6.62 ± 0.52
k_d, M	1.9×10^{-7}	2.4×10^{-8}	2.3×10^{-8}	5.3×10^{-8}
pGd/pZn	5.4	4.1	3.7	4.6

3.2.5 Relaxivity of ProCA1 variants

The ability of a contrast agent to change the relaxation rate is represented quantitatively as relaxivity, r_1 or r_2, where the subscript refers to either the longitudinal ($1/T_1$) or the transverse rate ($1/T_2$). Relaxivity is dependent on magnetic field, the electronic properties of the gadolinium, water exchange, rotational diffusion, first and second coordination sphere hydration, and the ion to water proton distance. Especially, relaxivity is dependent on molecular motion which based on molecular size, rigidity, and potential protein binding [173].

Domain 1 of CD2 has a rotational correlation time of 9 ns, which is optimized to achieve high relaxivity. We generated a Gd^{3+} binding pocket on the protein surface of domain 1 of CD2. After loading Gd^{3+} in this binding pocket, Gd^{3+} and its vector rotate together with a similar rotational correlation time of approximately 9 ns. In addition, due to the large hydrophilic surface of

protein, the 2nd and out-sphere water could play an essential role to improve the overall relaxivity.

The relaxivity of ProCA1 variants was measured at 60 MHz relaxometer (Bruker). The concentration of Gd^{3+} was fixed at 50 µM and a series of Gd^{3+} to protein ratios were designed to determine the relaxivity of ProCA1 variants. From the raw data (Fig. 3.21), using T1 value as an example, the relaxivity of ProCA1 increased while the concentration of protein increased until it reached to saturation.

r1 and r2 were calculated from the equation 3-3 when the T1 and T2 values of ProCA1 variants and buffer were measured. Theoretically, when the ratio of ProCA1 to Gd^{3+} was up to 1:1, the relaxivity saturate. Even when the ratio of ProCA1 to Gd^{3+} was up to 2:1 or 3:1, the relaxivity didn't increase. The relaxivity of ProCA1 at the 1:1 binding site was the relative intensity of this contrast agent in this specific magnetic field (1.4 T).

$R_{1,2} = (1/T_{1,2\,Sample} - 1/T_{1,2\,buffer})/[Gd^{3+}]$ **(3.3)**

The relaxivity of ProCA1 variants which were measured at 25°C were shown in the Fig.3.21. All ProCA1 variants showed much higher relaxivity (25.9 - 49.2 $mM^{-1}s^{-1}$, 25°C and 60MHz) than that of clinical contrast agents (3.5 $mM^{-1}s^{-1}$). ProCA1B14, ProCA1B10 and ProCA1G10 show much higher relaxivity than that of ProCA1. Such increases in relaxivity values are likely due to changes in the Gd^{3+} center [218], increase in correlation time, and water exchange properties after addition of a grafted targeting moiety. Such high relaxivity of ProCA1 variants indicate that ProCA1 variants requires lower local concentration to improve the contrast of tissue compared with that of clinical MRI contrast agents. Since cancer biomarker usually has a low expression lever at nM or pM range, high relaxivity and high sensitivity of ProCA1

variants make them at a better position to image these biomarkers than clinical MRI contrast agents.

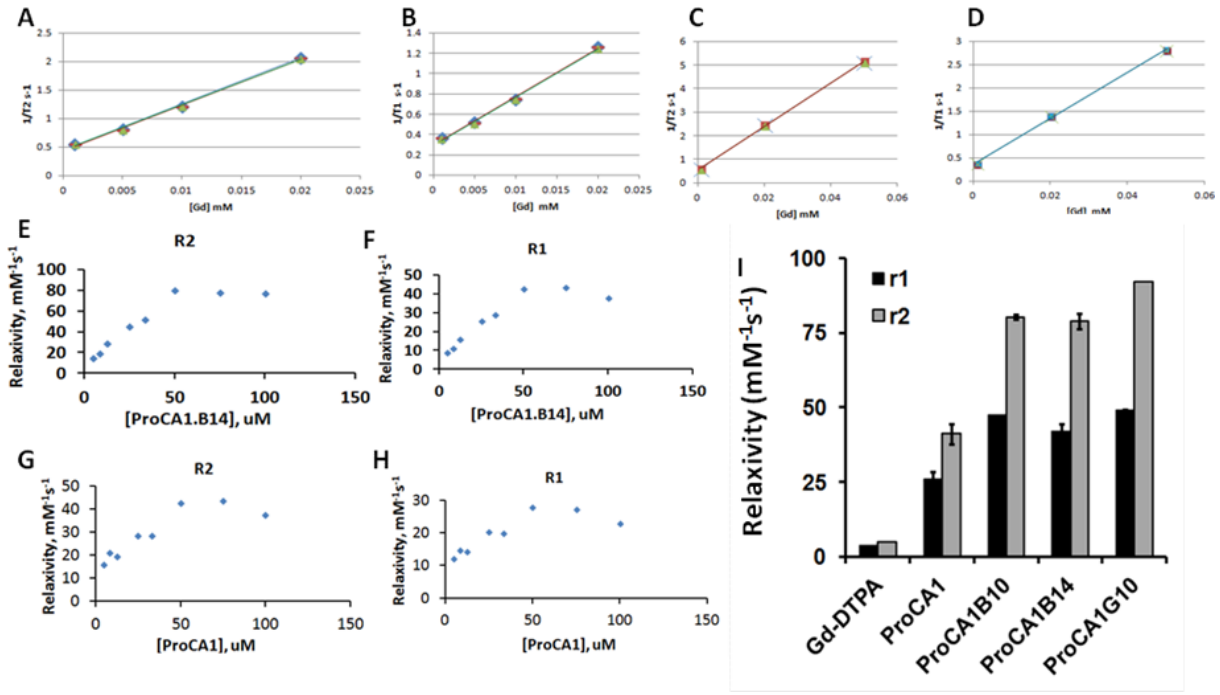

Figure 3.21 Compare relaxivity value (r1 and r2) of Gd-DTPA and ProCA1 variants.

A. Raw data to determine r2 for ProCA1B10. B. Raw data to determine r1 for ProCA1B10. C. Raw data to determine r2 for ProCA1G10. D. Raw data to determine r1 for ProCA1G10. E. Raw data to determine r2 for ProCA1B14. F. Raw data to determine r1 for ProCA1B14. G. Raw data to determine r2 for ProCA1. H. Raw data to determine r1 for ProCA1. I. The summery of relaxivities of Gd-DTPA and ProCA1 variants. The relaxivity of ProCA variants at 1.47 T relaxometer at 25°C in 10 mM HEPES buffer at pH 7.2. Those tubes were incubated in the relaxometer to an equilibrium state and then measured to get the T1 and T2 values.

3.2.6 Selection of cell lines

In order to study the targeting properties of gastrin-releasing peptide receptor (GRPR), two independent cell lines stably expressing GRPR were selected. PC3 is an androgen independent human prostate cancer cell line, which has relatively high GRPR expression. H441 is a human lung cancer cell line which shows relatively lower GRPR expression. Both of them are purchased from ATCC and cultured in our lab (Chapter 2).

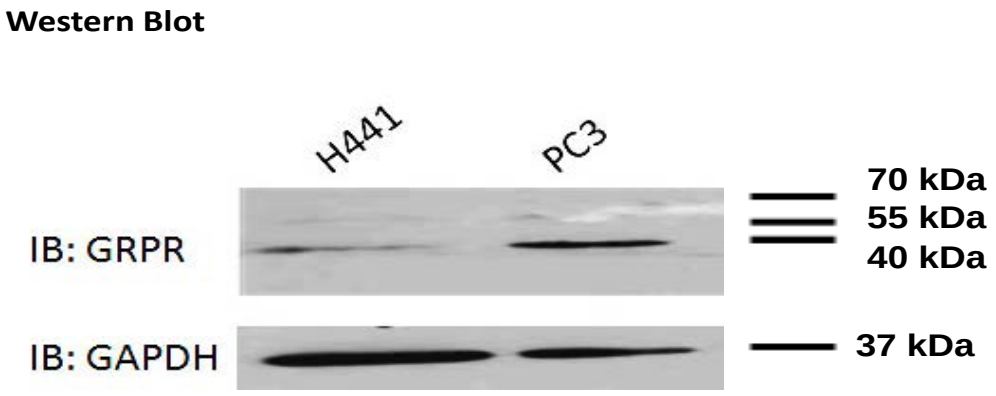

Figure 3.22 GRPR expression on PC3 and H441 cells lysates identified by Western Blot. The cell lysate of PC3 and H441 was added into the well of SDS-PAGE, separately. The primary antibody (mouse anti-GAPDH and rabbit anti-GAPDH) was added with different dilution ratios (0.33:1 and 1:1000) to incubate at 4°C overnight. ALP-conjugated goat anti-mouse secondary antibody diluted with a ratio of 1:10000 in 5% blocking milk was added to incubate the membranes at room temperature for 1 h.

3.2.7 Cell imaging of ProCA1 variants targeting GRPR

To further monitor the binding of GRPR on the cancer cells, we labeled GRPR-targeted ProCA1 variants with fluorescein. Fig. 3.23 shows that cells can be visualized by fluorescence microscope upon incubation with fluorescein-labeled GRPR targeted contrast agents (B10, G10 and B14). Under the same condition, three different targeting contrast agents exhibit different targeting capabilities for cancer cells. ProCA1B14 showed the highest intensity as it binds GPPR on PC3 cells which is about 2 and 2.4 fold higher than that of ProCA1B10 and ProCA1G10, respectively. In contrast, ProCA1 without GRP targeting moiety does not have any capability to label prostate cancer cells.

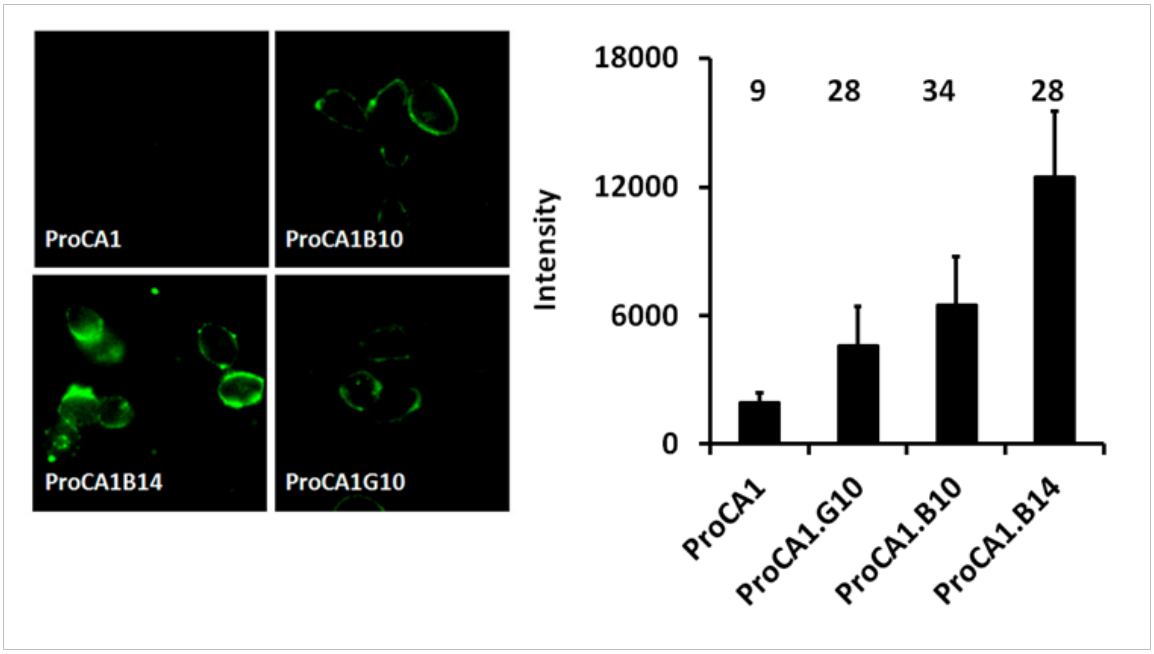

Figure 3.23 Fluorecin-labeled ProCA1s bind to GRPR on PC3 cells.

Left. Fluorescence imaging of PC3 cells incubated with fluorescein-labeled ProCA1 variants (green). Right. Fluorescence intensity of PC3 cells incubated with different ProCA1 variants. The mean and standard derivations (error bar) of fluorescence intensity were quantified from 9, 28, 34 and 28 cells after incubating with ProCA1, ProCA1G10, ProCA1B10 and ProCA1B14, respectively. Fluorescence imaging is collected with excitation wavelength of 488 nm.

3.2.8 Determination of the binding affinity of ProCA1 variants to GRPR and GRPR numbers on cell surface by ELISA and Scatchard Plot

Scachard Plot is a classic method to calculate K_d of ProCA1 variants to GRPR. GRPR number on different cell surface can be quantified by Scachard equation (III). In this equation, K_a is the association affinity constant, [B] is the concentration of the binding receptors, [F] is the concentration of the free receptors, and [Rt] is the total concentration of the receptors. A plot of B/F versus B is known as a Scachard plot.

$$[B]/[F]=Ka[R_T]-Ka[B] \qquad (3.4)$$

In this experiment, $[R_T]$ was the concentration of total ProCA1 variants added, [B] was the concentration of the binding ProCA1 variants, [F] was the concentration of the free receptors. A standard curve of absorbance at 450 nm versus the concentration of incubated ProCA1 variants is utilized to calculate [B] which corresponds to the absorbance of the wells of precultured PC3 cell lysate. [F] is calculated by $[R_T]$ minus [B]. K_a was the concentration of ProCA1 variants at which the GRPR is half-maximally occupied by ProCA1 variants. According to $K_d = 1/K_a$, dissociation constants of ProCA1 variants were calculated (Fig.3.26). The GRPR expression levels calculated from the Y intercept on the x axis value of $[B_{max}]$ are approximately 4×10^5 and 2×10^4 for PC-3 and H441, respectively. H441 has 20 fold lower GRPR expression than that of PC3. Consistent with this, the GRPR expression in PC3 cell lysate probed by antibody in western plot is significant greater than that in H441. We next determined the binding dissociation constant of targeting reagents to GRPR. Fig.3.26 shows that the calculated disassociation constants Kd from the slopes. ProCA1B14 had the highest binding affinity (K_d = 2.8 nM) while K_d for B10 and G10 are 3 and 5.7 fold lower than that of ProCA1B14.

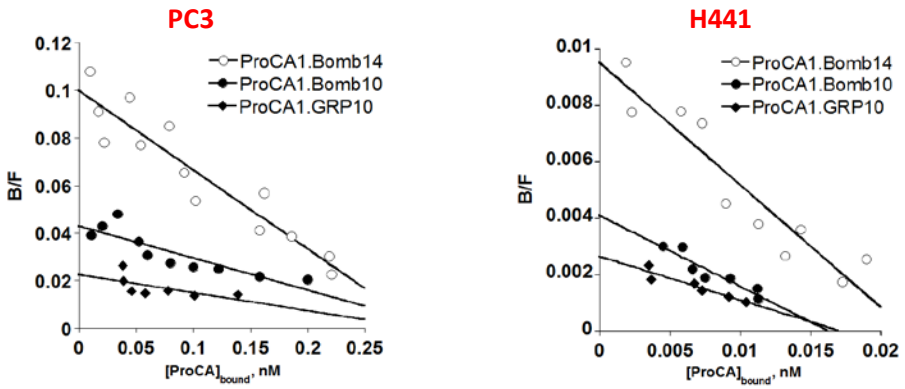

Cell	ProCA1 Variants	K_d, nM	B_{max} (Receptors/Cell)
PC3	ProCA1B14	2.7 ± 0.3	$3.5 \pm 0.3 \times 10^5$
	ProCA1B10	8.1 ± 4.4	$4.0 \pm 1.0 \times 10^5$
	ProCA1G10	15.4 ± 2.0	$4.3 \pm 0.1 \times 10^5$
H441	ProCA1B14	2.1 ± 0.3	$2.6 \pm 0.2 \times 10^4$
	ProCA1B10	3.4 ± 0.7	$1.7 \pm 0.4 \times 10^4$
	ProCA1G10	6.8 ± 2.3	$2.0 \pm 0.4 \times 10^4$

Figure 3.24 The binding affinity of ProCA1s to GRPR on PC3 and H441 cells and GRPR numbers per cell determined by indirect ELISA and Scatchard Plot.

The binding affinity and B_{max} were determined by ELISA coupled with Scatchard plot. PC3 and H441 cell lysate (from 5 x 10^4 cells) were coated in each well. After complete washing and blocking with 5% BSA, the coated cell lysates were incubated with different concentrations of ProCA1 variants in 10 mM HEPES buffer at pH 7.2. The interactions between ProCA1 variants and GRPR in cell lysates were quantified by ELISA using HRP-conjugated goat anti rabbit secondary antibody and one step ELISA kit. To quantify the concentration of the bounded ProCA1 variants to GRPR at different total ProCA1 concentrations, a standard curve was generated by direct coating of ProCA1 variants to the wells and visualized using the same primary, secondary antibody and one step ELISA kit.

3.2.9 MRI of xenograft model indicates the specific targeting of ProCA1 variants to GRPR

ProCA1B14 has the highest binding affinity to GRPR among all variants and better relaxivity than Gd-DTPA based on those *in vitro* investigations of ProCA1 variants. Thus, we chose ProCA1B14, for the *in vivo* molecular imaging of GRPR. ProCA1 and ProCA1B14 were pegylated to increase the solubility of the protein and decreased its immunogenicity. ProCA1B14 was also conjugated with NIR dye Cy5.5 to enable florescence animal imaging before it was used in the MRI scanning. The PEGylated ProCA1B14 has similar relaxivity compared with non-PEGylated ProCA1B14.

H441 and PC3 cancer cells (5×10^5), which express different levels of GRPR (Fig. 3.25 A), were injected in left and right flank of athymic mice which grew up as tumor (1 cm) xenograft models. The contrast agent ProCA1B14 (5 µM, 50 µl) was injected into the mice by tail vein injection. MR images were recorded at 7 T at different time points (pre-scan and 10 min, 30 - 40 min, 24 h, and 48 h after injection) to trace the change of contrast enhancement in tumor regions. Injection of GRPR-targeted contrast agent B14 results in significantly increase of both PC3 and H441 tumor at time point of 24 - 48 hours. In contrast, injection of PEGylated ProCA1 without the GRP targeting moiety to the xenograft mice model under the same condition and time point does not result any enhancement.

It is interesting to note that MRI contrast enhancement by B14 is different for both prostate cancer cell types. The contrast enhancement of H441 tumor increased gradually and reached the highest level at the time point 24h post injection. Then, the signal intensity of H441 began to decrease. While, the contrast enhancement of PC3 tumor increased gradually as a function of time and reached the highest level at the time point 48 h post injection. There is an

interesting phenomenon that the signal intensity of PC3 was lower than that of H441 before 24 h, however, the condition reversed after 24h. Interesting, both PC3 and H441 tumors shows heterogeneous enhancement post injection of ProCA1B14 for 24 - 48 hours, indicating the heterogeneous distribution of GRPR in these tumors.

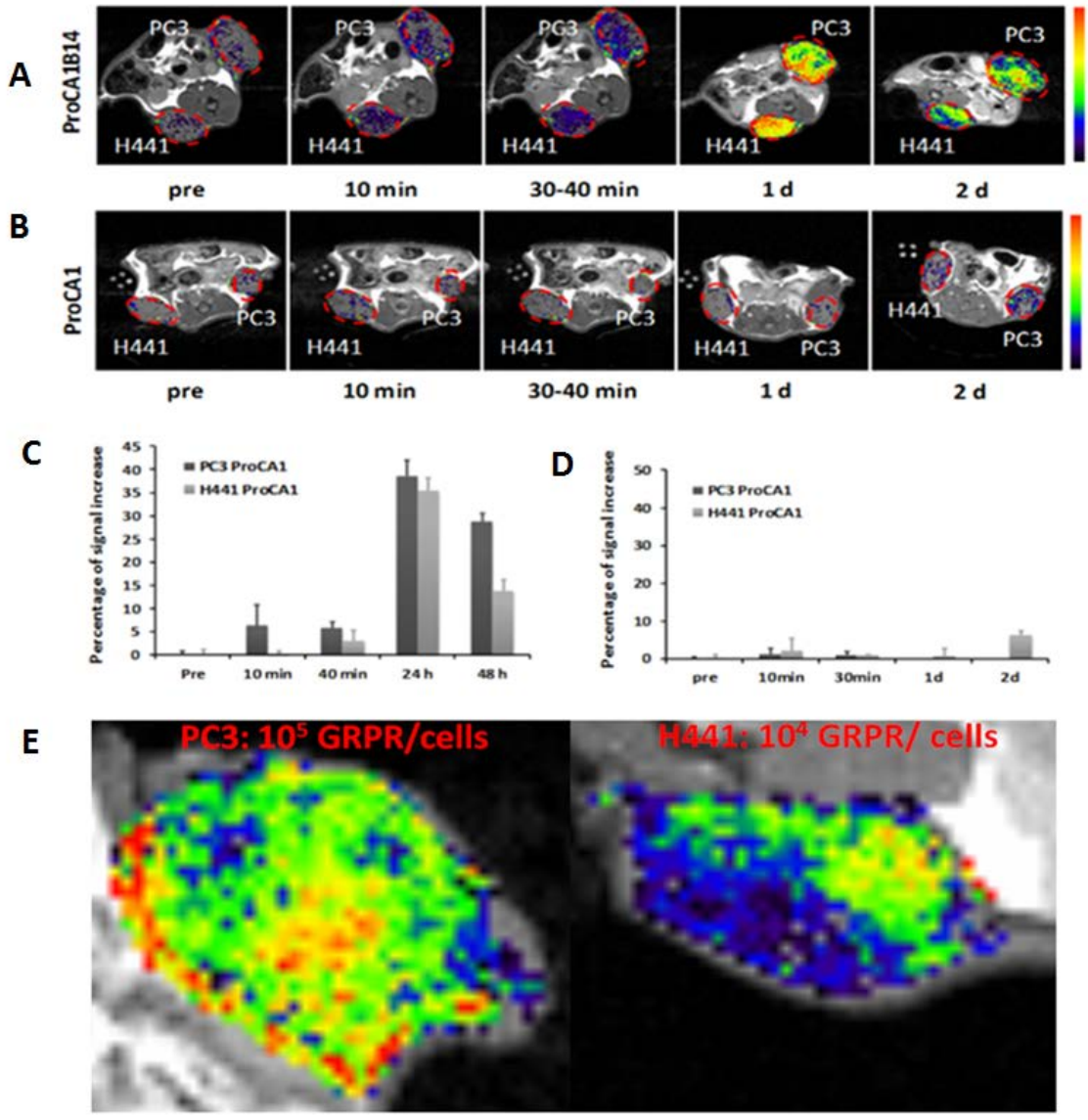

Figure 3.25 T1-weighted spin echo MR imaging of PC3 and H441 xenografted mice tumor.

A. T1-weighted spin echo MR imaging of ProCA1B14 targeting GRPR in PC3 and H441 xenografted mice tumor. B. T1-weighted spin echo MR imaging of ProCA1 in PC3 and H441

xenografted mice tumor. MRI were collect at 7 T Varian MRI scanner spin echo sequence with following parameters: TR = 500 ms, TE is set to be minimum, Fov = 4 cm x 4 cm, matrix = 128 x 128, slice thickness 1 mm. C. Quantitative analysis of MRI intensity from ProCA1 in mice tumor PC3 and H441 by Image J and MRIcron. D. Quantitative analysis of MRI intensity from ProCA1B14 in mice tumor PC3 and H441 by Image J and MRIcron. E. MRI shows heterogeneous enhancement in PC3 and H441 tumors after injection of ProCA1B14.

3.2.10 Statistical analysis of MRI results

Statistical analysis of MRI results (Section 3.2.10) was performed by Qian Yan in Dr. Gensheng Qin's group at Department of Math and Statistics.

3.2.10.1 MRI intensity (mean response)

To compare the MRI intensity of different tumors post contrast agent injection, we measured the MRI intensity of PC3 tumor and H441 tumor (n = 5) by Image J to calculate the mean intensity and the standard derivation. Table 3.3 and Table 3.4 summarized the mean MRI intensity of PC3 tumor post injection of ProCA1 and ProCA1B14 at different time points. Table 3.5 and Table 3.6 summarized the mean MRI intensity of H441 tumor post injection of ProCA1 and ProCA1B14 at different time points. Figure 3.26 and Figure 3.27 exhibit the trend of MRI mean intensity of PC3 tumor and H441 tumor over time after injection ProCA1 and ProCA1B14, respectively. As shown in Fig. 3.26 and Fig. 3.27, the mean MRI intensity of both tumors before ProCA1 and ProCA1B14 injection is similar, but the difference increased post 1 day injection. This phenomenon was observed in both PC3 xenografted tumor and H441 xenografted tumor.

In addition, the mean intensity of both tumors post injection of ProCA1B14 is significantly higher than that of ProCA1.

Table 3.4 Mean MRI intensity levels at 0, 10 min, 30 min, 1 day and 2 days post injection of 0.025 mmol/kg of ProCA1 with PC3 xenografted tumor. (Data from Yan Qian)

Mean MRI intensity of ProCA1 group with PC3 tumor		
Time (minute)	Mean	Std Dev
0	2.11×10^{-6}	4.14
10	2.05	4.72
30	5.31	2.92
1440	-3.92	3.83
2880	3.56	1.39

Table 3.5 Mean MRI intensity levels at 0, 10 min, 30 min, 1 day and 2 days post injection of 0.025 mmol/kg of ProCA1B14 with PC3 xenografted tumor. (Data from Yan Qian)

Mean MRI intensity of ProCA1B14 group with PC3 tumor		
Time (minute)	Mean	Std Dev
0	-1.51×10^{-6}	2.36
10	7.51	5.81
30	4.68	1.60
1440	38.61	1.73
2880	28.92	1.44

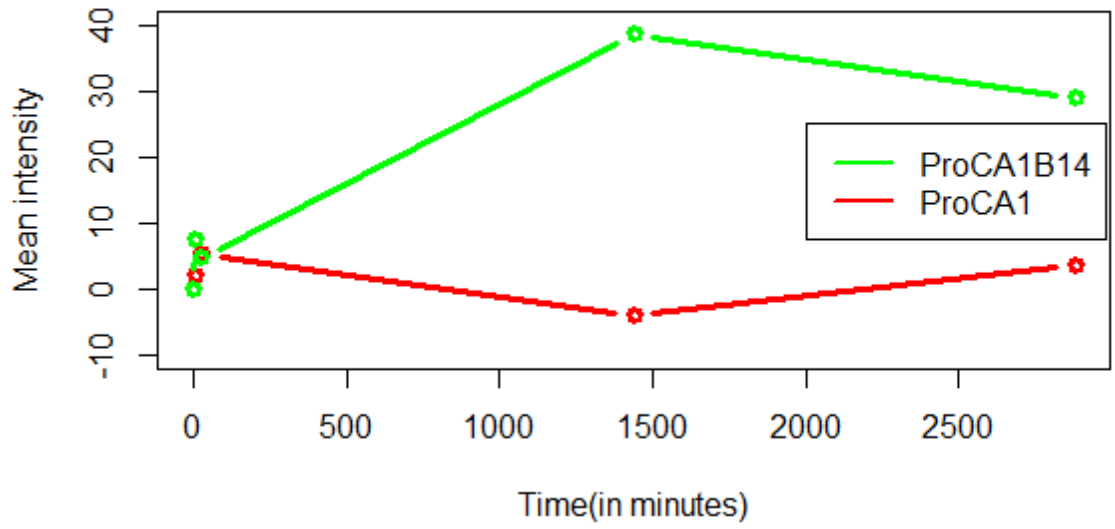

Figure 3.26 Timeplot of mean intensity pre injection and 10 min, 30 min, 1 day and 2 days post injection of ProCA1 and ProCA1B14 with PC3 xenografted tumor. (Data from Yan Qian)

Table 3.6 Mean MRI intensity levels at 0, 10 min, 30 min, 1 day and 2 days post injection of 0.025 mmol/kg of ProCA1 with H441 xenografted tumor. (Data from Yan Qian)

Mean MRI intensity of ProCA1 group with H441 tumor		
Time (minute)	Mean	Std Dev
0	-5.53×10-6	0.80
10	1.52	3.39
30	1.80	8.09
1440	-3.69	2.88
2880	5.30	2.65

Table 3.7 Mean MRI intensity levels at 0, 10 min, 30 min, 1 day and 2 days post injection of 0.025 mmol/kg of ProCA1B14 with H441 xenografted tumor. (Data from Yan Qian)

Mean MRI intensity of ProCA1B14 group with H441 tumor		
Time (minute)	Mean	Std Dev
0	-3.60×10-6	1.22
10	1.28	2.51
30	5.88	0.85
1440	32.97	6.15
2880	17.52	5.82

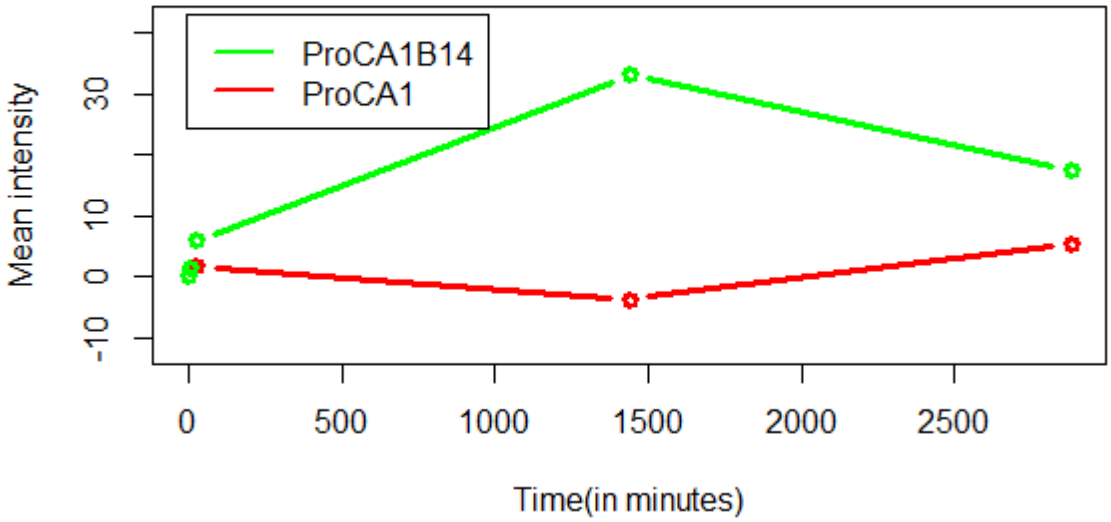

Figure 3.27 Timeplot of mean intensity pre injection and 10 min, 30 min, 1 day and 2 days post injection of ProCA1 and ProCA1B14 with H441 xenografted tumor. (Data from Yan Qian)

3.2.10.2 Statistical modeling

To investigate the effects of ProCA1 and ProCA1B14 in PC3 tumor and H441 tumor, we need to construct an optimized model. Considering the trend of mean response (mean intensity) over time is not linear and affected by time, test statistic was applied to compare three different models, including linear trends over time model, linear spline model and quandratic trend over time mode. After a series of comparison, quandratic trend over time model was selected because it best fitted the data among three candidates. As shown in Table 3.8, estimated regression coefficients, standard errors, and p-values were calculated based on the quadratic model.

For the mean response comparison of ProCA1 and ProCA1B14 in PC3 tumor, the final model is

$$Y_{ij} = \beta_1 + \beta_2 Group_i + \beta_3 Time_{ij} + \beta_4 Time_{ij}^{\ 2} + \beta_5 Group \times Time_{ij} + \beta_6 Group \times Time_{ij}^{\ 2} + \varepsilon_{ij},$$

where, $Group_i = \begin{cases} = 1 \text{ if Group=ProCA1B14} \\ = 0 \text{ if Group=ProCA1} \end{cases}$

ε_{ij}, are assumed to have a multivariate normal distribution with mean zero and covariance matrix denoted by R_i ($R_i = \sigma^2 I$, where I is an $n_i \times n_i$ identity matrix).

Model for the mean intensity ProCA1 in PC3 tumor group is

$$E(Y_{ij}) = \beta_1 + \beta_3 Time_{ij} + \beta_4 Time_{ij}^{\ 2} = 3.585 \times 10^{-6} Time_{ij}^2 - 0.01065 Time_{ij} + 3.8378.$$

For ProCA1B14 in PC3 tumor group, the model is

$$E(Y_{ij}) = (\beta_1 + \beta_2) + (\beta_3 + \beta_5) Time_{ij} + (\beta_4 + \beta_6) Time_{ij}^{\ 2} = -6.415 \times 10^{-6} Time_{ij}^2 + 0.03979 Time_{ij} + 3.244$$

.

The significance tests of variables in the model in Table 3.9 suggest that all the variables are significant ($p < 0.05$) except group effect. Test-statistic for group x time effect is 192.28 with 1 degree of freedom ($p < 0.0001$) and for group x time^2 is 144.82 with 1 degree of freedom ($p < 0.0001$) which indicate that the mean intensity in ProCA1 and ProCA1B14 change significantly different over the study time. Further, test-statistic for time effect is 64.14 with 1 degree of freedom ($p < 0.0001$) and for time^2 effect is 18.23 with 1 degree of freedom ($p = 0.0027$) which indicate that the mean intensity is significantly affected along the study time. For the group effect, we hypothesize there is no group effect. However, test-statistic equals to 0.34 with 1 degree of freem ($p = 0.5781$) which let us fail to reject the null hypothesis and conclude that the group is good randomized.

Table 3.8 Solution for fixed effects in the final model (with PC3 tumor) (Data from Yan Qian)

Solution for Fixed Effects						
Effect	group	Estimate	Standard Error	DF	t Value	Pr > |t|
Intercept		3.8378	0.7244	8	5.30	0.0007
group	ProCA1B14	-0.5938	1.0245	8	-0.58	0.5781
group	ProCA1	0	.	.	.	.
time		-0.01065	0.002572	8	-4.14	0.0032
$time^2$		3.585E-6	0	8	Infty	<.0001
group × time	ProCA1B14	0.05044	0.003637	8	13.87	<.0001
group × time	ProCA1	0	.	.	.	.
group × $time^2$	ProCA1B14	-0.00001	1.187E-6	8	-12.03	<.0001
group × $time^2$	ProCA1	0	.	.	.	.

Table 3.9 Type 3 tests of fixed effects in the final model (with PC3 tumor). (Data from Yan Qian)

Type 3 Tests of Fixed Effects						
Effect	Num DF	Den DF	Chi-Square	F Value	Pr > ChiSq	Pr > F
group	1	8	0.34	0.34	0.5622	0.5781
time	1	8	64.14	64.14	<.0001	<.0001
$time^2$	1	8	18.23	18.23	<.0001	0.0027
group × time	1	8	192.28	192.28	<.0001	<.0001
group × $time^2$	1	8	144.82	144.82	<.0001	<.0001

Figure 3.28 exhibits the estimated mean intensity change of ProCA1 and ProCA1B14 groups in PC3 tumor during the study time which is generated based on the quadric trend over time model. The change of mean intensity follows the quadric trend over time pattern. The mean intensity of ProCA1B14 group (green) is much higher than that of ProCA1 group (red) even they start from a similar start point.

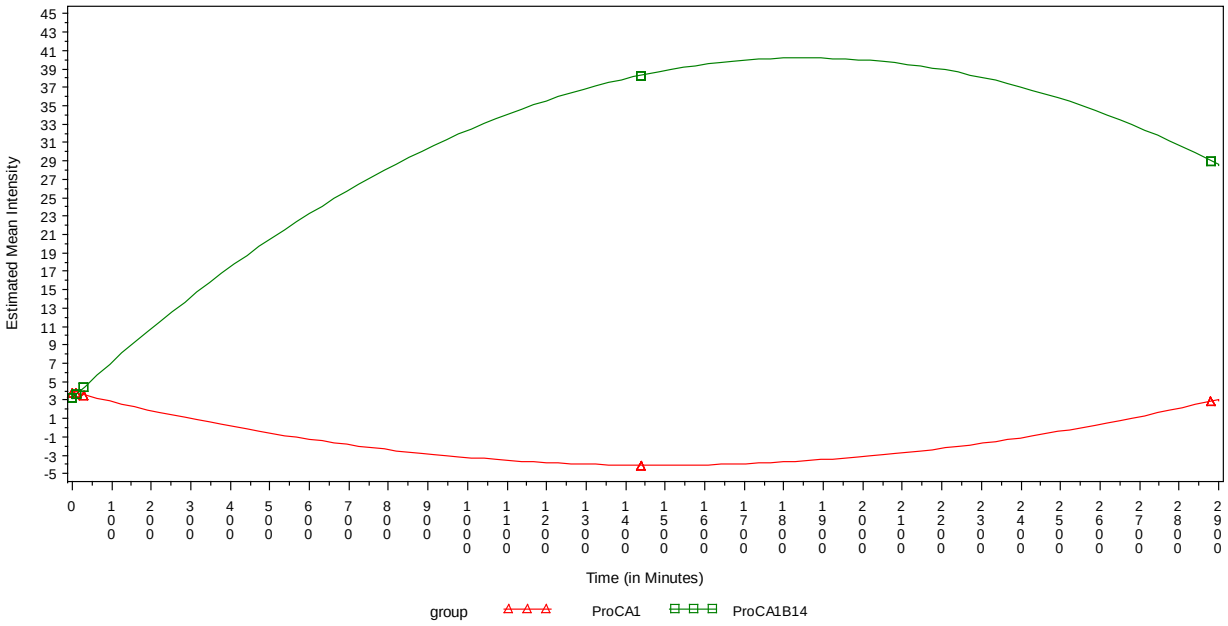

Figure 3.28 Timeplot of estimated mean intensity for ProCA1 and ProCA1B14 groups with PC3 tumor. (Data from Yan Qian)

To complete the longitudinal study analysis, we use transformed residuals (or scaled residual) which was achieved by Cholesky decomposition [219][201][201][201][201][201][200][200][200][200][170][170][169][169][168][168][162][160][152][150] to check the accuracy of the model. The graph of the scaled residuals in Fig. 3.29 means no appreciable departure from normality and not any definite outlying observation. [219]

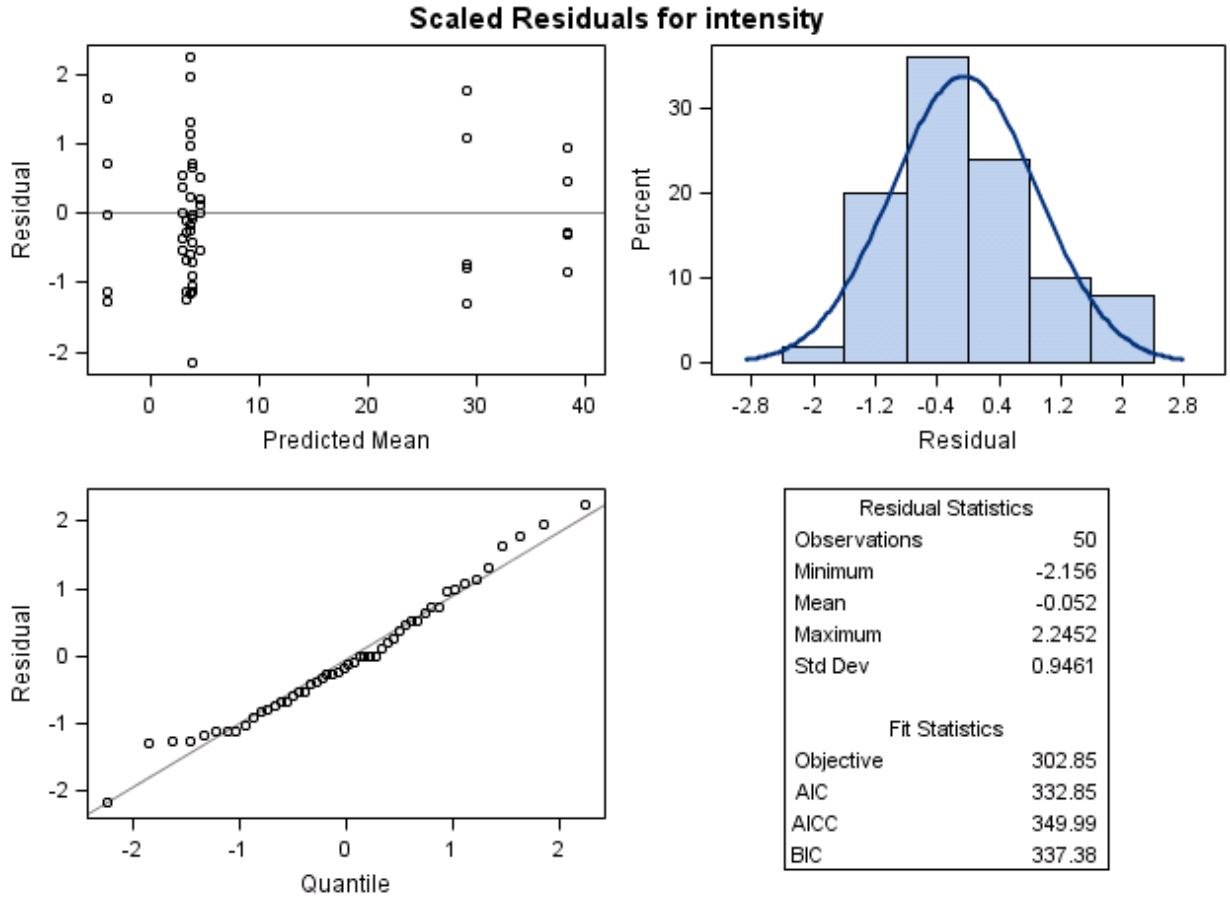

Figure 3.29 Scaled residual plots of the model for effect comparison of ProCA1 and ProCA1B14 with PC3 tumor. (Data from Yan Qian)

3.2.10.3 Effects of ProCA1 and ProCA1B14 in H441 tumor

We analyze the mean intensity of ProCA1 and ProCA1B14 in H441 tumor by fitting the data to the quadratic trend over time model. The models we used are listed as follows.

Model for the mean intensity for ProCA1in H441 tumor is

$$E(Y_{ij}) = \beta_1 + \beta_3 Time_{ij} + \beta_4 Time_{ij}^{\ 2} = 3.728\times10^{-6} Time_{ij}^2 - 0.00872 Time_{ij} + 0.334$$

Model for the mean intensity for ProCA1B14 group in H441 tumor, the model is

$$E(Y_{ij}) = (\beta_1 + \beta_2) + (\beta_3 + \beta_5) Time_{ij} + (\beta_4 + \beta_6) Time_{ij}^{\ 2} = -6.272\times10^{-6} Time_{ij}^2 + 0.03789 Time_{ij} - 0.0008.$$

Based on the results, we can conclude that the mean intensity change of ProCA1 and ProCA1B14 is significantly different over the study time. The mean intensity of ProCA1B14 (green) is much higher than that of ProCA1 (red) in H441 tumor (Figure 3.30). The scaled residual plot was also checked and no obvious violations of normality assumption and outliers.

Table 3.10 Solution for fixed effects in the final model (with H441 tumor). (Data from Yan Qian)

Solution for Fixed Effects						
Effect	group	Estimate	Standard Error	DF	t Value	Pr > |t|
Intercept		0.3340	0.1469	8	2.27	0.0525
Group	ProCA1B14	-0.3348	0.2077	8	-1.61	0.1456
Group	ProCA1	0	.	.	.	.
Time		-0.00872	0.003042	8	-2.87	0.0209
$time^2$		3.728E-6	1.169E-6	8	3.19	0.0129
group × time	ProCA1B14	0.04670	0.004302	8	10.85	<.0001
group × time	ProCA1	0	.	.	.	.
group × $time^2$	ProCA1B14	-0.00001	1.654E-6	8	-8.95	<.0001
group × $time^2$	ProCA1	0	.	.	.	.

Table 3.11 Type 3 tests of fixed effects in the final model (with H441 tumor) (Data from Yan Qian)

Type 3 Tests of Fixed Effects						
Effect	Num DF	Den DF	Chi-Square	F Value	Pr > ChiSq	Pr > F
Group	1	8	2.60	2.60	0.1070	0.1456
Time	1	8	46.23	46.23	<.0001	0.0001
$time^2$	1	8	10.16	10.16	0.0014	0.0129
group × time	1	8	117.82	117.82	<.0001	<.0001
group × $time^2$	1	8	80.06	80.06	<.0001	<.0001

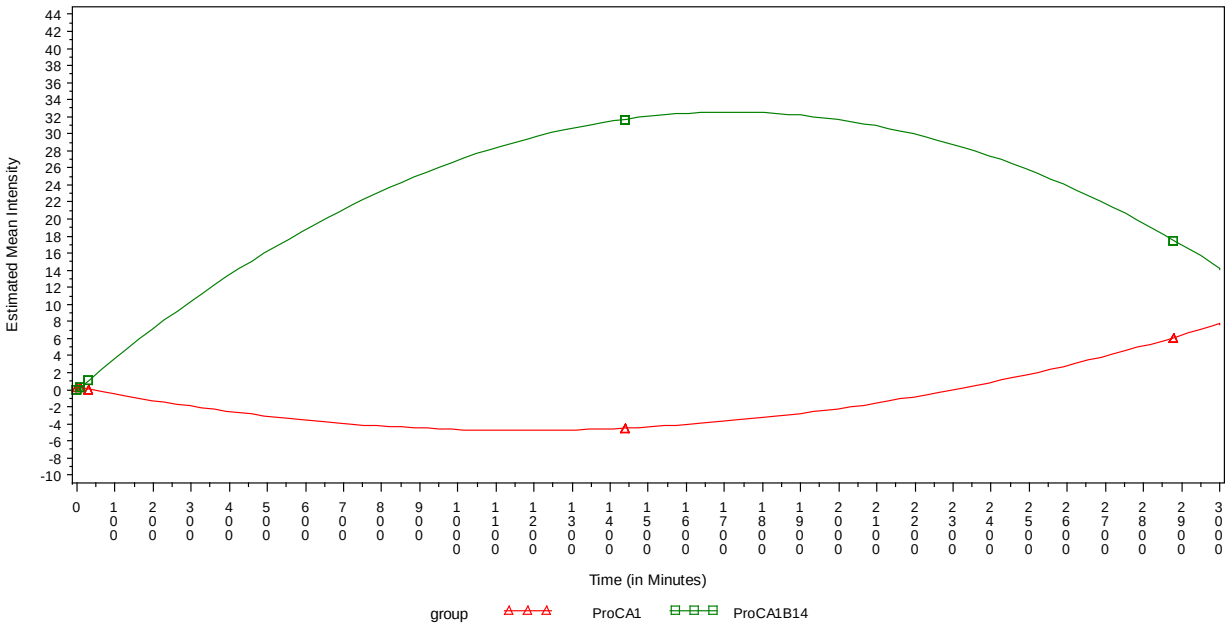

Figure 3.30 Timeplot of estimated mean intensity for ProCA1 and ProCA1B14 groups with H441 tumor. (Data from Yan Qian)

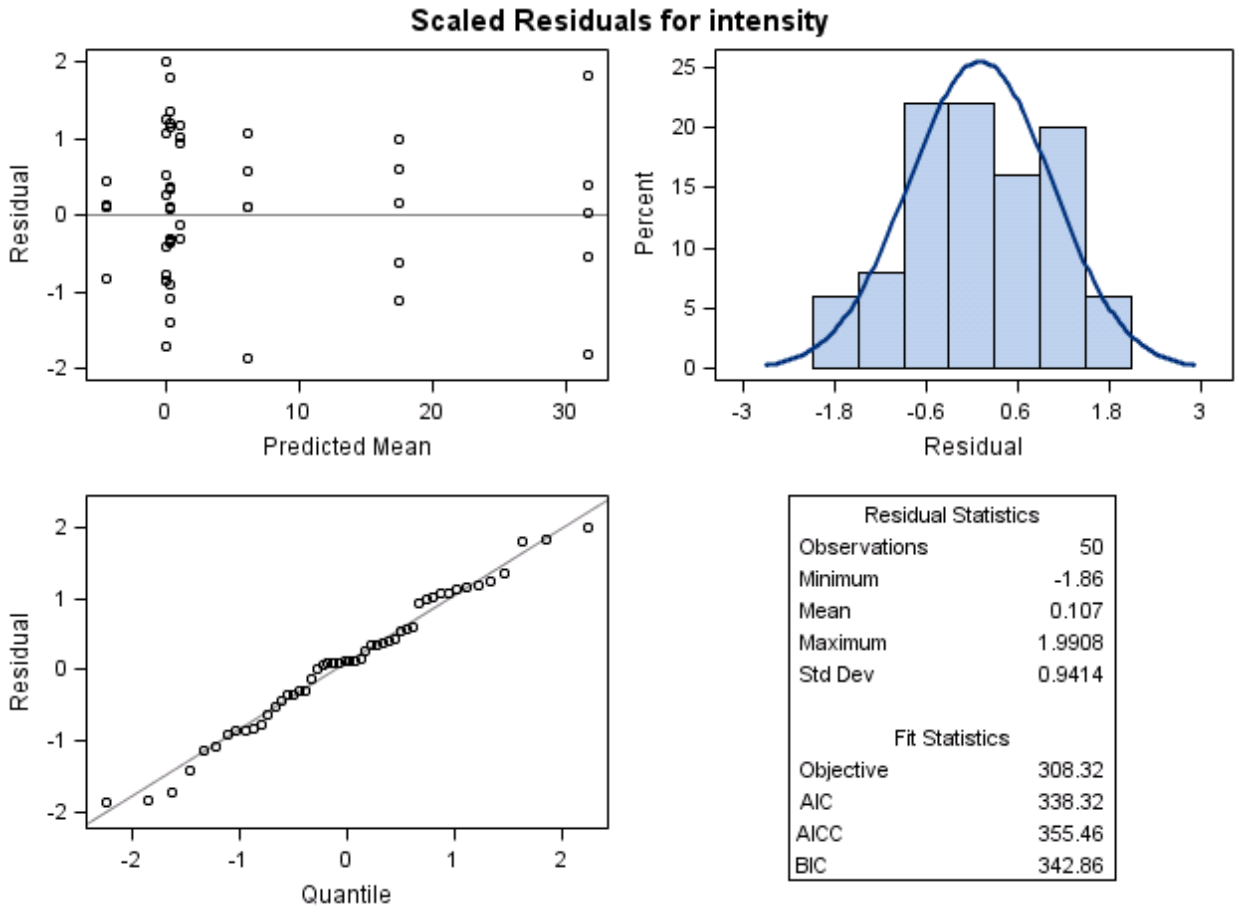

Figure 3.31 Scaled residual plots of the model for effect comparison of ProCA1 and ProCA1B14 with H441 tumor. (Data from Yan Qian)

3.2.11 NIR imaging confirms the specific targeting of ProCA1 variants

Our developed pegylated ProCA1B14 is not only a MRI contrast agent, it is also a NIR imaging agent. We conjugated ProCA1B14 with a NIR dye Cy5.5 at the C-terminal. Since the Cy5.5 can be monitored by IVIS imaging system (Xenogen Corporation) at an excitation wavelength of 650 nm, the fluorescence signal coming from Cy5.5 can be used to detect the distribution of the contrast agent. Since the mouse was scanned post 48 h injection of ProCA1B14, both the PC3 and H441 xenografted tumors are enhanced which is consistent with MR imaging. After

48 h scanning, we sacrificed the mouse and extracted different organs from the mouse. The extracted organs were scanned under IVIS imaging system (Xenogen Corporation) at an excitation wavelength of 650 nm. Comparing the intensities from different organs, the NIR intensities at H441 tumor site were much less than that of the PC3 tumor (Fig. 3.28).

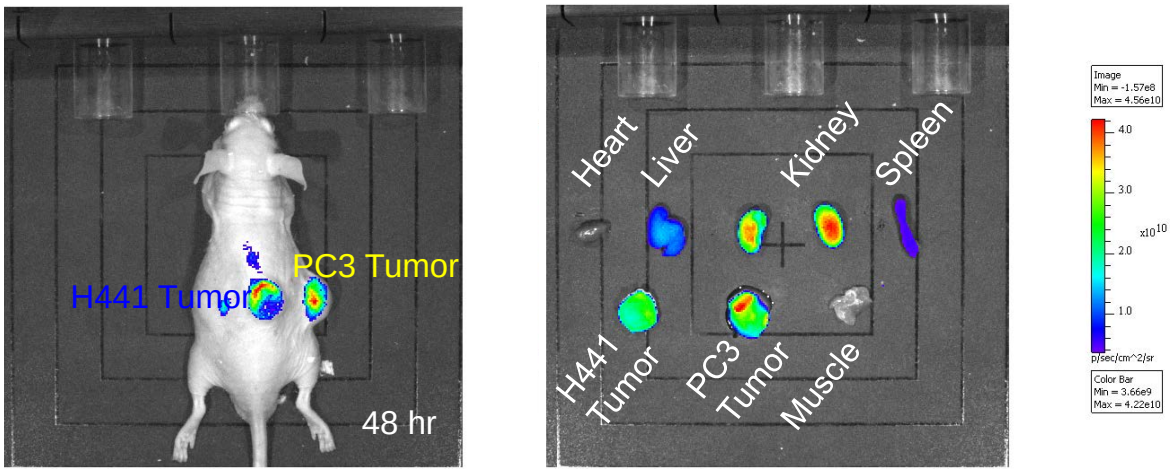

Figure 3.32 NIR image of mice after injection of 0.025 mmol/kg PEGylated ProCA1B14 . NIR imaging of mice and isolated tissues were collected under IVIS imaging system (at an excitation wavelength of 650 nm 48 hours post injection of pegylated and Cy5.5 labeled ProCA1B14.

3.2.12 ProCA1B14 target GRPR on PC3 and H441 xenografted tumors by immunofluorescence staining

To probe the distribution of ProCA1B14 in the tumor tissues post MRI scanning, an immunofluorescence staining was performed. The mice with xenografted tumors were sacrificed and representative organs were immersed in flek O.C.T and fixed by liquid nitrogen. All the samples were stored at -80˚C. The cryosectioning was performed by cryostas (Biology facility, GSU). The anti-ProCA1 primary antibody reacted with ProCAB14, which bound to GRPR and accumulated in the tissues. The goat-anti-rabbit secondary antibody conjugated with fluo 594 was added to react with the primary antibody. The immunofluorescence intensity signal was resulted from the binding of secondary antibody conjugated with fluorescence dye to anti-ProCA1 primary antibody. Compare the fluorescence intensity, ProCA1B14 bound to GRPR expressed by PC3 and H441 tumors. Some of ProCA1B14 were internalized in the cell. Overall, PC3 tumor showed fluorescence stronger staining than that of H441 tumor, which was consistent with the Gd^{3+} distribution studies by ICP-OES.

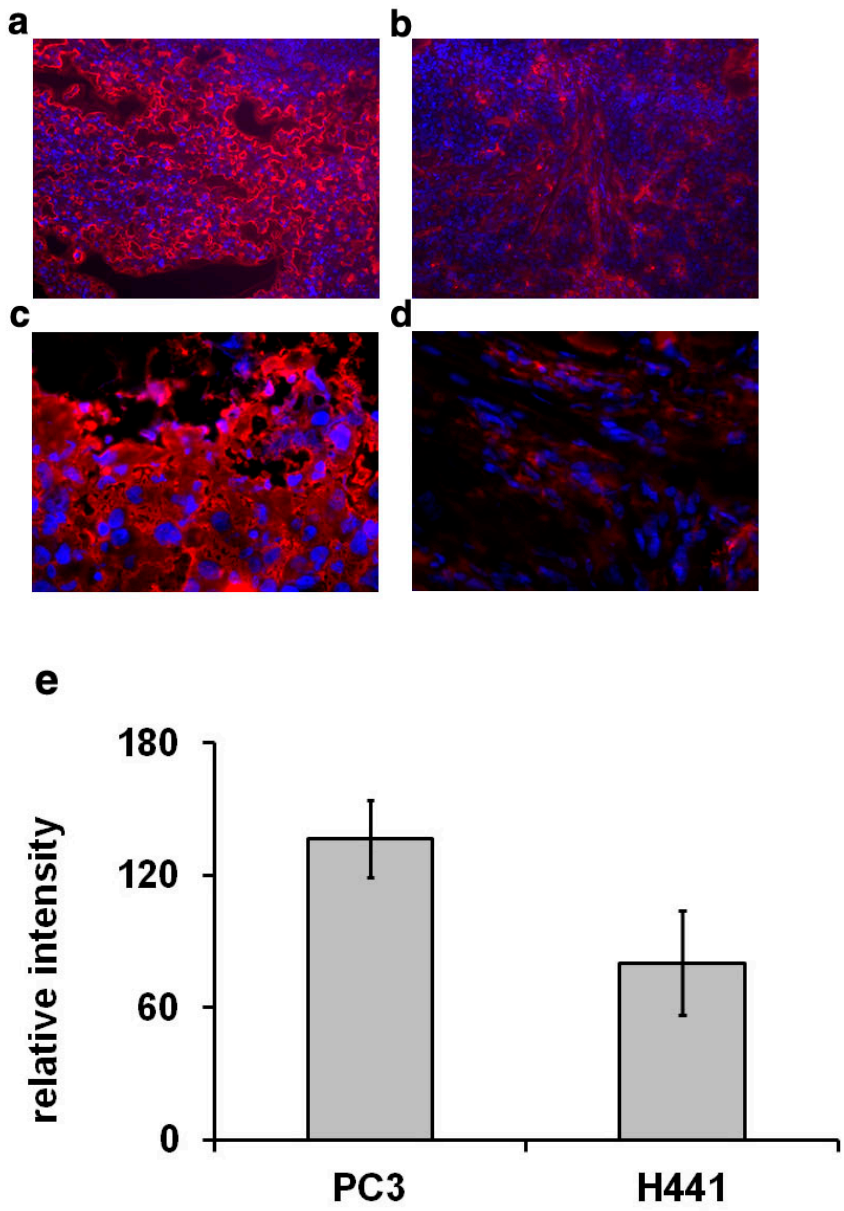

Figure 3.33 Immunofluorescence staining of ProCA1B14 target GRPR on tumor tissues. The red color indicates the staining of ProCA1B14 while the blue color represents nucleus staining. a and c show the IF staining of ProCA1B14 targeting GRPR on PC3 tumors magnified 10x and 40x respectively . b and d show the IF staining of ProCA1B14 targeting GRPR on H441 tumors magnified 10 x and 40 x respectively. e shows the comparison between the relative IF intensity of PC3 and H441 by Image J. The primary Ab (mouse anti-CD2 antibody OX-34) was

diluted at 1:500 ratios in 2.5% BSA and incubates at 4˚C overnight. Goat anti-mouse secondary antibody (red fluorescence) diluted at 1:1000 ratios in 2.5% BSA and incubates for 1h at room temperature.

3.2.13 IHC staining of GRPR expression on PC3 and H441 tumor in xenograft mice

To probe the distribution of ProCA1B14 and GRPR in the tumor tissues after MRI scan and further confirm the real binding between ProCA1B14 and GRPR exists, we did IHC staining. The mice with xenografted tumors were sacrificed and representative organs were immersed in flek O.C.T and fixed by liquid nitrogen. All the samples were stored at -80˚C. The cryosectioning was performed by cryostas (Biology facility, GSU). To identify the expression pattern of GRPR on PC3 and H441 tumor tissues, the primary antibody rabbit-anti-GRPR (diluted with 1:500) was added to the slides to react with the GRPR expressed on PC3 and H441 tumor tissues. The goat anti rabbit secondary antibody (diluted with 1:1000) was added to react with the primary antibody. The IHC intensity signal was coming from the interaction of secondary antibody binding to anti-GRPR primary antibody. As shown in Figure 3.34, the expression level of GRPR on PC3 is much higher than that of H441 which is consistent with the results on cell level (Fig. 3.34).

On the other hand, the anti-ProCA1 primary antibody was added to the sample slides and reacted with ProCAB14, which bound to GRPR and accumulated in the tissues. The goat-anti-rabbit secondary antibody (diluted with 1:1000) was added to react with the homemade rabbit-anti-ProCA1 primary antibody (diluted with 1:500). The IHC intensity signal was coming from the interaction of secondary antibody binding to anti-ProCA1 primary antibody. Comparing the IHC intensity, ProCA1B14 was found to bind to GRPR on PC3 and H441 tumors and some

of them were internalized in the cells. PC3 tumor showed stronger staining than that of H441 tumor which was consistent with the Gd^{3+} distribution studies by ICP-OES (Fig. 3.35).

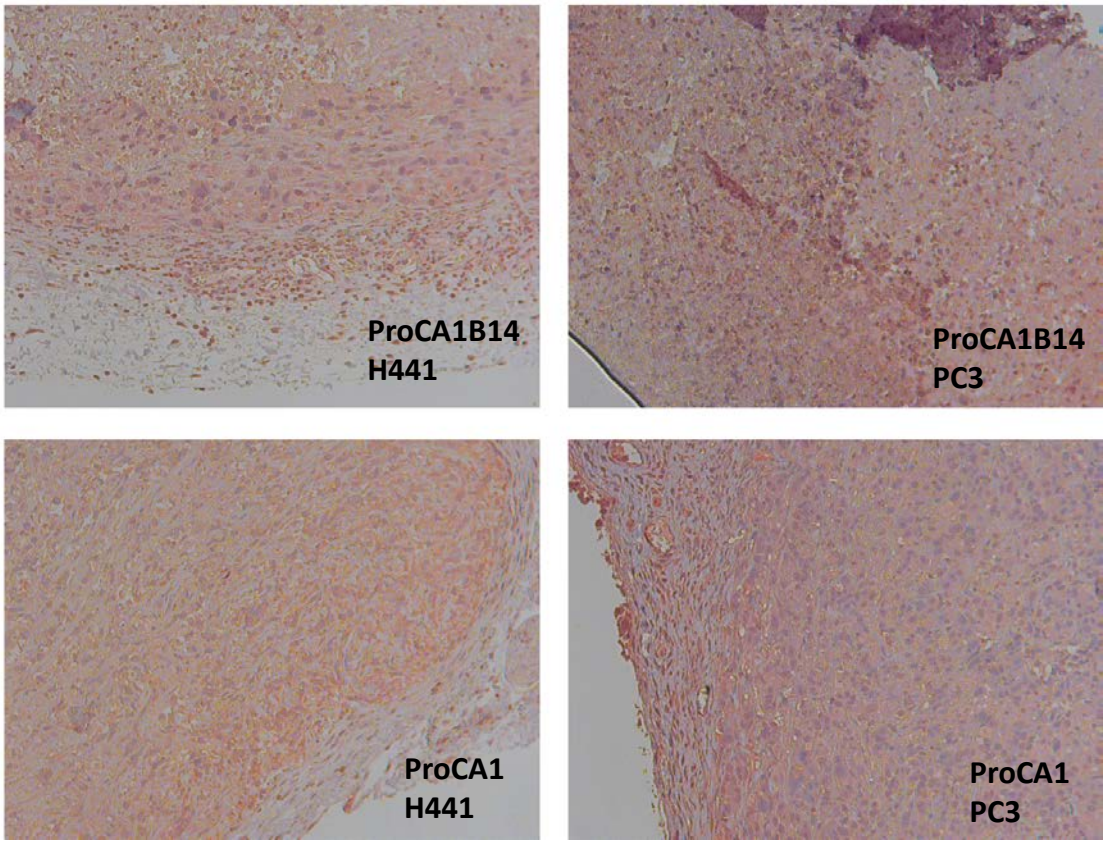

Figure 3.34 Immunohistological chemistry staining of GRPR on H441 (A, C) and PC3 (B, D) tumor from xenograft mice.

The tumor tissues are derived from tumor xenografted mice which injected with ProCA1 and ProCA1B14, respectively. A and B showed the GRPR expression on PC3 and H441 tumors from the mouse injected with ProCA1. C and D showed the GRPR expression on xenografted PC3 and H441 tumors from the mouse injected with ProCA1B14. In comparison with H441 tumors, GRPR shows stronger expression (red and brown color) on PC3 tumors. The primary Ab was

diluted at 1:500 ratios in 2.5% BSA and incubates at 4˚C overnight. Goat anti-mouse secondary antibody diluted at 1:1000 ratios in 2.5% BSA and incubates for 1 h at room temperature.

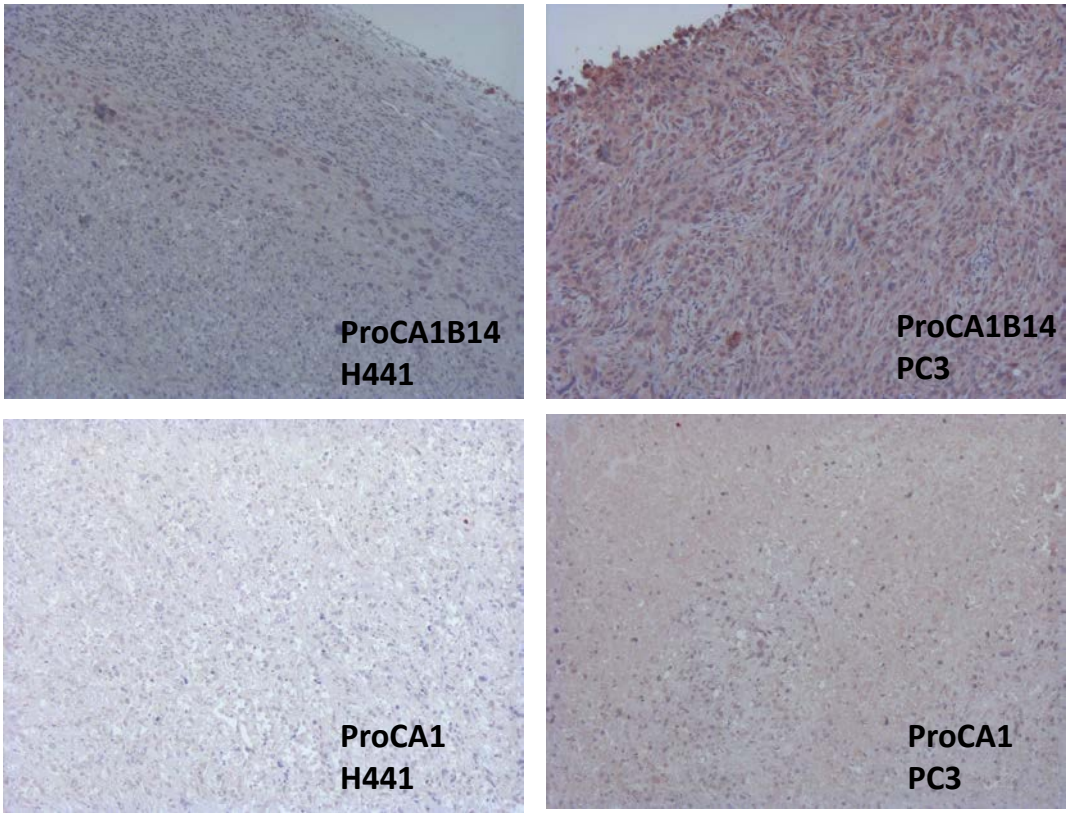

Figure 3.35 IHC staining of ProCA1 variants distribution in PC3 and H441 tumor tissues after injection of ProCA1 or ProCA1B14.

A. IHC staining of ProCA1B14 distribution in H441 tumor tissues after injection of ProCA1B14. B. IHC staining of ProCA1B14 distribution in PC3 tumor tissues after injection of ProCA1B14. C. IHC staining of ProCA1 distribution in H441 tumor tissues after injection of ProCA1. D. IHC staining of ProCA1 distribution in PC3 tumor tissues after injection of ProCA1. Consistent with MRI imaging, ProCA1 has low distribution in PC3 and H441 tumors. ProCAB14 has distribution

in both H441 and PC3 tumors and ProCA1B14 has higher distribution in PC3 tumors than that of H441 tumors. The primary Ab (mouse anti-CD2 antibody OX-34) was diluted at 1:500 ratios in 2.5% BSA and incubates at 4˚C overnight. Goat anti-mouse secondary antibody (red fluorescence) diluted at 1:1000 ratios in 2.5% BSA and incubates for 1h at room temperature.

3.2.14 H&E staining of PC3 and H441 tumor in xenograft mice

Hematoxylin and eosin (H&E) stain is a "golden standard" stain for medical diagnosis over a century. It has been widely used in clinical application for distinguishing various types of tissues and the morphological changes. It has been identified to work well with a series of fixatives and exhibits many important features such as cytoplasmic, nuclear and extracellular matrix [220]. The tumor tissues were derived from tumor xenografted mice which injected with ProCA1 and ProCA1B14, respectively. As shown in H&E staining, the morphological structure of xenografted PC3 and H441 tumors from the mouse injected with ProCA1 did not show any significant differences from that xenografted PC3 and H441 tumors from the mouse injected with ProCA1B14 (Fig. 3.36) .

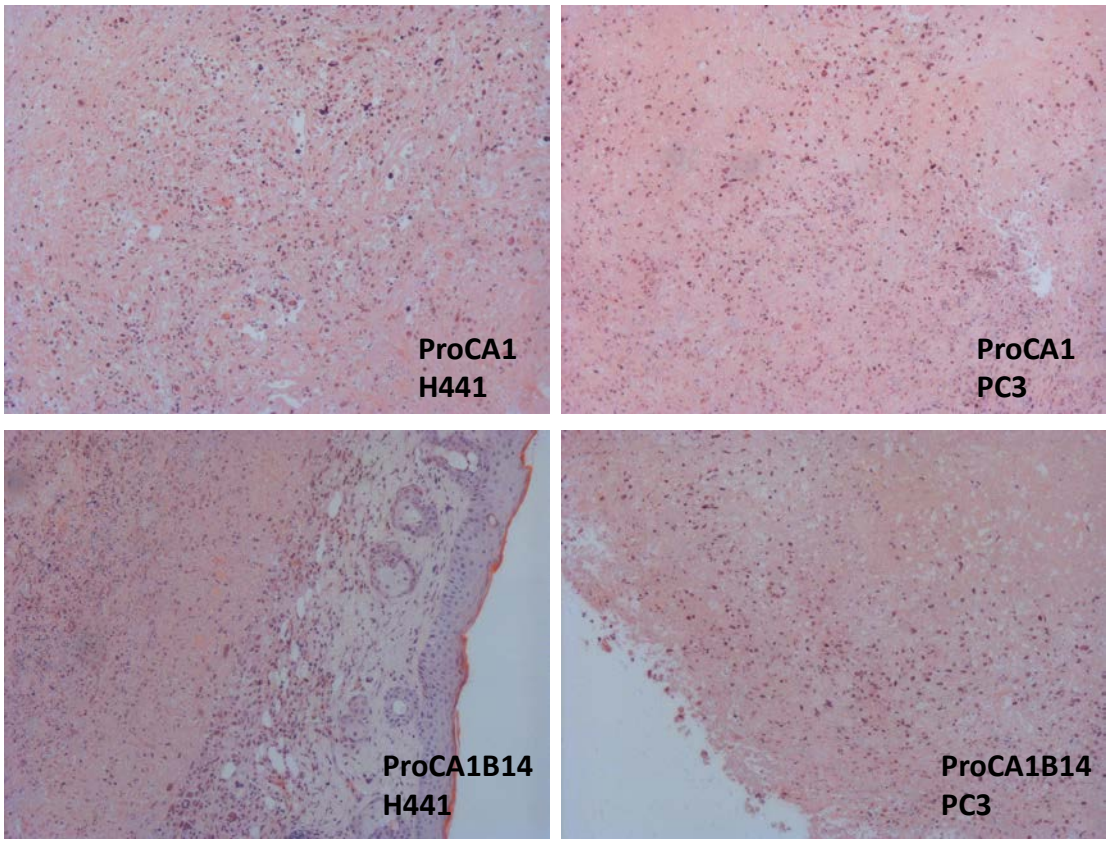

Figure 3.36 H&E staining of H441 (A, C) and PC3 (B, D) tumors from xenografted mice. The tumor tissues were derived from tumor xenografted mice which injected with ProCA1 and ProCA1B14, respectively. A and B showed the morphological structure of xenografted PC3 and H441 tumors from the mouse injected with ProCA1. C and D showed the morphological structure of xenografted PC3 and H441 tumors from the mouse injected with ProCA1B14.

3.2.15 Toxicity of ProCA1

3.2.15.1 Acute toxicity of ProCA1B14

To probe the clinical toxicity of ProCA1B14 in mice, we injected 0.025 mmol/kg PEGylated ProCA1B14 in normal mice and sacrifice the mice 2 days post injection. The blood was collected and sent to IDEXX Bioscience for toxicity study. Comparing the different pathological parameters of control mice and the mice injected with ProCA1B14, there is no differences in ASP, SGT, SGOT, BUN, creatinine, choleterol, gluoces, Ca^{2+}, Na^{+}, C^{l-}, PO^{3-}, CO_3^{2-}, albumin, total protein and globubin level between ProCA1B14 injected group and control group, indicating ProCAB14 has no toxicity to the mice post injection for 2 days**.** In comparison with normal mice, ProCA1B14 didn't show significant difference ($P < 0.05$) in acute renal and liver toxicity by *t*-test.

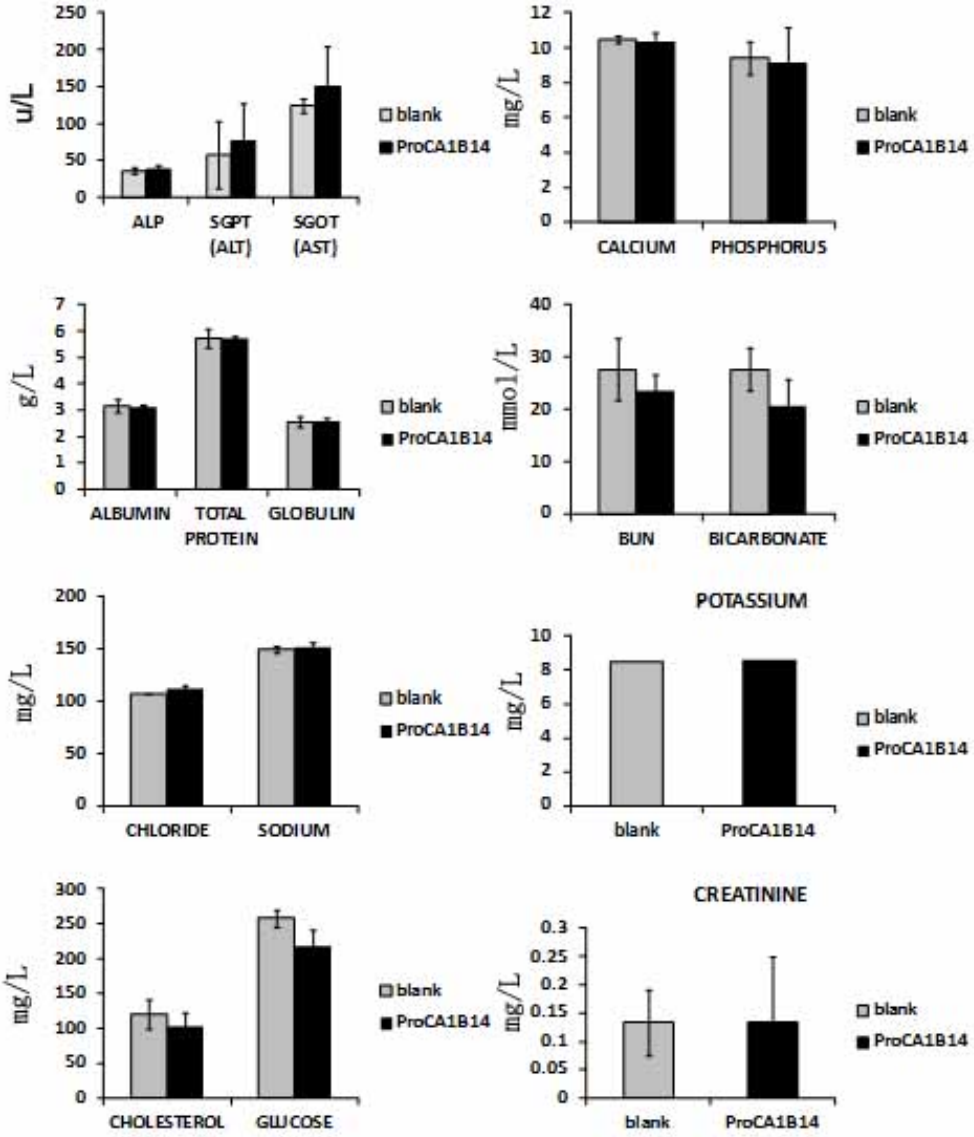

Figure 3.37 The acute toxicity study of ProCA1B14.

Blood chemistry test of the mice serum collected 2 days post injection of ProCA1B14 or saline (blank). There is no differences in ASP, SGT, SGOT, BUN, creatinine, choleterol, gluoces, Ca^{2+}, Na^{+}, C^{l-}, PO^{3-}, CO_3^{2-}, albumin, total protein and globubin level between ProCA1B14 injected group and control group, indicating ProCAB14 has no toxicity to the mice post injection for 2 days.

3.2.15.2 Pathological abnormality of ProCA1B14 in mice by HE staining

To probe the clinical toxicity of ProCA1B14 in mice, we injected 0.025 mmol/kg pegylated ProCA1B14 in CD1 mice and sacrifice the mice 2 days post injection. Different organs were separated and stained by H&E. (Fig. 3.38) Comparing the pathology of control mice and the mice injected with ProCA1B14 by Dr. Grossniklaus, we can conclude that there is no significant abnormal morphology. In comparison with normal mice, ProCA1B14 didn't show significant difference ($P < 0.05$) in acute renal and liver toxicity by student t-test.

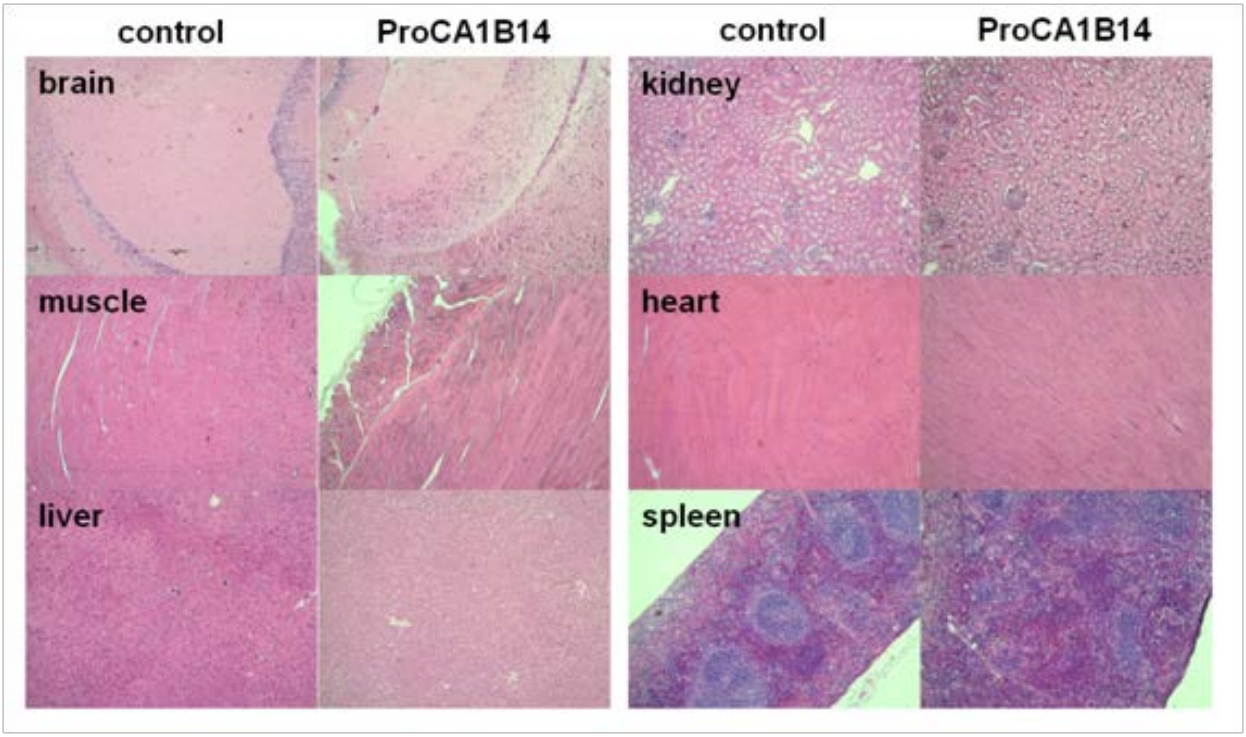

Figure 3.38 Toxicity study of ProCA1B14 in CD1 mice after 2 day injection of ProCA1B14 or saline.

Mice injected with saline were used as control group. H&E staining of mice organs was done after injection of saline (control) or ProCA1B14. These H&E staining images were evaluated by experienced pathologist Dr. Hans Grossniklaus. There are no pathological differences in any organ between control group and ProCA1B14 injected group.

3.2.16 Biodistribution of ProCA1B14 in mice measured by ICP-OES

After the MR and NIR imaging of mice with xenografted tumors, the mice were sacrificed. Tumor and various tissues were extracted and digested by 70% HNO_3 (Optima) to detect Gd^{3+} distribution in mice after 48 h injection by ICP-OES. From Fig. 3.35, we find that the concentration of Gd^{3+} in PC3 was much higher than that of H441, which was consistent with MRI data. However, Gd^{3+} was also found high in kidney and liver. Since both kidney and liver are important excretion and metabolic organs in the body, the contrast agents probably excrete out through both pathways. The feces and urine of the test mice were analyzed by ICP-OES and the results support this conclusion.

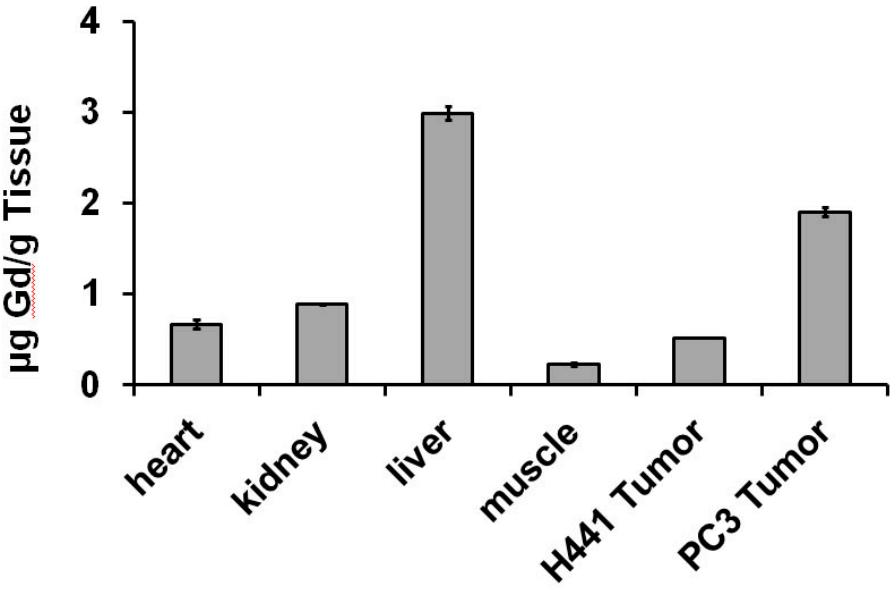

Figure 3.39 Gd^{3+} distributions in different mouse tissues detected by ICP-OES.

X-axis indicates different organs separated from the xenografted mice injected with ProCA1B14, Y-axis represents the distribution (concentrations) of gadolinium in different organs. Mice tissue and organs were collected two-day post injection of ProCA1B14. Mice tis-

sues were completely digested in 70% HNO_3. The samples were diluted in 4 ml and pass through 0.45 µm filter before ICP-OES analysis.

3.2.17 Pharmacokinetics of ProCA1B14

Seven serial plasma samples were obtained from the mice through one day post-ProCA1B14 injection. Those samples were assayed for total Gd^{3+} using an ICP-OES assay. In brief, a 0.5 ml sample of plasma was digested on a hot plate with 70% nitric acid. The amount of Gd^{3+} was determined with an ICP-OES by comparing the emission of the unknown sample to the emission of the external standard solutions. A set of calibration standards and QC samples (three concentrations each in duplicate) were included in each analysis session to generate a standard curve and to assess assay performance. A study about 0.03 mmol/kg ProCA1B14 in mice showed that the plasma concentration-time profile conformed to an open two-compartment model. ProCA1B14 concentration declined rapidly during distribution phase, ($t_{1/2\alpha}$) (0.48 hours) and more slowly during disposition phase, ($t_{1/2\beta}$) (8.61 hours). The mean total clearance was 6.6 $\pm$ 1.0 ml/h/kg. Total clearance values, Cl(t), and renal clearance Cl (r) values, increased with the dose of ProCA1B14. Total clearance and renal clearance are similar since urinary excretion was the main route of elimination of ProCA1B14. The mean terminal plasma half-life of ProCA1B14 did not vary remarkably with dose (range: 13.4 to 18.0 hrs). The steady-state volume of distribution, V_{dss}, tended to increase slightly with an increase in dose above 0.05mmol/kg. The V_{dss} (0.057 L/kg at 0.03 mmol/kg) indicates that ProCA1B14 was distributed to the extracellular space.

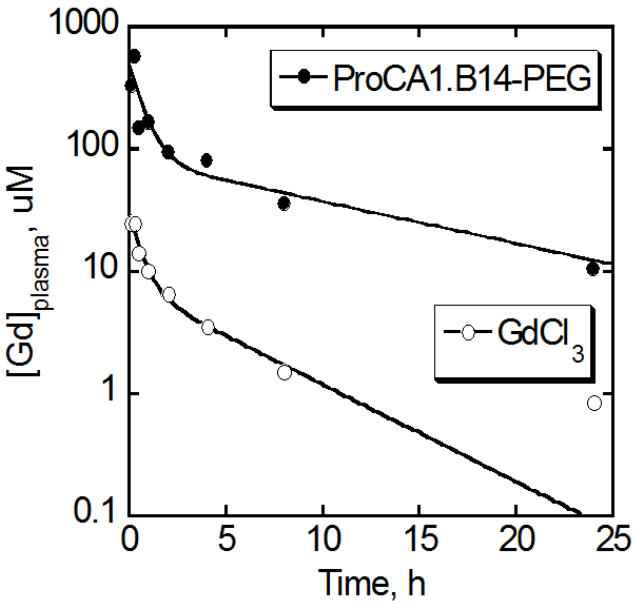

$$C_{p(t)} = ae^{-\alpha t} + be^{-\beta t}$$

$$Cp0 = a + b$$

$$C_{p_0} = \frac{D}{V_d}$$

$$V_{dss} = \frac{X_{ss}}{C_{pss}} = V_c + V_p = \frac{a\beta^2 + b\alpha^2}{(a\beta + b\alpha)^2} \bullet D$$

	ProCA1B14	$GdCl_3$
$t_{1/2}$, α	28.88 min	25.18 min
$t_{1/2}$, β	8.79 h	3.78 h
V_c	0.00832 l/kg	0.14 l/kg
V_{dss}	0.031 l/kg	0.32 l/kg

Figure 3.40 Pharmacokinetic studies of PEGylated ProCA1B14 and $GdCl_3$ by ICP-OES.

The blood of mice were collected at different time points post injection of ProCA1B14 or $GdCl_3$. These blood samples were completely digested in 70% HNO_3. The samples were diluted in 4 ml and pass through 0.45 µm filter before ICP-OES analysis. The pharmacokinetics of ProCA1B14 and $GdCl_3$ were characterized by fitting two-compartment model. ProCA1B14 has a distribution half-life of 28.88 min, elimination half-life of 8.79 h. The value of volume distribution indicates that ProCA1B14 is mainly distributed in the blood vessel and extra vascular space of central organs such as liver and kidney.

3.3 Discussion

Development of MRI contrast agents for molecular imaging of cancer biomarker is an attractive and challenging field. Non-invasively obtaining the biomarker expression level in cancer biomarkers, especially prognosis biomarkers, are of great importance for the early diagnosis and evaluation of cancer. Imaging biomarker could be also extremely helpful to follow the treatment effect of disease. MRI with high resolution, high depth penetration, and three-dimensional imaging capability, is the most desired imaging modality for the molecular imaging of biomarkers. However, molecular imaging of biomarkers by MRI has several challenges. First, MRI has low contrast between tissues and organs. Improving the contrast between tissues requires injection of high amount of the MRI contrast agents. However, the low relaxivity and low sensitivity of clinical MRI contrast agents requires 0.1 mM local concentration to show the differences of MRI among organs. Such high concentration requirement made molecular imaging extremely difficult by the injection of small molecule-based MRI contrast agents. In order to improve the sensitivity of the contrast agents and decreased required local concentration of contrast agents for molecular imaging by MRI, a MRI contrast agent with high relaxivities is strongly needed. Second, clinical MRI contrast agents don't have cancer biomarker targeting moiety. In order to imaging cancer biomarkers with high specificity, MRI contrast agent should incorporate a cancer biomarker targeting moiety which can target cancer biomarkers with high affinity and selectivity. Third, since free Gd^{3+} is toxic, MRI contrast agents should have good stability and metal selectivity to prevent *in vivo* releasing of Gd^{3+} from MRI contrast agents. Forth, since the distribution of the cancer biomarkers varies, MRI contrast agents should have

an optimized tissue penetration, pharmacokinetics to assess these biomarkers. Fifth, an efficient, optimized and reproducible approach to produce these contrasts agents is required.

We developed a novel protein MRI contrast agent to image gastrin-releasing peptide receptor (GRPR). To overcome above challenges for the molecular imaging of GRPR, we carefully designed the protein contrast agents and evaluated its properties. In this chapter, we reported the design, ProCA expression, purification, Gd^{3+} binding affinity, metal selectivity, and relaxivity of novel GRPR targeting protein MRI contrast agents. We evaluated the *in vitro* and *in vivo* GRPR binding property on cellular and tissue levels. We also reported the *in vivo* MR imaging and NIR imaging of GRPR in xenografted mice model. The Gd^{3+} distribution, short-term toxicity and pharmacokinetics were also investigated.

3.3.1 Molecular mechanism of ProCA1 variants interact with GRPR with binding affinities, high metal binding affinities and relaxivities predicted by HADDOCK

To image GRPR expression level by MRI, high GRPR binding affinity is required. The peptide ligand, angonist and antagonist of GRPR are well studied and well documented in the literature [135], while the binding affinity of these peptide ligands linked to proteins are not well studied yet.

GRPR belongs to the family B of bombesin receptor. Its nature peptide ligand, GRP, binds to GRPR with sub-nanomolar affinity. 7-10 amino acids at C-terminal of GRP were reported to bind to GRPR with similar affinity. Other mammalian peptides, such as neuromedin B, BRS-3, also binds GRPR, but the binding affinity is much lower than that of GRPR.[135] Interestingly, an amphibian peptide, named bombesin, shows higher affinity to GRPR than that of GRP. The full lengh bombesin peptide has affinity to GRPR around 2 nM. Similar to GRP, the C-

terminal 7-10 amino acids peptide, also binds to GRPR with reduced affinity. By comparing the reported affinity of different natural peptide ligands to GRPR, we found that full length bombesin has the strongest affinity to GRPR.

Our lab developed the grafting approach to insert peptide in the middle of the domain 1 of rat CD2 with flexible linker. Previously work in our lab has shown that inserting peptide in domain 1 of CD2 does not alter the structure of domain 1 of CD2 and inserted peptide can maintain their structure and function [185]. In addition, the serum stability of the peptide inserted in the scaffold protein was significantly improved [139]. Thus, in current work, we also inserted GRPR-targeting peptide in the middle of ProCA1 using grafting approach. We hypothesize that insertion of GRPR-targeting peptide in the ProCA1 by grafting approach can better function as GRPR-targeting moiety than peptide itself because of the well-maintained structure, function (targeting properties) and improved *in vivo* stability.

In addition, we inserted full length of bombesin, 10 amino acids peptide from C-terminal of bombesin or 10 amino acids peptide from C-terminal of GRP in ProCA1 by using the grafting approach, named ProCA1B14, ProCA1B10, ProCA1G10, respectively. Since full length bombesin has the highest binding affinity than C-terminal GRP or C-terminal bombesin, we hypothesize that ProCA1 inserted with full length bombsin has the highest affinity among these three designs.

We first tested our hypothesis using the computational approach. The modeled structure of GRPR, ProCA1B14, ProCA1B10, and ProCA1G10 were generated by I-TASSER. The interaction between ProCA1 variants to GRPR were modeled by HADDOCK. The key residues from GRPR (Ala2, Leu3, Asn4, Leu9, Asp14, Phe16, His18, Cys19, and Asn20), reported to influence

the binding affinity of GRPR to their ligands, and inserted bombesin or GRP peptide in ProCA1, were used as key residues for the interaction. As shown in HADDOCK, ProCA1B14 has the lowest binding energy to GRPR indicating that ProCA1B14 could be the best candidate for the GRPR imaging. We also determined the GRPR binding affinity of different ProCA1 variants by scatchard plot and evaluated the GRPR binding properties of different ProCA1 variants using cell imaging. Consistent with our hypothesis and docking analysis, ProCA1B14 shows the best GRPR targeting capability among different ProCA1 variants. Thus, ProCA1B14 is the best candidate for the molecular imaging of GRPR due to the highest GRPR binding affinity.

3.3.2 Protein expression and purification affected by experimental conditions

A right competent cell strain is critical for the recombinant protein expression. BL21 has been reported to be most widely used for recombinant protein expression based on its deficient in both Ion and ompT protease. DE3 means the host is a lysogen of λDE3 and has the phage T7 RNA polymerase gene which is controlled by the lacUV5 promoter. This promoter is an IPTG-inducible promoter and used for expressing proteins whose genes cloned in pET vectors. The plysS means the plasmid carries T7 lysozyme, an inhibitor of T7 RNA polymerase. BL21(DE3)plysS competent cell strain have an advantage for repressing basal expression of T7 RNA polymerase prior to IPTG induction and help stabilize the expression of recombinants proteins which affect the cell growth and viability. Tuner strain is also generated from BL21 cell strain in which lacZY is deleted. The lac permease (lacY) is mutated to affect the entry of IPTG to all the cells which lead to the homogenous expression of recombinant proteins is IPTG concentration dependent. [221]

Temperature is also an important factor which affects the growth of *E.Coli* competent cells and the yield of recombinant target proteins. As the data shows, after IPTG induction, the proteins expressed at lower temperature (25°C-30°C) experienced less degradation than those expressed at 37°C when the induction time is same. If the expression temperature was kept at 37°C, lower the induction time from overnight to 3h is more suitable to improve the yield of the target protein expression. In addition, the concentration of IPTG from 0.1 mM to 1 mM didn't show significant effects on the yield of protein expression. The possible reason is 0.1mM IPTG is totally enough to induce the protein expression and thus elevate the concentration of IPTG couldn't improve the effect. If we decrease the concentration to lower than 0.1 mM IPTG, the concentration dependent expression may occur.

Q column is a strong anion exchange column, which can be used for protein purification. ProCA1 variants are negatively charged at pH 8.0 in the buffer A which allowed them bind to Q column. As the percentage of the buffer B increased, the concentration of sodium chloride increased and free chloride ions compete with the sephorase packed in Q column with ProCA1 variants which lead to the protein gradually wash out from the Q column. (Fig. 3.14) The separation rate depends on the charge over pH value of different proteins. SP column is a strong cation exchange column which can be used for high-resolution, small-scale protein purification. ProCA1 variants are positively charged at pH 4.0 in the buffer A which allowed them bind to SP column. As the percentage of the buffer B increased, the pH value of the proteins changed from positive charge to negative charge which lead to the protein gradually wash out from the SP column. The separation rate depends on the charge over pH value of different proteins. Both Q column and SP column have high loading capacities over broad pH ranges. Although ProCA1

variants can be purified by both Q column and SP column, we inclined to purify them with Q column considering the low pH may cause the instability of the protein.

3.3.3 The advantage and disadvantage of tagless- and GST- fusion protein purification methods

In *E. Coli* competent cells, recombinant proteins usually expressed too fast to fold well, so they inclined to deposit as misfolded aggregates without any biological activity in the inclusion body. This part of protein can be recovered by denaturing and refolding method which is identified as a useful method for disulfide bond-containing protein purification. Inclusion body purification, the advantage is its high expression levels, high purity, allowance of toxic proteins expression and protection from proteolytic enzymes. However, this method is limited by its complicated purification process and optimal conditions cannot be predicted. GST-fusion protein purification is another kind of strategy. Glutathione S-transferase (GST) is an enzyme containing 220 amino acid residues. The target protein was fused with glutathione S-transferase (GST) which can help the target protein fold well in a soluble form. GST-tagged protein purification is based on the high affinity of GST to glutathione. When the GST-fused proteins were applied to the prepacked GSTrap column, they bind to the glutathione ligand and those unbound impurities were washed away with the binding buffer. Thrombin was added to remove the GST tag while the target protein was eluted out by PBS buffer. GST-tagged protein purification can produce more pure target proteins than the tagless method, but it still has its own disadvantage. First of all, the yield of GST-tagged protein is much lower than that was purified by the tagless method. It depends on the capacitiy of the GSTrap column. Second, GST-tagged protein is easily cleaved by protease existing in the cell lysis buffer which exhibit as multiple bands on

the SDS-PAGE. Third, sonication conditions should be milder to prevent the co-purification of host proteins with the target protein.

3.3.4 Metal binding affinity and selectivity of ProCA1 variants can be determined by dye competition methods

ProCA1 is a rational designed protein-based MRI contrast agent. We created a Gd^{3+}-binding pocket on the domain 1 of rat CD2 (CA1.CD2) by using the six potential oxygen ligands (Glu15, Glu56, Asp58, Asp62, and Asp64) from the carboxyl side chains to chelate free Gd^{3+}. As mentioned in Dr. Jenny Yang's paper [212], the five negatively charged residues are located in the coordination shell and provide six oxygen ligand atoms to chelate Gd^{3+}. As shown in Table 3.3 [212], these ligands not only have the metal binding affinity but also exhibit their unique metal selectivity, such as Gd^{3+} over physiological ions Ca^{2+}, Zn^{2+} and Mg^{2+}. Compared to the commercial MRI contrast agents DTPA and DTPA-BMA, the metal selectivity is better which is important for the *in vivo* application.

Table 3.12 Metal Binding Constants (log Ka) and Metal Selectivity of DTPA, DTPA-BMA, and CA.CD2, adapted from reference [137].

Table 1. Metal Binding Constants (log K_a) and Metal Selectivity of DTPA, DTPA-BMA, and CA1.CD2

sample	Gd^{3+}	Zn^{2+}	Ca^{2+}	Mg^{2+}	log (K_{Gd}/K_{Zn})	log (K_{Gd}/K_{Ca})	log (K_{Gd}/K_{Mg})
DTPA[40]	22.45	18.29	10.75	18.20	4.17	11.70	4.25
DTPA-BMA[49]	16.85	12.04	7.17	na[a]	4.81	9.68	na[a]
CA1.CD2	12.06	6.72	<2.22	<2.0	5.34	>9.84	>10.06

[a] na: not available.

ProCA1 variants including ProCA1B14, ProCA1B10 and ProCA1G10 are generated based on ProCA1 with additional GRPR targeting properties. These targeting peptides were grafted on flexible linker GGSGG on ProCA1 between Ser52 and Gly53, respectively. The grafting approach is helpful to maintain the tertiary structure of peptide well and protect it from proteolysis [139]. Although the structure of ProCA1 is very rigid [212], we still want to confirm whether the new design affects the metal binding affinity and metal selectivity of the ProCA1 variants in consideration of introducing relatively flexible moiety to the protein. Since the Gd^{3+} binding affinity of ProCA1 cannot be determined directly, we select dye competition assay to calculate it. Fluo-5N is a fluorescence dye, which can bind to Gd^{3+} and generate fluorescence signal. We mixed Fluo-5N with Gd^{3+} at 1:1 ratio and titrated different concentrations of ProCA1 variants to compete Gd^{3+} with the dye. Once the Gd^{3+} transferred from Fluo-5N to ProCA1, the fluorescence signal decreased. As shown in Fig. 3.19, ProCA1 has the Gd^{3+} binding affinity of 8.7×10^{-13} M, while ProCA1B14, ProCA1B10 and ProCA1G10 have the Gd^{3+} binding affinity of 2.1×10^{-12} M, 5.1×10^{-12} M and 1.3×10^{-12} M, respectively. This result indicates the ProCA1 variants keep the comparable Gd^{3+} binding affinity to the ProCA1, which wasn't affected by introducing targeting moieties.

The Zn^{2+} binding affinity of ProCA1B14, ProCA1B10 and ProCA1G10 is 2.4×10^{-8}, 2.3×10^{-8}, and 5.3×10^{-8}M, respectively by dye competition assay as well. To measure the Zn^{2+} binding affinity of ProCA1 variants, we did the competition with Fluozin-1, a Zn^{2+} binding fluorescence dye. As shown in Fig. 3.20, ProCA1B14, ProCA1B10 and ProCA1G10 have the Zn^{2+} binding affinity of 2.4×10^{-8},2.3×10^{-8}, and 5.3×10^{-7} M, respectively. Meanwhile, ProCA1 has Zn^{2+} binding affinity of 1.9×10^{-7} M.[212] This result suggests the ProCA1 variants keep the comparable Zn^{2+} binding affinity to the ProCA1 which wasn't affected by the introducing peptide. In addition,

the results suggest the metal selectivity of ProCA1 variants (ProCA1B14, ProCA1B10 and ProCA1G10) is as good as ProCA1.

The metal selectivity between Gd^{3+} and Zn^{2+} is one of the perimeters to evaluate the stability of MRI contrast agents *in vivo*. Physiological metal ions, such as Zn^{2+} or Ca^{2+} can function as a competitor to occupy the Gd^{3+} binding sites in contrast agents, which cause free Gd^{3+} release. Thus, a good MRI contrast agent should have high Zn^{2+} selectivity and low Zn^{2+} affinity. ProCA1B14 has Zn^{2+} selectivity about 4.1, which is also comparable with that of ProCA1. Such high metal selectivity and low Zn^{2+} affinity suggest that ProCA1 variants should have low Gd^{3+} release by Zn^{2+} competition.

3.3.5 High Relaxivity plays an important role in the molecular imaging and relaxivity is affected by protein design

Relaxivity is a parameter of MRI contrast agent used to describe the capability of enhancing the contrast between different tissues based on water protons under MRI scanner. Since the relaxivity signal is coming from water protons existing in different organs indicating that the signal can be easily disturbed by the background water. Relaxivity is positively related to the sensitivity of MRI scanning. In other words, high relaxivity leads to increase in the sensitivity of MRI scan at a low concentration level of contrast agent and provide a prerequisite for the molecular imaging at cellular level. Relaxivity of the current clinically available MRI contrast agents are in the range of 4 - 6 $mM^{-1}s^{-1}$ much lower than the theoretical upper limit 100 $mM^{-1}s^{-1}$. Our developed protein-based MRI contrast agent optimized τ_R, q and 2^{nd} sphere water and successfully improved the relaxivity up to 117 $mM^{-1}s^{-1}$ which is around 10 times higher than that of the commercial one. As a recent simulation of relaxivity and detection limits reported, when

the r_1 relaxivity per Gd^{3+} is 5, 20 or 100 $mM^{-1}s^{-1}$, the *in vivo* detection limits are 10, 4 or 0.69 µM, respectively.[176, 222] This simulation further proved that the optimized relaxivity significantly improved the detection limits *in vivo* compared to the commercial one at the same injection dosage. To achieve the molecular imaging at receptor level, the contrast agent should possess two important characteristics, high sensitivity and high specificity. Since specificity mainly depends on the targeting moiety such as antibody or peptide binding ligand, sensitivity provides another kind of support. As papers reported, when the r_1 relaxivity per Gd^{3+} is 5, 20 or 100 $mM^{-1}s^{-1}$, the *in vivo* detection limits are 10, 4 or 0.69 µM, respectively. [176, 222] Thus, this is the major reason why the traditional contrast agent with low relaxivity can't achieve molecular imaging at cellular level.

Similar to ProCA1, the GRPR-targeted ProCA1 variants also have high relaxivities. The per Gd^{3+} relaxivity for ProCA1B14, ProCA1B10,ProCA1G10 are 41.2 ± 3.1, 47.5 ± 0.1, 49.2 ± 0.2, respectively, which indeed has around 10 times higher r1 relaxivity than that of clinical MRI contrast agents. Because of this reason, ProCA1 variants have at least 10 times improved sensitivity than that of clinical MRI contrast agents. Such high relaxivity serve as basics for the molecular imaging cancer biomarkers such as GRPR.

In addition, ProCA1 variants also have high r2 relaxivities. The r2 relaxivity for ProCA1 variants varies from 79 to 92 $mM^{-1}s^{-1}$. Such high r2 relaxivity made ProCA1 variants promising to function as T2-weighted MRI contrast agents.

3.3.6 ProCA1B14 shows high GRPR targeting capability

GRPR is an important biomarker for many types of cancers, such as prostate cancer, breast cancer and small cell lung cancer.[139] High GRPR expression were detected in these

cancers, while GRPR has low expression in most normal tissues. Thus, GRPR became an ideal biomarker for the imaging these cancer.

The GRPR expression level in different types of tumor cells were tested using different methods, including western blot, ELISA and Scatchard plot. Consistent with literature report, PC3 cells has high GRPR expression and H441 has low GRPR expression in cultured cells and xenograft tumor model. The maximum binding sites per cell (B_{max}) were determined by Scatchard plot. PC3 has a B_{max} of 3.5×10^5 receptors/cell and H441 has 2.6×10^4 receptors/cell.

GRPR binding affinity to GRPR-targeted ProCA1 variants were also determined by Scatchard plot. Interestingly, three GRPR-targeted ProCA1 variants show different GRPR binding affinity at nM and sub nM level. (Fig. 3.24) Consistent with our *in silicon* evaluation, ProCA1B14 shows the highest GRPR binding affinity (2.7 nM), while ProCA1G10 shows the lowest GRPR binding affinity (15.4 nM). Such high GRPR binding affinity for ProCA1B14 than other variants could be caused by three major reasons. First, full length bombesin peptide reported to have a higher affinity than that of GRP to GRPR. Jensen et al. reported that GRP has an affinity to GRPR of 18 nM, while bombesin has an affinity to GRPR of 4 nM. [135] Thus, after inserting different length or type of GRPR targeting peptides in ProCA1, full length bombesin could also show better targeting properties than that of C-terminal bombesin or GRP. Second, docking results shows that ProCA1B14 has a lowest energy to bind GRPR than that of other two ProCA1 variants. Thus, ProCAB14 has a higher GRPR binding affinity because of the lowest energy. Third, full length bombesin in ProCA1B14 could provide the native confirmation to mimic the real interaction between GRPR and peptide ligand. However, possibly because of shorter peptide in ProCA1B10 and ProCA1G10, the molecular interaction between GRPR and targeting peptide

grafted in these two peptides is insuffient, which cause the decreased GRPR binding affinity. Since ProCA1B14 has the highest GRPR targeting properties, we use ProCA1B14 to perform the following *in vivo* study.

3.3.7 Molecular imaging of GRPR expression in mice

Molecular imaging is an advanced imaging technique, which refers to non-invasive image biomarker at cellular and molecular level using contrast agents. In addition, imaging prognosis biomarkers could be very useful to non-invasively predict disease development and to follow the drug treatment. However, most biomarkers usually have very limited expression levels at nM or pM level, which requires highly sensitive and selective contrast agents to visualize them. Mainly because of the high sensitivity of PET and SPECT, molecular imaging of disease biomarkers is mainly developed for PET and SPECT imaging.

On the other hand, MRI is a promising imaging technique for molecular imaging because it has the extremely high resolution and high depth penetration. MRI is also a routine clinical diagnosis method widely distributed in almost every major hospital in USA, while the number of PET and SPECT scanners are much limited. Besides, MRI does not use radioactive isotopes, thus could be considered much safer than PET and SPECT. Unfortunately, the molecular imaging using MRI is lack of the good contrast agents with high sensitivity. Because of the low relaxivity, clinical MRI contrast agents can only show the obvious contrast difference when the local concentration reached to sub-mM. Since most biomarkers have a local concentration less than μM and even lower to the pM, it is impossible to detect these biomarkers using clinical MRI contrast agents. In addition, most clinical MRI contrast agents do not have biomarker targeting

moieties, which also made them impossible to target these biomarkers for the molecular imaging.

We developed protein-based MRI contrast agents to overcome the limitation of molecular imaging by clinical MRI contrast agents. In this chapter, we use molecular imaging of GRPR as an example to demonstrate the capability to image biomarkers using ProCA variants.

In vitro study shows that ProCA1B14 is the best candidate for the molecular imaging of GRPR because of its high relaxivity, high metal selectivity and high GRPR binding affinity. Besides, ProCA1B14 has a size of 2 -3 nm, which allows high tissue penetration and high excretion. In addition, since ProCA1B14 has about 10 times higher relaxivity than that of clinical MRI contrast agents, ProCA1B14 could be much more sensitive than clinical MRI contrast agents. Furthermore, GRPR has high receptor-mediated endocytosis [223], which could also accumulate contrast agents to achieve high local concentration.

Interestingly, ProCA1B14 not only can enhance the tumor through the interaction with GRPR, but also semi-quantitatively enhance the tumor at different intensity levels based on the GRPR expression level differences in different tumors. GRPR high expression cells (PC3, B_{max} = 3.9 x 10^5 receptor/cell) and GRPR low expression cells (H441, B_{max} = 2.1 x 10^4 receptor /cell) were implanted on the left and right flank of the mice. After injection of ProCA1B14 for 2 days, PC3 tumor doubled the percentage of intensity increase than that of H441 tumors. The Injection of ProCA1 without GRPR targeting peptide result in no significant enhancement of MRI signal in both PC3 and H441 tumor, which further proves that the MRI enhancement in tumors after ProCA1B14 injection is not caused by non-specific accumulation of the contrast agents in tumor tissue. Taken together, our results strongly show that ProCA1B14 is a superior MRI con-

trast agent for the molecular imaging of GRPR in cancer. Since GRPR is also a biomarker for itch [224], ProCA1B14 could be also applied for the molecular imaging of GRPR in itching. Furthermore, our work demonstrates that molecular imaging of cancer biomarker is achievable by MRI with good contrast agents, which has high relaxivity, high biomarker targeting capability, optimized pharmacokinetics and high tumor tissue penetration. The success of imaging GRPR by targeted ProCAs also allowed us to speculate that other cell surface disease biomarker can be imaged by targeted ProCAs after replacing GRPR targeting peptide to other peptides with high affinity to these biomarkers.

3.3.8 ProCA1B14 has low toxicity

The potential toxicity of the contrast agents could be caused due to either free Gd^{3+} or the chelator. Free Gd^{3+} is toxic with a LD_{50} = 0.2 mmol/kg. [225]For proteins, additional immunogenicity and toxicity need to be carefully evaluated. The toxicity of ProCA1B14 was evaluated by blood chemistry test. The results confirm that ProCA1B14 has no short-term toxicity to mice liver, kidney, metabolism, and circulation system. The H&E staining of the tissues, such as brain, muscle, heart, spleen, kidney and liver were further examined by experienced pathologists, confirm that injection of ProCA1B14 did not cause any tissue damage in mice. ProCA1B14 has a dramatic different pharmacokinetics compared with $GdCl_3$ and Gd-DTPA. ProCA1B14 has a half-life of 8 hours and mainly distributed in the blood, liver and kidney with good elimination. In summary, ProCA1B14 has good pharmacokinetics and no short-term toxicity in mice.

3.4 Conclusion

GRPR is an important biomarker for many types of cancers, such as prostate cancer, small cell lung cancer, and breast cancer. There is a huge need to develop non-invasive approach to evaluate GRPR expression level using imaging methods. Although MRI is the one of the ideal imaging modalities for disease diagnosis, the application of MRI for the molecular imaging of cancer biomarker is limited by the lack of good MRI contrast agents with high relaxivity, high sensitivity, high metal stability and strong targeting affinity and specificity.

We developed GRPR-targeting MRI contrast agents by inserting different GRP/bombesin peptides into the middle of ProCA1 using grafting approach. Since the full length bombesin peptides are reported to have the strongest GRPR binding affinity among different GRPR-targeting peptides, we hypothesize that full length bombesin grafted in ProCA1 also shows the highest GRPR binding affinity compared with that of other peptides grafted in ProCA1. Our primary docking study confirmed our hypothesis that ProCA1B14 has the lowest binding energy and highest binding affinity among all design GRPR-targeting ProCA1 variants. We further tested this hypothesis using Scatchard plot and cell imaging.

The expression and purification conditions for ProCA1 variants were optimized. The optimized condition for ProCA1 variants expression was expressing ProcA1 variants with *E.Coli* BL21DE3 competent cells at 25°C post 0.5 mM IPTG induction overnight. The optimized conditions of ProCA1 variants purification are as follows: First, the inclusion body should be washed by 1% triton as many times as possible till the color turns to white. Second, the washed inclusion body should be dissolved in 8 M urea and those insoluble impurities were removed by centrifuge. Third, during the refolding processes, the concentration of urea must be decreased

slowly to prevent protein misfolding. Besides, we improved the FPLC protocol for ProCA1 variants purification. Instead of using SP column elution based on pH gradient change, we used HiTrap Q column and proteins were eluted with the increasing salt percentage in the elution buffer. Such improvement help the protein to maintain the right structure at constant pH and avoid pH induced denaturing or the conformation change. The final yield of the protein using this optimized procedures are 50 - 100 mg /L LB medium depending the expression level of the proteins in the bacteria.

Similar to ProCA1, GRPR-targted ProCA1 variants showed strong Gd^{3+} binding affinity. The Gd^{3+} binding affinity of these GRPR-targeted ProCA1 variants is around 10^{-13} M. On the other hand, GRPR-targeted ProCA1 variants showed much weaker Zn^{2+} binding affinity at 10^{-7} -10^{-8} M level and good metal selectivity of Gd^{3+} over Zn^{2+}. These data suggest that GRPR-targeted ProCA1 variants forms stable complex with Gd^{3+} *in vitro* and *in vivo*.

In addition, ProCA1 variants have 10 times higher r1 relaxivities than that of clinical MRI contrast agents, such as Gd-DTPA. Such high relaxivities indicate that ProCA1 variants have much lower detection limit and much higher sensitivity than that of clinical MRI contrast agents. ProCA1 variants also have high r2. Such property suggests that ProCA1 can be used as T2-weighted MRI contrast agents.

The *in vivo* properties of GRPR-targeted ProCAs were evaluated in this chapter. GRPR-targeted ProCAs shows strong GRPR binding affinity in nM and sub nM level. Among three contrast agents, ProCA1B14 showed the highest GRPR binding affinity (2.7 nM). ProCA1B14 also shows the highest enhancement in the fluorescence imaging. We also established an ELISA-Scatchard plot method to determine the B_{max} and binding affinity of GRPR to ProCA1 variants.

Consistent with literature, our ELISA- Scatchard Plot method demonstrate that PC3 has a B_{max} of 3.9×10^5 and H441 has a B_{max} of 2.1×10^4. MRI of xenografted mice implanted with PC3 and H441 tumors shows the semi-quantitative enhancement of both tumors and because of high GRPR expression in PC3 cells, PC3 tumor has double enhancement than that of H441 tumors. ProCA1B14 has good pharmacokinetics and no toxicity in mice. Thus, ProCA1B14 is a promising MRI contrast agent for the molecular imaging of GRPR. The success of imaging GRPR by target-ed-ProCAs also allow us to speculate that other cell surface disease biomarkers can be imaged by targeted ProCAs after replacing GRPR-targeting peptide to other peptides with high affinity to these biomarkers.

In summary, we designed GRPR-targeted ProCA1 variants by the grafting approach. The-se ProCA1 variants show strong Gd^{3+} affinity, high metal selectivity, and high relaxivity. We also optimized the expression and purification conditions of these ProCA1 variants. In addition, we will report their high GRPR-targeting capability. These properties made GRPR-targeted ProCA1 variants promising to be applied for the molecular imaging of cancer biomarkers, such as GRPR, by MRI. We will further introduce my progress of molecular imaging of VEGFR and PSMA in chapter 4 and 5.

4 DESIGN PSMA-TARGETED PROTEIN-BASED CONTRAST AGENTS TO ACHIEVE MOLECULAR IMAGING OF PROSTATE CANCER BY MRI

4.1 Introduction

As Discussion in Chapter 1.3.1, prostate specific membrane antigen (PSMA) is a type II transmembrane glycoprotein which belongs to G protein coupled receptor (GPCR) family. It is a glutamate carboxypeptidase II (EC 3.4.17.21) and acts as folate hydrolase and N-acetyl-α-linked acidic dipeptidase I (NAALADase I). [25] PSMA plays important roles in some physiological processes such as signal transduction, receptor function, nutrient uptake and cell migration. Although overexpression of PSMA is already identified to be related with prostate cancer, the role PSMA plays in prostate cancer is still under intensive investigations. It provides an attractive potential for diagnostics and stage analysis by molecular imaging and drug treatment (Table 1.3).

The expression of PSMA is androgen dependent. The expression level of PSMA increases when the androgen receptor is down regulated. This unique mechanism makes PSMA a favorable biomarker for the imaging of prostate cancer. PSMA is also expressed in tumor metastasis from prostate to spleen and bone. Therefore, there is a strong need to evaluate the prostate tumor progression by imaging the expression level of PSMA during cancer progression and treatment.

Several strategies are available for PSMA targeting. Imaging agents can be conjugated to antibody, peptide, aptamer, or inhibitors to enable the binding between PSMA and imaging agents. Each targeting strategy has its own advantages and disadvantages. Antibodies usually have high binding affinity and specificity, but the large size limits its tumor penetration (Table

1.3). Several antibodies against PSMA have been applied for the diagnosis of prostate cancer (Table 1.3). However, some of these antibodies, such as 7E11[97], target to the intracellular region of PSMA, which hampers the application of the PSMA antibody for *in vivo* imaging, such as MRI. The monoclonal antibody J591, which is in clinical trials, was designed to target the extracellular domain of PSMA to specifically deliver imaging agents or drugs to PSMA-expression cells [25]. Currently, PSMA antibodies have been linked to radioactive isotopes and quantum dots for preclinical and clinical image of prostate cancer. However, no PSMA-targeted MRI contrast agents were reported to date, mainly due to the lack of a sensitive MRI contrast agent and the penetration problem of an antibody with a large size of 150 kDa. Aptamers and inhibitors require additional steps before conjugation with imaging agents, such modification could change their binding affinity to receptors [123, 226, 227].

As shown in Table 1.4, using PSMA-specific targeting peptides is an alternative way of molecular imaging PSMA with high tissue penetration without the limitation of large size. PSMA-targeting peptide sequences were reported by three research groups (Table 4.1). ELISA and immunofluorescence results show the dimer of this PSMA-targeting peptide, named Sau peptide in my dissertation, can target PSMA. The monomer form of Sau peptide, however, has low affinity to PSMA [105]. Wu et al. found Sau peptide lost its PSMA-targeting capability after engineering Sau peptide in the fiber of adenovirus [198]. Wu et al. also made an improved version of PSMA-targeting peptide by adding additional 3 amino acids at both flanks of the Sau peptide. The improved peptide in virus can bind to PSMA after such modifications. [198] Recently, a series of PSMA peptides were developed by phase display technique. Three promising peptides, named 562, 563, and 564 peptides, show strong PSMA-targeting properties. Alpha

screening assay shows that these targeting peptides have PSMA binding affinity at μM level.[162]. Overall, the binding affinities of the reported peptide are very weak likely due to the high flexibility and undefined structure. In addition, peptides have low stability *in vivo* because of the protease cleavage [104, 176].

Our lab has developed a grafting approach to insert a biomarker targeting peptide in the middle of the ProCAs. Such design allows the peptide to maintain a stable conformation, and it is protected from protease cleavage [176]. As shown in chapter 3, inserting the GRPR binding peptide in ProCA1 by the grafting approach yields a GRPR binding affinity of 2.7 nM.

In this chapter, we first report the design of several PSMA-targeted MRI contrast agents and their expression and purification. We then report our effort in identification and determination of their PSMA targeting capability using various assays discussed in Chapter 1. We next determine the relaxivity and metal binding affinity of selected PSMA targeted reagents.

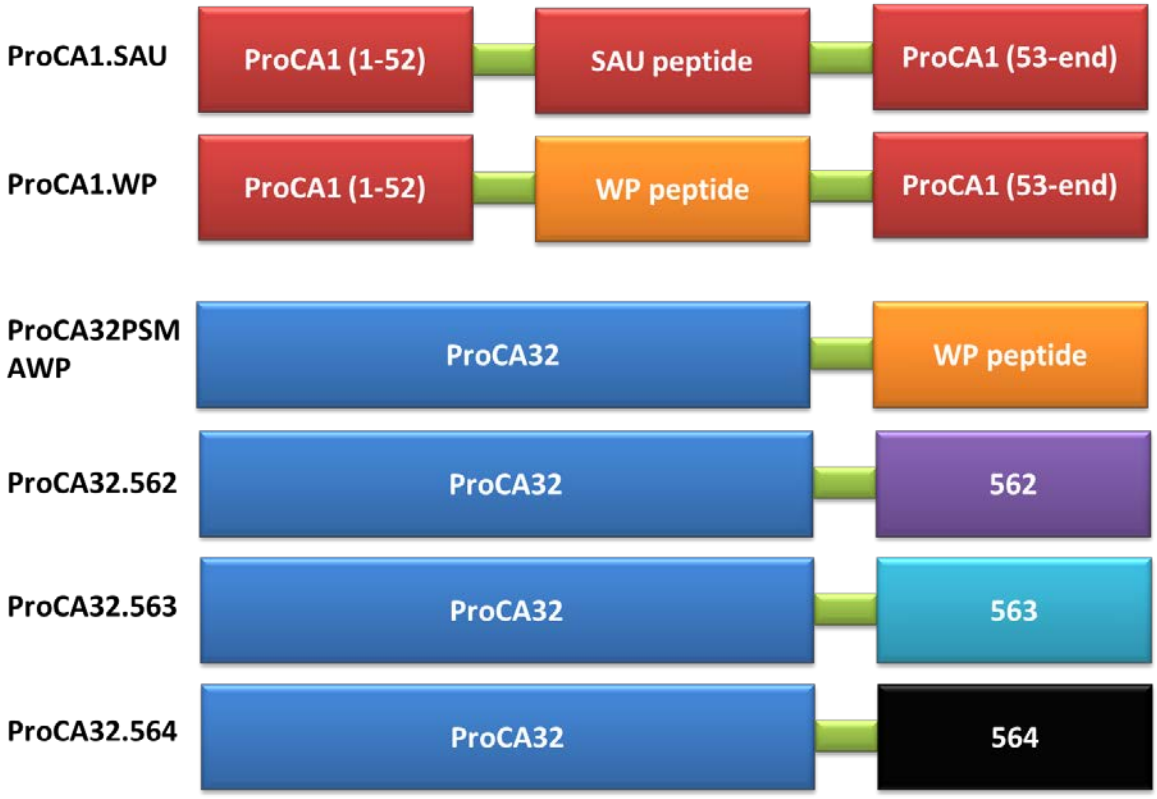

Figure 4.1 Design of PSMA-targeted ProCAs.

Different PSMA targeting peptides were fused into ProCA1 or ProCA32 to generate PSMA-targeted ProCAs. WP peptide was inserted into the 52 position of ProCA1 using grafting approach and 562, 563 and 564 peptides were fused at the C-terminal of ProCA32 using flexible linkers.

Table 4.1 Reported PSMA-targeting peptides.

Peptide name	Sequence	Affinity	Reference
SAU	WQPDTAHHWATL	NA	[105]
SAUwp	MAEWQPDTAHHWATLPDP	NA	[198]
562	SHSFSVGSGDGSPFT	NA	[162]
563	GRFLTGGTGRLLRIS	708 nM	[162]
564	LSFFSCWLRRSFSLT	1.72 μM	[162]

4.2 Results

4.2.1 Design of Protein-based MRI contrast agents with PSMA targeting capability

Our overall hypothesis is that PSMA targeting capability of peptide sequences can be improved after engineering into a protein environment. High affinity and sensitive PSMA –targeted MRI contrast agents can be achieved by engineering targeted peptide sequences to our developed protein contrast agents with high relaxivity. Fig. 4.1 summaries the design of several of these reagents we created.

First, we hypothesize that inserting PSMA-targeting peptide into ProCA1 by a grafting approach will maintain the native structure of the peptide, which will improve its binding affinity to PSMA. We inserted PSMA-targeting WP peptide in the middle of ProCA1 through the grafting approach.

Second, we linked several PSMA-targeting peptides at the C-terminal of ProCA32. ProCA32 is the third generation of ProCAs with multiple Gd^{3+} binding sites with high stability and high relaxivity. Fusion of a PSMA-targeting peptide to ProCA32 could also generate PSMA-

targeted MRI contrast agents (Fig. 4.1). A flexible linker is used to ensure the targeting capability of the peptide is not affected by the protein frame.

We also hypothesize that by these delicate designs, our protein-based MRI contrast agents will be able to quantitatively evaluate the PSMA expression in prostate tumor.

4.2.2 Protein expression and purification

4.2.2.1 Expression of ProCA32.wp and ProCA32.564

In the contrast agent design, PSMA-targeting peptides (wp and 564) were linked to the C-terminal of ProCA32 by the flexible linker GGSGG. The expression method was as described in chapter 2. *E.Coli* competent cell strain BL21(DE3)plysS was transfected with a 1 µl plasmid of ProCA32 variants. The transfected competent cells were scratched on the LB plate with 1% ampicillin and cultured at 37°C overnight. The next day, a single colony was selected to inoculate in 250 ml LB broth with 1% ampicillin and cultured at 37°C overnight. On the third day, 50 ml of the inoculated culture was added to 1L LB broth with 1% ampicillin. The protein expression was induced by 0.5 mM IPTG when the bacterial growth is up to the exponential phase. After IPTG induction, the culture temperature was kept at 37°C for 3 h, and then decreased to 25°C overnight. On the fourth day, the culture was centrifuged to get the cell pellet. As shown in Fig. 4.2, lane 2 and 3 represent the expression of ProCA32.wp before IPTG induction, while lane 6 and 7 show the expression of ProCA32.wp after IPTG induction at 25°C overnight. Lane 4 and 5 represent the expression of ProCA32.564 before IPTG induction, while lane 8 and 9 show the expression of ProCA32.564 after IPTG induction at 25°C overnight. Comparing the expression condi-

tions before and after IPTG induction, we can clearly find that IPTG induction significantly promotes the expression of ProCA32 variants at 25°C overnight.

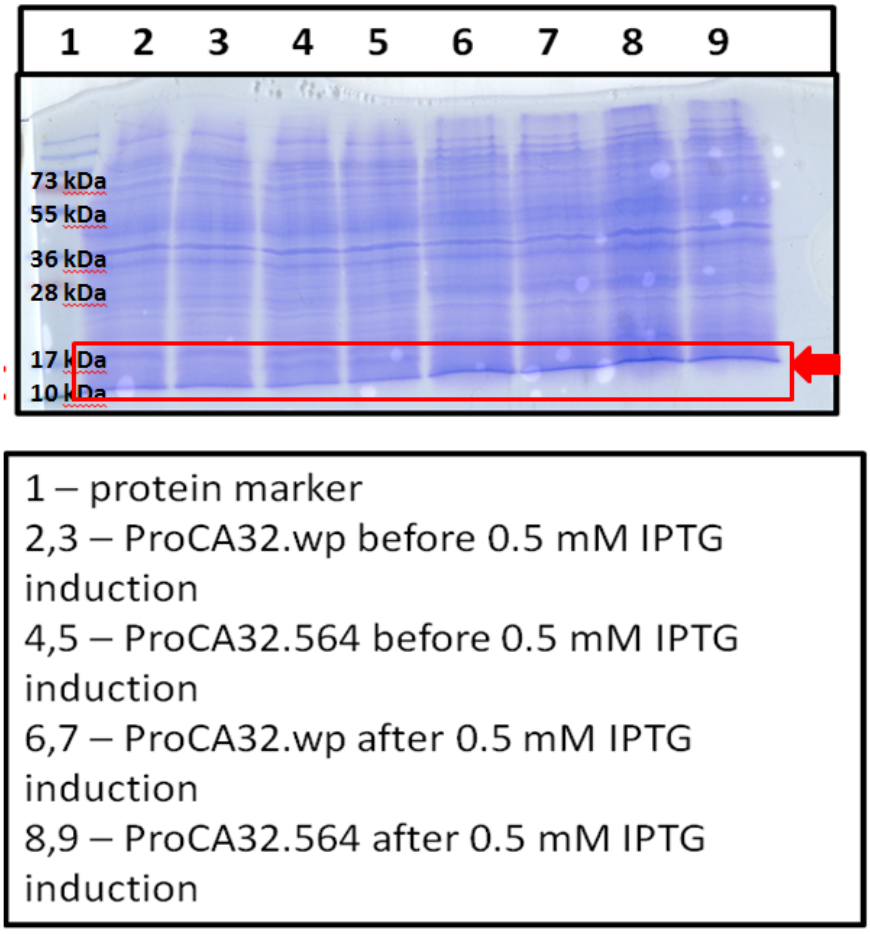

Figure 4.2 Protein expression of ProCA32.wp and ProCA32.564.

Lane 1 indicates the protein marker. Lane 2 and 3 represent the expression of ProCA32.wp before 0.5 mM IPTG induction. Lane 4 and 5 represent the expression of ProCA32.564 before 0.5 mM IPTG induction. Lane 6 and 7 represent the expression of ProCA32.wp after 0.5 mM IPTG induction. Lane 8 and 9 represent the expression of ProCA32.564 after 0.5 mM IPTG in-

duction. The plasmids of pET22b-ProCA32 variants were used to transfect *E. Coli* competent cell stain BL21(DE3)plysS. The molecular weight of ProCA32 variants was around 11 kDa.

After the cell pellets were collected, they were re-suspended in PBS buffer supplemented with 1 µl benzonuclase and 100 µl PMSF. The re-suspended cell pellets were completely broken by a sonicator and cell disruptor, separately. The supernatant was collected by centrifuging at 17000 rpm for 20 min at 4°C and boiled at 90-95℃ for 10 min. After boiling, most of the impure proteins were denatured and formed opalescent floc which were removed by centrifuge. The supernatant was mixed with 3% streptomycin sulfate and placed at 4°C overnight to precipitate DNA in the solution. On the next day, the precipitate DNA was removed by centrifuge and the supernatant was dialyzed in 10 mM HEPES buffer (pH 8.0) at 4°C overnight. After dialysis, the protein solution was filtered by 0.45 µm filter and further purified by FPLC-Q column. The FPLC separated components were identified by SDS-PAGE and UV spectrum. As shown in the SDS-PAGE in Fig. 4.3, FPLC peak 2 and peak 3 contain ProCA32.wp or ProCA32.564, respectively. FPLC peak 1 contains non-binding impurities and peak 4 contains DNA fragments. Since both of the ProCA32 variants have a cysteine in the terminal which forms a disulfide bond between two protein molecules, both ProCA32.wp and ProCA32.564 show a dimer band on the SDS-PAGE.

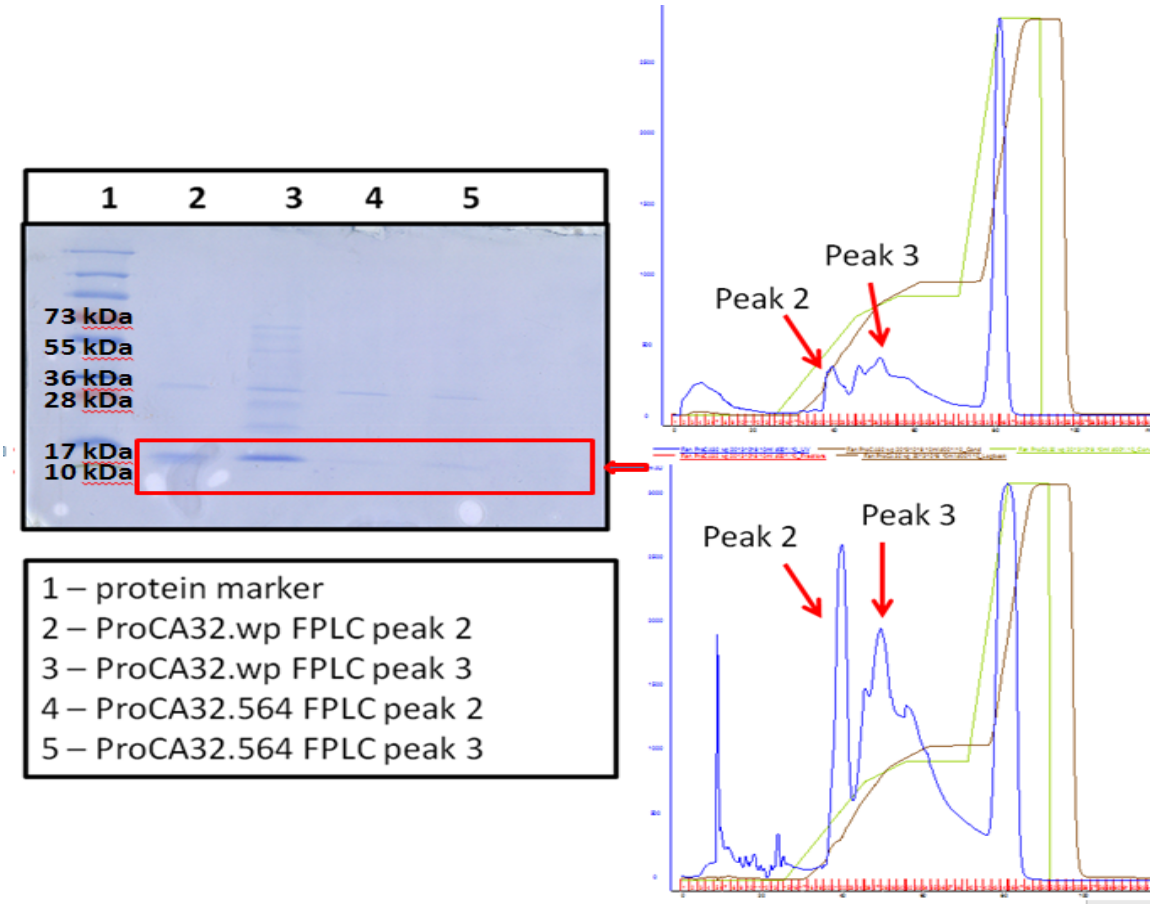

Figure 4.3 Protein purification of ProCA32.wp and ProCA32.564.

ProCA32.wp and ProCA32.564 were purified by heat and streptomycin precipitation methods. After dialysis against 10 mM HEPES at pH 8.0 overnight, the supernatants were injected into the FPLC system equipped with HP Q column. The ProCA32.wp and ProCA32.564 were eluted from peak 2 and peak 3 from FPLC by increasing the concentration of NaCl in 10 mM HEPES buffer at pH 8.0.

4.2.3 PSMA expression on LnCaP cells by Western Blot

To investigate the interaction between ProCA32 variants and PSMA, the proper cell lines should be considered ahead. Both PC3 and LnCaP cell lines are prostate cancer cell lines. PC3

cell is an androgen-independent cell line while LnCaP is an androgen-dependent cell line. To identify the PSMA expression in PC3 and LnCaP cell lines, the same amount of cell lysate was applied to run western blot. The homemade polyclone rabbit-anti-mouse ProCA32 antibody was applied with 1:1000 dilution ratios as the primary antibody to directly interact with ProCA32. Then, ALP-conjugated goat anti-mouse secondary antibody diluted with 1:10000 ratios was added to recognize the primary antibody. After washing the non-specific secondary antibody, substrate was added to expose the film.

As shown in Fig. 4.4, LnCaP cell lysate exhibited a double band which is located between 100 kDa and 130 kDa, while PC3 cell lysate didn't exhibit any band in the western blot. This result clearly indicates that LnCaP cell has PSMA expression but PC3 cells do not. These results are consistent with the reported literature which state that LnCaP cells are high in PSMA expression levels with Bmax = 95,000 sites/cell [228]. This conclusion supports us to further utilize the LnCaP cell line as our PSMA positive cell line as well as the PC3 cell line as a PSMA negative cell line.

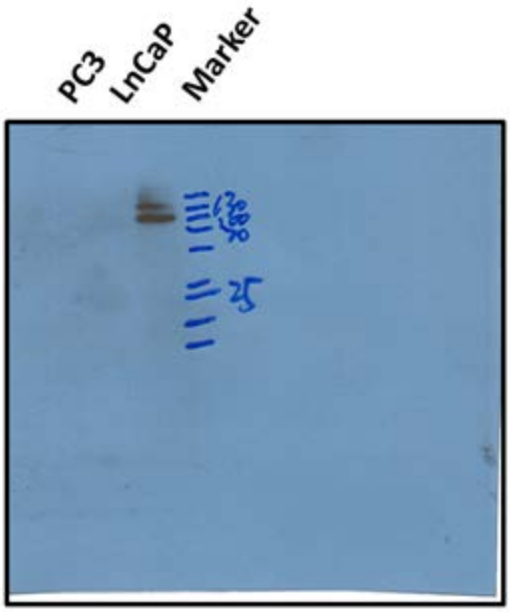

Figure 4.4 PSMA expression on LnCaP and PC3 cells identified by Western Blot.

To detect the PSMA expression in LnCaP cells, proteins were separated in 15% SDS-PAGE and then transferred onto the membrane. After blocking with 5% non-fat milk, the PSMA was visualized by monoclonal PSMA antibody (ABCaM 1:1000 dilution) and HRP-conjugated goat-anti-rabbit antibody (BioRad 1:10,000). PC3 cell lysate was used as a negative control, which does not have any bands, indicating that PC3 cells do not have PSMA expression.

4.2.4 Binding capability determination of ProCA variants to PSMA on LnCaP cells

4.2.4.1 Binding capability determination of ProCA1.wp to PSMA on LnCaP cells by indirect ELISA

To probe the binding capability of ProCA1.wp to PSMA in LnCaP cells, a series of indirect ELISA experiments were designed as shown in Fig. 4.5. ProCA1.wp is a protein-based MRI contrast agent grafted with a PSMA-targeting peptide (wp). At initial, the same amount of PC3 and LnCaP cell lysates were incubated on 96-well plates and blocked with 5% BSA. Then, different concentrations of ProCA32.wp were added to the wells, separately. The homemade polyclone rabbit-anti-mouse ProCA1 antibody was applied with 1:1000 dilution ratios as the primary antibody to directly interact with ProCA1.wp. A stabilized goat-anti-rabbit HRP-conjugated antibody (Pierce) was used as the secondary antibody. The absorbance intensity was detected by the FLUOstar OPTIMA plate reader at an absorbance wavelength of 450 nm.

As shown in Fig. 4.5, the binding capability of ProCA1.wp to LnCaP cell lysate is significantly higher than that of the PC3 cell lysate (Fig. 4.5 A) at different concentrations. Additionally, the binding of ProCA1.wp to LnCaP cell lysate showed the proportional increase along with the concentration. ProCA1 was also used as a control to interact with LnCaP and PC3 cell lysate (Fig. 4.5 B and C). Comparing the binding capability of ProCA1.wp and ProCA1 to LnCaP cell lysate, we can find that ProCA1.wp shows much stronger binding ability to LnCaP cell lysate than ProCA1. The binding ability was measured through the optical absorbance at 450 nm. The absorbance value, which is lower than 0.1, should be categorized as being generated from a non-specific binding process. Based on this category, the real binding of ProCA1.wp to PSMA in LnCaP cell lysate occurs when the concentration of ProCA1.wp was up to a 1 μM level. The

binding affinity of ProCA1.wp to PSMA in LnCaP cell lysate was estimated at around 1.8 µM by fitting the 1:1 equation.

Unfortunately, ProCA1.wp shows a similar binding ability to PC3 as that of ProCA1. We already proved that there is no PSMA expression in PC3 cells, so the binding of ProCA1.wp and ProCA1 to PC3 cells can be considered as non-specific binding.

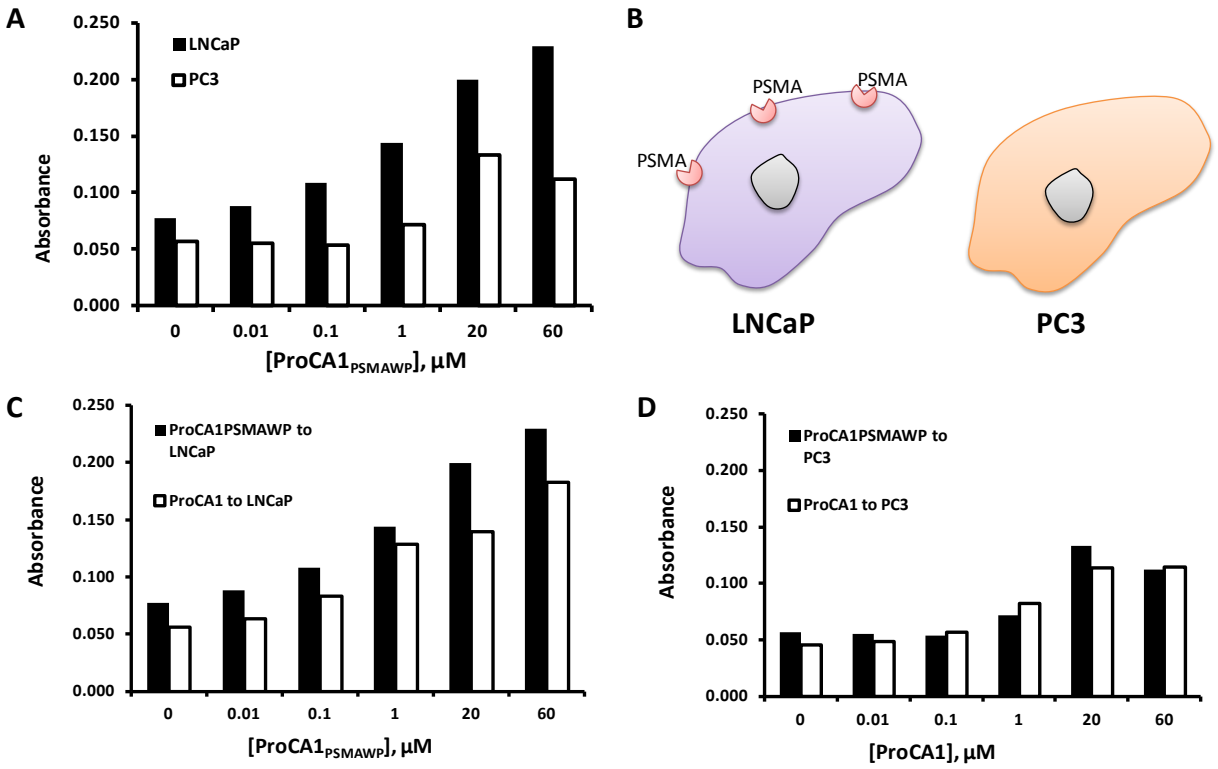

Figure 4.5 Comparison of binding capability between ProCA1PSMAwp and ProCA1 in LnCaP and PC3 cells by indirect ELISA.

The binding capacity of ProCA1PSMAwp and PSMA were determined by ELISA. PC3 and LnCaP cell lysates (from 5 x 10^4 cells) were coated in each well. After complete washing and blocking with BSA, the coated cell lysate were incubated with different concentrations of ProCA1 variants. The interaction between ProCA1 variants and PSMA in cell lysates was quantified by

ELISA using HRP-conjugated goat-anti-rabbit secondary antibody and one step ELISA kit. A. ELISA absorbance differences between PC3 and LnCaP cells after incubation with different concentration of ProCA1PSMAwp. B. Carton illustration of PSMA expression in LnCaP cells but not in PC3 cells. C. ELISA absorbance differences between ProCA1 and ProCA1PSMAWP in the wells coated with LnCaP cell lysate (from 5 x 10^4 cells). Different concentrations of ProCA1 and ProCA1PSMAWP were incubated with LnCaP cell lysate. D. ELISA absorbance differences between ProCA1 and ProCA1PSMAWP in the wells coated with PC3 cell lysate (from 5 x 10^4 cells). Different concentrations of ProCA1 and ProCA1PSMAWP were incubated with PC3 cell lysate.

4.2.4.2 Binding capability determination of ProCA32.wp and ProCA32.564 to PSMA on LnCaP cells

To further narrow the range of the binding capability of ProCA32.wp and ProCA32.564 to PSMA in LnCaP cell lysate, a series of different concentrations of ProCA32.wp and ProCA32.564 were added to interact with PSMA in LnCaP cell lysate. Wp and 564 are two different PSMA binding peptides which are linked to the C-terminal of ProCA32 to generate PSMA-targeted contrast agents. The concentration range of ProCA32.wp and ProCA32.564 was limited to 1 nM to 100 μM level. At initial, the same amount of LnCaP cell lysate was incubated in a 96-well plate at 4°C overnight and on the next day 5% BSA was added to block the unbound space in the well. Then, ProCA32, ProCA32.564 and ProCA32.wp were added to interact with PSMA in LnCaP cell lysate, separately. After incubation, the unbounded ProCA32 variants were washed away by TBST three times. The homemade polyclone rabbit-anti-mouse ProCA32 antibody was applied with 1:1000 dilution ratios as the primary antibody to directly interact with ProCA32

variants. A stabilized goat-anti-rabbit HRP-conjugated antibody (Pierce) was used as the secondary antibody. The absorbance intensity was detected by the FLUOstar OPTIMA plate reader at an absorbance wavelength of 450 nm.

As shown in Fig. 4.6, when the concentrations of ProCA32 variants were lower than 1 μM, the binding capability of ProCA32 variants to PSMA in LnCaP cell lysate showed no significant difference. In other words, the optical absorbance at 450 nm was lower than 0.1 which indicates this binding should be categorized as non-specific binding. When the concentration of ProCA32.564 was increased from 1 μM to 100 μM, the optical absorbance increased correspondingly, meaning ProCA32.564 indeed shows its specific binding capability in this range. As compared to ProCA32 and ProCA32.wp, ProCA32.564 exhibited an excellent pattern of specific binding which can be used for further *in vivo* application such as molecular imaging.

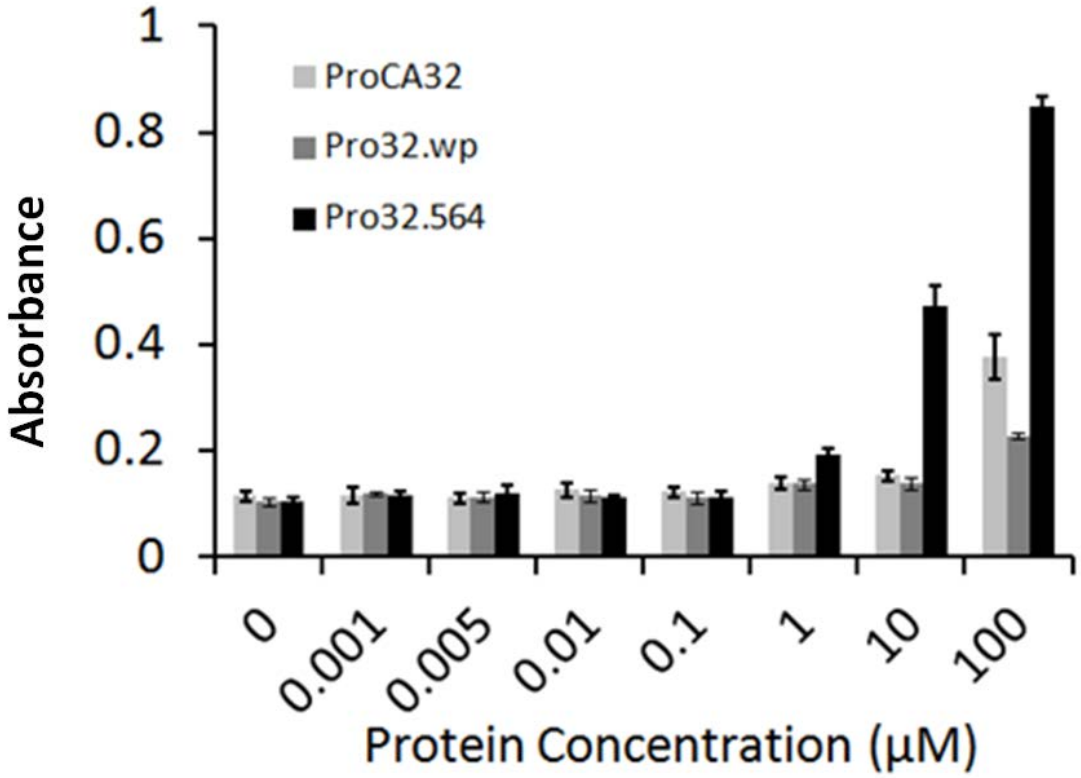

Figure 4.6. Comparison of the binding capability between ProCA32.wp and ProCA32.564 in LnCaP cell lysate by indirect ELISA.

LnCaP cell lysates were coated in a 96-well plate and 5% BSA was used as blocking agent. Then, 0-100 µM of ProCA32, ProCA32.564 and ProCA32wp were added to interact with PSMA in the coated cell lysates. The interaction between ProCA32 variants and PSMA in cell lysates was quantified by ELISA using HRP-conjugated goat-anti-rabbit secondary antibody and one step ELISA kit.

4.2.5 Cell imaging of ProCA1PSMAwp binding to LnCaP cells

To directly observe the binding process of ProCA1 variants to PSMA on LnCaP cells, fluorescence dye, Fluorescein, was conjugated with ProCA1 variants to do cell imaging. LnCaP cells were incubated with different concentrations of ProCA1.wp at 37°C for 30 min and washed with PIPES buffer to remove those nonspecific binding dyes. DAPI was used to stain the nucleus. As shown in Fig. 4.7, ProCA1.wp shows direct binding to PSMA on LnCaP cells as its concentration is above 10 nM.

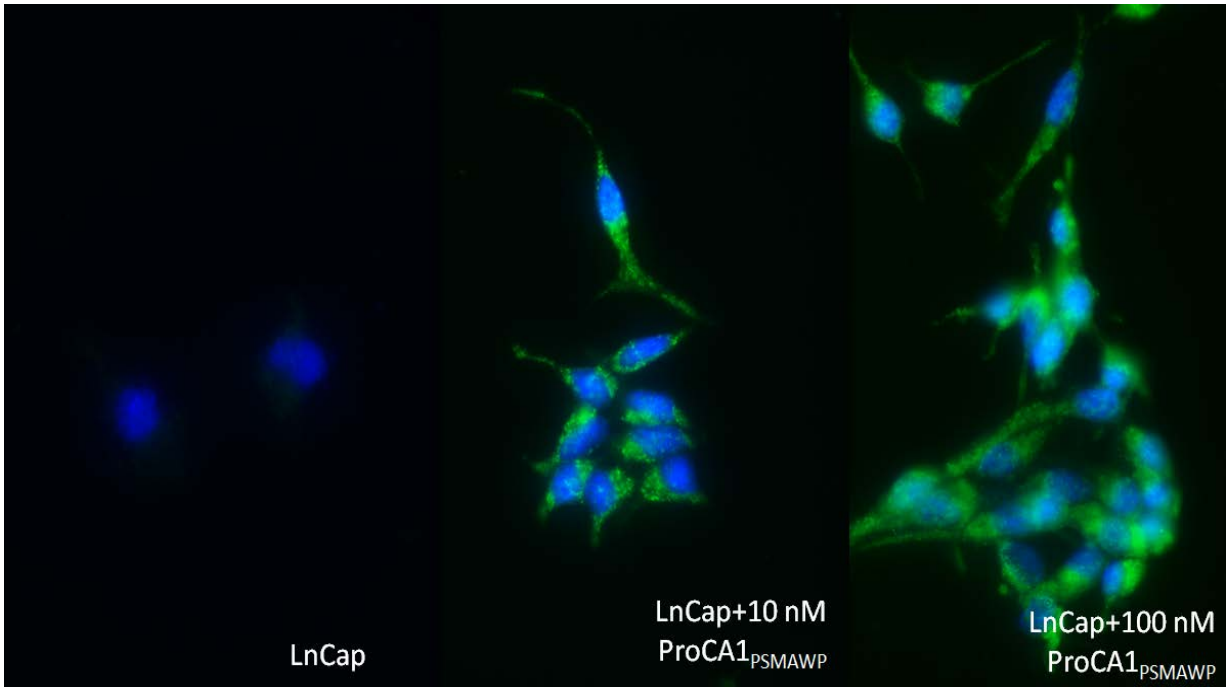

Figure 4.7 ProCA1PSMAwp targeting PSMA on LnCaP cells by cell imaging.

The interaction between ProCA1PSMAwp and PSMA was confirmed by fluorescence imaging using a Zeiss fluorescence microscope. The LnCaP shows enhanced green fluorescence after incubating with 10 nM or 100 nM of ProCA1PSMAwp. 100 nM ProCA1PSMAwp shows the highest fluorescence intensity.

4.2.6 Binding capability determination of ProCA variants to PSMA on LnCaP cells by fluorescence anisotropy

To quantitatively analyze the binding capability of ProCA32 variants to PSMA, fluorescence anisotropy was used to detect the signal change when ProCA32 variants bind to PSMA. ProCA32 variants were labeled with fluorescein. The basic mechanism of fluorescence anisotropy is based on rotational motions decreased when fluorescein-labeled ProCA32 bind to PSMA. Initially, 1% BSA and rabbit-anti-mouse ProCA32 antibody (homemade) were chosen as negative or positive controls, respectively with the concentration of ProCA32 at 15 μM. Then, different concentrations of antibody or BSA were titrated to ProCA32 in the fluorescence cuvette. The anisotropy signal of ProCA32 interacting with antibody or BSA was collected by fluorometer. Comparing the anisotropy signals, we can clearly see that titrating the antibody significantly enhanced the anisotropy signal than BSA did, which means the antibody shows much stronger binding affinity than BSA. Furthermore, this set of experiments proved fluorescence anisotropy can be used to quantitatively analyze the binding capability of ProCA32 variants to other molecules with relatively larger molecular weight.

ProCA32.564 is a ProCA32 variant grafted with a PSMA-binding peptide named as 564. [162] To identify that ProCA32.564 has the PSMA binding capability and to further quantify its binding constant, we titrated different volumes of LnCaP cell lysate to interact with ProCA32.564. LnCaP cell is a prostate cancer cell line which has high levels of PSMA expression. Once the binding process happens, the rotation rate of fluorescein-labeled ProCA32.564 changes which leads to anisotropy signal changes. ProCA32 was used as a control. As shown in Fig. 4.9, ProCA32.564 exhibit stronger anisotropy signal rather than that of ProCA32.

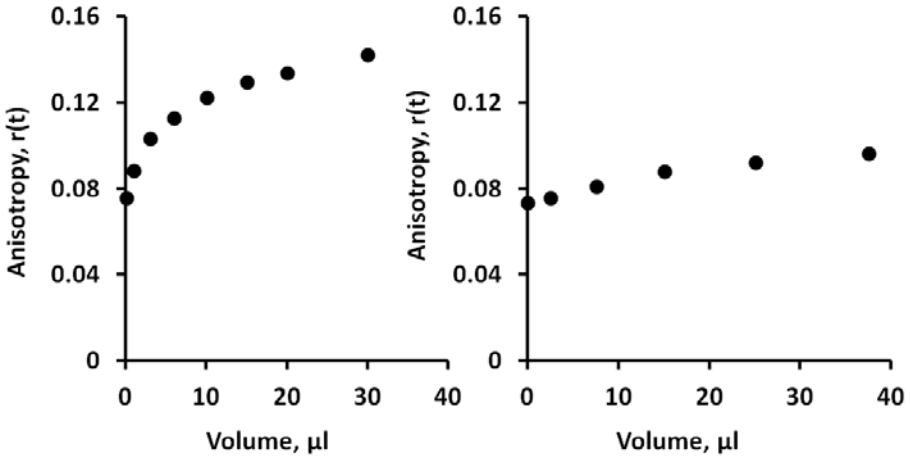

Figure 4.8 Probe the interaction between ProCA32 and antibody or BSA by anisotropy. The anisotropy fluorescein labeled protein was collected using PTI fluorometer with excitation wavelength of 495 nm and emission wavelength of 518 nm in 10 mM HEPES at pH 7.2. Fluorescein-labeled ProCA32 (left) or BSA (right) with concentration of 10 nM was gradually titrated with different volumes of antibody against ProCA32 until it reached the final volume of 30 or 40 µl. 7.2.

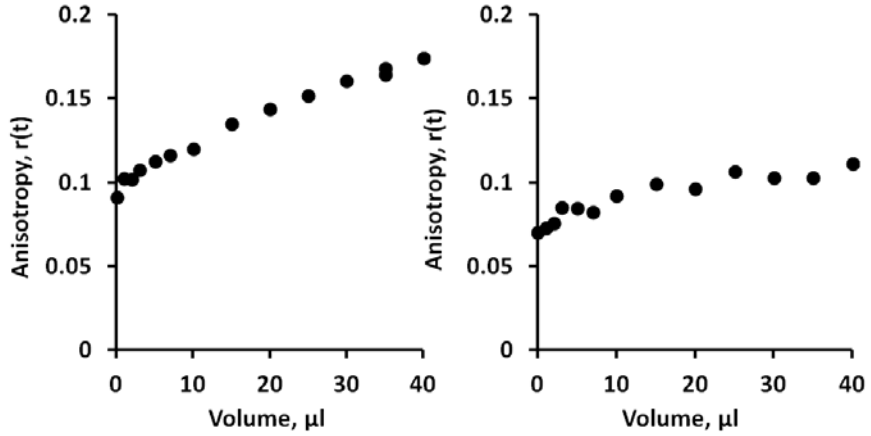

Figure 4.9 Probe the interaction between ProCA32.564 or ProCA32 and PSMA by anisotropy.

the interaction between ProCA32.564 or ProCA32 and PSMA by anisotropy.

The anisotropy 10 nM fluorescein-labeled ProCA32.564 (left) and ProCA32 (right) were collected using PTI fluorometer using excitation wavelength of 495 nm and emission wavelength of 518 nm in 10 mM HEPES buffer at pH 7.2. Fluorescein labeled ProCA32.564 has much higher anisotropy change compared with non-targeted ProCA32, indicating the interaction between ProCA32.564 and PSMA in LnCaP cell lysate.

4.2.7 Determination of the binding affinity between ProCA32.564 and PSMA

Next, we use ELISA to determine the binding affinity between ProCA32.564 and PSMA. Different concentrations of ProCAs ranging from 10^{-9} M to 10^{-4} M were incubated with LnCaP cell lysate. After adding HRP-conjugated secondary antibody and thoroughly washing, the interaction between PSMA and LnCaP were detected by colormetric substrate to HRP. As shown in Fig. 4.10, ProCA32.564 shows a sharp increased absorbance with a K_d if 0.52 ± 0.04 µM, indicating strong binding between PSMA and ProCA32.564. As a negative control, incubation of

ProCA32 without PSMA-targeting peptide yields low absorbance at any incubating contraction of ProCA32. Thus, the interaction between PSMA and ProCA32.564 is mediated by the conjugated 564 peptide.

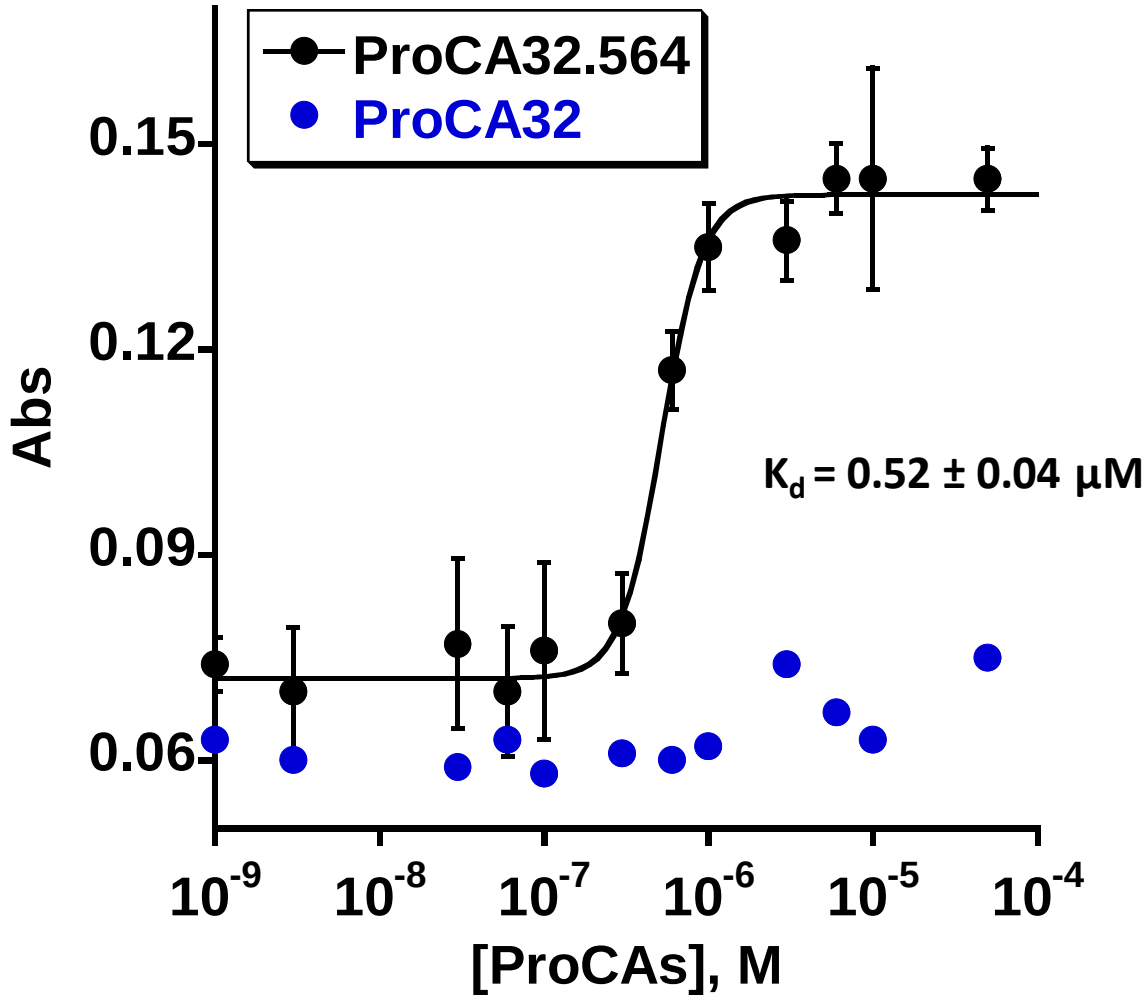

Figure 4.10 Determine the PSMA binding affinity to ProCA32.564 using ELISA.

LnCaP cell lysate was coated in a 96-well plate and 5% BSA was used as blocking agent. Then, 10^{-9}-10^{-4} M of ProCA32.564 (black dots) was added to interact with PSMA in the coated cell lysate. The interaction between ProCA32.564 and PSMA in cell lysates was quantified by ELISA using HRP-conjugated goat-anti-rabbit secondary antibody and one step ELISA kit. The

K_d of ProCA32.564 to PSMA was determined by Hill equation. ProCA32 (blue dots) was also tested in this experiment using the same experimental conditions. No absorbance enhancement was observed after increasing ProCA32 concentration indicating that ProCA32 itself without targeting moiety cannot bind to PSMA and LnCaP cell lysate.

4.2.8 Relaxivity measurement of ProCA32.564 and ProCA32.562

The sensitivity of MRI contrast is characterized by relaxivity. A clinical MRI contrast agent, such as Gd-DTPA, has an r1 relaxivity of 4 $mM^{-1}s^{-1}$ and r2 relaxivity of 5 $mM^{-1}s^{-1}$. Because of such low relaxivity, a local concentration of 0.1 mM is needed to generate significant signal change. As I mentioned in the previous chapter, the expression level of biomarkers is usually relatively low (at nM or pM level). Thus, there is a big gap to detect these biomarkers using clinical MRI contrast agents. MRI contrast agents with high biomarker targeting capability and high relaxivity are strongly desired for the molecular imaging of cancer biomarkers by MRI.

The relaxivity of ProCA32.564 and ProCA32.562 were measured at 37 °C 1.47 T. As shown in Fig. 4.11, both ProCA32.564 and ProCA32.562 show about 7-8 times higher r1 and r2 relaxivities than that of Gd-DTPA. ProCA32.564 has per Gd relaxivity of 27.6 $mM^{-1}s^{-1}$ and 37.9 $mM^{-1}s^{-1}$ for r1 and r2, respectively. ProCA32.562 has per Gd relaxivity of 21.5 $mM^{-1}s^{-1}$ and 29.8 $mM^{-1}s^{-1}$ for r1 and r2, respectively. Since both of these contrast agents have two Gd^{3+} binding sites, the relaxivities per particle are twice as high than the relaxivity per Gd. In summary, ProCA32.564 has a relaxivity of 55.2 $mM^{-1}s^{-1}$ and 75.8 $mM^{-1}s^{-1}$ per particle for r1 and r2, respectively. While ProCA32.562 has a relaxivity of 43.0 $mM^{-1}s^{-1}$ and 59.6 $mM^{-1}s^{-1}$ per particle for r1

and r2, respectively. These results indicate that ProCA32.564 and ProCA32 could have high sensitivity for the molecular imaging of PSMA by *in vivo* MRI.

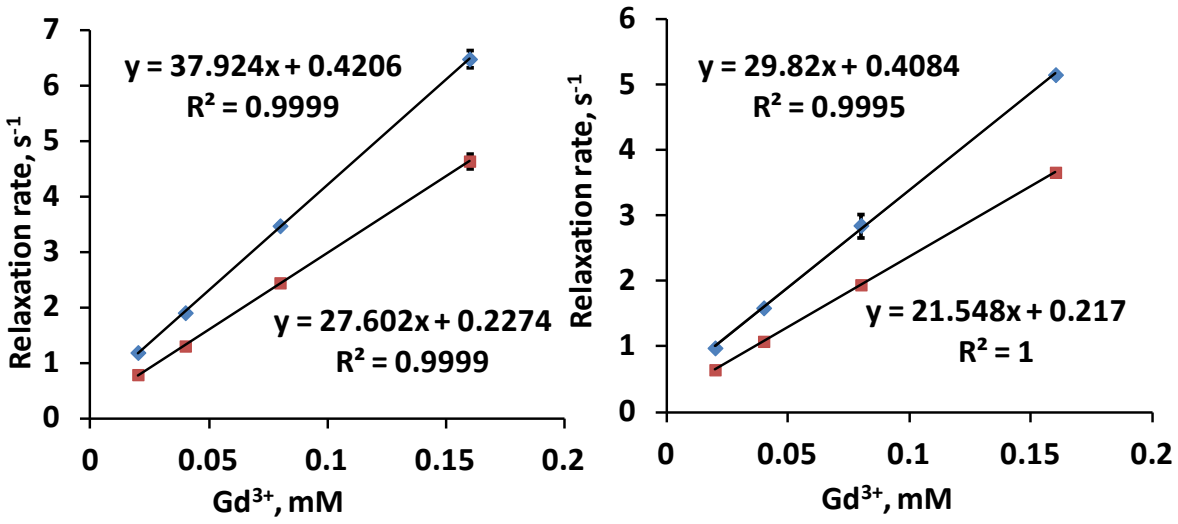

Figure 4.11 Relaxivity measurements of（r1 and r2） of ProCA32.564 (left) and ProCA32.562 (right) at 37°C under 60 MHz by Bruker Minispec. The experiments were performed in 10 mM HEPES at pH 7.2.

4.2.9 Determining Tb^{3+} and Gd^{3+} binding affinity of ProCA32.562 and ProCA32.564 using Tb^{3+}-DTPA (or EGTA) buffer system and competition methods

Another essential requirement for *in vivo* application of MRI contrast agents is that MRI contrast agents must have high Gd^{3+} binding affinity. The physiological metal ions, such as Zn^{2+}, and phosphate could function as potential competitors to cause free Gd^{3+} release, free Gd^{3+} is toxic *in vivo*. Thus, strong Gd^{3+} binding affinity are needed to allow the Gd^{3+} and ProCAs to form stable complex *in vivo*. We applied Tb^{3+}-DTPA buffer system to determine the Tb^{3+} affinity to

ProCA32.562 and ProCA32.564. We further used competition assay to determine the Gd^{3+} binding affinity to ProCAs.

As shown in Fig. 4.12, the FRET fluorescence between Tb^{3+} and Trp in ProCAs increase when the free Tb^{3+} concentration is higher than 10^{-22} M, indicating an extremely strong binding between ProCAs and Tb^{3+}. The K_d between ProCA32.562 and Tb^{3+} is $2.53 \pm 0.25 \times 10^{-22}$ M, and the K_d between ProCA32.564 and Tb^{3+} is $3.25 \pm 0.03 \times 10^{-22}$ M.

The Gd^{3+} binding affinity to PSMA-targeted ProCAs were determined by competition assay. PSMA-targeted ProCAs were first incubated with Tb^{3+} at 1:2 ratios, and then titrated with different concentrations of Gd^{3+}. The mixture was incubated overnight to reach equilibrium. As shown in Fig. 4.13, the fluorescence intensity decreased when Gd^{3+} concentration increased, indicating that Gd^{3+} can compete Tb^{3+} out of the metal binding pockets. The Gd^{3+} binding affinity of ProCA32.562 and ProCA32.564 are 2.53×10^{-22} and 9.03×10^{-22} M, respectively. Similar to other ProCA32 variants, the Gd^{3+} binding affinity of ProCA32.562 and ProCA32.564 are comparable with the clinical MRI contrast agents, such as Magnevist. Thus, ProCA32.562 has strong Gd^{3+} stability for *in vivo* applications.

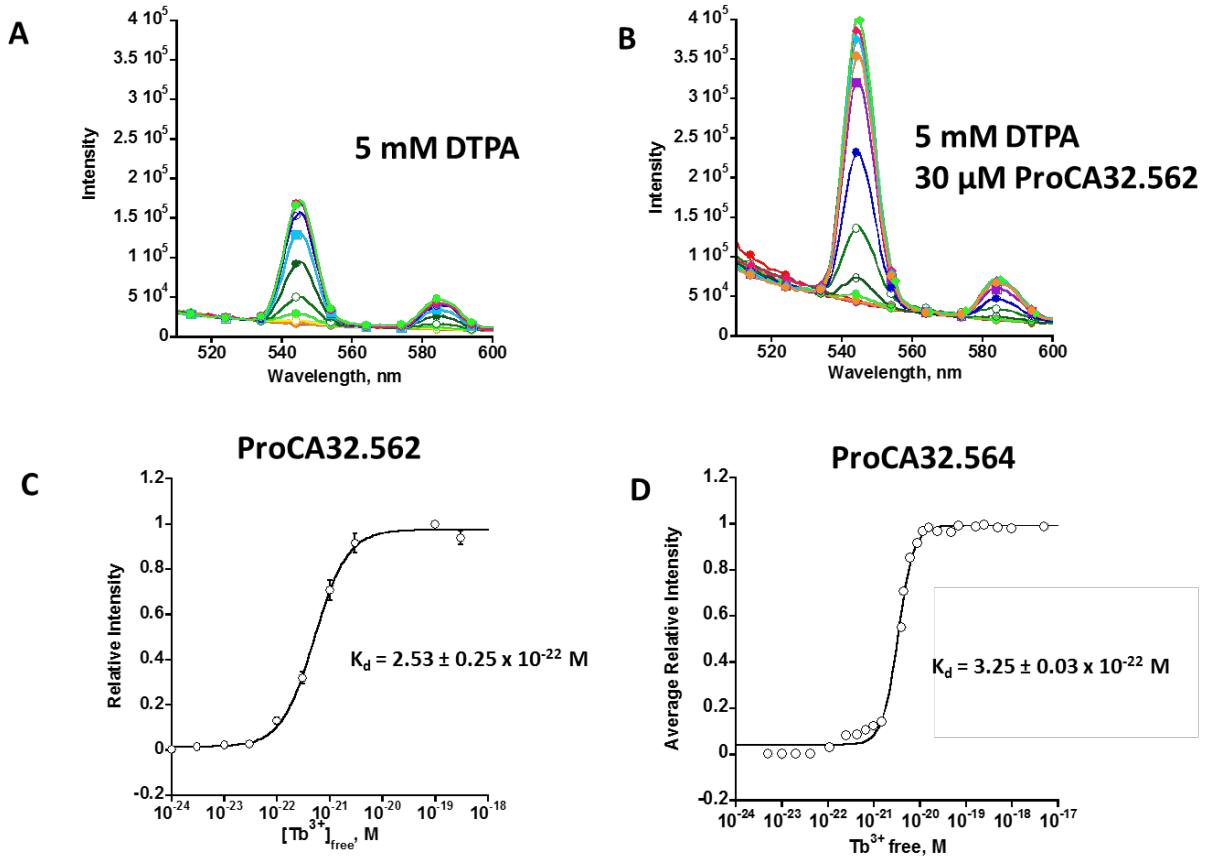

Figure 4.12 Tb^{3+} binding affinity of ProCA32.562 and ProCA32.564 by using Tb^{3+}- DTPA buffer system.

The K_d of ProCA32 variants to Tb^{3+} was determined using Gd-DTPA buffer system, which contains 50 mM HEPES, 100 mM NaCl, 5 mM DTPA and 30 µM of ProCA32 variants (562 and 564) at pH 7.0. In this procedure, 5 mM $TbCl_3$ was titrated into the system to generate a free Gd^{3+} concentration ranging from 10^{-23} to 10^{-18} M. K_d of ProCA32 variants to Tb^{3+} was determined by Hill equation. Figure 4.12 A shows the signal of Tb^{3+} in buffer without the protein. Figure 4.12 B illustrates the Tb^{3+} in the presence of protein. Figure 4.12 C and D are the normalized data for each ProCA variants. The fluorescence spectrums were collected under excitation wavelength of 280 nm, and emission wavelength between 500 - 600 nm.

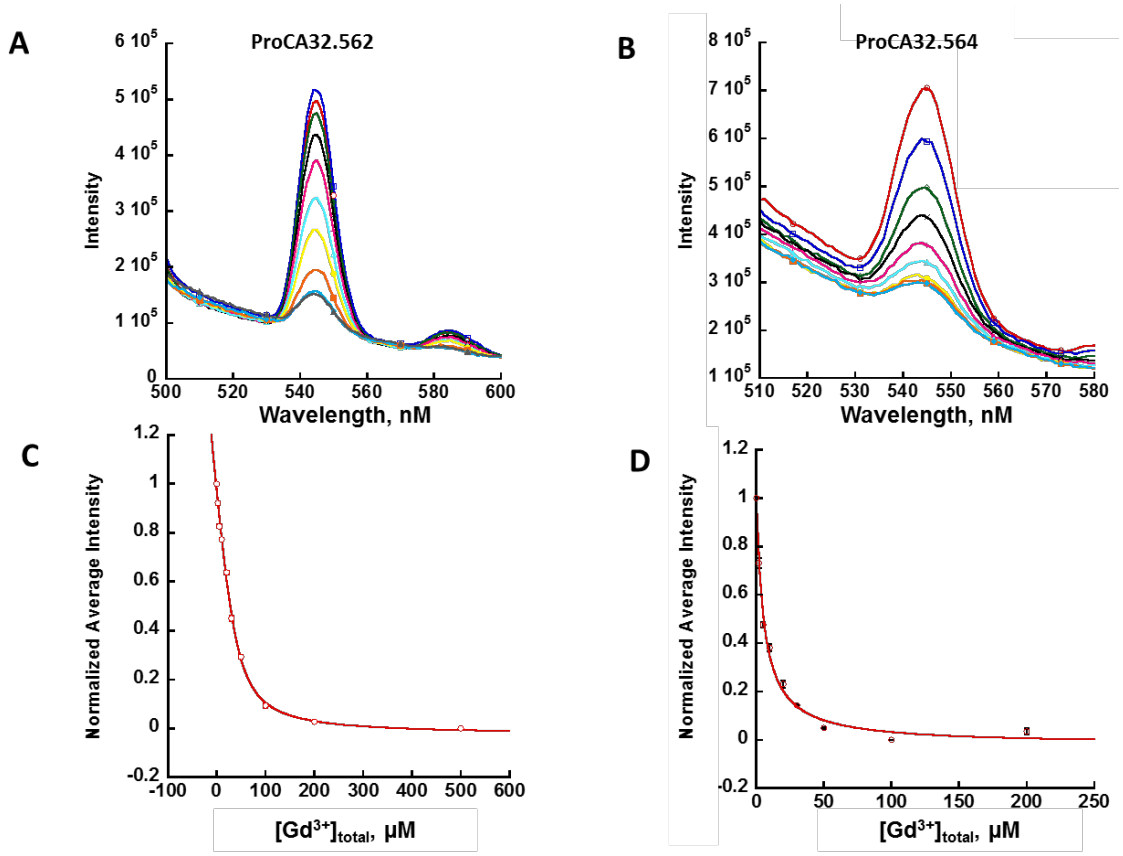

Figure 4.13 Determination of Gd^{3+} binding affinity to ProCA32.562 and ProCA32.564 using Tb^{3+} competition assay.

This experiment was performed in PTI using excitation wavelength of 280 nm by incubating different concentrations of Gd^{3+} in 50 mM HEPES, 100 mM NaCl, 10 µM ProCA variants and 20 µM Tb^{3+}. Since Gd^{3+} variants can compete Tb^{3+} out of the metal binding pocket in ProCA variants, Tb^{3+} shows decreased fluorescence signal as Gd^{3+} concentration increases. Figure 4.13 A and B show the decrease in Tb^{3+} signal in each ProCA variants and Figure 4.13 C and D demonstrate the normalized signal of Tb^{3+} after adding different amount of Gd^{3+}. The fluores-

cence spectrum were collected under excitation wavelength of 280 nm, and emission wavelength between 500 - 600 nm for ProCA32.562 and 510 - 580 nm for ProCA32.564.

4.3 Discussion

4.3.1 PSMA is a promising prostate cancer biomarker

As discussed in Chapter 1, the development of molecular imaging exhibits great potential to overcome the limitations in diagnosis and stage determination of prostate cancer [229], the non-invasive imaging techniques with high sensitivity and resolution are highly desired for prostate cancer diagnosis. Prostate specific membrane antigen (PSMA) is one of the most promising biomarkers for the diagnosis and treatment of prostate cancer. PSMA expressed on the prostate cancer surface, allows binding to contrast agents through IV injection. PSMA has low expression levels in normal prostate tissue and has high expression in prostate carcinoma and prostate cancer. The expression level of PSMA in normal prostate is usually 10 times higher than that of other types of tissues, while the expression level of PSMA in prostate cancer is usually 10 times higher than that in normal prostate tissue. In addition, PSMA is also expressed in the secondary tumors metastasis from prostate cancer. Thus, imaging PSMA provides a unique and promising aspect to detect primary prostate cancer and prostate cancer metastasis to other organs. Owning to these unique properties, PSMA became one of the hottest targets for the diagnosis and treatment of prostate cancer. A PSMA antibody-based SPECT contrast agent, named Prostascint, has been approval by the FDA. Inhibitor-based PSMA targeting molecule has also been robustly developed in the preclinical field for PET and SPET/CT imaging [163, 165]. Unfortunately, although MRI has superior resolution, no radiation compared with other imag-

ing techniques, the PSMA- targeted MRI contrast agents haven't been successfully developed. This is because the clinical MRI contrast agents lack enough resolution to induce significant local signal changes after binding to PSMA. In this chapter, we aim to develop PSMA-targeted ProCAs with high relaxivity and low detection limits for imaging of PSMA by MRI.

Here, we have created several PSMA-targeted ProCAs by linking PSMA-targeting peptide, such as 562, 563 and 564, to the C-terminal of ProCA32 and grafting the WP sequence to ProCA1 (Fig. 4.1). Several methods were used to characterize the interaction between PSMA and ProCAs. First, the interaction between PSMA and targeted ProCAs can be visualized by immunofluorescence. Strong immunofluorescence can be detected in the intracellular region indicating that PMSA-targeted ProCAs can be internalized by LnCaP cells. Second, the interaction between PSMA and PSMA-targeted ProCAs were confirmed by fluorescence polarization and anisotropy techniques. The increase of polarized fluorescence signal and anisotropy in Fluorecein-labeled targeted ProCAs was observed by titrating LnCaP cell lysate, which indicates that the LnCaP cell lysate binds to PSMA-targeted ProCAs. Third, the interaction between PSMA and PSMA-targeted ProCA variants was characterized by ELISA.

Among all PSMA-targeted ProCAs created (summarized in Fig. 4.1), ProCA32.564 shows the best PSMA binding affinity determined by ELISA with EC_{50} of 0.52 μM, which is 3 times stronger than the reported affinity of the 564 peptide (1.72 μM). As a negative control, ProCA32 has no binding to LnCaP cell lysate studied by ELISA. Although literature reported that SAU peptide and WP peptide has capacity to target PSMA, the PSMA binding affinity hasn't been reported. In order to make PSMA-targeted contrast agents, we fused or inserted these peptides into ProCA1 or ProCA32. After insertion in the 52 position of ProCA1, this new protein (ProCA1.WP) can selectively target LnCaP cells but not target to PC3 cells, indicating the specific interaction between ProCA1.WP and PSMA. However, when we linked WP peptide in the C-

terminal of ProCA32, it completely lost PSMA targeting capacity in ELISA experiments. On the other hand, 564 peptide fusing to the C-terminal of ProCA32 shows acceptable PSMA targeting capability with EC_{50} of 0.52 μM, which is 3 times stronger than the reported affinity of 564 peptide (1.72 μM)[162].

4.3.2 Relaxation and metal binding properties of PSMA-targeted reagents

High Gd^{3+} binding affinity and high relaxivity are strongly needed for the molecular imaging of PSMA. Our previous lab member shows that ProCA32 has comparable Gd^{3+} stability to Gd-DTPA, while ProCA32 has about 10 times higher per Gd^{3+} relativity and about 20 times higher per particle relaxivity than that of Gd-DTPA. In this chapter, we further determined the relaxivity of ProCA32.562 and ProCA32.564 summarized in Table 4.2.

These PSMA-targeted ProCAs has high per Gd^{3+} relaxivties (r1 = 29 $mM^{-1}s^{-1}$, r2 = 37 $mM^{-1}s^{-1}$), which are 8 times (r1) and 7 times (r2) higher than that of Gd-DTPA, respectively. High stability and high relaxivity make ProCAs promising to be applied to image PSMA *in vivo*.

We further show that PSMA-targeted ProCAs has comparable Gd^{3+} binding affinity to Gd-DTPA. ProCA32.562 has Gd^{3+} binding affinity of 2.53 x 10^{-22} M while ProCA32.564 has Gd^{3+} binding affinity of 9.03 x 10^{-22} M. Both of them has comparable Gd^{3+} affinity to clinical MRI contrast agent, Gd-DTPA (1.86 x 10^{-21} M).

Table 4.2 Summary of relaxivities, metal binding affinities and PSMA targeting capabilities of ProCAs.

Contrast agents	r1, $mM^{-1}s^{-1}$	r2, $mM^{-1}s^{-1}$	Tb^{3+} affinity, M	Gd^{3+} affinity, M	PSMA affinity, μM
ProCA1.SAU	NT	NT	NT	NT	NT
ProCA1.WP	NT	NT	NT	NT	NT
ProCA32.PSMAWP	NT	NT	NT	NT	NT
ProCA32.562	21.5	29.8	$2.53 \pm 0.25 \times 10^{-22}$	2.53×10^{-22}	NT
ProCA32.563	NT	NT	NT	NT	NT
ProCA32.564	27.6	37.9	$3.25 \pm 0.03 \times 10^{-22}$	9.03×10^{-22}	0.52 ± 0.04
Gd-DTPA	3.5	5	9.54×10^{-22} *	1.86×10^{-21} *	Not bind

NT stands for "was not tested". * from NIST database 46.

4.4 Conclusion

PSMA-targeted MRI contrast agents were developed based on a series of reported PSMA-targeting peptides. The newly constructed PSMA-targeted MRI contrast agents maintain high relaxivity, and metal binding affinity as non-targeted ProCA32. The binding capability of PSMA-targeted MRI contrast agents was evaluated by cell imaging, fluorescence polarization and ELISA. Among all of those candidates, ProCA32.564 exhibits the best binding affinity (EC_{50} = 0.52 ± 0.04 μM) to PSMA and provides the potential to develop it as a molecular imaging agent for prostate cancer prognosis and diagnosis. ProCA32.562 and ProCA32.564 has high r1 and r2 relaxivities (r1 = 29 $mM^{-1}s^{-1}$, r2 = 37 $mM^{-1}s^{-1}$ for ProCA32.562), which allows detecting PSMA levels at low local concentration. In addition, ProCA32.562 has strong Gd^{3+} binding affinity (2.53 x 10^{-22} M). The Gd^{3+} binding affinity of ProCA32.562 is similar to Gd-DTPA. Thus, these *in vitro*

results demonstrate that PSMA-targeted ProCAs has high PSMA binding affinity, high relaxivity and high Gd^{3+} stability and PMSA-targeted ProCAs are promising for the molecular imaging of PSMA *in vivo* by MRI.

4.5 Future plan

In the future, cell imaging of ProCA32.562 and ProCA32.564 will need to be monitored by fluorescence microscope. After evaluation of our ProCA32 variants with PSMA targeting capability, we need to establish the LnCaP xenografted mice model to further do the molecular imaging of biomarkers. After MRI scanning, tissue IHC staining and Gd^{3+} distribution needs to be investigated correspondingly.

5 A Protein-based MRI Contrast Agent with VEGFR-2 targeting capability for Molecular Imaging of Tumor Angiogenesis

5.1 Introduction

Angiogenesis is primarily used to describe a pathological process and development in which new blood vessels generated and is critical for tumor growth and metastasis. Vascular endothelial growth factor (VEGF) is a homodimeric glycoprotein (45 kDa) and has been identified to stimulate the proliferation of endothelial cells which form the inner lining of blood vessels and existed in numerous tumor types. Endothelial cells play important roles in angiogenesis such as degradation of the basement membrane, migration to form a sprout, and extension of the new vessels. VEGF plays a key role in angiogenesis, regulating vaspermeability, proliferation and migration of endothelial cells. The VEGF family mainly includes VEGF-A (VEGF), VEGF-B, VEGF-C, VEGF-D and Placenta growth factor (PlGF). Correspondingly, three VEGF tyrosine kinase receptors have been discovered, including VEGF-1 receptor (flt-1), VEGFR-2 (flt-1/KDR) and VEGFR-3 (flt-4). VEGFR-2 mediates almost all the known cellular responses to VEGF and therefore become the principal target of anti-angiogenic therapies. VEGFR-3 mediates lymphangiogenesis in response to VEGF-C and VEGF-D. VEGFR-1 is a decoy receptor. The function of VEGFR-1 is less well defined and it is thought to modulate VEGFR-2 signaling. When VEGFs bind these receptors, the downstream signaling pathway will be triggered and a series of events will happen such as endothelial cell migration, proliferation, survival and permeability. The following figure exhibits the interaction between VEGFs and VEGF-Rs. Right now, VEGF and angiogenesis has been the target of anti-cancer therapeutics in many cases [230], [231].

The natural ligands for VEGFR-2 are VEGF-A, VEGF-C and VEGF-E. Co-crystallization between ECD and VEGF demonstrate that the Loop1, loop2, loop3 and N-terminal helix of VEGF-A, VEGF-C and VEGF-E bind to the D2 and D3 domain of VEGFR-ECD.[232] The interaction between VEGFR-2 and its ligands, such as VEGF-A, activates multiple downstream signaling cascade, such as MAP kinase pathway and PI3K-Akt pathway, which promote endothelial cell migration, increase vascular permeability, and mobilize the endothelial precursor cells.

Anti-VEGFR-2 antibodies are another set of VEGFR-2 binding proteins extensively used for VEGFR-2 imaging and cancer treatment. Ramucirumab is a human monoclonal antibody against VEGFR-2, which has been approved for the treatment of gastric, gastroesophageal junction adenocarcinoma, and stomach cancer. Moreover, other single chain antibody against VEGFR-2 has been applied for the near infrared imaging, SPECT and PET imaging [233]. These imaging probes show highly specific uptake in the vasculature of tumor and surrounding tissues *in vivo* through receptor mediated endocytosis.

A series of peptides targeting VEGFR-2 for the MRI detection of VEGFR-2 were developed by Sherry A. D.'s group [234]. These synthetic peptides were further conjugated with 8 Gd-DOTA having a per particle r1 relaxivity of about 48 $mM^{-1}s^{-1}$. The VEGFR-2 binding affinity of these peptides can reach 215 nM. These peptides were further demonstrated to bind VEGFR-2 *in vivo* for MRI.

VEGFR-2 targeted peptides were developed using a phage display method. The monomer form of these peptides has the VEGFR-2 binding affinity between 3 - 280 nM. Heterobivalent dimmers of these peptides further improve the VEGFR binding affinity to 0.6 nM. [235]

[236]. Such peptides provide a big potential to generate anti-angiogenesis molecular imaging agents.

Since VEGFR-2 plays an essential role in the cancer angiogenesis, non-invasive imaging of VEGFR-2 could provide additional information to aid in cancer prognosis and diagnosis. PET and ultrasound based imaging agents have been developed in the past 10 years [51, 54-56] [96, 98] . However, due to the lack of contrast agents with high relxivity related to sensitivity and high targeting specificity, the development of VEGFR-2 targeted MRI contrast agents lags behind other imaging techniques [234].

Previously lab member Dr. Shenghui Xue developed the third generation of non-targeted MRI contrast agents, ProCA32, with high relaxivity, stability and multiple Gd^{3+} binding sites. ProCA32 has both high r1 and r2 relaxivities, which can be applied for both T1-weighted and T2-weighted MR imaging. Such unique feature made ProCA32 able to detect liver metastasis with both T1-weighted and T2-weighted MRI, which improves the detection accuracy compared with either T1-weighted or T2-weighted MRI. SinceProCA32 is a non-targeted MRI contrast agent, the detection of tumor by ProCA32 is based on the distribution differences of ProCA32 between liver and tumor.

In this chapter, I will explain the design of VEFGR2- targeted contrast agents by addition of the VEGFR-2 targeting peptide at the C-terminal of ProCA32, named ProCA32.VEGF. I will then show the *in vitro* and *in vivo* evaluation of this VEGFR-2 targeted MRI contrast agent for the imaging of VEGFR-2 in breast cancer and melanoma.

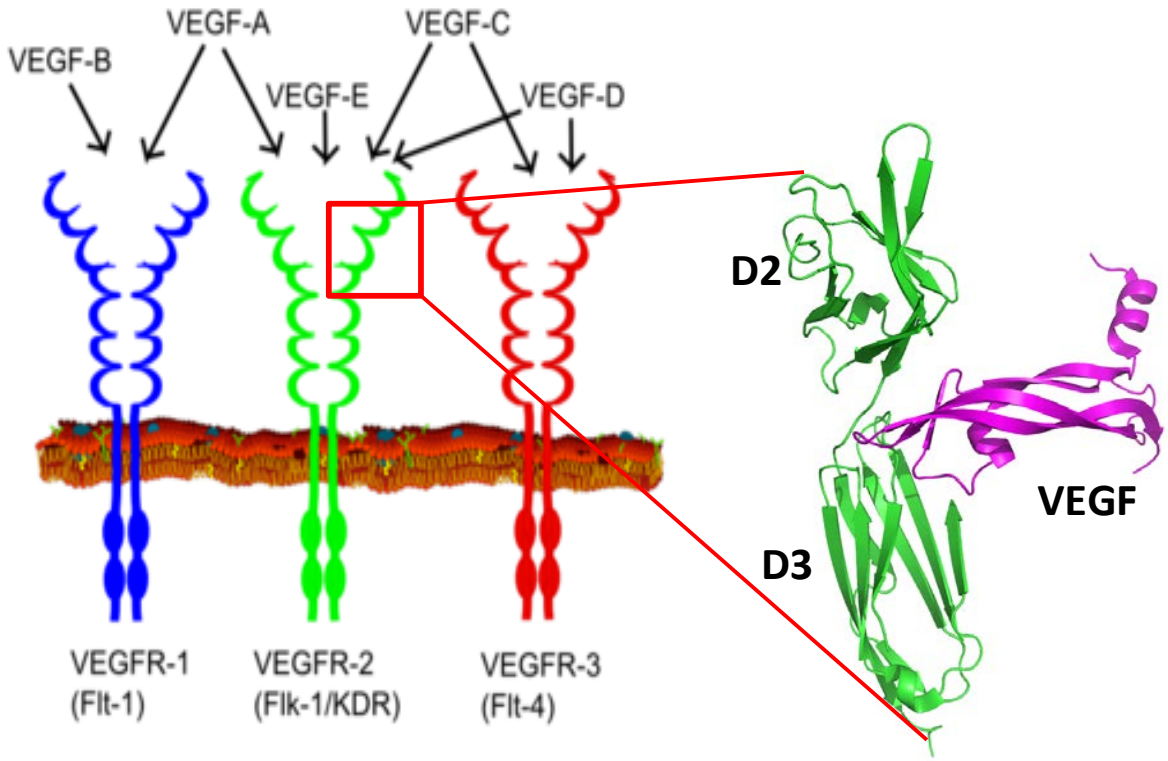

Figure 5.1 The interaction of VEGFs and VEGFRs.

VEGF loops L1 - L3 are interacted with D2 and D3 domain of VEGFR-2 [pdb: 3V2A].

5.2 Results

5.2.1 Design and molecular cloning of VEGFR targeted contrast agent ProCA32.VEGF

Pillai et al. [235, 236]developed a VEGFR-2 targeted peptide which has VEGFR-2 binding affinity at 3 nM. This peptide is screened by multistep phage screening and the interaction between this peptide and VEGFR2 is tested by fluorescence polarization and SPR. Since this peptide only contains natural amino acids, it is easy to create a fusion protein with ProCA32 for VEGFR2 targeted. Fig. 5.2 shows our design of VEGFR2 targeted ProCA32. VEGFR2 targeting peptide is linked to the C-terminal of ProCA32 through GGG flexible linker. Because this peptide has a VEGFR-2 binding affinity of 3 nM, this fusion protein should be strong enough to target

VEGFR-2 *in vivo*. Because ProCA32.VEGF has high r1 and r2 relaxivities, we hypothesize that ProCA32.VEGF can be applied for the molecular imaging of VEGFR-2 in both T1- weighted and T2-weighted MRI sequences.

We inserted this peptide into wild-type plasmid of ProCA32 in pET-22b vector at the C-terminal to generate a VEGFR-2 targeting contrast agent. The newly constructed plasmid was sequenced by GENEWIZ. The sequence was aligned with another ProCA32 variant and proven to be correct (Fig. 5.2).

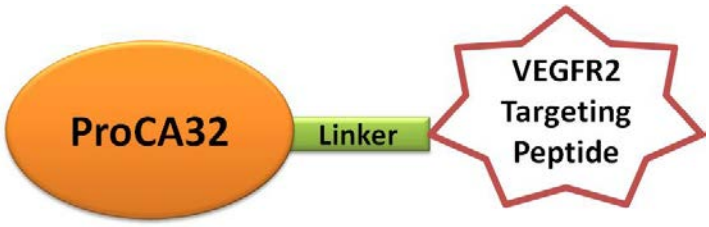


```
ProCA32.SAU       MSMTDLLSAEDIKKAIGAFTAADSFDHKKFFQMVGLKKKSADDVKKVFHILDKDKDGFIE 60
ProCA32.VEGF      MSMTDLLSAEDIKKAIGAFTAADSFDHKKFFQMVGLKKKSADDVKKVFHILDKDKDGFIE 60
                  ************************************************************

ProCA32.SAU       EDELGSILKGFSSDARDLSAKETKTLMAAGDKDGDGKIGVEEWSTLVAESGGGWQP---D 117
ProCA32.VEGF      EDELGSILKGFSSDARDLSAKETKTLMAAGDKDGDGKIGVEEWSTLVAESGGGAGPTWCE 120
                  ********************************************************  *   :

ProCA32.SAU       TAHHWATL------- 125
ProCA32.VEGF      DDWYYCWLFGTGGGK 135
                     ::. *
```

Figure 5.2 Design and Sequence alignment of ProCA32.VEGF.

Top. A carton demonstration of the design of VEGFR-2 targeted ProCA32. VEGFR-2 targeting peptide is fused to the ProCA32 (orange) through a GGG linker (green). Bottom. Sequence alignment of ProCA32.VEGF with ProCA32.SAU

5.2.2 Protein expression and purification

Since the plasmid of ProCA32.VEGF was cloned successfully, we used bacteria *E.Coli* competent cell BL21(DE3)plysS to express the protein. The expression procedure was following the protocol mentioned in Chapter 2. IPTG with 0.5 mM was added to the medium to induce the protein expression when the OD absorbance was up to 0.6 to 0.8. After induction for 3 h at 37°C, the temperature of the shaker was adjusted to 25°C overnight. The speed of the shaker was fixed at 220 rpm. The samples of LB culture before IPTG induction and after IPTG induction overnight were collected separately and run SDS-PAGE to quantify the protein expression. From Fig. 5.3, we can clearly see the expression of ProCA32.VEGF after IPTG induction.

The molecular weight of ProCA32.VEGF is around 11 kDa. As shown in Fig. 5.4, both peak 2 and peak 3 contain ProCA32.VEGF. Peak 3 shows two bands while peak 2 shows one band. The possible reason is because peak 3 contain two kinds of ProCA32.VEGF. One is Ca^{2+}-binding form, another one is Ca^{2+} free form. Maybe the structure of ProCA32.VEGF is rigid even mixed with SDS sample buffer. The apo- form and holo- form of ProCA32.VEGF exhibit different running rate on the SDS-PAGE and thus show two adjacent bands on the gel.

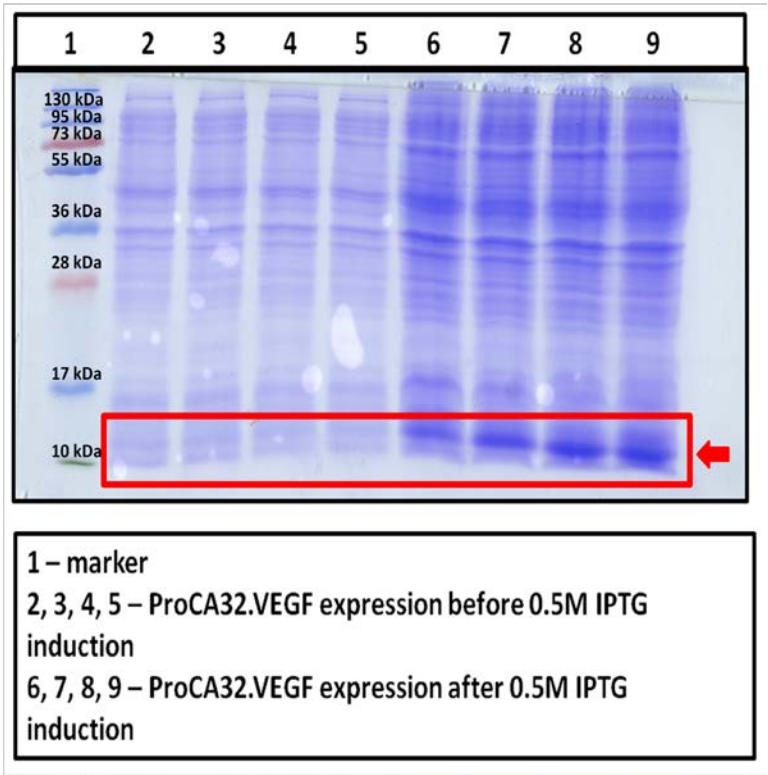

Figure 5.3 ProCA32.VEGF expression before and after IPTG induction.

Lane 1 indicates the protein marker. Lane 2 - 5 represent ProcA32.VEGF expression conditions by bacteria *E.Coli* competent cell BL21(DE3)plysS before 0.5 mM IPTG induction. Lane 6 - 9 represent ProcA32.VEGF expression conditions by bacteria *E.Coli* competent cell BL21(DE3)plysS before 0.5 mM IPTG induction.

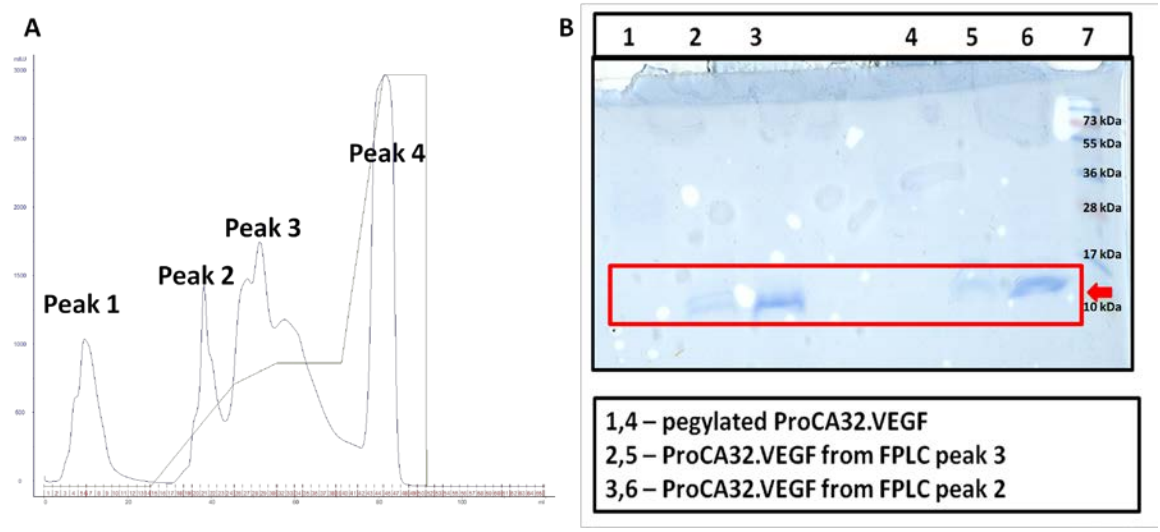

Figure 5.4 Protein purification of ProCA32.VEGF.

A. FPLC spectrum of ProCA32.VEGF purification. B. SDS-PAGE analysis of FPLC peaks. Lane 1 and 4 represent the PEGylated ProCA32.VEGF. Lane 2 and 5 represent the ProCA32.VEGF purified from FPLC equipped with HiTrap Q column peak 3. Lane 3 and 6 represent the ProCA32.VEGF purified from FPLC peak 2. Lane 7 represents the protein marker.

5.2.3 Pegylation of ProCA32.VEGF

To increase the solubility and decrease the immunogenecity of ProCA32.VEGF, we pegylated the protein at a lysine residue by TMS-PEG40. The detailed pegylation protocol was mention in Chapter 2. The molecular weight of PEG40 is 2.3 kDa. Considering the existence of multiple lysine residues in ProCA32.VEGF, the pegylation is not accurately limited to certain residues. In another word, the pegylated products are a mixture of proteins with different pegylation percentage (Fig. 5.5). The unreacted free PEG40 can be removed from the product by a FPLC system. The exact pegylation percentage need to be determined by the following MS study.

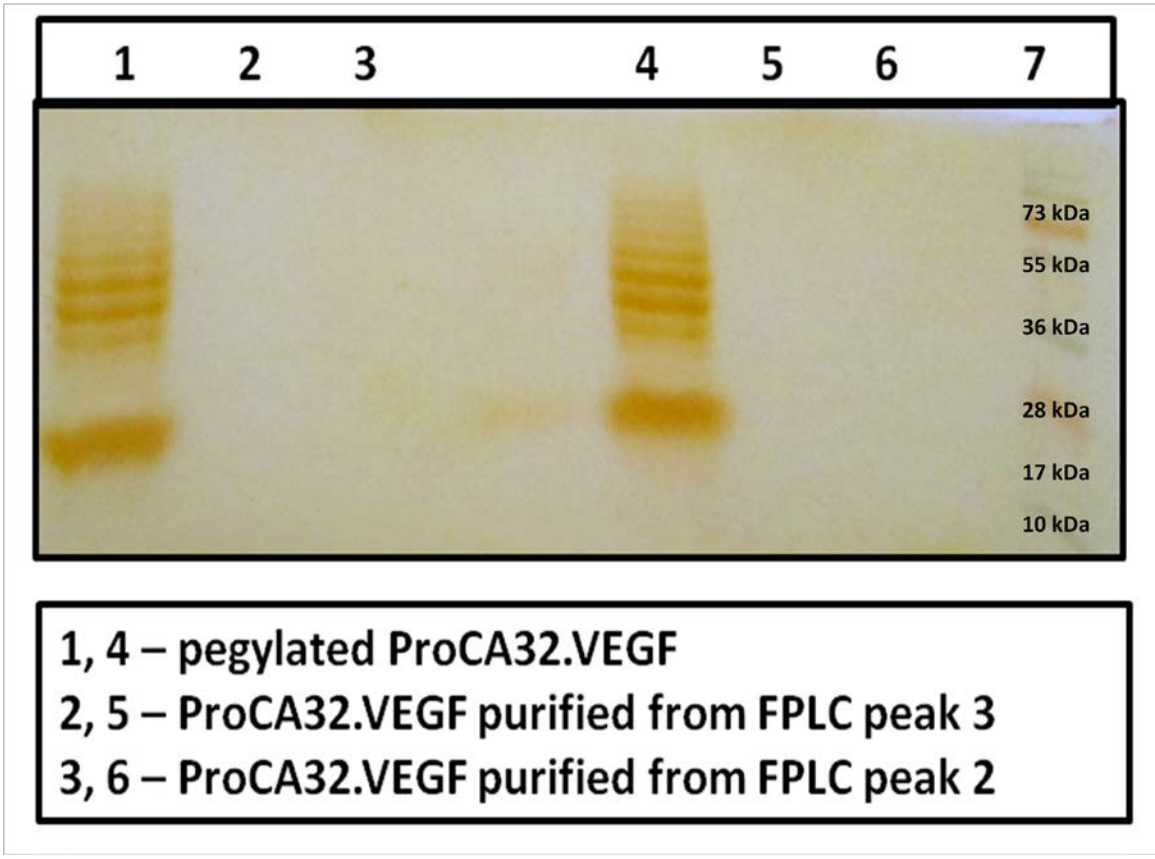

Figure 5.5 Lysine pegylation of ProCA32.VEGF by TMS-PEG40.

Lane 1 and 4 represent the pegylated ProCA32.VEGF. Lane 2 and 5 represent the ProCA32.VEGF purified from FPLC peak 3. Lane 3 and 6 represent the ProCA32.VEGF purified from FPLC peak 2. Lane 7 represents the protein marker.

5.2.4 Relaxivity of ProCA32.VEGF

To probe the efficiency of ProCA32.VEGF as a MRI contrast agent, we did a relaxivity measurement study. ProCA32.VEGF was prepared in 10 mM HEPES buffer at pH 7.4. The ratio of ProCA32.VEGF to Gd^{3+} was fixed at 1:2. The concentration of protein was prepared at 10 µM, 20 µM, 40 µM and 80 µM, respectively. The protein mixed with Gd^{3+} was incubated at 37°C for 5 min and then measure the T1 and T2 values under 1.47 T by Bruker Minispec. The r1 per Gd^{3+}

of ProCA32.VEGF is 31.1 $mM^{-1}s^{-1}$ while the r2 per Gd^{3+} is 43.6 $mM^{-1}s^{-1}$ as indicated in Fig. 5.6. The relaxivity suggests ProCA32.VEGF has good sensitivity even if the concentration is low when it was injected *in vivo*.

5.2.5 The metal binding affinity of ProCA32.VEGF

In order to apply ProCA32.VEGF in *in vivo* detection of VEGFR2, ProCA32.VEGF must have high Gd^{3+} binding affinity compared with other physiological metal ions, such as Ca^{2+}, Mg^{2+} and Zn^{2+}. Low stability of Gd^{3+} to contrast agents will cause the release of the Gd^{3+} *in vivo* due to the competition of physiological metal ions or chelators. The Tb^{3+} binding affinity of ProCA32.VEGF was determined by Tb^{3+}-DTPA buffer system. The free Tb^{3+} concentration can be maintained in the range of 10^{-23} to 10^{-20} M. The fluorescence of Trp in ProCA32.VEGF was excited at 280 nM and it shows enhanced fluorescence signal in 545 nm when free Tb^{3+} concentration is higher than 10^{-22} M due to the fluorescence energy transfer between Tb^{3+} and Trp. The dissociation constant (K_d) between Tb^{3+} and ProCA32.VEGF was 1.4×10^{-21} M. Using the K_d of Tb^{3+} to ProCA32.VEGF, we applied Gd^{3+} competition assay to further determine the interaction K_d of Gd^{3+} to ProCA32.VEGF. As shown in Fig. 5.6, the Tb-Trp FRET signal decreased when the Gd^{3+} concentration increased, suggesting Gd^{3+} has a K_d to ProCA32.VEGF comparable to that of Tb^{3+} to ProCA32.VEGF. The K_d between Gd^{3+} and ProCA32.VEGF was 3.5×10^{-22} M. Such high binding affinity of Gd^{3+} to ProCA32.VEGF suggest that Gd^{3+} loaded ProCA32.VEGF is stable and Gd^{3+} is less likely to be released *in vivo*.

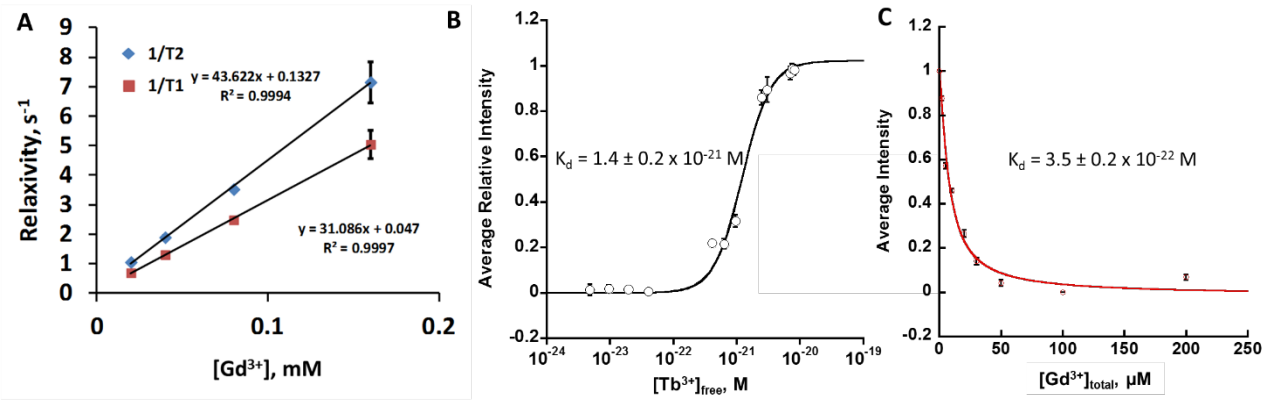

Figure 5.6 Relaxivity (A), Tb^{3+} binding affinity (B) of Gd^{3+} binding affinity (C) of ProCA32.VEGF. A. Relaxivities of ProCA32.VEGF were measured at 37°C under 1.47 T magnetic field in 10 mM HEPES buffer at pH 7.2. Gd^{3+} was loaded to ProCA32 at 2:1 ratio. The relaxivity of the ProCA32.VEGF were calculated based on slop of this plot using linear fitting. B. The Tb^{3+} binding affinity of ProCA32.VEGF was determined using Tb-DTPA buffer system with 30 µM of ProCA32.VEGF, 5 mM DTPA 150 mM NaCl in 50 mM HEPES buffer at pH 7.2. During titration, 0 - 5 mM of $TbCl_3$ were titrated into the system. The fluorescence intensity were collected at each titration points under excitation wavelength of 280 nm and emission wavelength of 545 nm. C. The Gd^{3+} binding affinity of ProCA32.VEGF was determined by Tb^{3+} and Gd^{3+} competition assay 10 µM ProCA32.VEGF, 20 µM of $TbCl_3$ and different concentration of (0 - 200 µM) $GdCl_3$ were mixed in 50 mM HEPES, 150 mM NaCl at pH 7.2. and incubated at room temperature overnight. The fluorescence intensity were collected after overnight incubation under excitation wavelength of 280 nm and emission wavelength of 545 nm.

5.2.6 MRI of B16LS9 melanoma in mice liver

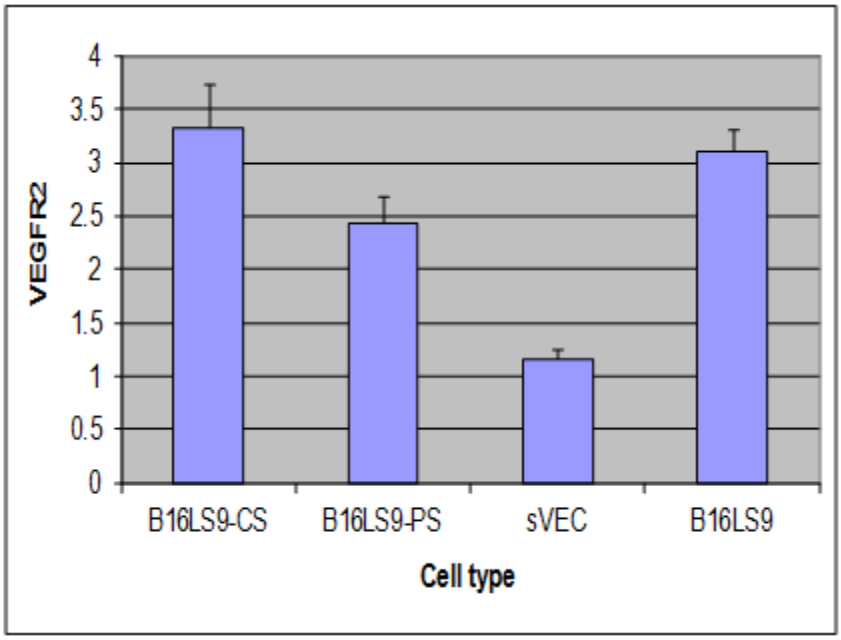

Figure 5.7 VEGFR2 expression in normal and tumor cells.

VEGFR2 expressions in different types of cells were studied by flowcytometery. B16LS9 is mouse melanoma cell line, B16LS9-CS and B16LS9-PS are modified melanoma cells from B16LS9. sVEC is mouse vascular endothelium cells. Melanoma cells shows higher VEGFR2 expression than that of mouse vascular endothelium cells. This experiment was performed by Dr. Hua Yang.

5.2.7 VEGFR-2 expression in various cancer cells

The VEGFR-2 expression levels in cancer and normal cells were studied by Dr. Hua Yang using flow cytometry. Fourteen different cells including two normal cells, eight human melanoma and 5 mouse melanoma cells were studied in this experiment. The VEGFR-2 expression

levels in most human melanoma cells, including 02-1486, Mel270, Mel290, OMM3, and MM2.5, are much lower than that of human vascular endothelium (HUVEC) cells. Other human melanoma cells, such as 92.1 and OCM1, have comparable VEGFR2 expression level in eVECs. On the other hand, mouse vascular endothelium cell (eVEC) shows 2 -3 times lower expression of VEGFR2 than that of mouse melanoma cells, such as B16LS9, B16LS9-CS and B16LS9-PS (Fig. 5.7). B16SL9, B16LS9-CS and B16LS9-PS have the highest VEGFR2 expression level among all the tested normal and tumor cells. Thus, we selected B16SL9 to generate liver implanted mouse model for test the molecular imaging of VEGFR2 targeted ProCA32 in mice.

5.2.8 T2W FSE MRI of B16LS9 melanoma, liver and kidney in mice

Next, we tested the molecular imaging of VEGFR2 using our designed MRI contrast agents in a liver implantation model using mice melanoma cell line B16LS9 created by Dr. Hua Yang in Dr. Hans Grossniklaus group at Emory University. Tumors with a size larger than 1.5 cm were formed in the mice liver after implantation for 10 days. Tumor formation was confirmed by surgery three days before MRI. Transverse section of mice abdomen regions were obtained by both T2-weighted fast spin echo and T1-weighted gradient echo sequences before and after injection of VEGFR-2 targeted MRI contrast agents. Because ProCA32.VEGF have both high per Gd r1 and r2 relaxivities (r1 = 31.1 $mM^{-1}s^{-1}$, r2= 43.6 $mM^{-1}s^{-1}$), we hypothesize that ProCA32.VEGF lead to decreased MRI signal in T2-weighted MRI sequence and ProCA32.VEGF induced increased MRI signal in T1-weighted MRI sequence.

As shown in Fig. 5.7, ProCA32.VEFR caused a decreased MRI signal in the kidney, liver and tumor. Since the liver and kidney is the major organ for the distribution of ProCA32, it was not a surprise to observe the decreased signal in these two organs in T2-weighted fast spin

echo sequence. The MRI signal of the kidney region decreased 5 minutes post injection of ProCA32.VEGF with a signal to noise ratio decrease from 40 to 30. The kidney signal further decreased to 28 after injection of ProCA32.VEGF for 2 hours. The decreased signal of the kidney can serve as a positive control to indicate that ProCA32.VEGF can induce the MRI signal decrease *in vivo* in T2-weighted MRI sequences.

Injection of ProCA32.VEGF also caused the decreased MRI signal in the liver. To better characterize the effects of ProCA32.VEGF in the liver, regions were further divided into normal liver region and unhealthy liver region. The normal liver region refers to the area of liver which does not have any tumor formation, while unhealthy liver region refers to the liver area which has huge tumor growth. The SNR of the normal liver region decreased right after injection. As shown in Fig. 5.8, the SNR of normal liver region decreased from 25 to 23 at 5 min post injection of contrast agents. It further decreased to 20 at 30 min and 19 at 3 hours. On the contrary, no significant decrease was obtained in the unhealthy liver region at 5 min and 30 min post injection of the contrast agent. The SNR of unhealthy liver shows ambient decrease from 23 (pre) to 21 after injection of ProCA32.VEGF. The different MRI signal change in normal and unhealthy liver suggests that the blood architecture and sinusoid space in unhealthy liver region are altered.

Different from liver and kidney signal changes, the tumor signal doesn't show any significant decrease at 5 min and 30 min post injection of ProCA32.VEGF. However, the tumor signal shows dramatic decrease at 3 hours post injection of the MRI contrast agents, suggesting contrast agents were distributed in the tumor region 3 hours post injection of the MRI contrast agents. As a comparison, CXCR4-targeted ProCA32 failed to show any tumor signal decrease at

3 hours suggesting that the tumor signal decrease post injection of ProCA32.VEGF is mediated by the specific interaction between ProCA32.VEGF and tumor biomarker VEGFR2.

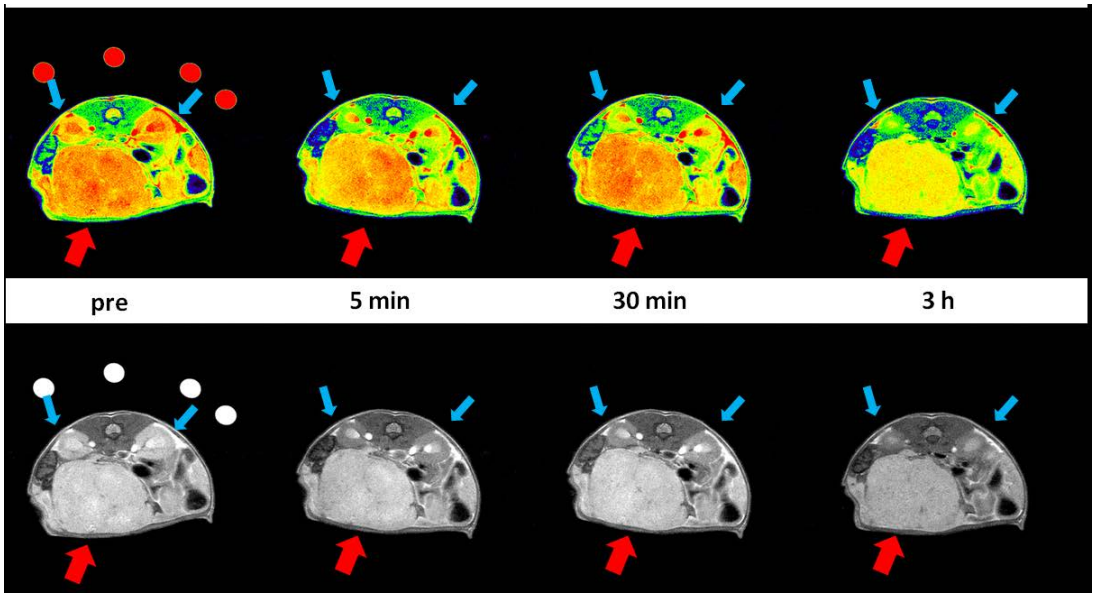

Figure 5.8 Abdomen MRI of liver tumors before and after injection of ProCA32.VEGF in T2-weighted fast spin echo sequence.

MRI was performed at 4.7 T Varian MRI scanner using T2-weighted fast spin echo sequence with TR = 5 s, TE = 28 ms, fov = 4 cm x 4 cm, matrix = 512 x 512, slice thickness = 1 mm. 0.025 mmol/kg ProCA32.VEGF was injected into the tumor mice. MRI was performed before injection of ProCA32.VEGF, and post injection of ProCA32.VEGF at different length of time (5 min, 30 min and 3 h). MR imaging was presented by rainbow color (top) or grey scale color (bottom) based on the MRI intensity in each pixel.

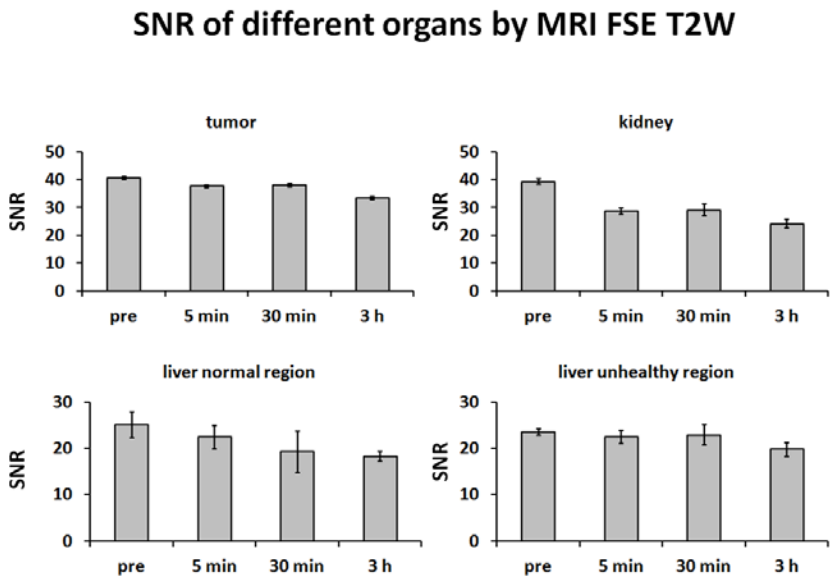

Figure 5.9 MRI SNR of tumor liver and kidney before and after injection of ProCA32.VEGF in T2-weighted fast spin echo sequence.

MRI was performed at 4.7 T Varian MRI scanner using T2-weighted fast spin echo sequence with TR = 5 s, TE = 28 ms, fov = 4 cm x 4 cm, matrix = 512 x 512, slice thickness = 1 mm. 0.025 mmol/kg ProCA32.VEGF was injected into the tumor mice. MRI was performed before injection of ProCA32.VEGF, and post injection of ProCA32.VEGF at different length of time (5 min, 30 min and 3 h).

5.2.8.1 T1W GE MRI of B16LS9 melanoma, liver and kidney in mice

Since ProCA32.VEGF has both high r1 and r2, ProCA32.VEGF could be applied in both T1-weighted MRI and T2-weighted MRI sequence. A T1-weighted gradient sequence was applied to evaluate the capacity of the molecular imaging of VEGFR by ProCA32.VEGF in T1-weighted MRI sequences. As shown in Fig. 5.8 and 5.9, the intensity of the kidney increased about 50% post

injection of ProCA32.VEGF. Such enhancement can serve as a positive control to demonstrate that ProCA32.VEGF can induce enhanced MRI signal in T1-weighted MRI. Consistent with T2-weighted MRI, injection of ProCA32.VEGF does not show dramatic signal change in tumor region at 5 min and 30 min post injection and tumor region shows about 10% signal enhancement at 3 hours post injection of ProCA32.VEGR imaged by T1-weighted gradient echo sequence. As a negative control, a CXCR4-targeted ProCA32 variants failed to enhance the tumor at the same time point in same MRI sequence, suggesting that the tumor enhancement in T1- weighted MRI is mediated by the specific interaction between VEGFR and ProCA32.VEGF.

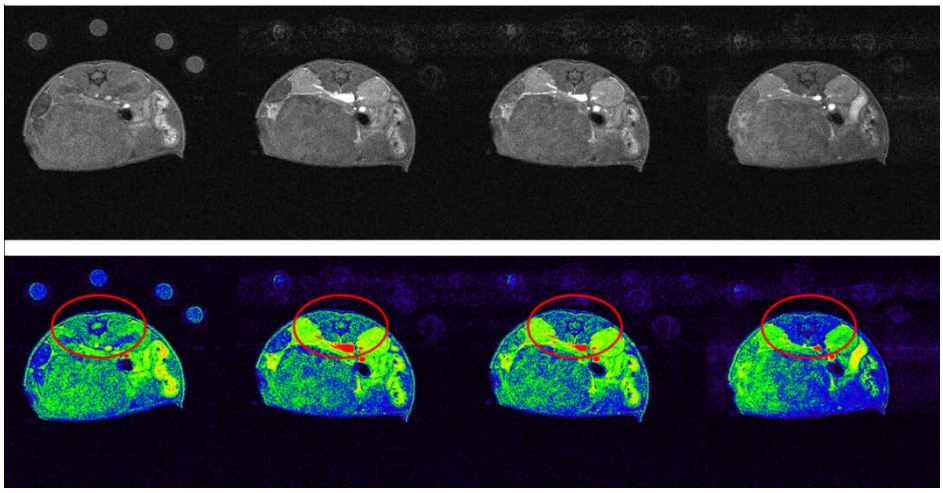

Figure 5.10 Abdomen MRI of liver tumors before and after injection of ProCA32.VEGF in T1-weighted gradient echo sequence.

MRI was performed at 4.7 T Varian MRI scanner using T1-weighted gradient echo sequence with TR = 140 ms, TE = 3.5 ms, fov = 4 cm x 4 cm, matrix = 512 x 512, slice thickness = 1 mm. 0.025 mmol/kg ProCA32.VEGF was injected in tumor mice. MRI was performed before injection of ProCA32.VEGF, and post injection of ProCA32.VEGF at different length of time (5 min,

30 min and 3 h). MR imaging was presented by rainbow color (top) or grey scale color (bottom) based on the MRI intensity in each pixel.

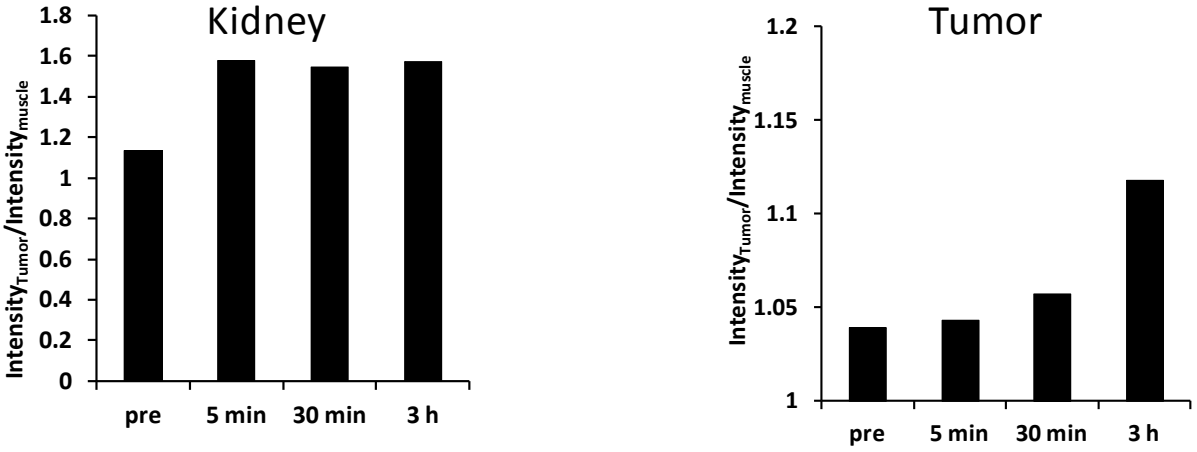

Figure 5.11 MRI Signal differences of tumor and kidney before and after injection of ProCA32.VEGF in T1-weighted gradient echo sequence.

MRI was performed at 4.7 T Varian MRI scanner using T1-weighted gradient echo sequence with TR = 140 ms, TE = 3.5 ms, fov = 4 cm x 4 cm, matrix = 512 x 512, slice thickness = 1 mm. 0.025 mmol/kg ProCA32.VEGF was injected in tumor mice. MRI was performed before injection of ProCA32.VEGF, and post injection of ProCA32.VEGF at different length of time (5 min, 30 min and 3 h).

5.2.8.2 T1/T2 ratio MRI of B16LS9 melanoma, liver and kidney in mice

Since ProCA32.VEGF has both high r1 and r2 relaxivities, I.V. injection of ProCA32.VEGF lead to the decreased signal of tumor in T2-weighted MRI and increased signal of tumor in T1-weighted MRI. To further improve the dynamic range of MRI, we applied the T1/T2 ratio imag-

ing by dividing the signal intensity of corresponding T1-weighted MRI from T2-weighted MRI. As shown in Fig. 5.12, both tumor and kidney showed enhanced signal after injection of ProCA32.VEGF for 3 hours in T1/T2 ratio imaging and no significant enhancement were observed after injection of ProCA32.VEGF in 5 and 30 minutes. This is the first result in the literature to show that T1/T2 ratio imaging can be applied for the molecular imaging of cancer biomarkers.

5.2.8.3 ProCA32.VEGF was distributed in implanted B16LS9 tumor

To further confirm that tumor signal decrease in T2-weighted MRI and tumor signal increase in T1 and T1/T2 ratio MRI, we did immunofluorescence staining of ProCA32 and ProCA32.VEGF in implanted B16LS9 tumor in the liver after I.V. injection of ProCA32 and ProCA32.VEGF, respectively. As shown in Fig. 5.13, no ProCA32 was stained in the tumor and large amount of ProCA32.VEGF were stained in the tumor. Thus, ProCA32.VEGF distributed in tumor region through the VEGFR2-mediated interaction with VEGFR2-targeting peptide in ProCA32.VEGF. This result also support that molecular imaging of VEGFR2 in B16LS9 tumor in T2-weighted, T1-weighted and T1/T2 ratio imaging is caused by the distribution of ProCA32.VEGF through the interaction with VEGFR2.

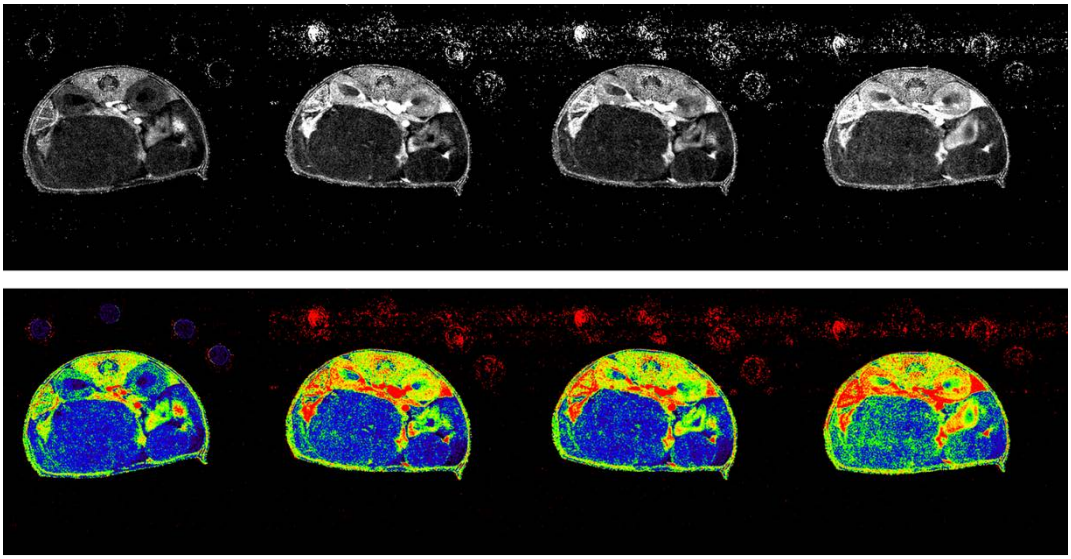

Figure 5.12 Abdomen MRI of liver tumors before and after injection of ProCA32.VEGF in T1/T2 ratio imaging.

Top: T1/T2 ratio imaging displayed by gray scale. Bottom: T1/T2 ratio imaging displayed by pseudo color. T1/T2 ratio imaging were generated by dividing the signal intensity of corresponding T1-weighted MRI from T2-weighted MRI. Both tumor and kidney shows enhanced signal after injection of ProCA32.VEGF in T1/T2 ratio imaging.

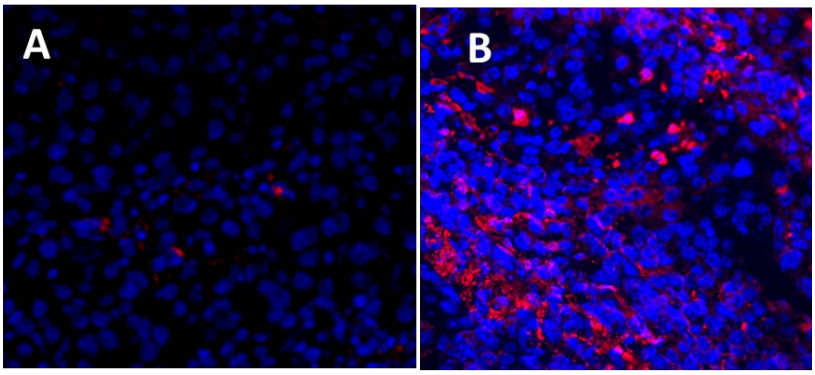

Figure 5.13 Immunofluoresecence staining of ProCA32 (A) and ProCA32.VEGF (B) in B16LS9 tumors.

B16LS9 tumors were implanted in the liver of the mice for less than 2 weeks. After injection of 0.025 mmol/kg of ProCA32.VEGF or ProCA32 for 3 hours, the mice were euthanized and mice liver (with implanted tumor tissue) was isolated for immunofluorescence staining. The ProCA32 or ProCA32.VE in implanted B16LS9 tumors was stained by homemade rabbit anti ProCA32 antibody with 1:1000 dilution and Alexa Fluor 555 conjugated goat anti rabbit 2nd antibody. Blue color standard for nuclear staining by DAPI.

5.2.8.4 ProCA32.VEGF has different distribution in blood and liver.

Interestingly, the T1-weighted gradient MRI shows ProCA32.VEGF dynamic distribution in the liver blood vessel. As show in Fig. 5.14, the blood vessel shows enhanced MRI signal at 5 min post injection of ProCA32.VEGF. Such enhancement is slightly decreased at 30 minutes post injection of ProCA32.VEGF. The blood vessel shows much pronounced enhancement than that liver in 5 min and 30 min post injection of ProCA32.VEGF. However, no blood vessels were enhanced at 3 hours post injection of ProCA32.VEGF. These MR images also suggest that ProCA32.VEGF have short blood half-life less than 3 hours, while liver has much longer half-life.

These results pave a way to generate liver vessel trees using ProCA32-based MRI contrast agents.

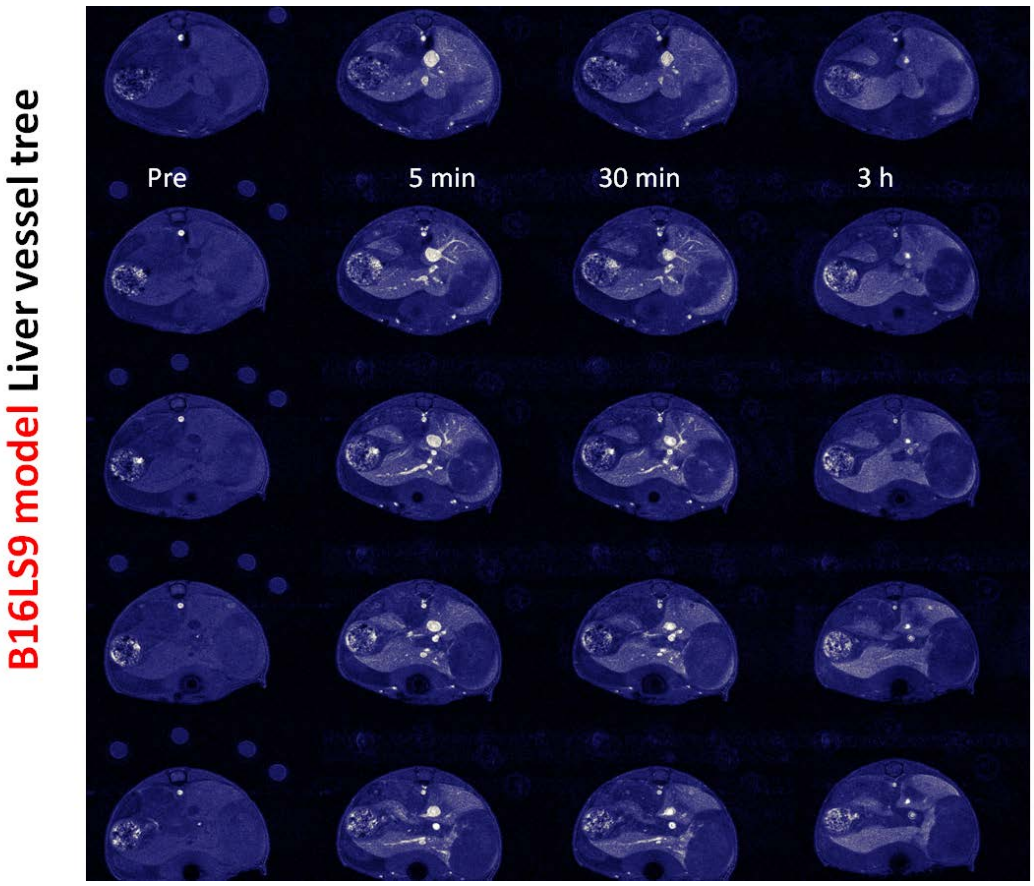

Figure 5.14 Liver vessel trees of B16LS9 melanoma model.

MRI was performed at 4.7 T Varian MRI scanner using T1-weighted gradient echo sequence with TR = 140 ms, TE = 3.5 ms, fov = 4 cm x 4 cm, matrix = 512 x 512, slice thickness = 1 mm. 0.025 mmol/kg ProCA32.VEGF was injected in tumor mice. MRI was performed before injection of ProCA32.VEGF, and post injection of ProCA32.VEGF at different length of time (5 min, 30 min and 3 h).

5.2.8.5 T2W FSE MRI of MCF10DCIS tumor in mice

The VEGRF2 targeting capability of ProCA32.VEGF was also evaluated by breast cancer isotropic model created by Dr. Lily Yang's group at Emory. As shown in Fig. 5.15, MCF10-DCIS tumors shows enhanced MRI signal 3 hours and 1 day post injection of 0.025 mmol/kg ProCA32.VEGF in fast spin sequence. The enhancement decreased 2 day post injections. The enhancement of MRI signal in T2-weighted fast spin echo may suggest that ProCA32.VEGF has much lower distribution in MCF10DCIS tumor compared with that of B16LS9 tumor, as MRI signal could increase in T2-weighted sequence when the ProCAs accumulated in the tissues with lower concentration.

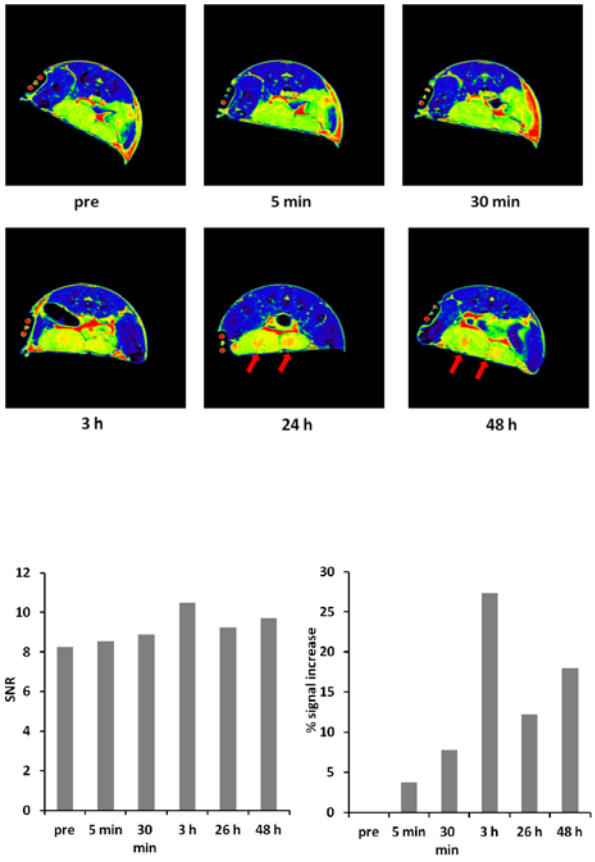

Figure 5.15 MRI of MCF10DCIS tumors before and after injection of ProCA32.VEGF in T2W fast spin echo sequence.

Top. MRI was performed at 4.7 T Varian MRI scanner using fast spin echo sequence with TR = 5 s, TE = 28 ms, fov = 4 cm x 4 cm, matrix = 512 x 512, slice thickness = 1 mm. 0.025 mmol/kg ProCA32.VEGF was injected in tumor mice. MRI was performed before injection of ProCA32.VEGF, and post injection of ProCA32.VEGF at different length of time (5 min, 30 min, 3 h, 24 h and 48 h). Bottom. MRI Signal to noise ratio (SNR. left) and percentage signal increase (right) of tumor before and after injection of ProCA32.VEGF at different time points.

5.2.8.6 T1W GE MRI of MCF10DCIS tumor in mice

We also imaged the MCF10DCIS mice using T1-weighted gradient echo sequence before and after injection of 0.025 mmol/kg ProCA32.VEGF. As shown in Fig. 5.16, NCF10DCIS tumors showed enhanced MRI signal 3 hours post injection, and such enhancement was decreased 2 day post injection. Interestingly, although gradient echo sequence is T1-weighted and fast spin echo sequence in this test is more T2-weighted, the MRI enhancement trend in gradient echo image is very similar to that in fast spin echo sequence. According to simulation, T2-weighted MRI could has enhanced signal when increase MRI contrast agents in low concentration. Thus, these results suggest that ProCA32.VEGF has tumor distribution with low concentration. We will further confirm this conclusion by ICP-OES and IHC.

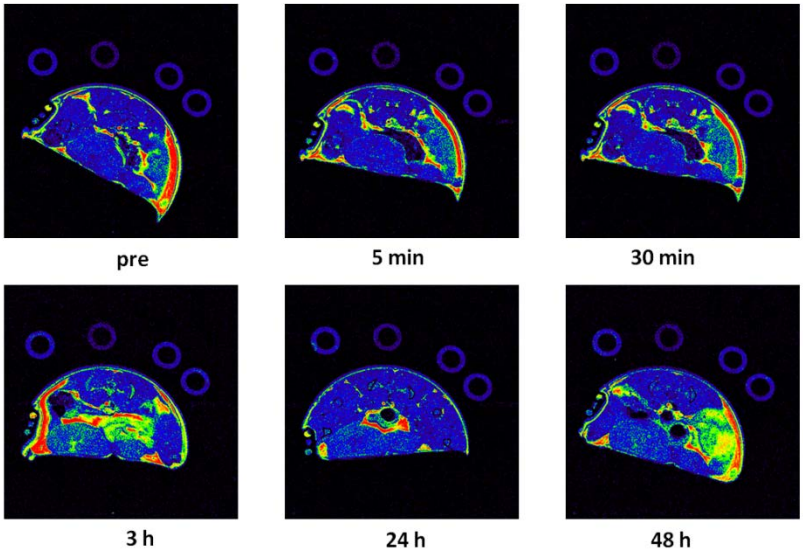

Figure 5.16 T1W GE MRI of MCF10DCIS breast tumor in mice.

0.025 mmol/kg ProCA32.VEGF was injected in tumor mice. MRI was performed at 4.7 T Varian MRI scanner using gradient sequence with TR = 140 s, TE = 3.9 ms, fov = 4 cm x 4 cm, matrix = 512 x 512, slice thickness = 1 mm. MRI was performed before injection of ProCA32.VEGF, and post injection of ProCA32.VEGF at different lengths of time (5 min, 30 min, 3 h, 24 h and 48 h).

5.3 Discussion

5.3.1 Angiogenesis and cancer

Angiogenesis is primarily used to describe a pathological process and development in which new blood vessels generated and is critical for tumor formation, growth, development and metastases. The angiogenesis happened in the early stage of tumor formation, when the tumor reached 1 mm. Tumor growth and maintenance requires large amount of nutrition. The newly formed blood vessels by angiogenesis process help the tumor to get the nutrition they needed. To induce angiogenesis, tumor cells and stroma cells produce various angiogenic pro-

teins, such as vascular endothelial growth factor (VEGF), fibroblast growth factor, and matrix metalloproteinase. VEGF has been identified to play a major role on the angiogenesis of tumor blood vessel. Vascular endothelial growth factor (VEGF) is a homodimeric glycoprotein (45 kDa) and has been identified to stimulate the tumor and endothelia cells signal network. Such signaling transduction in these cells is initiated by membrane receptors in the vascular endothelial growth factor receptor (VEGFR) family.

VEGFR-2 belongs to the receptor tyrosine kinase family. It usually contains an extracelluar domain, a single transmembrane domain and an intracellular domain. Ligand binding induces dimerization and phosphorylation of VEGFR, which serve as the initial steps to transfer extracellular signal to intracellular signal cascade, such as PLCγ/Ca^{2+} pathway, PI3K/AKT pathway, FAK and MAPK pathway, which further regulates cell migration, proliferation, and survival [237].

VEGFR contains three family numbers: VEGFR1, VEGFR2, and VEGFR3. VEGFR2 mediates almost all the cellular responses for VEGF, while VEGFR1 serves as decoy receptor to regulate the cell responses by VEGF. VEGFR-3 responses to VEGFC and VEGFD to regulate lymphangiogenesis.

VEGFR-2 is reported to be expressed in uveal melanoma and cultured uveal melanoma cell lines, such as 92.1. In addition, VEGFR-2 is highly expressed in the tumor blood vessel and play multiples roles as angiogenesis, survival, vescular permeability, cell migration, cell division and actin remodeling [237].

5.3.2 VEGFR-2 expression in various cancer cells

In order to test the molecular imaging of VEGFR2 by MRI, we must carefully select animal models. The VEGFR2 expression level in 14 different cells including two normal cells, 12 melanoma cells were studied by flow cytometry. As shown in Fig. 5.7, mouse vascular endothelium cell (eVEC) shows 2 -3 times lower expression of VEGFR2 than that of mouse melanoma cells, such as B16LS9, B16LS9-CS and B16LS9-PS and B16SL9, B16LS9-CS and B16LS9-PS have the highest VEGFR2 expression level among all the tested normal and tumor cells. Thus, we selected B16SL9 to generate liver implanted mouse *in vivo* MRI tests using ProCA32.VEGF.

5.3.3 The in vitro properties of ProCA32.VEGF

Similar to ProCA32, ProCA32.VEGF has both high r1 and r2 relaxivitys. The relaxivities per Gd of ProCA32.VEGF are 31.0 and 43.6 $mM^{-1}s^{-1}$, respectively. Because ProCA32.VEGF has two Gd binding sites in a single molecule, the relaxivities per particle for ProCA32.VEGF are 62.1 and 87.2 $mM^{-1}s^{-1}$, respectively. Interestingly, the relaxivities per particle r1 and r2 are about 20 times higher than that of Gd-DTPA. Because of such high relaxivities, the sensitivity of ProCA32.VEGF could be much better than that of Gd-DTPA in both T1- and T2- weighted MRI. In addition, the high affinity VEGFR-2 targeting peptide incorporated in this contrast agents made ProCA32.VEGF effectively bind to VEGFR-2 *in vitro* and *in vivo*.

5.3.4 The molecular imaging of VEGFR-2 in mice models after injection ProCA32.VEGF

The VEGFR-2 imaging properties of ProCA32.VEGF were tested in two mice models. First, the imaging properties of VEGFR-2 were tested in uveal melanoma implanted mice. The uveal melanoma was implanted in the liver of the mice for 10 days. 5 mM of 100 µl of PEGylated

ProCA32.VEGF were I.V. injected in mice for tumor imaging. The T1- and T2- weighted MRI were collected before contrast agent injection and 5 min - 3 hours after contrast agent injection. The tumor shows enhanced MRI signal in T1- weighted MRI and shows decreased MRI signal in T2-weighted MRI. These results demonstrate that ProCA32.VEGF can be used for molecular imaging using both T1- weighted MRI and T2- weighted MRI because of high VEGFR-2 binding affinity and high r1 and r2 relaxivities. Interestingly, unlike other biomarker-targeted MRI contrast agents, ProCA32.VEFR enhances the tumor within 3 hours instead of 24 or 48 hours for HER-2 and GRPR imaging. Such times difference are mainly caused by the different location of the biomarkers. VEGFR-2 is a cancer biomarker located on the surface of blood vessel; MRI contrast agents after I.V. injection can easily access these biomarkers. GRPR and HER-2 receptor on the other hand, were expressed on the surface of the tumor cells, which usually deeply buried outside of the blood vessel. In order to bind to GRPR and HER-2, MRI contrast need to escape of the blood vessel, deeply penetrate to the tumor tissue, and bind to the receptors. The unbounded contrast agents need to be washed out to avoid false positive results. Because of such complicated process, the true tumor enhancement through GRPR and HER-2 binding can be observed 24 -48 hours post injection.

The molecular imaging of VEGFR-2 by ProCA32.VEGF was also tested in breast cancer orthotropic mice model using MCF10DCIS cells. Different from the liver implantation model, tumor shows slightly enhanced MRI signal in both T1- and T2- weighted MRI. According to the simulation, MRI contrast agents with both high r1 and r2 relaxivities could cause increase of MRI signal when the contrast agents' concentration is low. Thus, these results suggest that

ProCA32.VEGF can enhance breast cancer in orthotropic mice model with low concentration. Further studies such as ICP-OES and IHC are needed to confirm these findings.

5.4 Conclusion

We designed a VEGFR-2 targeted contrast agent ProCA32.VEGF. This targeted ProCA shows high r1 and r2 relaxivities. Injection of ProCA32.VEGF in implanted uveal melanoma model shows enhanced signal in T1-weighted MRI and shows decreased signal in T2-weighted MRI. ProCA32.VEGF also shows enhance MRI signal in T1-weighted MRI sequence in isotropic breast cancer model. Thus, ProCA32.VEGF is promising to function as T1-weighted and T2-weighted dual reagent for the molecular imaging of VEGFR2. ProCA32.VEGF can be applied to imaging tumor angiogenesis by MRI.

5.5 Future plan

In the next step, Gd^{3+} distribution in different organs need to be analyzed by ICP-OES. The interaction between ProCA32.VEGF and VEGRF2 should be confirmed by ELISA, cell imaging and other methods.

6 A PROTEIN-BASED BLOOD-POOL CONTRAST AGENT: TUNE AND RELAXIVITY

6.1 Introduction

With the development of technology, 3 T clinical MRI scanners have been widely applied in major hospitals for the diagnosis of brain disease and in the research institutes for brain functional study. However, the development of MRI contrast agents is lag behind the development of MRI scanners. Most MRI contrast agents have been reported to have optimized relaxivity at low field strengths ranging from 0.47 – 1.5 T. However, the MRI contrast agents with τ_R-optimized at clinical field do not have optimized τ_R at high field strength [238]. According to SMB theory, Gd^{3+}- based MRI contrast agents have the optimized τ_R at clinical field strength (0.47 T - 1.5 T). The r1 relaxivity values of these contrast agents are dramatically reduced at high field strengths. According to the simulation by Helm [176, 238, 239], the optimized τ_R at 3 T is around 2 ns, while optimized τ_R at 7 T is around 0.5 ns. Interestingly, according to their simulation, contrast agents with a τ_R of 2 ns have a r1 of 20 $mM^{-1}s^{-1}$ at 1.5 T, which is still at least 5 times higher than that of clinical MRI contrast agents at 1.5 T. Thus, we believe that an MRI contrast agent with τ_R of 2 ns and with other optimized other parameters is ideal to be applied to a broad field strengths and especially optimized for the MRI at 3 T.

The size of MRI contrast agents is one of the major factors which influences the *in vivo* distribution and elimination of the MRI contrast agents. In order to achieve faster renal excretion, the particles must have a size less than 7 nm, as the glomeruli in the kidney has a pole size of approximately 7 nm. Cancer is characterized by the abundance of blood vessels with discontinuous vessel walls. Due to this reason, particles can be accumulated in the tumor regions. The efficiency of tumor penetration and retention also depend on the size and charge of the parti-

cle. Dreher shows small molecules such as dextrans with a molecular weight of 4.7 and 10 kDa have a deep tumor penetration, while large molecules such as dextrans with a molecular weight lager than 40 kDa only have limited tumor penetration [104, 176]. Thus, MRI contrast agents with optimized size are highly required for *in vivo* applications. ProCAs with a size of 2 nm has its unique niche for the distribution, elimination, tumor penetration and retention.

Because of the above reasons, we developed a series of novel MRI contrast agents with the smallest protein size, named ProCA4 variants. ProCA4 variants were designed based on Calbindin D9K, the smallest Ca^{2+}-binding protein with two paired EF-hands (75 amino acids; Mr = 8500). Calbindin D9K is a member of EF-hand intracellular calcium-binding proteins family. Calmodulin, parvalbumin, the S-100 proteins and skeletal- and heart-muscle troponin C are well-known members of this family. The EF-hand is consisted of two helices separated by a calcium-binding loop which is typically 12 amino acids long and is wrapped around the Ca^{2+} ion in such a way that the ion is approximately pentagonal bipyrimidal coordinated with oxygen atoms. Different from calmodulin with all canonical EF-hand motifs, Calbinidin D9K has one canonical EF-hand and one pseudo EF-hand motif formed by 14-residue calcium binding loop flanked by two helices. The major function of Calbindin D9K is to control intracellular calcium concentration.

We hypothesize that Calbindin D9K is an ideal scaffold to design protein-based MRI contrast agents with better tissue and tumor penetration and faster renal elimination due to its small size. Metal binding affinity and relaxivity of its variants (ProCA4 variants) can be engineered and optimized by modifying metal binding ligand residues and water coordination.

In this chapter, I summarized my current research on the development of the smallest protein MRI contrast agents based on Calbindin D9K. We name these contrast agents as ProCA4 variants. The tuning of the inner sphere coordination water and the relaxivities of ProCA4 variants are reported in this chapter. We also report the metal binding affinity, selectivity, and *in vivo* MRI properties of ProCA4 variants.

6.2 Results

6.2.1 Design of ProCA4 variants.

The selection of Calbindin D9k as the scaffold protein for designing Gd^{3+} protein-based contrast agent is based on several considerations. First, Calbindin D9K is the smallest calcium binding protein with complete paired Ca^{2+} binding sites in EF-hand motif. Calbindin D9K only has 79 amino acids and almost every amino acid contributes to the formation of EF-hand. This is the smallest number of amino acid we can achieve to design the Gd^{3+} binding protein without sacrificing the metal binding affinity. Second, the calcium binding affinity of Calbindin D9K is about 10^{-6} M. According to our previous studies, sites with higher Ca^{2+} binding affinity usually have higher lanthanide binding affinity, which benefit our design of Gd^{3+} binding protein with extremely high affinity. Third, because of its small size, the r1 relaxivity of ProCA4 could be optimized at high field due to smaller τ_R than that of other protein-based MRI contrast agents. Fourth, the crystal and X-ray structure of Calbinidin D9k is available, which provides plenty of information for the design of Gd^{3+} binding pockets in this protein based on the existing structure information. In addition, since ProCA4 variants have a size of less than 2 nm, they should have good tissue penetration and renal excretion.

We designed several MRI contrast agents (ProCA4 variants based on Calbindin D9k). Calbindin D9k wild type (named ProCA4) is formed by a pair of EF-hand. EF-hand II of ProCA4 is classic EF-hand, which has conserved amino acids at position 1, 3, 5, 7, 9 and 12 to form a pentagonal bipyramid structure to bind metal ions. Among these conserved positions, position 7 uses main chain oxygen to function as a ligand for metal ion. The amino acid of the most conserved positions (1, 3, 5, and 12) use side chain oxygen to serve as metal binding ligands. Position 9 of EF-hand usually bridges with a water molecule to interact with metal ions. We hypothesize that ProCA4 could have strong Gd^{3+} affinity and serves as a contrast agent with significant relaxivity.

As shown in Fig. 6.1, position 9 of ProCA4 is Ser, which interacts with the inner sphere water. Some proteins, such as parvalbumin with high calcium binding affinity, have Glu at position 9. Instead of using bridged water molecule, Glu in position 9 directly interacts with metal ions. Gd^{3+} is trivalent instead of Ca^{2+} which is a divalent metal ion. Gd^{3+} binding usually requires higher numbers of negatively charged residues than calcium binding.

Thus, we hypothesize that mutation Ser 66 to Glu in the position 9 of EF-hand II of ProCA4, can increase Gd^{3+} binding affinity as well as decrease the inner-sphere coordination water. As the inner-sphere coordination water plays a critical role in regulating metal binding affinity and relaxivity, we hypothesize that mutation Ser 66 to Glu (S66E) of EF-hand II further causes the increase of metal binding affinity and decreases relaxivites of ProCA4. We name this new ProCA4 variant as ProCA4 S66E. We have also designed other ProCA4 variants, such as F70W and S28E.

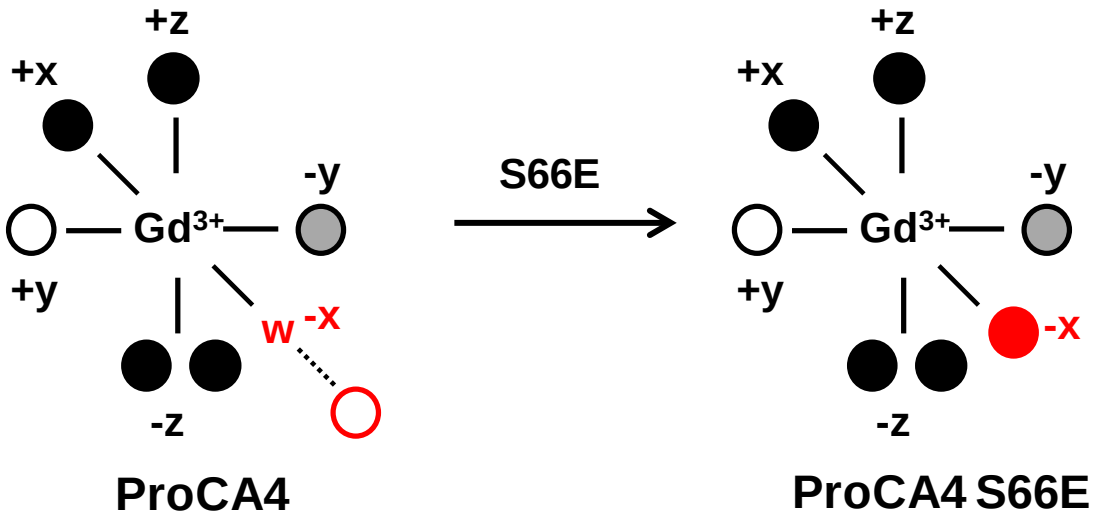

Figure 6.1 Design of ProCA4 variants by increasing the number of charged number residues and reducing the water number at the inner coordination sphere .

We hypothesize that mutation S66E in ProCA4 decreases the water number, which causes an increase in metal binding affinity and decreases relaxivities of ProCA4.

6.2.2 Molecular cloning, expression and purification of ProCA4 variants.

The pUC-ProCA4 plasmid was purchased from ATCC. To express ProCA4 in *E. coli*, ProCA4 DNA was constructed in pRSETb vector. The S66E mutations were generated by site-direct mutagenesis.

ProCA4 variants were expressed by *E. coli* competent cells BL21(DE3)plysS after adding 0.5 - 1 mM IPTG to induce the expression. The cell pellet was harvested after continuously culture at 25 °C overnight. The purification procedure of ProCA4 variants is similar to that of ProCA3.VEGF discussed in Chapter 5. In brief, *E coli* cell pellets were broken by cell disruptor

and sonication. To remove other unwanted proteins, the supernatant of the cell lysate were incubated at 100 °C for 10 min. Most proteins are precipitated at this temperature, while ProCA4 variants remain in the supernatant because of their superior thermo-stability. The DNA was removed by adding Streptomycin Sulfate and incubating at 4 °C overnight. The ProCA4 in the supernatant was further purified by passing it through the HiTrap Q column in FPLC. As show in Fig. 6.2, the purified ProCA4 variants show single band at 8-9 kDa in SDS-PAGE. Since the sequence of ProCA4 variants do not contains Trp, the UV spectrum of ProCA4 variants shows highest peak at 278 nm and low absorbance at 260 nm.

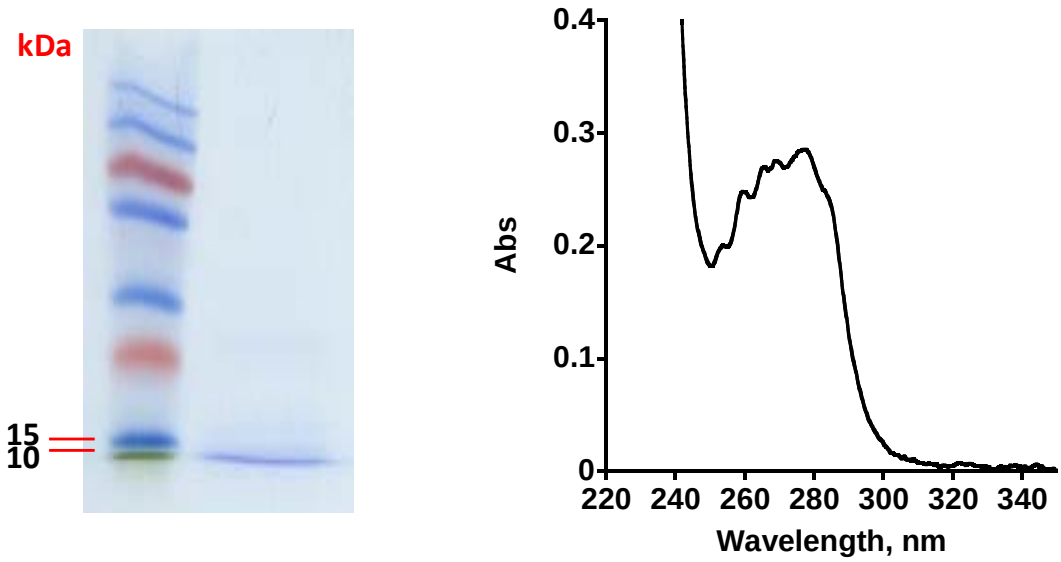

Figure 6.2 Characterization of purified ProCA4 variants by SDS-PAGE (left) and UV spectrum (right).

The UV spectrum of ProCA4 was collected in 10 mM Tris/HCl at pH 7.2 between 220 nm and 350 nm.

6.2.3 Metal stability and metal selectivity of ProCA4

The calcium binding affinity of ProCA4 is determined by Ca^{2+}-EGTA buffer system by monitoring Tyr fluorescence after titration of Ca^{2+} (Fig. 6.3). The dissociation constant between ProCA4 and Ca^{2+} is 1.05 ± 0.11 x 10^{-7} M, which is consistent with reported calcium binding affinity of ProCA4 measured by competition method [240].

In order to function as MRI contrast agents, ProCA4 variants and Gd^{3+} must form stable complex both *in vitro* and *in vivo*. The stability of ProCA4 to Gd^{3+} is determined by Fluo-5N competition assay [212]. As shown in Fig. 6.3, Fluo 5N shows high fluorescence with emission peak at 520 nm, when it forms complex with Gd^{3+}. The fluorescence signal decreased after titrating different concentrations of ProCA4. Apparent K_d in competition assay is 1.01 ± 0.11 x 10^{-6} M, and the Gd^{3+} dissociation constant of ProCA4 is 1.99 ± 0.21 x 10^{-12} M.

Interestingly, ProCA4 has good metal selectivity (pGd/pCa) of 4.8, indicating that Gd^{3+} in ProCA4 is less likely to be competed out of the binding pockets by Ca^{2+} *in vivo*.

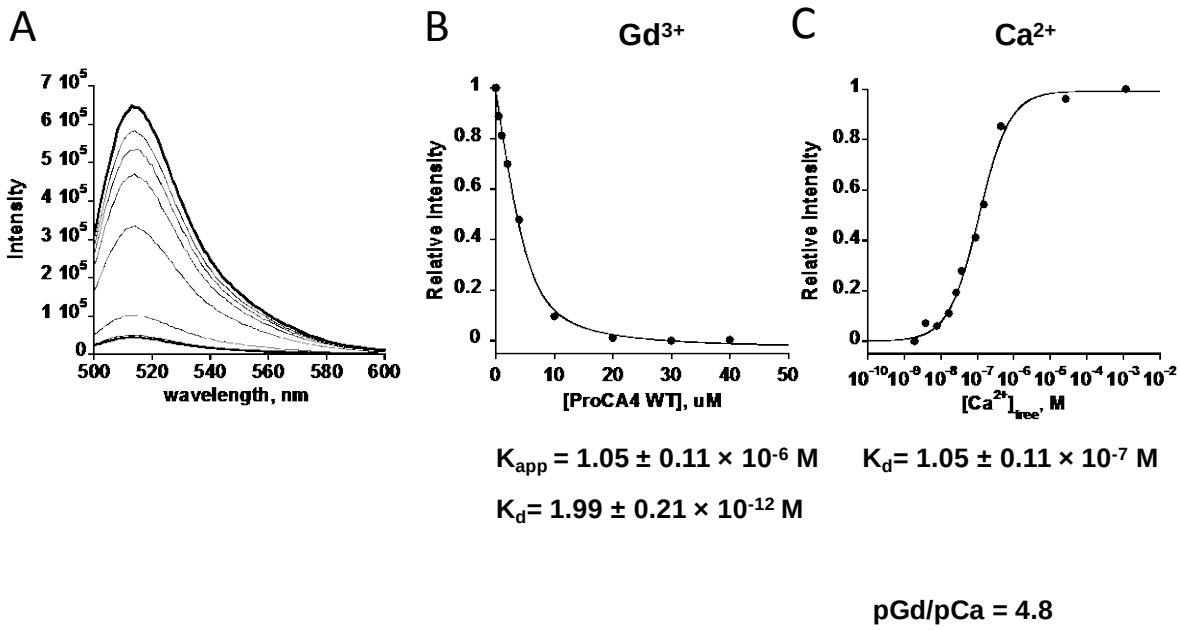

Figure 6.3 Determination of the Gd^{3+} and Ca^{2+} disassociation constants.

A. The emission spectrum of Gd^{3+} loaded Fluo-5N after titration of different concentrations of ProCA4. The fluorescent emission spectra of Fluo-5N were collected by excitation wavelength of 488 nm and emission wavelength between 500 - 600 nm in 50 mM HEPES, 1 µM Fluo-5N and different concentrations of ProCA4. The emission spectrum of Fluo-5N-Gd^{3+} complex decreased after titration with ProCA4, indicating that ProCA4 can compete Gd^{3+} from Fluo-5N. B. Relative fluorescence intensity decreased after adding ProCA4. The fluorescent intensity was collected at exicitation wavelength of 488 nm and emission wavelength of 515 nm after titrating different concentrations of ProCA4. C. Relative Tyr fluorescence signal increased after titrating Ca^{2+} in 10 mM HEPES at pH 7.2, 5 mM EGTA and 5 µM ProCA4. The fluorescence intensities of Trp were collected at excitation wavelength of 280 nm and emission wavelength of 320 nm after titrating different concentration of $CaCl_2$.

6.2.4 Determination of inner sphere water number

Similar to most EF-hand proteins, residues in position 9 in EF-hand II of ProCA4 are bridged with a water molecule. We hypothesize that mutation of S66E in this position will decrease the inner sphere water and Glu will direct the interaction with metal ions instead of using bridged water to interact with metal. Tb^{3+} luminescent life time decay experiments were carried out to test this hypothesis. Tb^{3+} has a long luminescence life time with half-life ranged from sub-mili seconds to a few seconds depending on the Tb^{3+} environment. The interaction with H_2O causes a decrease in luminescence life time of Tb^{3+}, while interaction with D_2O does not cause the significant decrease of luminescence life time of Tb^{3+}. This mechanism can be used to characterize the number of water coordinated in the inner sphere of Tb^{3+}.

As shown in Fig. 6.4A, a linear standard curve was established based on ΔK_{obs}, the decay constant differences of Tb^{3+} in H_2O and D_2O, and water number in DTPA (q = 1), EDTA (q = 3), NTA (q = 5) and Tb^{3+} in aqueous solution (q = 9). Then we determined the inner-sphere water number in ProCA4 and ProCA4 S66E using this method. Fig.6.3B and C show the luminescence life time decay of Tb^{3+} in H_2O and D_2O loaded in ProCA4 and ProCA3 S66E. Consistent with our hypothesis, ProCA4 shows much higher differences in H_2O and D_2O than that of ProCA4 S66E. ProCA4 has a calculated q = 2.71 ± 0.17 and ProCA4 S66E has q = 1.59 ± 0.03. Thus, mutation S66D decreases the inner-sphere water number of ProCA4 variants.

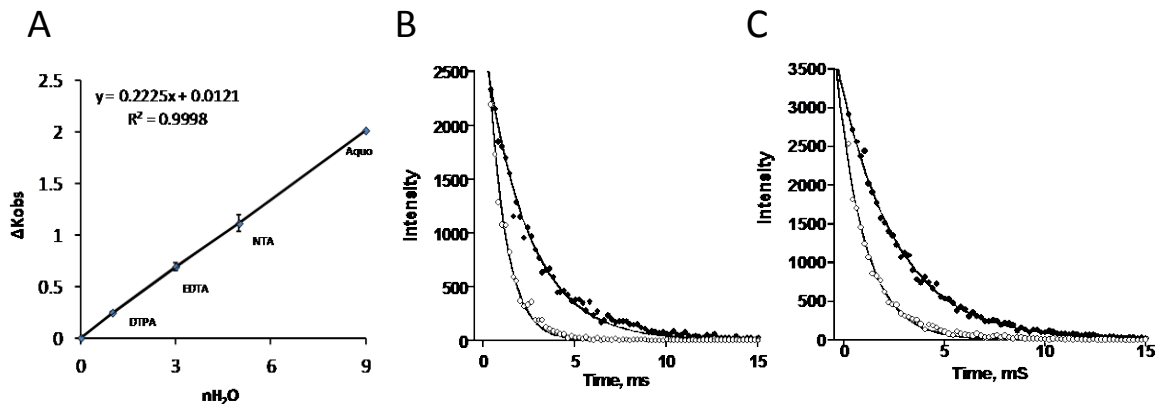

Figure 6.4 Determination of the water number of ProCA4 variants by lifetime luminescence decay experiments.

A. The standard curve of the lifetime luminescence decay experiments based on DTPA (q = 1), EDTA (q = 3), NTA (q = 5) and Tb^{3+} in aqueous solution (q = 9). B. The lifetime luminescence decay difference in H_2O and D_2O for ProCA4. C. The lifetime luminescence decay difference in H_2O and D_2O for ProCA4 S66E. The luminescence life time decays were collected in H_2O or D_2O at pH 7.2 using excitation wavelength of 280 nm and emission wavelength of 545 nm.

6.2.5 The relaxivity of ProCA4 variants.

According to SMB theory, q is one of the key factors to influence the r1 and r2 relaxivities. Decrease of water number leads to the decrease in relaxivity. In the previous section, we demonstrated that mutation S66E decreased inner sphere water number from 2.71 to 1.59. Thus, we hypothesized that S66E decrease both r1 and r2 relaxivities. The r1 and r2 relaxivity of ProCA4 and ProCA4 S66E were determined using 60 MHz relaxometer (Bruker). As shown in Fig.6.5 and Table 6.1, both r1 and r2 relaxivities of ProCA S66E decreased 50% compared with ProCA4. The per Gd r1 and r2 relaxivities of ProCA4 are 24.9 $mM^{-1}s^{-1}$ and 31.5 mM^{-}

$^{1}s^{-1}$, respectively. The per Gd r1 and r2 relaxivities of ProCA4 S66E is 12.7 $mM^{-1}s^{-1}$ and 16.7 $mM^{-1}s^{-1}$, respectively. Since ProCA4 variants have two Gd^{3+} binding sites, the per particle relaxivities for ProCA4 are 49.8 $mM^{-1}s^{-1}$ and 63.0 $mM^{-1}s^{-1}$ for r1 and r2, respectively. The per particle relaxivity for ProCA4 S66E are 25.4 $mM^{-1}s^{-1}$ and 33.4 $mM^{-1}s^{-1}$ for r1 and r2, respectively. These results indicate that S66E mutation decreases the inner sphere coordination water and further causes the decreased r1 and r2 relaxivities compared to ProCA4 wild type.

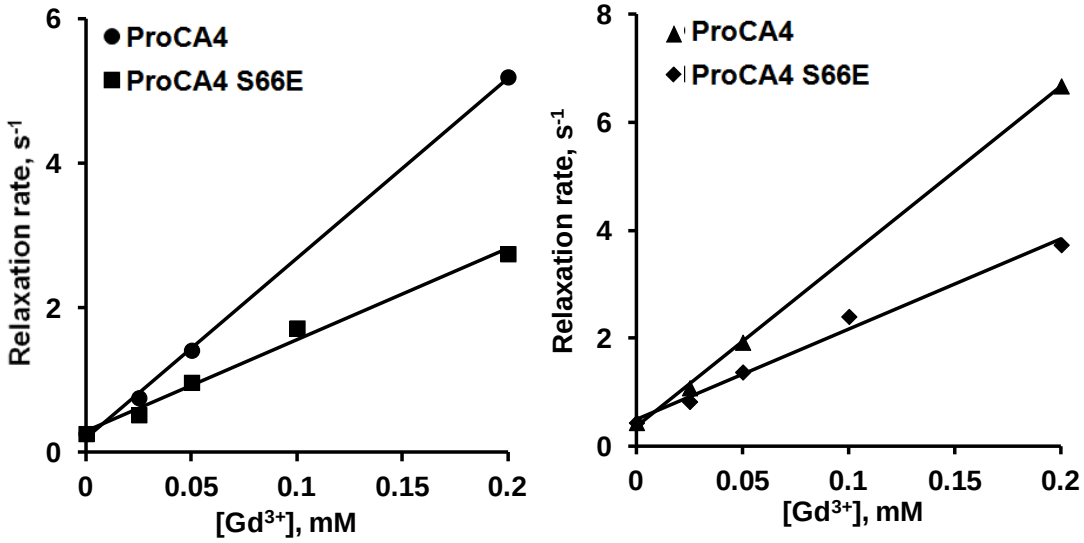

Figure 6.5 r1 (left) and r2 (right) relaxivity of ProCA4 and ProCA4 S66E at 37 °C 60 MHz. The relaxivity of ProCA4 variants was measured in 10 mM HEPES at pH 7.2 using 1.47 T Bruker relaxometer 37 °C. Gd^{3+} was loaded to ProCA4 at 2:1 ratio. The relaxivities of the ProCA4 variants were calculated based on the slope of this plot using linear fitting.

Table 6.1 Per particle relaxivity of ProCA4 and ProCA4 S66E at 37°C in 60 MHZ.

Protein	r_1 (mM^{-1} s^{-1})	r_2 (mM^{-1} s^{-1})
ProCA4	24.9	31.5
ProCA4 S66E	12.7	16.7

6.2.6 MRI of mice before and after injection of ProCA4.

ProCA4 has good metal selectivity, Gd^{3+} stability and high relaxivity. It is very interesting to test whether ProCA4 can function as a MRI contrast agent *in vivo*. In addition, due to the small size, ProCA4 could have a better penetration to the tumor tissue. T1-weighted 3D gradient echo sequence was used to image H441 xenografted mice before and after injection of 70 µl of 5 mM PEGylated ProCA4. As shown in Fig. 6.6, the mice shows nice enhancement of kidney and liver. The kidney enhancement reached to the peak 24 hours post injection. As a negative control tissue, muscle did not have significant enhancement after injection of ProCA4. Interestingly, H441 tumor also shows enhancement after injection of ProCA4 and the enhancement of H441 tumor does not decrease even after injection of ProCA4 for 48 hours.

To further confirm the MRI enhancement, the Gd^{3+} distribution in each organ 48 hours after injection was analyzed by ICP-OES (Fig. 6.9). Consistent with MRI, ProCA4 shows highest distribution in liver, kidney, spleen and tumor. In contrast, we did not detect Gd^{3+} content in mouse muscle that was used as a negative control.

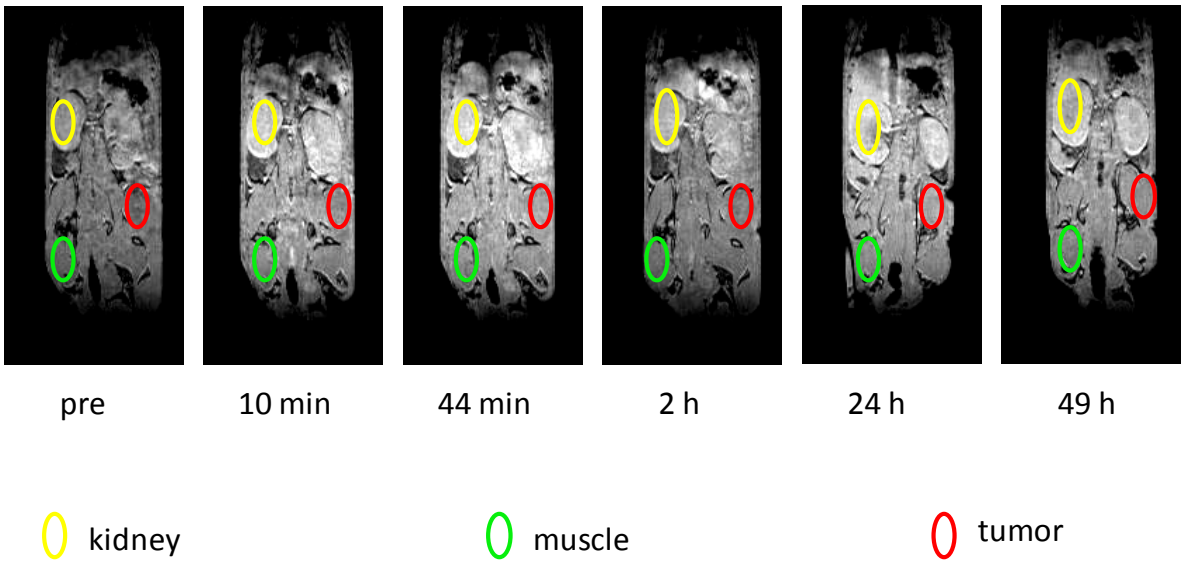

Figure 6.6 MRI of H441 xenografted mice before and after injection of PEGylated ProCA4. T1-weighted 3D gradient echo sequence (TR = 40 ms, TE 2.9 ms, Fov 8 x 4 x 4 cm) was performed to image H441 xenografted mice before and after injection of 70 µl of 5 mM PEGylated ProCA4.

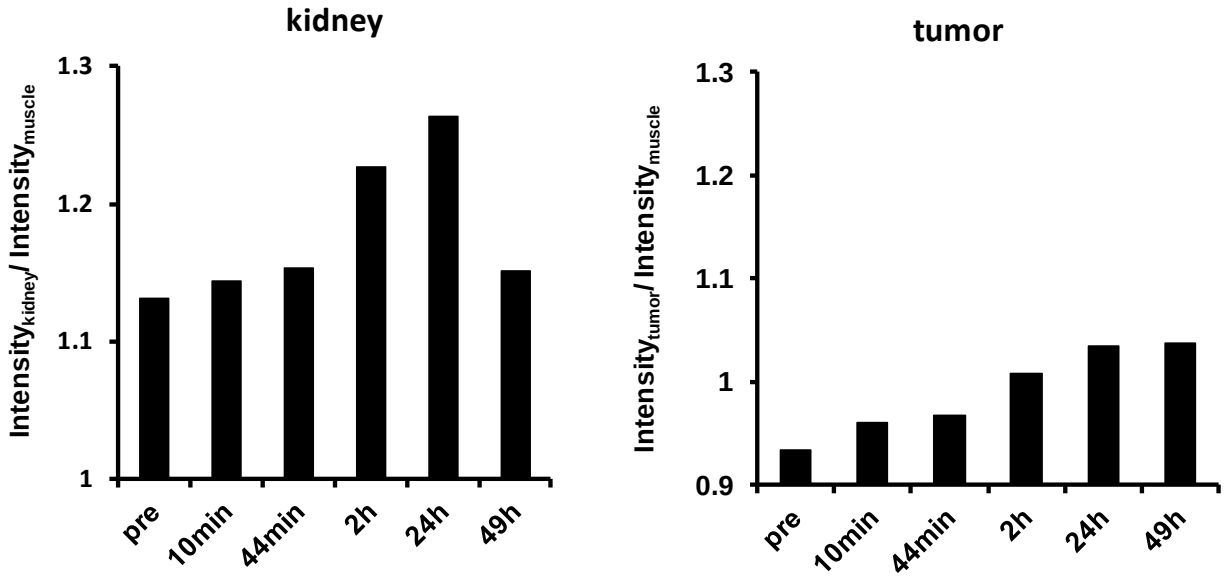

Figure 6.7 Relative MRI signal intensity (the intensity of tissue over the intensity of muscle) of kindey (left) and tumor (right) in H441 xenografted mice before and after injection of PEGylated ProCA4.

T1-weighted 3D gradient echo sequence (TR = 40 ms, TE 2.9 ms, Fov 8 x 4 x 4 cm) was performed to image H441 xenografted mice before and after injection of 70 µl 5 mM PEGylated ProCA4.

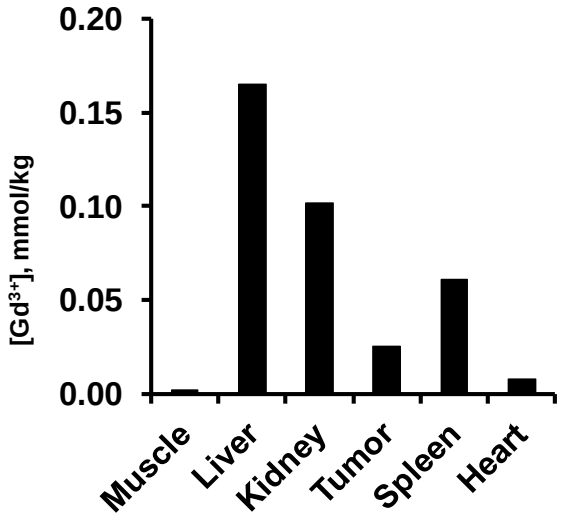

Figure 6.8 Distribution of ProCA4 in tissue after injection for 48 hours.

ProCA4 shows highest distribution in liver, kidney, spleen and tumor after injection of ProCA4 in H441 xenografted mice for 48 hours. As a negative control tissue, ProCA4 does not distribute in muscle.

6.3 Discussion

6.3.1 Modulate Gd^{3+} binding sites in ProCA4

Although both nitrogen and oxygen can be used to chelate Gd^{3+}, Gd^{3+} has a strong preference to utilize oxygen as its ligand. [241] Co-crystallization of Gd^{3+} and proteins always show that Gd^{3+} uses oxygen as its chelator with a strong preference to bind charged oxygen ligands. The average number of oxygen to bind to Gd^{3+} is 7.2. [242]

With 7 oxygen and pentagonal bipyramidal geometry, EF-hand motif became an ideal motif to further design Gd^{3+} binding pocket in proteins. The amino acids in position 1, 3, 5, 7, 9

and 12 of EF-hand form the metal binding sites. Among them, amino acids in position1, 3, 5 and 12 of side chain, main chain oxygen in position 7 and bridged water molecule in position 9 are responsible for the metal binding. Interestingly, the Ca^{2+} binding affinity of EF-hand varies from mM to nM due to their differences in ligand type, ligand charge and dynamic properties in these positions.

Position 9 in canonical EF-hands usually uses a bridged water molecule to bind to metal. Such water ligand can be placed by side chain amino acid of Glu in some proteins, such as parvalbumin [243]. As shown in Fig g.3, ProCA4 has a Gd^{3+} binding affinity of $1.99 \pm 0.21 \times 10^{-6}$ M that is $10^{4.8}$ fold greater than Ca^{2+} (Kd of $1.05 \pm 0.11 \times 10^{-7}$ M). Our study here report the first determination of Gd^{3+} binding of calbindin D9K with a strong Gd^{3+} affinity and metal selectivity over Ca^{2+}.

6.3.2 Tuning the relaxivity by modulating inner sphere water number of ProCA4 variants.

Since the number of coordination water in the inner sphere of Gd^{3+} plays critical role in the stability and relaxivity of the contrast agents. We performed S66E mutation located on the position 9 of the EF-hand II of ProCA4. We hypothesize that S66E mutation decreases the inner-sphere coordination water of ProCA4. As a consequence, the relaxivity of ProCA4S66E will be lower than ProCA4 and the ProCA4S66E has a higher metal stability than that of ProCA4.

The water number of ProCA4 variants was determined by Tb^{3+} luminescence life time decay experiments. The water number of ProCA4 is 2.71 which decrease to 1.59 in ProCA4S66E. Thus, this result suggests that position 9 in EF-hand is a sensitive location to tune the water number and the inner sphere water in position 9 which can be replaced by carboxyl ligand by mutating the original amino acid to Glu. Such mutation also has a profound influence on the

relaxivity of the protein MRI contrast agent. The relaxivity of ProCA4 variants was tested at 60 MHz at 37 °C. The r1 relaxivity of S66E decreased from 24.9 $mM^{-1}s^{-1}$ to 12.7 $mM^{-1}s^{-1}$ and r2 relaxivity decreased from 31.5 $mM^{-1}s^{-1}$ to 16.7 $mM^{-1}s^{-1}$. The relaxivity decrease in S66E mutation is consistent with the water number decrease in S66E mutation suggesting that mutating amino acid to Glu in position 9 of EF-hand can decrease the water number and relaxivity.

6.3.3 ProCA4 distribution and ProCA4 enhanced MRI

The distribution of ProCA4 *in vivo* is studied by MRI and ICP-OES. As shown in Fig.6.6, 6.7 and 6.8, the ProCA4 is mainly distributed in the liver and kidney. The highest distribution of ProCA4 in kidney is achieved at 24 hours. Because of such preferred distribution in liver and kidney, ProCA4 is promising to be applied to detect tumor and other diseases in the liver and kidney. ProCA4 could also be used to evaluate liver and kidney function.

Interestingly, ProCA4 has good tumor penetration and retention because of its small size. As shown in Fig.6.7, the tumor intensity in MRI starts to increase after injection of ProCA4 for 10 minutes, and the MRI signal reached plateau after 24 hours. Different from kidney intensity, the MRI signal intensity of tumor is similar between 24 hours and 48 hours. These results suggest that ProCA4 variants are promising MRI contrast agents for imaging multiple organs and tumors.

6.4 Conclusions

We designed the smallest protein-based MRI contrast agents with two Gd^{3+} binding sites. ProCA4 has Gd^{3+} affinity of $1.99 \pm 0.21 \times 10^{-12}$ M, Ca^{2+} affinity of $1.05 \pm 0.11 \times 10^{-7}$ M and strong metal selectivity (pGd/pCa) of 4.8. ProCA4 also has strong relaxivity of 24.9 $mM^{-1}s^{-1}$ that

is 7 fold greater than DTPA. Mutation S66E can modulate the inner-sphere water number of Gd^{3+}. The inner-sphere water number decreased from 2.71 to 1.59. The r1 relaxivity of S66E decreased from 24.9 $mM^{-1}s^{-1}$ to 12.7 $mM^{-1}s^{-1}$ and r2 relaxivity decreased from 31.5 $mM^{-1}s^{-1}$ to 16.7 $mM^{-1}s^{-1}$. IV injection of ProCA4 in H441 xenografted mice enhances liver, kidney and tumor. These results suggest that ProCA4 variants can be used as MRI contrast agents for imaging multiple organs and tumors.

6.5 Future plan

In the next step, the metal binding affinity (Gd^{3+}, Tb^{3+}, Zn^{2+}, Ca^{2+}) of ProCA4 variants needs to be determined by fluorometer. In addition, the water numbers of ProCA4.S28E need to be determined by luminescence life time decay. The relaxivity of ProCA4.S28E also need to be performed by Bruker Minispec.

7 *LARGE SCALE EXPRESSION, PURIFICATION AND EVALUATION OF PROTEIN-BASED MRI CONTRAST AGENTS*

7.1 Introduction

Exploration of the application of protein-based MRI contrast agents as disease diagnostic tools requires access to the resources to produce a large amount of ProCAs. MR imaging of large animals requires the large amount of ProCAs in order to achieve similar MRI contrast enhancement. A dog of 25 kg requires 1000 times higher amount ProCAs than that of the mice. Thus, an efficient approach with low cost is of great importance for the further application of ProCAs.

Unfortunately, the expression and purification of ProCAs is not a major task. The expression and purification procedures usually take around two weeks. Depending on the expression level of the ProCAs, we can harvest 50 - 100 mg of purified ProCAs from 1 liter medium. If the dog injection dosage is 5 g of ProCAs (1000 times higher amount of ProCAs required in mice), 100 - 200 liters of bacteria cell culture are needed. To express and purify such high amount of ProCAs, a tremendous amount of time and efforts is required. Large scale expression and purification of ProCAs using GMP-like procedures are highly desired. However, establishing such a method requires tremendous time and efforts. In this chapter, I describe our initial trial of the large scale expression and purification of ProCA32. The purified protein was further characterized by SDS-PAGE and UV absorbance.

7.2 Results

7.2.1 Preliminary study of large scale expression and purification of ProCA32

Due to the limited resources, we needed to divide the expression work of ProCA32 in several weeks. ProCA32 was expressed in LB medium with IPTG induction after OD reach 0.6 - 0.8. The bacteria were further cultured at 25 °C over night. The bacteria pellets were harvested by centrifuge at 7000 rpm for 30 minutes. The harvested bacteria were stored at - 80 °C before purification. Fig. 7.1 shows the time scheme of the ProCA32 expression. After expression of the protein for one month, 217.88 g bacteria pellets were harvested from 60 liter LB medium.

7.2.2 Expression and purification of ProCA32

Fig. 7.2 shows that ProCA32 was expressed after IPTG induction. The plasmid PET20b-ProCA32 was transformed into *E. coli* bacteria competent cell strain BL21DE3. The molecular weight of ProCA32 is 11 kDa. As shown in Fig. 7.2, before IPTG induction, lane 2 shows lower level of ProCA32 expression while lane 3-10 shows much stronger expression band of ProCA32 after 100 µl 1 M IPTG induction.

ProCA32 was purified using previously well-established procedure in our lab. The cell pellet was broken using French press. After centrifuge, the supernatant was collected for further purification. After the boiling process to remove most unwanted proteins and DNA contaminants, the protein solutions were injected into Q column by FPLC system to further purify. As shown in Fig. 7.3 SDS-PAGE, lane 2 and 6 represents the protein solution before FPLC. Lane 3, lane 4 and lane 5 represent FPLC peak 1, 2 and 3, respectively. All of lane 3, lane 4 and lane 5 contain a strong band around 11 kDa, and the purity of ProCA32 can reach about 90% according

to the results on the SDS-PAGE. Interestingly, regular SDS-PAGE of FPLC shows two major bands. One possible reason causing double bands on SDS-PAGE is the conformation of the protein. Theoretically, the protein will bind strictly to SDS and the movement of the complex is only related to the mass of the protein. When ProCA32 binds to Ca^{2+}, the structure of the holo-form protein is too rigid to be broken by the SDS, so the bands of ProCA32 represents the conditions of apo- and holo- form mixture as shown in lane 3 and lane 4 (Fig.7.4). After addition of 20 mM EDTA as a calcium chelator to remove calcium in the protein solution, all the ProCA32 exist as apo-form protein as shown in lane 6 and 7(Fig.7.4). We also added 8 M urea to unfold the protein ProCA32 and try to see the difference on SDS-PAGE, but we didn't see the clear band in lane 9 and lane 10. The mechanism behind this phenomenon is under investigation.

The quality of ProCA32 was further analyzed by UV absorbance. As shown in Fig.7.5, the purified ProCA32 shows a unique sharp absorbance peak at 290 nm and a broad absorbance at 280 nm, which are the unique signature peaks for ProCA32. Thus, SDS-PAGE and UV absorbance confirm that the ProCA32 were purified. Finally, 800 mg of ProCA32 were purified from bacteria cultured from 30 liter LB bacterial culture medium, which is 267 mg ProCA32 per liter LB. Thus, it is feasible to use established purification procedure to perform large scale expression and purification of ProCA32.

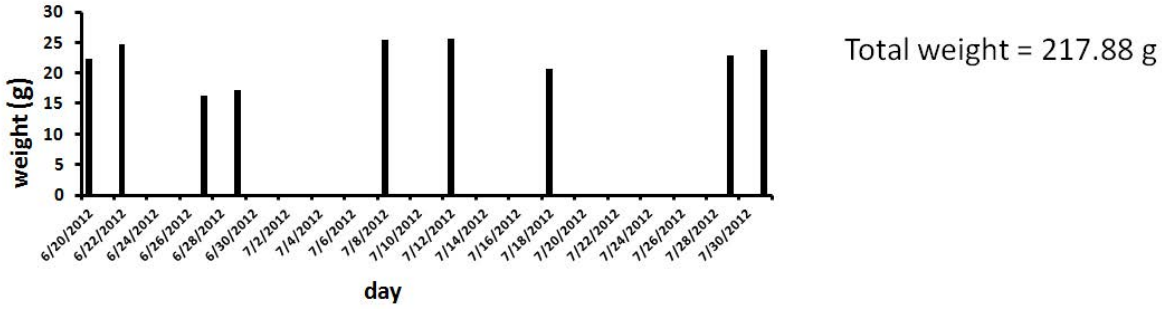

Figure 7.1 ProCA32 cell pellets harvested from 60 L LB culture.

ProCA32 was expressed in *E. Coli* BL21DE3 cells using shaker for 10 times. This whole process takes around 1.5 month. 60 liters LB medium were used to express ProCA32, which yield 217.88 g of bacteria pellets.

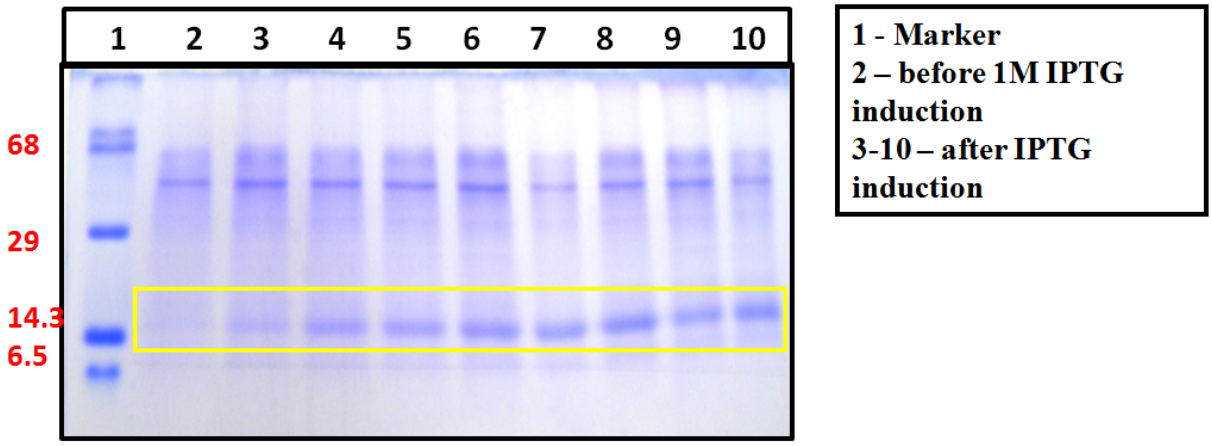

Figure 7.2 Expression of ProCA32 by *E. Coli* bacteria.

Lane 1 indicates the protein marker. Lane 2 represents the expression condition of ProCA32 by *E. coli* bacteria competent cell strain BL21DE3 before 1 M IPTG induction. Lane 3 - 10 represent the expression condition of ProCA32 after 1 M IPTG induction.

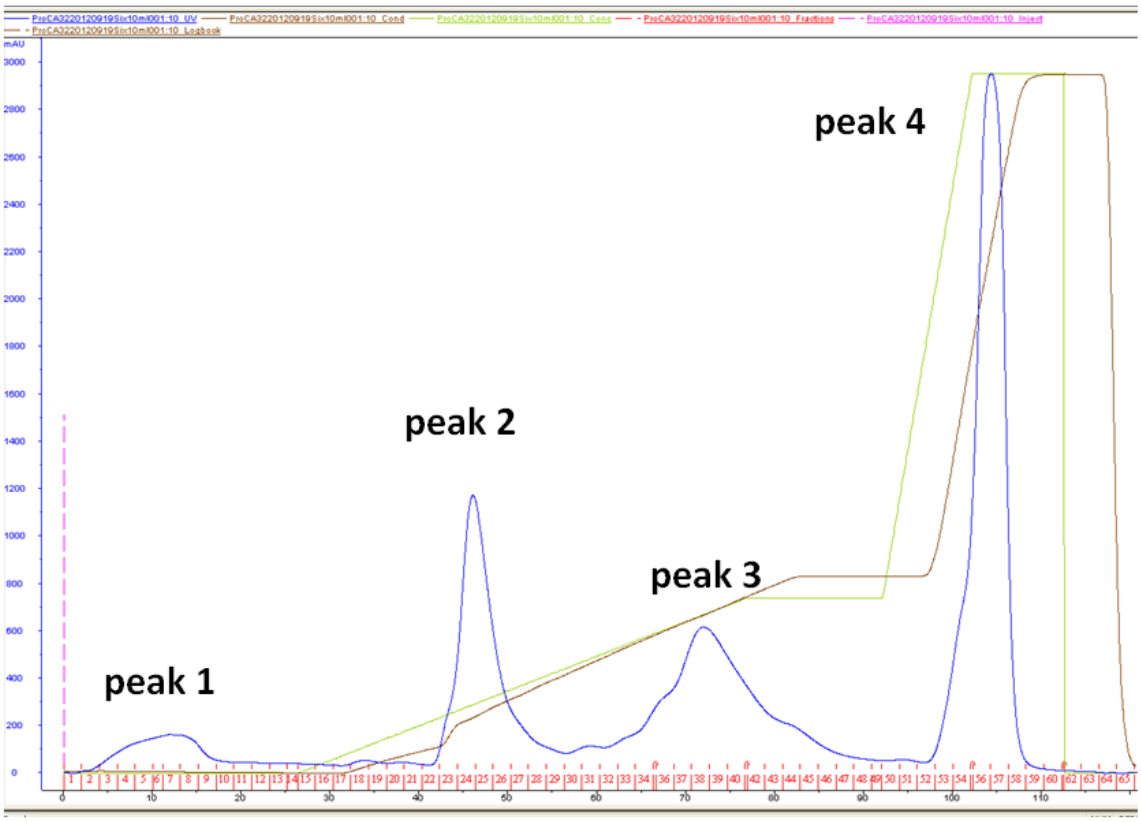

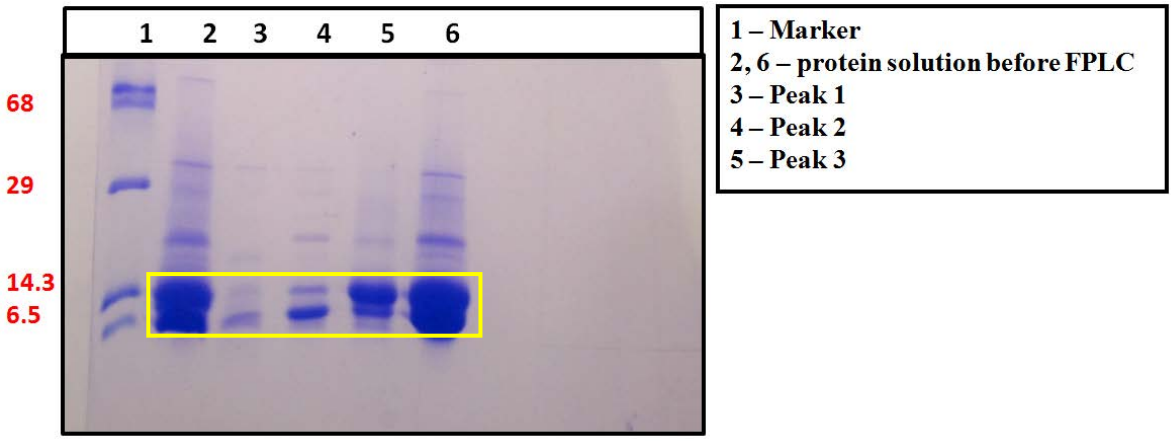

Figure 7.3 Purification of ProCA32 by FPLC.

FPLC spectrum of ProCA32 purification. (Top) SDS-PAGE exhibits the protein purification before and after FPLC. (Bottom) Lane 1 indicates the protein marker. Lane 2 and 6 represent the

ProCA32 solution before FPLC purification. Lane 3, 4 and 5 represent FPLC purification peak 1, 2 and 3 of ProCA32, respectively.

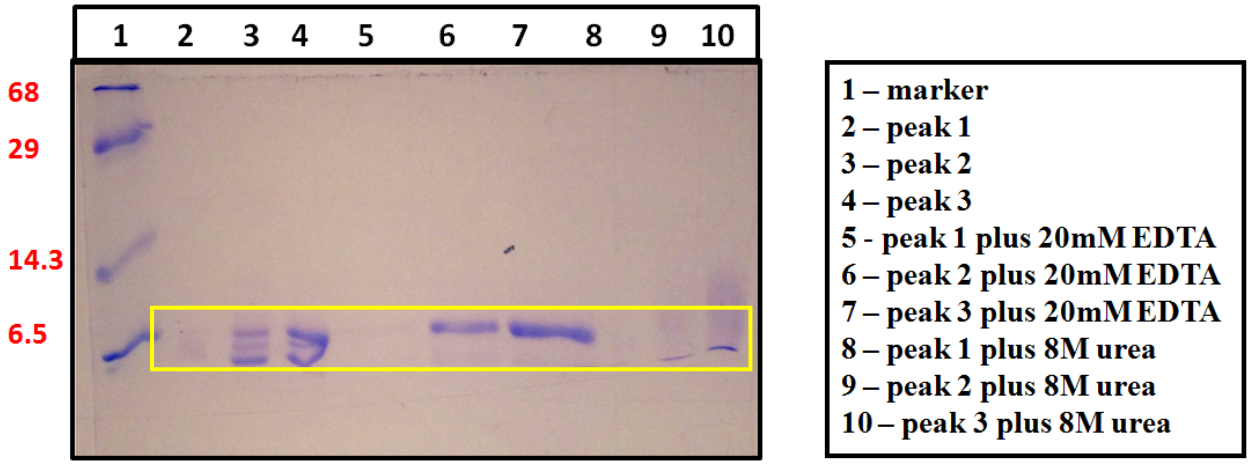

Figure 7.4 Ca^{2+} plays an important role in protein structure.

Lane 1 indicates the protein marker. Lane 2, 3 and 4 represents FPLC purification peak 1, 2 and 3, respectively. Lane 5, 6 and 7 represents samples from peak 1, 2 and 3 plus 20 mM EDTA, respectively. Lane 8, 9 and 10 represents samples from peak 1, 2 and 3 plus 8 M urea, respectively.

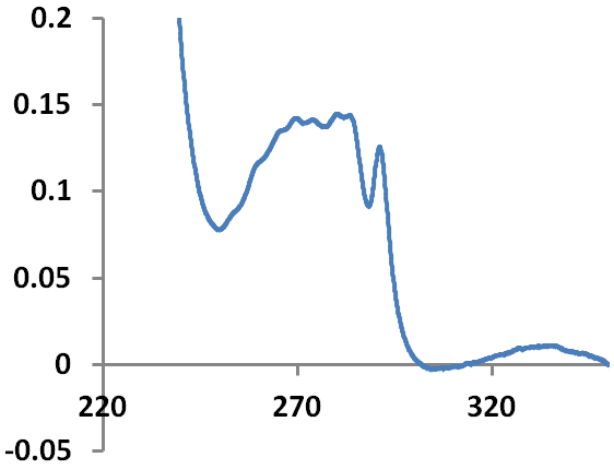

For one mouse:

5mM*100ul=0.005M*0.1/1000L=5E-7mole

For one dog (minimum):

5E-7mole*100=5E-5mole=5E-5*12000=600mg

Total yield: 800mg ProCA32 (coming from cell pellets of 30L culture)

Figure 7.5 Final yield of ProCA32 purified from cell pellets of 30 l LB culture.

After purification and concentration, the final concentration of ProCA32 was determined by UV absorbance. The UV spectrum indicated that the purified protein did not have DNA/RNA contamination. 800 mg ProCA32 were purified from 30 liters bacteria culture. According to the calculation, the minimal injection dosage for one dog is 600 mg ProCA32. Thus, we are able to procedure enough ProCA32 from 30 liters bacteria culture for MRI and PK/PD experiment for one dog.

7.3 Discussion

ProCA32 is a protein-based MRI contrast agent (core size, 11 kDa) with 30 $mM^{-1}s^{-1}$ relaxivity under 1.4 T. It has been reported to detect 0.16 mm uveal melanoma metastasis tumor in liver.[244] Because of its unique magnetic properties, ProCA32 can serve as a strong MRI contrast agent for multiple applications. Translation of this promising imaging-guided therapeutic approach into human clinical trials requires demonstration of the safety and efficacy of ProCA32 study in a larger mammals like dog and primate models.

Because of this reason, we explored the feasibility of large scale expression and purification of ProCA32 using a method originally established for small scale (1 liter LB culture) expression and purification. The results showed that this method is feasible, although time consuming. We were able to harvest 217.88 g of bacteria from 60 liter of LB medium. Due to the limited availability of instrument and equipment, this process took more than 1 month. We further demonstrated that the traditional methods for small scale purification of ProCA32 can be used for large scale purification of ProCA32. SDS-PAGE and UV absorbance analysis confirmed that high quality of ProCA32 was purified by this method.

Although a big achievement has been made for the large scale expression and purification of ProCA32, such expression and purification method have several limitations. First, this expression and purification process is time consuming for large scale production of ProCA32. Second, such expression and purification procedures are not GMP-like procedure and it is hard to adapt this method to the larger expression and purification system. Thus, establishment of GMP-like expression and purification procedures are critical. In the GMP-like procedure, the protein can be expressed using fermentation method, which could easily produce large amount

of protein with low cost and time. Third, endotoxin in protein purified by traditional method is hard to be reduced to the FDA acceptable level and additional procedure to remove endotoxin is a very important step to obtain ProCA32 with high purity and less endotoxin.

7.4 Conclusion

The application of ProCAs to the large animals and different types of animal models requires a large amount of contrast agents. Unfortunately, the traditional small scale expression and purification method only yields around 50 - 100 mg from 1 liter medium. Establishing a feasible approach to attempt large scale expression and purification of ProCAs is critical. To meet the urgent need, I explored the large scale expression and purification methods of ProCA32 according to our lab's well-established small scale expression and purification method. In this chapter, we show that it is possible to produce enough proteins for the MRI of dog using routine procedures to express and purify ProCAs, which requires about 1000 times higher dosage of ProCAs than mouse. More than 200 g of bacteria pellet was harvested after growing the cell culture for one month and around 800 mg ProCA32 were purified from 30 liter LB medium. Thus, this method could be used for the large scale expression and purification, even though it is time consuming and of high cost. We should establish new GMP-like methods to overcome the limitation of current established methods for large scale expression and purification.

8 MAJOR FINDING

Disease biomarkers, especially cancer biomarkers are important indicators of disease formation and progression. Disease biomarkers have been extensively applied in the disease diagnosis for the identification of disease, prediction of disease progression and follow the effects of drug treatment. Image and quantify these biomarkers provides valuable information for the disease evaluation and treatment. Although huge progress has been made during the past few decades, immunohistochemistry after biopsy is still the major approach to evaluate biomarkers. Unfortunately, biopsy is an invasive technique; patient suffers huge pain during this process. Moreover, only limited samples can be collected by biopsy which could easily lead to false positive and false negative results. Therefore, non-invasive imaging techniques, which enables image the biomarker in the whole disease tissue, are in urgent need for the disease diagnosis, especially cancer diagnosis and evaluation.

Although molecular imaging of cancer biomarkers has been widely developed in the PET and SPECT imaging field, the molecular imaging of biomarkers using MRI is under developed. MRI is a powerful imaging technique, which captures the differences between proton signals to generate anatomic structures with high resolution and no depth limitation. Due to these advantages among imaging techniques, MRI became one of the most desired imaging techniques for molecular imaging of disease biomarkers. The major reason which limits the application of MRI for the molecular imaging is the lack of sensitive MRI contrast agents. Most clinical MRI contrast agents have r1 relaxivity of about 5 $mM^{-1}s^{-1}$. In order to generate significant signal change in MRI, a local concentration of at least 30 µM are needed [173]. However, most of biomarkers only have limited local concentration in the nM range or below. Thus, it is impossible

to generate considerable MRI signal change even assuming 100% of the biomarkers bind to the clinical MRI contrast agents with 1 to 1 ratio. In order to generate good signal of biomarkers using MRI, injection of MRI contrast agent with high relaxivity is one of the predominant requirements. In addition, clinical MRI contrast agents are lack of targeting moieties to interact with cancer biomarkers. In order to image biomarkers using MRI, MRI contrast agents must incorporate a biomarker targeting moiety which has high specificity and high affinity to biomarker. Moreover, pharmacokinetics and tissue penetration also play essential roles for the successful imaging. As tumor biomarker buried deeply in the tumor mass which is outside of the blood vessels, antibody-based and nanoparticle-based MRI contrast agents face huge challenges to pass through the blood vessel to access the biomarkers. On the other hand, small molecules, such as Gd-DTPA, has extremely short half-life, which don't have enough time to allow contrast agent to fully interact with these biomarkers. In summary, low relaxivity, none-specific biomarker binding and non-optimized pharmacokinetics and distribution made molecular imaging of biomarkers hard to be achieved.

Our lab developed protein-based MRI contrast agents with 10 - 20 fold higher relaxivity than that of clinical MRI contrast agents. Our previous lab member demonstrated that by fusing ProCA1 with HER-2 affibody, this new MRI contrast agent is able to image HER-2 biomarkers by MRI. [104] Previous lab member also generate GRPR-targeted ProCAs. Unfortunately, the molecular imaging of GRPR is not achieved by IV injection, largely due to the non-optimized GRPR-targeting capability. [139]

Under Dr. Yang's guidance, I developed a series of new GRPR-targeted ProCAs, based on extensive literature study and detailed docking study (chapter 3). Different lengths and types of

GRPR-targeting peptides were inserted into ProCA1 using grating approach. We further demonstrated that these GRPR-targeted ProCAs have extremely high relaxiativity. The per Gd relaxivity of these MRI contrast agents can reach 40 $mM^{-1}s^{-1}$. Thus, these contrast agents are much more sensitive than current existing contrast agents. High relaxivity of these MRI contrast agents provide great advantage for the molecular imaging of biomarker level at low local concentration. We further show that GRPR-targeted ProCAs have comparable metal selectivities compared with clinical MRI contrast agents, suggesting how much Gd^{3+} chelated with contrast agents will be substituted by other physical metals *in vivo*. One of the major limitations for peptide-based targeting moiety is its stability. ProGRP has a serum stability less than 4 hours [196], 6-28% of which is degraded in serum within 2 h. [176, 197] In our design by using grafting approach to insert the peptide in the middle of the ProCA1, we hypothesize that grafting approach improve the serum stability of the peptide. As shown in chapter 3, GRPR-targeted ProCA1 variant were stable in serum for 24 hours, which is at least 6 times more stable than proGRP. Thus, our work clearly demonstrates that grafting approach significantly improve the stability of the targeting peptide *in vivo*, which is another advantage to use protein-based MRI contrast agents for the molecular imaging.

High GRPR binding affinity is another important feature for a good MRI contrast agent to image GRPR. In chapter 3, multiple imaging techniques were applied to evaluate the GRPR-targeting capabilities of ProCA1 variants, including fluorescence imaging, ELISA and Scatchard Plot. Consistent with our docking study, ProCA1B14, which has inserted full length of bombesin sequence in 52 position of ProCA1, shows the best GRPR-targeting capability. Interesting, the binding affinity between GRPR and ProCA1B14 reached to 2.7 nM, such high binding affinity

confirmed that ProCA1B14 can bind to GRPR very strong. Scatchard plot coupled with radioactive probes is a useful method to determine the receptor numbers. Because of the radioactivity of this assay, it could cause potential damage to people if not properly operated. We successfully developed a new Scatchard Plot method using ELISA signal to quantify the bounded ProCAs. Consistent with literature (ref), PC3 has 10^5 receptors per cell and H441 has 10^4 receptors per cell using our new established scatchard plot methods coupled with ELISA.

Since ProCA1B14 has good metal selectivity, high relaxivity, high GRPR binding affinity, and high serum stability, we hypothesize that ProCA1B14 can be applied for the molecular imaging of GRPR in tumor tissue. Our results in chapter 3 demonstrate that ProCA1B14 not only image GRPR, but also semi-quantitatively differentiate the GRPR expression levels between PC3 cells and H441 cells. This is a big achievement, because these results suggest that ProCA1B14 not only can image the GRPR *in vivo*, but also can be used to evaluate biomarker expression levels in different tumors, which can be further applied to evaluate tumor properties non-invasively based on biomarker expression levels instead of biopsy.

Results in chapter 3 also show that ProCA1B14 do not have any acute toxicity by H&E staining and clinical chemistry analysis of mice post injection of ProCA1B14 for 2 days. Thus, we are in a good position to further apply this GRPR-targeted MRI contrast agents in different types of cancers and different types of animal models.

GRPR is not only a biomarker for prostate cancer but also a biomarker for other types of cancers, such as small cell lung cancer (SCLC), breast cancer and ovarian cancer. Recently, GRPR was found to play critical roles in itches, thus, our GRPR-targeted ProCAs could also be applied for diagnosis of itches.

GRPR-targeted ProCAs have broad applications in the detection of different types of cancers, as GRPR is a biomarker for different types of cancers, such as breast cancer, prostate cancer and small cell lung cancer (SCLC). There is also a huge market need for the developed MRI contrast agents which are able to detect specific type of cancer. Such probes could be used to identify certain type of cancer, to track the origin of the metastatic tumor, and some could be also used to evaluate cancer progression.

In chapter 4, we developed a new class of protein-based MRI contrast agents which specifically target primary and metastatic prostate cancer by targeting PSMA, a prostate specific membrane antigen. Prostate cancer is the second leading cause of tumor-related death in men in the western world. Until now, there is still no accurate method developed for diagnosis and prognosis of early-stage prostate cancer. Thus, early detection and evaluation of prostate cancer is urgently needed. PSMA has low expression in all kinds of tissues except prostate and prostate cancer. The PMSA expression level in normal prostate is 10 times higher than that in other types of organs, and the PSMA expression level in prostate cancer is 10 times higher than that in normal prostate. In addition, PSMA is also expressed in the metastatic prostate cancer. Thus, molecular imaging of PMSA by MRI could be applied to detect both primary prostate cancer and metastatic prostate cancer.

Molecular imaging of PSMA is mainly developed by SPECT imaging. Although the MRI has unprecedented resolution than other imaging techniques, the MRI contrast agents which can image PSMA haven't been developed. Such delay is mainly caused by the lack of MRI contrast agents with high sensitivity. The clinical MRI contrast agents has a r1 relaxivity of 3-5 $mM^{-1}s^{-1}$, which means at least 0.03 mM local contrast agent in tumor mass is needed to generate

significant MRI signal changes. We developed protein-based MRI contrast agents with high relaxivity and multiple Gd^{3+} binding sites in a single molecule. Because of the high relaxivity, the sensitivity of the MRI contrast agents dramatically improved. In chapter 4, we linked different PSMA-targeting peptides to the ProCAs for the molecular imaging of PSMA. Our experiments demonstrate that one of our ProCA variants, ProCA32.564 can bind to PSMA with affinity of 0.52 ± 0.04 μM. Such high affinity should be good enough for the *in vivo* targeting PSMA. In addition, the relaxivity of ProCA32.564 was also tested. Similar to non-targeted ProCA32, PSMA-targeted ProCA variant ProCA32.564 have r1 = 27.6 $mM^{-1}s^{-1}$ and r2 = 37.9 $mM^{-1}s^{-1}$. Such high relaxivities provide high sensitivity for the molecular imaging of PSMA. The stability of ProCA32.564 was also determined by fluorescence spectroscopy. Similar to ProCA32, ProCA32.564 has Gd binding affinity of 3.3×10^{-21} M. Thus, this data suggest that PSMA-targeted ProCAs should be stable *in vivo*.

Another important application for molecular imaging of cancer biomarker is to image the angiogenesis. Angiogenesis is an important process for the cancer formation and development. Tumor cells have robust metabolism, and the growth of the tumor cells requires nutrient and energy. Tumors cells with a size larger than 1 – 2 mm requires the growth of the new blood vessel to provide enough nutrition for tumor growth. [245] Since angiogenesis is such an important process for the tumor formation and development, administration of anti-angiogenesis drugs is an effective way for the tumor treatment. The current detection of angiogenesis is mainly relying on the immunohistochemistry staining of the biopsy specimen from the patients. Unfortunately, biopsy detection can only focus on the late stage of the tumor and biopsy is an invasive technique. There is an urgent need to develop novel techniques for the early detection

of angiogenesis at early stage. In chapter 6, we report our development of protein- based MRI contrast agents for the molecular imaging of angiogenesis. VEGFR-2, a transmembrane receptor in the receptor tyrosine kinase family, is a key biomarker for angiogenesis. Upon binding its nature ligands, VEGFs, VEGFR-2 can initiate several downstream pathways, such as PLCγ/Ca^{2+} pathway, PI3K/AKT pathway, FAK and MAPK pathway, which further regulate cell migration, proliferation, and survival. We linked the VEGFR-2 targeted peptide at the C-termimal of ProCA32 so that the newly developed protein MRI contrast agents are able to target VEGFR-2. In chapter 5, we demonstrate that the VEGFR-2 targeted ProCA has both high r1 and r2 relaxivity. The per Gd relaxivities of ProCA32.VEGF are 31.0 $mM^{-1}s^{-1}$ of r1 and 43.6 $mM^{-1}s^{-1}$ of r2, respectively. Because ProCA32.VEGF has two Gd^{3+} binding sites in a single molecule, the per particle relaxivities for ProCA32.VEGF are 62.1 and 87.2 $mM^{-1}s^{-1}$, which are about 20 times higher than the r1 and r2 of Gd-DTPA. High relaxivity makes this protein contrast agent have high sensitivity to detect biomarker (VEGFR-2) at low concentrations. In addition, because both r1 and r2 of the VEGFR-2 targeted ProCAs are high, we hypothesize that this contrast agent can be used for both T1-weighted and T2-weighted MRI sequence for the molecular imaging of biomarkers. Indeed, in chapter 5, we demonstrate that IV injection of these contrast agents in liver implanted tumor model shows enhanced tumor signal in T1-weighted MRI sequence as well as decreased tumor signal in T2-weighted MRI sequence. Thus, this VEGFR-2 targeted MRI contrast agents can be used for the molecular imaging of tumor biomarker by following both T1w and T2w MRI signal. This is the first report in the literature that MRI contrast agents can target biomarkers for the molecular imaging using both T1-weighted and T2- weighted MRI. Such advantage of this MRI contrast agents could improve the specificity and sensitivity of mo-

lecular imaging of biomarkers using both T1-weighted and T2-weighted MRI sequences. This new dual weighted MRI imaging technique can be further used to detect other biomarkers using MRI.

Understanding the ligand type, charge and coordination of Gd^{3+} binding pocket is very important for the successful design of MRI contrast agents. Like other lanthanides, Gd^{3+} prefers oxygen ligand other than nitrogen ligand. The highest coordination number for oxygen to Gd^{3+} is 9. In chapter 6, we designed a new class of MRI contrast agents, ProCA4 variants, based on natural Ca^{2+} binding protein, Calbindin D9k. We demonstrate that the water number of ProCA4 variants can be tuned by replacing non-charged residue, Ser66, to charge residue, Glu. Thus, Glu provide two oxygen ligands to Gd^{3+} and decrease water number. In chapter 6, we also demonstrate that water coordination number can be tuned by protein design. As the water number in S66E mutants decrease, the relaxivity of S66E mutants also decrease 50% compared to wild type. In addition, according to the simulation, ProCA4 could also have high relaxivity at high magnetic field because of the small size and fast τ_R. Moreover, because of the small size, ProCA4 has great advantages for better penetration of the tumor tissue and faster renal elimination. We further show that ProCA4 is able to be applied for the *in vivo* MRI in mice with significant enhancement of liver, kidney and muscle. Thus, ProCA4 could be a promising MRI contrast agent with high relaxivity at clinical field and high field, and high tumor penetration.

To apply ProCAs to the large animals, such as dogs and monkeys, requires huge amount of contrast agents. However, the current flask shaking method only yields around 50 – 100 mg from 1 liter LB medium. Thus, establishing a feasible approach to large scale expression and purification of ProCAs is very essential to explore new applications of ProCAs, and it is also critical

to commercialization of ProCAs. In chapter 7, we demonstrate that it is achievable to produce enough proteins for the MRI of dog using routine procedures to express and purify ProCAs, which requires about 1000 times higher dosage of ProCAs than that of mouse. We also show that the UV absorbance, protein purity, and NMR spectrum of these large scale purified proteins are similar to that from small scale purification. Such effects will be much helpful for the commercialization of ProCAs, to explore the application of ProCAs in disease models in large animals.

In summary, in my Ph.D work, I developed several biomarker-targeted protein-based MRI contrast agents for the molecular imaging of cancer, such as prostate cancer and breast cancer. These targeted MRI contrast agents exhibit superior properties compared with clinical MRI contrast agents, such as high r1, r2 relaxivities, high metal binding affinity and selectivities, high biomarker-targeting affinity and specificity, optimized pharmacokinetics and tissue distribution. In addition, we developed smallest non-targeted protein MRI contrast agents, ProCA4 variants, with high relaxivity. Because of its small size, ProCA4 variants exhibit several unique properties, such as high tumor penetration and high relaxivity at high field. We also demonstrate that the water coordination number and relaxivity can be tuned by protein design. In addition, I also explored the large scale expression and purification of ProCAs. These contrast agents could be applied as useful tools for the disease diagnosis and following disease treatment.

9 REFERENCES

1. Routh, J.C. and B.C. Leibovich, *Adenocarcinoma of the prostate: epidemiological trends, screening, diagnosis, and surgical management of localized disease.* Mayo Clin Proc, 2005. **80**(7): p. 899-907.
2. Cowherd, S.M., *Tumor staging and grading: a primer.* Methods Mol Biol, 2012. **823**: p. 1-18.
3. Gleason, D.F., *Classification of prostatic carcinomas.* Cancer Chemother Rep, 1966. **50**(3): p. 125-8.
4. Orozco, R., et al., *Observations on pathology trends in 62,537 prostate biopsies obtained from urology private practices in the United States.* Urology, 1998. **51**(2): p. 186-95.
5. O'Dowd, G.J., et al., *Update on the appropriate staging evaluation for newly diagnosed prostate cancer.* J Urol, 1997. **158**(3 Pt 1): p. 687-98.
6. Epstein, J.I., K. Lecksell, and H.B. Carter, *Prostate cancer sampled on sextant needle biopsy: significance of cancer on multiple cores from different areas of the prostate.* Urology, 1999. **54**(2): p. 291-4.
7. O'Dowd G, J., et al., *Analysis of repeated biopsy results within 1 year after a noncancer diagnosis.* Urology, 2000. **55**(4): p. 553-9.
8. Sakr, W.A., et al., *Gleason score 7 prostate cancer: a heterogeneous entity? Correlation with pathologic parameters and disease-free survival.* Urology, 2000. **56**(5): p. 730-4.
9. Chan, T.Y., et al., *Prognostic significance of Gleason score 3+4 versus Gleason score 4+3 tumor at radical prostatectomy.* Urology, 2000. **56**(5): p. 823-7.
10. Epstein, J.I., *Gleason score 2-4 adenocarcinoma of the prostate on needle biopsy: a diagnosis that should not be made.* Am J Surg Pathol, 2000. **24**(4): p. 477-8.
11. Simmons, M.N., R.K. Berglund, and J.S. Jones, *A practical guide to prostate cancer diagnosis and management.* Cleve Clin J Med, 2011. **78**(5): p. 321-31.
12. Graves, H.C., *Nonprostatic sources of prostate-specific antigen: a steroid hormone-dependent phenomenon?* Clin Chem, 1995. **41**(1): p. 7-9.
13. Monne, M., et al., *Molecular characterization of prostate-specific antigen messenger RNA expressed in breast tumors.* Cancer Res, 1994. **54**(24): p. 6344-7.
14. Yu, H. and E.P. Diamandis, *Prostate-specific antigen in milk of lactating women.* Clin Chem, 1995. **41**(1): p. 54-8.
15. Menez, R., et al., *Crystal structure of a ternary complex between human prostate-specific antigen, its substrate acyl intermediate and an activating antibody.* J Mol Biol, 2008. **376**(4): p. 1021-33.
16. Balk, S.P., Y.J. Ko, and G.J. Bubley, *Biology of prostate-specific antigen.* J Clin Oncol, 2003. **21**(2): p. 383-91.
17. Selley, S., et al., *Diagnosis, management and screening of early localised prostate cancer.* Health Technol Assess, 1997. **1**(2): p. i, 1-96.
18. Seaman, E., et al., *PSA density (PSAD). Role in patient evaluation and management.* Urol Clin North Am, 1993. **20**(4): p. 653-63.

19. Bretton, P.R., et al., *The use of prostate specific antigen density to improve the sensitivity of prostate specific antigen in detecting prostate carcinoma.* Cancer, 1994. **74**(11): p. 2991-5.
20. Leventhal, E.K., et al., *The effects of exercise and activity on serum prostate specific antigen levels.* J Urol, 1993. **150**(3): p. 893-4.
21. Kane, R.A., et al., *Prostate-specific antigen levels in 1695 men without evidence of prostate cancer. Findings of the American Cancer Society National Prostate Cancer Detection Project.* Cancer, 1992. **69**(5): p. 1201-7.
22. Lee, F., et al., *Predicted prostate specific antigen results using transrectal ultrasound gland volume. Differentiation of benign prostatic hyperplasia and prostate cancer.* Cancer, 1992. **70**(1 Suppl): p. 211-20.
23. Catalona, W.J., et al., *Detection of organ-confined prostate cancer is increased through prostate-specific antigen-based screening.* JAMA, 1993. **270**(8): p. 948-54.
24. Catalona, W.J., et al., *Use of the percentage of free prostate-specific antigen to enhance differentiation of prostate cancer from benign prostatic disease: a prospective multicenter clinical trial.* JAMA, 1998. **279**(19): p. 1542-7.
25. Davis, M.I., et al., *Crystal structure of prostate-specific membrane antigen, a tumor marker and peptidase.* Proc Natl Acad Sci U S A, 2005. **102**(17): p. 5981-6.
26. Stura, E.A., et al., *Crystal structure of human prostate-specific antigen in a sandwich antibody complex.* J Mol Biol, 2011. **414**(4): p. 530-44.
27. Borley, N. and M.R. Feneley, *Prostate cancer: diagnosis and staging.* Asian J Androl, 2009. **11**(1): p. 74-80.
28. Washington, S.L., et al., *Transrectal ultrasonography-guided biopsy does not reliably identify dominant cancer location in men with low-risk prostate cancer.* BJU Int, 2011.
29. Ruutu, M. and A. Rannikko, *Words of wisdom. Re: Active surveillance for the management of prostate cancer in a contemporary cohort. Dall'Era MA, Konety BR, Cowan JE, Shinohara K, Stauf F, Cooperberg MR, Meng MV, Kane CJ, Perez N, Master VA, Carroll PR. Cancer 2008;112:2664-70.* Eur Urol, 2009. **55**(1): p. 244-5.
30. Mullerad, M., et al., *Comparison of endorectal magnetic resonance imaging, guided prostate biopsy and digital rectal examination in the preoperative anatomical localization of prostate cancer.* J Urol, 2005. **174**(6): p. 2158-63.
31. Kattan, M.W., et al., *A preoperative nomogram for disease recurrence following radical prostatectomy for prostate cancer.* J Natl Cancer Inst, 1998. **90**(10): p. 766-71.
32. D'Amico, A.V., et al., *Biochemical outcome after radical prostatectomy or external beam radiation therapy for patients with clinically localized prostate carcinoma in the prostate specific antigen era.* Cancer, 2002. **95**(2): p. 281-6.
33. Megwalu, II, et al., *Evaluation of a novel precision template-guided biopsy system for detecting prostate cancer.* BJU Int, 2008. **102**(5): p. 546-50.
34. Flanigan, R.C., et al., *Accuracy of digital rectal examination and transrectal ultrasonography in localizing prostate cancer.* J Urol, 1994. **152**(5 Pt 1): p. 1506-9.
35. Carter, H.B., et al., *Evaluation of transrectal ultrasound in the early detection of prostate cancer.* J Urol, 1989. **142**(4): p. 1008-10.

36. Catalona, W.J., et al., *Comparison of digital rectal examination and serum prostate specific antigen in the early detection of prostate cancer: results of a multicenter clinical trial of 6,630 men.* J Urol, 1994. **151**(5): p. 1283-90.
37. Babaian, R.J., et al., *The relationship of prostate-specific antigen to digital rectal examination and transrectal ultrasonography. Findings of the American Cancer Society National Prostate Cancer Detection Project.* Cancer, 1992. **69**(5): p. 1195-200.
38. Babaian, R.J. and J.L. Camps, *The role of prostate-specific antigen as part of the diagnostic triad and as a guide when to perform a biopsy.* Cancer, 1991. **68**(9): p. 2060-3.
39. Cooner, W.H., et al., *Prostate cancer detection in a clinical urological practice by ultrasonography, digital rectal examination and prostate specific antigen.* J Urol, 1990. **143**(6): p. 1146-52; discussion 1152-4.
40. Drago, J.R. and J.P. York, *Prostate-specific antigen, digital rectal examination, and transrectal ultrasound in predicting the probability of cancer.* J Surg Oncol, 1992. **49**(3): p. 172-5.
41. Nachman, R.L., *The thrombotic process in atherogenesis. Summary of workshop a: endothelium.* Adv Exp Med Biol, 1978. **104**: p. 247-56.
42. Cooner, W.H., et al., *Prostate cancer detection in a clinical urological practice by ultrasonography, digital rectal examination and prostate specific antigen. 1990.* J Urol, 2002. **167**(2 Pt 2): p. 966-73; discussion 973-5.
43. Mettlin, C., et al., *The American Cancer Society National Prostate Cancer Detection Project. Findings on the detection of early prostate cancer in 2425 men.* Cancer, 1991. **67**(12): p. 2949-58.
44. Baran, G.W., et al., *Biologic aggressiveness of palpable and nonpalpable prostate cancer: assessment with endosonography.* Radiology, 1991. **178**(1): p. 201-6.
45. Brawer, M.K., N.R. Ploch, and S.A. Bigler, *Prostate cancer tumor location as predicted by digital rectal examination transferred to ultrasound and ultrasound-guided prostate needle biopsy.* J Cell Biochem Suppl, 1992. **16H**: p. 74-7.
46. Mettlin, C., *Early detection of prostate cancer following repeated examinations by multiple modalities: results of the American Cancer Society National Prostate Cancer Detection Project.* Clin Invest Med, 1993. **16**(6): p. 440-7.
47. Chodak, G.W. and H.W. Schoenberg, *Early detection of prostate cancer by routine screening.* JAMA, 1984. **252**(23): p. 3261-4.
48. Chodak, G.W., P. Keller, and H.W. Schoenberg, *Assessment of screening for prostate cancer using the digital rectal examination.* J Urol, 1989. **141**(5): p. 1136-8.
49. Varenhorst, E., et al., *Repeated screening for carcinoma of the prostate by digital rectal examination in a randomly selected population.* Acta Oncol, 1992. **31**(8): p. 815-21.
50. Pedersen, K.V., et al., *Screening for carcinoma of the prostate by digital rectal examination in a randomly selected population.* BMJ, 1990. **300**(6731): p. 1041-4.
51. Ghai, S. and A. Toi, *Role of transrectal ultrasonography in prostate cancer.* Radiol Clin North Am, 2012. **50**(6): p. 1061-73.
52. Watanabe, H., et al., *Development and application of new equipment for transrectal ultrasonography.* J Clin Ultrasound, 1974. **2**(2): p. 91-8.

53. Watanabe, H., *History and applications of transrectal sonography of the prostate.* Urol Clin North Am, 1989. **16**(4): p. 617-22.
54. Bree, R.L., *The role of color Doppler and staging biopsies in prostate cancer detection.* Urology, 1997. **49**(3A Suppl): p. 31-4.
55. Pelzer, A., et al., *Prostate cancer detection in men with prostate specific antigen 4 to 10 ng/ml using a combined approach of contrast enhanced color Doppler targeted and systematic biopsy.* J Urol, 2005. **173**(6): p. 1926-9.
56. Roy, C., et al., *Contrast enhanced color Doppler endorectal sonography of prostate: efficiency for detecting peripheral zone tumors and role for biopsy procedure.* J Urol, 2003. **170**(1): p. 69-72.
57. Turkbey, B., et al., *Functional and molecular imaging: applications for diagnosis and staging of localised prostate cancer.* Clin Oncol (R Coll Radiol), 2013. **25**(8): p. 451-60.
58. Kim, C.K., B.K. Park, and B. Kim, *Localization of prostate cancer using 3T MRI: comparison of T2-weighted and dynamic contrast-enhanced imaging.* J Comput Assist Tomogr, 2006. **30**(1): p. 7-11.
59. Nakashima, J., et al., *Endorectal MRI for prediction of tumor site, tumor size, and local extension of prostate cancer.* Urology, 2004. **64**(1): p. 101-5.
60. Turkbey, B., et al., *Correlation of magnetic resonance imaging tumor volume with histopathology.* J Urol, 2012. **188**(4): p. 1157-63.
61. Bouchelouche, K., et al., *Imaging prostate cancer: an update on positron emission tomography and magnetic resonance imaging.* Curr Urol Rep, 2010. **11**(3): p. 180-90.
62. Panebianco, V., et al., *Conventional imaging and multiparametric magnetic resonance (MRI, MRS, DWI, MRP) in the diagnosis of prostate cancer.* Q J Nucl Med Mol Imaging, 2012. **56**(4): p. 331-42.
63. Tan, C.H., et al., *Diffusion-weighted MRI in the detection of prostate cancer: meta-analysis.* AJR Am J Roentgenol, 2012. **199**(4): p. 822-9.
64. Wu, L.M., et al., *Usefulness of diffusion-weighted magnetic resonance imaging in the diagnosis of prostate cancer.* Acad Radiol, 2012. **19**(10): p. 1215-24.
65. Iraha, Y., et al., *Diffusion-weighted MRI and PSA correlations in patients with prostate cancer treated with radiation and hormonal therapy.* Anticancer Res, 2012. **32**(10): p. 4467-71.
66. Rinaldi, D., et al., *Role of diffusion-weighted magnetic resonance imaging in prostate cancer evaluation.* Radiol Med, 2012. **117**(8): p. 1429-40.
67. Jung, J.A., et al., *Prostate depiction at endorectal MR spectroscopic imaging: investigation of a standardized evaluation system.* Radiology, 2004. **233**(3): p. 701-8.
68. Ocak, I., et al., *Dynamic contrast-enhanced MRI of prostate cancer at 3 T: a study of pharmacokinetic parameters.* AJR Am J Roentgenol, 2007. **189**(4): p. 849.
69. Nicholson, B., G. Schaefer, and D. Theodorescu, *Angiogenesis in prostate cancer: biology and therapeutic opportunities.* Cancer Metastasis Rev, 2001. **20**(3-4): p. 297-319.
70. Concato, J., et al., *Molecular markers and mortality in prostate cancer.* BJU Int, 2007. **100**(6): p. 1259-63.
71. Noworolski, S.M., et al., *Dynamic contrast-enhanced MRI and MR diffusion imaging to distinguish between glandular and stromal prostatic tissues.* Magn Reson Imaging, 2008. **26**(8): p. 1071-80.

72. Pinto, F., et al., *Imaging in prostate cancer staging: present role and future perspectives.* Urol Int, 2012. **88**(2): p. 125-36.
73. Bloch, B.N., et al., *Prostate cancer: accurate determination of extracapsular extension with high-spatial-resolution dynamic contrast-enhanced and T2-weighted MR imaging--initial results.* Radiology, 2007. **245**(1): p. 176-85.
74. Jadvar, H., *Molecular imaging of prostate cancer with PET.* J Nucl Med, 2013. **54**(10): p. 1685-8.
75. Hara, T., N. Kosaka, and H. Kishi, *PET imaging of prostate cancer using carbon-11-choline.* J Nucl Med, 1998. **39**(6): p. 990-5.
76. Oyama, N., et al., *MicroPET assessment of androgenic control of glucose and acetate uptake in the rat prostate and a prostate cancer tumor model.* Nucl Med Biol, 2002. **29**(8): p. 783-90.
77. Rietbergen, D.D., et al., *Mediastinal lymph node uptake in patients with prostate carcinoma on F18-choline PET/CT.* Nucl Med Commun, 2011. **32**(12): p. 1143-7.
78. DeGrado, T.R., et al., *Pharmacokinetics and radiation dosimetry of 18F-fluorocholine.* J Nucl Med, 2002. **43**(1): p. 92-6.
79. Brogsitter, C., K. Zophel, and J. Kotzerke, *18F-Choline, 11C-choline and 11C-acetate PET/CT: comparative analysis for imaging prostate cancer patients.* Eur J Nucl Med Mol Imaging, 2013. **40 Suppl 1**: p. S18-27.
80. Watanabe, H., et al., *Preoperative detection of prostate cancer: a comparison with 11C-choline PET, 18F-fluorodeoxyglucose PET and MR imaging.* J Magn Reson Imaging, 2010. **31**(5): p. 1151-6.
81. Mariani, G., et al., *A review on the clinical uses of SPECT/CT.* Eur J Nucl Med Mol Imaging, 2010. **37**(10): p. 1959-85.
82. Romer, W., et al., *Assessment of aseptic loosening of the acetabular component in a total hip replacement with 99mTc-DPD-SPECT/spiral-CT hybrid imaging.* Nuklearmedizin, 2005. **44**(6): p. N58-60.
83. Gao, X. and S. Nie, *Molecular profiling of single cells and tissue specimens with quantum dots.* Trends Biotechnol, 2003. **21**(9): p. 371-3.
84. Jaiswal, J.K. and S.M. Simon, *Potentials and pitfalls of fluorescent quantum dots for biological imaging.* Trends Cell Biol, 2004. **14**(9): p. 497-504.
85. Alivisatos, A.P., W. Gu, and C. Larabell, *Quantum dots as cellular probes.* Annu Rev Biomed Eng, 2005. **7**: p. 55-76.
86. Smith, A.M., et al., *Multicolor quantum dots for molecular diagnostics of cancer.* Expert Rev Mol Diagn, 2006. **6**(2): p. 231-44.
87. Ballou, B., L.A. Ernst, and A.S. Waggoner, *Fluorescence imaging of tumors in vivo.* Curr Med Chem, 2005. **12**(7): p. 795-805.
88. Song, L., et al., *Photobleaching kinetics of fluorescein in quantitative fluorescence microscopy.* Biophys J, 1995. **68**(6): p. 2588-600.
89. Kim, S., et al., *Near-infrared fluorescent type II quantum dots for sentinel lymph node mapping.* Nat Biotechnol, 2004. **22**(1): p. 93-7.
90. Tanaka, E., et al., *Image-guided oncologic surgery using invisible light: completed pre-clinical development for sentinel lymph node mapping.* Ann Surg Oncol, 2006. **13**(12): p. 1671-81.

91. Kirchner, C., et al., *Cytotoxicity of colloidal CdSe and CdSe/ZnS nanoparticles.* Nano Lett, 2005. **5**(2): p. 331-8.
92. Lin, Z., et al., *A novel aptamer functionalized CuInS2 quantum dots probe for daunorubicin sensing and near infrared imaging of prostate cancer cells.* Anal Chim Acta, 2014. **818**: p. 54-60.
93. Shi, C., et al., *Quantum dots: emerging applications in urologic oncology.* Urol Oncol, 2008. **26**(1): p. 86-92.
94. Sardana, G., B. Dowell, and E.P. Diamandis, *Emerging biomarkers for the diagnosis and prognosis of prostate cancer.* Clin Chem, 2008. **54**(12): p. 1951-60.
95. Ristau, B.T., D.S. O'Keefe, and D.J. Bacich, *The prostate-specific membrane antigen: lessons and current clinical implications from 20 years of research.* Urol Oncol, 2014. **32**(3): p. 272-9.
96. Osborne, J.R., et al., *Prostate-specific membrane antigen-based imaging.* Urol Oncol, 2013. **31**(2): p. 144-54.
97. Wynant, G.E., et al., *Immunoscintigraphy of prostatic cancer: preliminary results with 111In-labeled monoclonal antibody 7E11-C5.3 (CYT-356).* Prostate, 1991. **18**(3): p. 229-41.
98. Troyer, J.K., M.L. Beckett, and G.L. Wright, Jr., *Location of prostate-specific membrane antigen in the LNCaP prostate carcinoma cell line.* Prostate, 1997. **30**(4): p. 232-42.
99. Fu, G., et al., *Structural basis for executioner caspase recognition of P5 position in substrates.* Apoptosis, 2008. **13**(11): p. 1291-302.
100. Fang, B., et al., *Caspase-3 binds diverse P4 residues in peptides as revealed by crystallography and structural modeling.* Apoptosis, 2009. **14**(5): p. 741-52.
101. Weber, I.T., et al., *Reaction intermediates discovered in crystal structures of enzymes.* Adv Protein Chem Struct Biol, 2012. **87**: p. 57-86.
102. Xue, S., et al., *Designing Single Fluorescent Protein Based Caspase Sensor For Monitoring Apoptosis In Living Cells.* Biophysical Journal, 2009. **96**(3): p. 425a.
103. Chen, N., et al., *CHAPTER 24-Enzyme Sensors for Living Cells.* Methods in Cell Biology, 2012. **112**: p. 421.
104. Qiao, J., et al., *HER2 targeted molecular MR imaging using a de novo designed protein contrast agent.* PLoS One, 2011. **6**(3): p. e18103.
105. Aggarwal, S., et al., *A dimeric peptide that binds selectively to prostate-specific membrane antigen and inhibits its enzymatic activity.* Cancer Res, 2006. **66**(18): p. 9171-7.
106. Horoszewicz, J.S., E. Kawinski, and G.P. Murphy, *Monoclonal antibodies to a new antigenic marker in epithelial prostatic cells and serum of prostatic cancer patients.* Anticancer Res, 1987. **7**(5B): p. 927-35.
107. Troyer, J.K., et al., *Biochemical characterization and mapping of the 7E11-C5.3 epitope of the prostate-specific membrane antigen.* Urol Oncol, 1995. **1**(1): p. 29-37.
108. Liu, H., et al., *Monoclonal antibodies to the extracellular domain of prostate-specific membrane antigen also react with tumor vascular endothelium.* Cancer Res, 1997. **57**(17): p. 3629-34.
109. Michaels, E.K., M. Blend, and J.C. Quintana, *111Indium-capromab pendetide unexpectedly localizes to renal cell carcinoma.* J Urol, 1999. **161**(2): p. 597-8.

110. Bander, N.H., et al., *Phase I trial of 177lutetium-labeled J591, a monoclonal antibody to prostate-specific membrane antigen, in patients with androgen-independent prostate cancer.* J Clin Oncol, 2005. **23**(21): p. 4591-601.
111. Holland, J.P., et al., *89Zr-DFO-J591 for immunoPET of prostate-specific membrane antigen expression in vivo.* J Nucl Med, 2010. **51**(8): p. 1293-300.
112. Gao, X., et al., *In vivo cancer targeting and imaging with semiconductor quantum dots.* Nat Biotechnol, 2004. **22**(8): p. 969-76.
113. Alt, K., et al., *High-resolution animal PET imaging of prostate cancer xenografts with three different 64Cu-labeled antibodies against native cell-adherent PSMA.* Prostate, 2010. **70**(13): p. 1413-21.
114. Grauer, L.S., et al., *Identification, purification, and subcellular localization of prostate-specific membrane antigen PSM' protein in the LNCaP prostatic carcinoma cell line.* Cancer Res, 1998. **58**(21): p. 4787-9.
115. Murphy, G.P., et al., *Isolation and characterization of monoclonal antibodies specific for the extracellular domain of prostate specific membrane antigen.* J Urol, 1998. **160**(6 Pt 2): p. 2396-401.
116. Chen, Y., et al., *Synthesis and biological evaluation of low molecular weight fluorescent imaging agents for the prostate-specific membrane antigen.* Bioconjug Chem, 2012. **23**(12): p. 2377-85.
117. Kim, D., Y.Y. Jeong, and S. Jon, *A drug-loaded aptamer-gold nanoparticle bioconjugate for combined CT imaging and therapy of prostate cancer.* ACS Nano, 2010. **4**(7): p. 3689-96.
118. Tse, B.W., et al., *PSMA-targeting iron oxide magnetic nanoparticles enhance MRI of preclinical prostate cancer.* Nanomedicine (Lond), 2014: p. 1-12.
119. Abdolahi, M., et al., *Synthesis and in vitro evaluation of MR molecular imaging probes using J591 mAb-conjugated SPIONs for specific detection of prostate cancer.* Contrast Media Mol Imaging, 2013. **8**(2): p. 175-84.
120. Ruggiero, A., et al., *Targeting the internal epitope of prostate-specific membrane antigen with 89Zr-7E11 immuno-PET.* J Nucl Med, 2011. **52**(10): p. 1608-15.
121. Foss, C.A., et al., *Radiolabeled small-molecule ligands for prostate-specific membrane antigen: in vivo imaging in experimental models of prostate cancer.* Clin Cancer Res, 2005. **11**(11): p. 4022-8.
122. Zechmann, C.M., et al., *Radiation dosimetry and first therapy results with a (124)I/ (131)I-labeled small molecule (MIP-1095) targeting PSMA for prostate cancer therapy.* Eur J Nucl Med Mol Imaging, 2014. **41**(7): p. 1280-92.
123. Banerjee, S.R., et al., *(6)(4)Cu-labeled inhibitors of prostate-specific membrane antigen for PET imaging of prostate cancer.* J Med Chem, 2014. **57**(6): p. 2657-69.
124. Lesche, R., et al., *Preclinical evaluation of BAY 1075553, a novel (18)F-labelled inhibitor of prostate-specific membrane antigen for PET imaging of prostate cancer.* Eur J Nucl Med Mol Imaging, 2014. **41**(1): p. 89-101.
125. Afshar-Oromieh, A., et al., *Comparison of PET/CT and PET/MRI hybrid systems using a 68Ga-labelled PSMA ligand for the diagnosis of recurrent prostate cancer: initial experience.* Eur J Nucl Med Mol Imaging, 2014. **41**(5): p. 887-97.

126. Kampmeier, F., et al., *Design and preclinical evaluation of a 99mTc-labelled diabody of mAb J591 for SPECT imaging of prostate-specific membrane antigen (PSMA).* EJNMMI Res, 2014. **4**(1): p. 13.
127. Hillier, S.M., et al., *99mTc-labeled small-molecule inhibitors of prostate-specific membrane antigen for molecular imaging of prostate cancer.* J Nucl Med, 2013. **54**(8): p. 1369-76.
128. Wang, L., et al., *Construction and in vitro/in vivo targeting of PSMA-targeted nanoscale microbubbles in prostate cancer.* Prostate, 2013. **73**(11): p. 1147-58.
129. DiPippo, V.A., et al., *Efficacy studies of an antibody-drug conjugate PSMA-ADC in patient-derived prostate cancer xenografts.* Prostate, 2014.
130. Dhar, S., et al., *Targeted delivery of cisplatin to prostate cancer cells by aptamer functionalized Pt(IV) prodrug-PLGA-PEG nanoparticles.* Proc Natl Acad Sci U S A, 2008. **105**(45): p. 17356-61.
131. Patel, O., A. Shulkes, and G.S. Baldwin, *Gastrin-releasing peptide and cancer.* Biochim Biophys Acta, 2006. **1766**(1): p. 23-41.
132. Shin, C., et al., *Conformational analysis in solution of gastrin releasing peptide.* Biochem Biophys Res Commun, 2006. **350**(1): p. 120-4.
133. Anastasi, A., V. Erspamer, and M. Bucci, *Isolation and structure of bombesin and alytesin, 2 analogous active peptides from the skin of the European amphibians Bombina and Alytes.* Experientia, 1971. **27**(2): p. 166-7.
134. Schroeder, R.P., et al., *Peptide receptor imaging of prostate cancer with radiolabelled bombesin analogues.* Methods, 2009. **48**(2): p. 200-4.
135. Jensen, R.T., et al., *International Union of Pharmacology. LXVIII. Mammalian bombesin receptors: nomenclature, distribution, pharmacology, signaling, and functions in normal and disease states.* Pharmacol Rev, 2008. **60**(1): p. 1-42.
136. Young, S.H. and E. Rozengurt, *Qdot nanocrystal conjugates conjugated to bombesin or ANG II label the cognate G protein-coupled receptor in living cells.* Am J Physiol Cell Physiol, 2006. **290**(3): p. C728-32.
137. Chen, H., et al., *A fast tumor-targeting near-infrared fluorescent probe based on bombesin analog for in vivo tumor imaging.* Contrast Media Mol Imaging, 2014. **9**(2): p. 122-34.
138. Cai, Q.Y., et al., *Near-infrared fluorescence imaging of gastrin releasing peptide receptor targeting in prostate cancer lymph node metastases.* Prostate, 2013. **73**(8): p. 842-54.
139. Wei, L., et al., *Protein-based MRI contrast agents for molecular imaging of prostate cancer.* Mol Imaging Biol, 2011. **13**(3): p. 416-23.
140. Pan, D., et al., *PET imaging of prostate tumors with (18) F-Al-NOTA-MATBBN.* Contrast Media Mol Imaging, 2014. **9**(5): p. 342-8.
141. Varasteh, Z., et al., *In vitro and in vivo evaluation of a (18)F-labeled high affinity NOTA conjugated bombesin antagonist as a PET ligand for GRPR-targeted tumor imaging.* PLoS One, 2013. **8**(12): p. e81932.
142. Liu, Y., et al., *A comparative study of radiolabeled bombesin analogs for the PET imaging of prostate cancer.* J Nucl Med, 2013. **54**(12): p. 2132-8.
143. Asti, M., et al., *Influence of different chelators on the radiochemical properties of a 68-Gallium labelled bombesin analogue.* Nucl Med Biol, 2014. **41**(1): p. 24-35.

144. Varasteh, Z., et al., *The effect of mini-PEG-based spacer length on binding and pharmacokinetic properties of a 68Ga-labeled NOTA-conjugated antagonistic analog of bombesin.* Molecules, 2014. **19**(7): p. 10455-72.
145. Kahkonen, E., et al., *In vivo imaging of prostate cancer using [68Ga]-labeled bombesin analog BAY86-7548.* Clin Cancer Res, 2013. **19**(19): p. 5434-43.
146. Jimenez-Mancilla, N., et al., *Multifunctional targeted therapy system based on (99m) Tc/(177) Lu-labeled gold nanoparticles-Tat(49-57)-Lys(3) -bombesin internalized in nuclei of prostate cancer cells.* J Labelled Comp Radiopharm, 2013. **56**(13): p. 663-71.
147. Mather, S.J., et al., *GRP Receptor Imaging of Prostate Cancer Using [(99m)Tc]Demobesin 4: a First-in-Man Study.* Mol Imaging Biol, 2014. **16**(6): p. 888-95.
148. Zhou, Z., et al., *Synthesis and in vitro and in vivo evaluation of hypoxia-enhanced 111In-bombesin conjugates for prostate cancer imaging.* J Nucl Med, 2013. **54**(9): p. 1605-12.
149. Chang, Y.J., et al., *Molecular imaging and therapeutic efficacy of 188Re-(DXR)-liposome-BBN in AR42J pancreatic tumor-bearing mice.* Oncol Rep, 2012. **28**(5): p. 1736-42.
150. Dapp, S., et al., *PEGylation, increasing specific activity and multiple dosing as strategies to improve the risk-benefit profile of targeted radionuclide therapy with 177Lu-DOTA-bombesin analogues.* EJNMMI Res, 2012. **2**(1): p. 24.
151. Wang, X.L., et al., *Targeted systemic delivery of a therapeutic siRNA with a multifunctional carrier controls tumor proliferation in mice.* Mol Pharm, 2009. **6**(3): p. 738-46.
152. Sioud, M. and A. Mobergslien, *Efficient siRNA targeted delivery into cancer cells by gastrin-releasing peptides.* Bioconjug Chem, 2012. **23**(5): p. 1040-9.
153. Schol, D., et al., *Anti-PSMA antibody-coupled gold nanorods detection by optical and electron microscopies.* Micron, 2013. **50**: p. 68-74.
154. Kim, D., et al., *Tribody: robust self-assembled trimeric targeting ligands with high stability and significantly improved target-binding strength.* Biochemistry, 2013. **52**(41): p. 7283-94.
155. Black, C.B., et al., *Cell-based screening using high-throughput flow cytometry.* Assay Drug Dev Technol, 2011. **9**(1): p. 13-20.
156. Gonzalez, L.C., *Protein microarrays, biosensors, and cell-based methods for secretome-wide extracellular protein-protein interaction mapping.* Methods, 2012. **57**(4): p. 448-58.
157. van der Merwe, P.A. and A.N. Barclay, *Transient intercellular adhesion: the importance of weak protein-protein interactions.* Trends Biochem Sci, 1994. **19**(9): p. 354-8.
158. van der Merwe, P.A., et al., *Affinity and kinetic analysis of the interaction of the cell adhesion molecules rat CD2 and CD48.* EMBO J, 1993. **12**(13): p. 4945-54.
159. van der Merwe, P.A. and A.N. Barclay, *Analysis of cell-adhesion molecule interactions using surface plasmon resonance.* Curr Opin Immunol, 1996. **8**(2): p. 257-61.
160. Schulke, N., et al., *The homodimer of prostate-specific membrane antigen is a functional target for cancer therapy.* Proc Natl Acad Sci U S A, 2003. **100**(22): p. 12590-5.
161. Sugimoto, Y., et al., *The therapeutic potential of a novel PSMA antibody and its IL-2 conjugate in prostate cancer.* Anticancer Res, 2014. **34**(1): p. 89-97.
162. Shen, D., F. Xie, and W.B. Edwards, *Evaluation of phage display discovered peptides as ligands for prostate-specific membrane antigen (PSMA).* PLoS One, 2013. **8**(7): p. e68339.

163. Hillier, S.M., et al., *Preclinical evaluation of novel glutamate-urea-lysine analogues that target prostate-specific membrane antigen as molecular imaging pharmaceuticals for prostate cancer.* Cancer Res, 2009. **69**(17): p. 6932-40.
164. Varasteh, Z., et al., *Synthesis and characterization of a high-affinity NOTA-conjugated bombesin antagonist for GRPR-targeted tumor imaging.* Bioconjug Chem, 2013. **24**(7): p. 1144-53.
165. Banerjee, S.R., et al., *A modular strategy to prepare multivalent inhibitors of prostate-specific membrane antigen (PSMA).* Oncotarget, 2011. **2**(12): p. 1244-53.
166. Chen, X., et al., *microPET and autoradiographic imaging of GRP receptor expression with 64Cu-DOTA-[Lys3]bombesin in human prostate adenocarcinoma xenografts.* J Nucl Med, 2004. **45**(8): p. 1390-7.
167. Prasanphanich, A.F., et al., *[64Cu-NOTA-8-Aoc-BBN(7-14)NH2] targeting vector for positron-emission tomography imaging of gastrin-releasing peptide receptor-expressing tissues.* Proc Natl Acad Sci U S A, 2007. **104**(30): p. 12462-7.
168. Chanda, N., et al., *Bombesin functionalized gold nanoparticles show in vitro and in vivo cancer receptor specificity.* Proc Natl Acad Sci U S A, 2010. **107**(19): p. 8760-5.
169. Qiao, J., et al., *HER2 targeted molecular MR imaging using a de novo designed protein contrast agent.* PLoS One, 2011. **6**(3): p. e18103.
170. Yu, W.W., et al., *Water-soluble quantum dots for biomedical applications.* Biochem Biophys Res Commun, 2006. **348**(3): p. 781-6.
171. Michalet, X., et al., *Quantum dots for live cells, in vivo imaging, and diagnostics.* Science, 2005. **307**(5709): p. 538-44.
172. Pinaud, F., et al., *Advances in fluorescence imaging with quantum dot bio-probes.* Biomaterials, 2006. **27**(9): p. 1679-87.
173. Caravan, P., *Strategies for increasing the sensitivity of gadolinium based MRI contrast agents.* Chem Soc Rev, 2006. **35**(6): p. 512-23.
174. De Jong, W.H., et al., *Particle size-dependent organ distribution of gold nanoparticles after intravenous administration.* Biomaterials, 2008. **29**(12): p. 1912-9.
175. Fang, J., H. Nakamura, and H. Maeda, *The EPR effect: Unique features of tumor blood vessels for drug delivery, factors involved, and limitations and augmentation of the effect.* Adv Drug Deliv Rev, 2011. **63**(3): p. 136-51.
176. Xue, S., et al., *Design of a novel class of protein-based magnetic resonance imaging contrast agents for the molecular imaging of cancer biomarkers.* Wiley Interdiscip Rev Nanomed Nanobiotechnol, 2013. **5**(2): p. 163-79.
177. Xue, S., et al., *Design of ProCAs (protein-based Gd(3+) MRI contrast agents) with high dose efficiency and capability for molecular imaging of cancer biomarkers.* Med Res Rev, 2014. **34**(5): p. 1070-99.
178. Qiao, J., et al., *Molecular imaging of EGFR/HER2 cancer biomarkers by protein MRI contrast agents.* J Biol Inorg Chem, 2014. **19**(2): p. 259-70.
179. Qiang, G., et al., *Identification of a small molecular insulin receptor agonist with potent antidiabetes activity.* Diabetes, 2014. **63**(4): p. 1394-409.
180. Liu, X., et al., *Biochemical and biophysical investigation of the brain-derived neurotrophic factor mimetic 7,8-dihydroxyflavone in the binding and activation of the TrkB receptor.* J Biol Chem, 2014. **289**(40): p. 27571-84.

181. Yang, J.J., et al., *CONTRAST AGENTS, METHODS FOR PREPARING CONTRAST AGENTS, AND METHODS OF IMAGING*, 2010, EP Patent 2,257,316.
182. Liu, Z.-r., et al., *PROTEIN AGENT FOR DIABETES TREATMENT AND BETA CELL IMAGING*, 2012, US Patent 20,120,244,080.
183. Ye, F., et al., *A peptide targeted contrast agent specific to fibrin-fibronectin complexes for cancer molecular imaging with MRI.* Bioconjug Chem, 2008. **19**(12): p. 2300-3.
184. Li, S., et al., *PEGylation of protein-based MRI contrast agents improves relaxivities and biocompatibilities.* J Inorg Biochem, 2012. **107**(1): p. 111-8.
185. Ye, Y., et al., *Probing site-specific calmodulin calcium and lanthanide affinity by grafting.* J Am Chem Soc, 2005. **127**(11): p. 3743-50.
186. Ye, Y., et al., *A grafting approach to obtain site-specific metal-binding properties of EF-hand proteins.* Protein Eng, 2003. **16**(6): p. 429-34.
187. Zhou, Y., T.K. Frey, and J.J. Yang, *Viral calciomics: interplays between Ca2+ and virus.* Cell Calcium, 2009. **46**(1): p. 1-17.
188. Huang, Y., et al., *Calmodulin regulates Ca2+-sensing receptor-mediated Ca2+ signaling and its cell surface expression.* J Biol Chem, 2010. **285**(46): p. 35919-31.
189. Jiang, Y., et al., *Elucidation of a novel extracellular calcium-binding site on metabotropic glutamate receptor 1{alpha} (mGluR1{alpha}) that controls receptor activation.* J Biol Chem, 2010. **285**(43): p. 33463-74.
190. Yanyi, C., et al., *Calciomics: prediction and analysis of EF-hand calcium binding proteins by protein engineering.* Sci China Chem, 2010. **53**(1): p. 52-60.
191. Chen, Y., et al., *Role of calcium in metalloenzymes: effects of calcium removal on the axial ligation geometry and magnetic properties of the catalytic diheme center in MauG.* Biochemistry, 2012. **51**(8): p. 1586-97.
192. Zhou, Y., S. Xue, and J.J. Yang, *Calciomics: integrative studies of Ca2+-binding proteins and their interactomes in biological systems.* Metallomics, 2013. **5**(1): p. 29-42.
193. Zhou, Y., et al., *Probing Ca2+-binding capability of viral proteins with the EF-hand motif by grafting approach.* Methods Mol Biol, 2013. **963**: p. 37-53.
194. Chen, Y., et al., *Myoplasmic resting Ca2+ regulation by ryanodine receptors is under the control of a novel Ca2+-binding region of the receptor.* Biochem J, 2014. **460**(2): p. 261-71.
195. Zhou, Y., S. Xue, and J.J. Yang, *Calcium and Viruses*, in *Encyclopedia of Metalloproteins*. 2013, Springer New York. p. 415-424.
196. Kim, S.Y., et al., *Progastrin-releasing peptide is a candidate marker for quality control in clinical sample processing and storage.* Am J Clin Pathol, 2012. **137**(2): p. 277-82.
197. Yoshimura, T., et al., *Stability of pro-gastrin-releasing peptide in serum versus plasma.* Tumour Biol, 2008. **29**(4): p. 224-30.
198. Wu, P., et al., *Adenovirus targeting to prostate-specific membrane antigen through virus-displayed, semirandom peptide library screening.* Cancer Res, 2010. **70**(23): p. 9549-53.
199. Milla, P., F. Dosio, and L. Cattel, *PEGylation of proteins and liposomes: a powerful and flexible strategy to improve the drug delivery.* Curr Drug Metab, 2012. **13**(1): p. 105-19.

200. Bickers, B. and C. Aukim-Hastie, *New molecular biomarkers for the prognosis and management of prostate cancer--the post PSA era.* Anticancer Res, 2009. **29**(8): p. 3289-98.
201. Reile, H., P.E. Armatis, and A.V. Schally, *Characterization of high-affinity receptors for bombesin/gastrin releasing peptide on the human prostate cancer cell lines PC-3 and DU-145: internalization of receptor bound 125I-(Tyr4) bombesin by tumor cells.* Prostate, 1994. **25**(1): p. 29-38.
202. Reubi, J.C., et al., *Bombesin receptor subtypes in human cancers: detection with the universal radioligand (125)I-[D-TYR(6), beta-ALA(11), PHE(13), NLE(14)] bombesin(6-14).* Clin Cancer Res, 2002. **8**(4): p. 1139-46.
203. Markwalder, R. and J.C. Reubi, *Gastrin-releasing peptide receptors in the human prostate: relation to neoplastic transformation.* Cancer Res, 1999. **59**(5): p. 1152-9.
204. Gugger, M. and J.C. Reubi, *Gastrin-releasing peptide receptors in non-neoplastic and neoplastic human breast.* Am J Pathol, 1999. **155**(6): p. 2067-76.
205. Ananias, H.J., et al., *Expression of the gastrin-releasing peptide receptor, the prostate stem cell antigen and the prostate-specific membrane antigen in lymph node and bone metastases of prostate cancer.* Prostate, 2009. **69**(10): p. 1101-8.
206. Tokita, K., et al., *Molecular basis of the selectivity of gastrin-releasing peptide receptor for gastrin-releasing peptide.* Mol Pharmacol, 2002. **61**(6): p. 1435-43.
207. Cheng, L.L., et al., *Correlation of high-resolution magic angle spinning proton magnetic resonance spectroscopy with histopathology of intact human brain tumor specimens.* Cancer Res, 1998. **58**(9): p. 1825-32.
208. Hricak, H., *MR imaging and MR spectroscopic imaging in the pre-treatment evaluation of prostate cancer.* Br J Radiol, 2005. **78 Spec No 2**: p. S103-11.
209. Winter, P.M., et al., *Molecular imaging of angiogenesis in nascent Vx-2 rabbit tumors using a novel alpha(nu)beta3-targeted nanoparticle and 1.5 tesla magnetic resonance imaging.* Cancer Res, 2003. **63**(18): p. 5838-43.
210. Wu, C.L., et al., *Metabolomic imaging for human prostate cancer detection.* Sci Transl Med, 2010. **2**(16): p. 16ra8.
211. Yu, K.K., et al., *Prostate cancer: prediction of extracapsular extension with endorectal MR imaging and three-dimensional proton MR spectroscopic imaging.* Radiology, 1999. **213**(2): p. 481-8.
212. Yang, J.J., et al., *Rational design of protein-based MRI contrast agents.* J Am Chem Soc, 2008. **130**(29): p. 9260-7.
213. Erspamer, V., G.F. Erpamer, and M. Inselvini, *Some pharmacological actions of alytesin and bombesin.* J Pharm Pharmacol, 1970. **22**(11): p. 875-6.
214. Mansi, R., et al., *Targeting GRPR in urological cancers--from basic research to clinical application.* Nat Rev Urol, 2013. **10**(4): p. 235-44.
215. Wang, L.H., et al., *Activation of neuromedin B-preferring bombesin receptors on rat glioblastoma C-6 cells increases cellular Ca2+ and phosphoinositides.* Biochem J, 1992. **286 (Pt 2)**: p. 641-8.
216. Gayen, A., S.K. Goswami, and C. Mukhopadhyay, *NMR evidence of GM1-induced conformational change of Substance P using isotropic bicelles.* Biochim Biophys Acta, 2011. **1808**(1): p. 127-39.

217. Yang, W., et al., *Design of a calcium-binding protein with desired structure in a cell adhesion molecule.* J Am Chem Soc, 2005. **127**(7): p. 2085-93.
218. Fulton, D.A., et al., *Efficient relaxivity enhancement in dendritic gadolinium complexes: effective motional coupling in medium molecular weight conjugates.* Chem Commun (Camb), 2005(4): p. 474-6.
219. Pourahmadi, M., *Joint mean-covariance models with applications to longitudinal data: unconstrained parameterisation.* Biometrika, 1999. **86**(3): p. 677-690.
220. Fischer, A.H., et al., *Hematoxylin and eosin staining of tissue and cell sections.* CSH Protoc, 2008. **2008**: p. pdb prot4986.
221. Fernandez-Castane, A., et al., *Evidencing the role of lactose permease in IPTG uptake by Escherichia coli in fed-batch high cell density cultures.* J Biotechnol, 2012. **157**(3): p. 391-8.
222. Hanaoka, K., et al., *The detection limit of a Gd3+-based T1 agent is substantially reduced when targeted to a protein microdomain.* Magn Reson Imaging, 2008. **26**(5): p. 608-17.
223. Ming, X., et al., *Intracellular delivery of an antisense oligonucleotide via endocytosis of a G protein-coupled receptor.* Nucleic Acids Res, 2010. **38**(19): p. 6567-76.
224. Sun, Y.G. and Z.F. Chen, *A gastrin-releasing peptide receptor mediates the itch sensation in the spinal cord.* Nature, 2007. **448**(7154): p. 700-3.
225. Weinmann, H.J., et al., *Characteristics of gadolinium-DTPA complex: a potential NMR contrast agent.* AJR Am J Roentgenol, 1984. **142**(3): p. 619-24.
226. Pavlicek, J., et al., *Structural characterization of P1'-diversified urea-based inhibitors of glutamate carboxypeptidase II.* Bioorg Med Chem Lett, 2014. **24**(10): p. 2340-5.
227. Subramanian, N., et al., *A strain-promoted alkyne-azide cycloaddition (SPAAC) reaction of a novel EpCAM aptamer-fluorescent conjugate for imaging of cancer cells.* Chem Commun (Camb), 2014.
228. Smith-Jones, P.M., et al., *In vitro characterization of radiolabeled monoclonal antibodies specific for the extracellular domain of prostate-specific membrane antigen.* Cancer Res, 2000. **60**(18): p. 5237-43.
229. Ben Jemaa, A., et al., *Co-expression and impact of prostate specific membrane antigen and prostate specific antigen in prostatic pathologies.* J Exp Clin Cancer Res, 2010. **29**: p. 171.
230. Murukesh, N., C. Dive, and G.C. Jayson, *Biomarkers of angiogenesis and their role in the development of VEGF inhibitors.* Br J Cancer, 2010. **102**(1): p. 8-18.
231. Millauer, B., et al., *Dominant-negative inhibition of Flk-1 suppresses the growth of many tumor types in vivo.* Cancer Res, 1996. **56**(7): p. 1615-20.
232. Brozzo, M.S., et al., *Thermodynamic and structural description of allosterically regulated VEGFR-2 dimerization.* Blood, 2012. **119**(7): p. 1781-8.
233. Backer, M.V., et al., *Molecular imaging of VEGF receptors in angiogenic vasculature with single-chain VEGF-based probes.* Nat Med, 2007. **13**(4): p. 504-9.
234. De Leon-Rodriguez, L.M., et al., *MRI detection of VEGFR2 in vivo using a low molecular weight peptoid-(Gd)8-dendron for targeting.* J Am Chem Soc, 2010. **132**(37): p. 12829-31.
235. Tweedle, M.F., *Peptide-targeted diagnostics and radiotherapeutics.* Acc Chem Res, 2009. **42**(7): p. 958-68.

236. Shrivastava, A., et al., *A distinct strategy to generate high-affinity peptide binders to receptor tyrosine kinases.* Protein Eng Des Sel, 2005. **18**(9): p. 417-24.
237. Norden, A.D., J. Drappatz, and P.Y. Wen, *Antiangiogenic therapies for high-grade glioma.* Nat Rev Neurol, 2009. **5**(11): p. 610-20.
238. Helm, L., *Optimization of gadolinium-based MRI contrast agents for high magnetic-field applications.* Future Med Chem, 2010. **2**(3): p. 385-96.
239. Caravan, P., et al., *Influence of molecular parameters and increasing magnetic field strength on relaxivity of gadolinium- and manganese-based T1 contrast agents.* Contrast Media Mol Imaging, 2009. **4**(2): p. 89-100.
240. Kragelund, B.B., et al., *Hydrophobic core substitutions in calbindin D9k: effects on Ca2+ binding and dissociation.* Biochemistry, 1998. **37**(25): p. 8926-37.
241. Moore, E.G., A.P. Samuel, and K.N. Raymond, *From antenna to assay: lessons learned in lanthanide luminescence.* Acc Chem Res, 2009. **42**(4): p. 542-52.
242. Pidcock, E. and G.R. Moore, *Structural characteristics of protein binding sites for calcium and lanthanide ions.* J Biol Inorg Chem, 2001. **6**(5-6): p. 479-89.
243. Henzl, M.T., S. Agah, and J.D. Larson, *Rat alpha- and beta-parvalbumins: comparison of their pentacarboxylate and site-interconversion variants.* Biochemistry, 2004. **43**(29): p. 9307-19.
244. Xue, S., *Design of Novel Protein-based MRI Contrast Agernets with High Relaxivity and Stability for Biomedical Imaging.* 2013.
245. Russo, G., et al., *Angiogenesis in prostate cancer: onset, progression and imaging.* BJU Int, 2012. **110**(11 Pt C): p. E794-808.